Characterising the Young Sco-Cen Association

By

Aaron Rizzuto

A thesis submitted to Macquarie University

for the degree of

Doctor of Philosophy

Department of Physics and Astronomy

March 2015

MACQUARIE
UNIVERSITY
FACULTY OF SCIENCE

Typeset in $\LaTeX\,2_\varepsilon$.

Except where acknowledged in the customary manner, the material presented in this thesis is, to the best of my knowledge, original and has not been submitted in whole or part for a degree in any university.

____

Aaron Rizzuto

Acknowledgements

Firstly, I would like to express enormous gratitude to my PhD supervisor Mike Ireland, for providing just the right balance of direction and freedom to allow me to develop my own ideas while not losing track of the goals we had planned, for providing me with the opportunity to be involved in international collaborations, and for always treating me like a friend and colleague rather than a student. I would also like to thank Gordon Robertson, for providing carefully thought-out comments to reports and papers I had written and for his encouraging words, and Dan Zucker, for lots of proof reading.

Thanks to the SUSI group members for assistance in observing and engineering for SUSI. A particular mention to Yitping Kok, for our interesting nights tandem observing. I also thank our Adam Kraus for our various discussions which helped improve this thesis. Thanks to fellow PhD students and postdocs, including Niyas Alikutty, Dimitri Douchin, Izabella Spelaniak, Joao Bento, and Carlos Bacigalupo for providing good conversation and company, and thanks to Bjorn Sturmberg for the climbing excursions.

Thank you to my family, including my mother who set me on this path that I have taken and supported me along the way, and to my brothers David and Michael who always provided encouragement and showed pride in what I was doing.

Finally I would like to thank my wife Vaness, who has provided tremendous support over the past two years. Thank you for always putting a smile on my face.

- Aaron C. Rizzuto

Publications

- **Rizzuto, A. C.**, Ireland, M. J., Zucker, D. B.,*Wise Circumstellar Disks in the Young Sco-Cen Association.* **Monthly Notices of the Royal Astronomical Society: Letters**, Volume 421, Issue 1, pp. L97-L101. (2012)
- **Rizzuto, A. C.**, Ireland, M. J., Robertson, J. G., Kok, Y.; Tuthill, P. G., Warrington, B. A., Haubois, X., Tango, W. J.; Norris, B., ten Brummelaar, T., Kraus, A. L., Jacob, A., Laliberte-Houdeville, C., *Long-Baseline Interferometric Multiplicity Survey of the Sco-Cen OB Association.* **Monthly Notices of the Royal Astronomical Society**, Volume 436, Issue 2, p.1694-1707. (2013)
- Kok, Y., Ireland, M. J., Tuthill, P. G.; Robertson, J. G., Warrington, B. A., **Rizzuto, A. C.**, Tango, W. J., *Phase-Referenced Interferometry and Narrow-Angle Astrometry with SUSI* **Journal of Astronomical Instrumentation**, Volume 2, Issue 2, id. 1340011. (2013)
- Kok, Y., Ireland, M. J., **Rizzuto, A. C.**, Tuthill, P. G.; Robertson, J. G., Warrington, B. A., Tango, W. J., *Alternative approach to precision narrow-angle astrometry for Antarctic long baseline interferometry*, **SPIE Astronomical Telescopes and Instrumentation conference**, June 2014, Paper ID 9146-103.
- **Rizzuto, A. C.**, Ireland, M. J., Kraus, A. L., *New Pre-main-Sequence Stars in the Upper Scorpius Subgroup of Sco-Cen*, **Monthly Notices of the Royal Astronomical Society**, in press. (2015)

Abstract

The young Sco-Cen association provides a unique astrophysical laboratory for the study of many different stellar properties. In this thesis we present the results of our characterisation of the young OB association Scorpius-Centaurus via four different avenues; the stellar membership of the association, the multiplicity of the high-mass stars, the prevalence of circumstellar disks among Sco-Cen members, and age-dating the association with close binary systems. These are presented in the form of four chapters, two of which are journal publications.

In the first section we present an analysis of the WISE photometric data for 829 B, A and F-type stars in the Sco-Cen association, using the latest high-mass membership probabilities. We detect debris disks associated with 134 Sco-Cen stars, with a clear increase in IR excess fraction with membership probability. We determine that 41±5% of Sco-Cen BAF stars have IR excesses, compared to 1±4% of field stars, and do not see any change in excess fraction between the Sco-Cen subgroups. Within our sample, we have observed that B-type association members have a significantly smaller excess fraction than A and F-type association members.

In the second section we present a search for new low-mass members of the Sco-Cen association, focussing on the Upper Scorpius subgroup. We developed a Bayesian kinematic selection method to prioritise candidate members, and spectroscopically confirmed 232 new Upper-Scorpius G to M-type members via their Li absorption with the WiFeS IFU. Among these new members we also identify eight companions in H-α emission using spectro-astrometric techniques, four of which are candidate wide gas-giant planets. Additionally, we observed the wide gas-giant planet host GSC-6214-0210 to have a significantly reduced H-α equivalent width of -0.63 Å, compared to the previous observation of -1.51 Å , suggesting that the rate of accretion onto the planetary companion has slowed or stopped.

In the third section we present the first multiplicity-dedicated long baseline optical interferometric survey of Sco-Cen. We have surveyed 58 Sco-Cen B-type stars with the Sydney University Stellar Interferometer and detected 23 companions at separations ranging from 7-130 mas, 13 of which are new detections. We then apply a Bayesian analysis to all available information in the literature to determine the multiplicity distribution of the 58 stars in our sample, showing that the companion frequency is $F = 1.35^{+0.27}_{-0.20}$ and the mass ratio distribution is best described by q^γ with $\gamma = -0.46$, agreeing with previous Sco-Cen high-mass star work and differing significantly from lower-mass stars in Tau-Aur. Based on our analysis, we estimate that among young B-type stars in moving groups, up to 27% are apparently single.

In the final section we present the results of a Keck NIRC2 aperture-masking program of 7 G to M-type members of the Upper Scorpius subgroup of the Sco-Cen OB association. We present orbital solutions for the binary systems we have monitored, and also determine the age, component masses, distance and reddening for each system using the orbital solutions and multi-band photometry using a Bayesian fitting procedure. We find that the age of the Upper Scorpius subgroup is 7 ± 2 Myr, with some members as old as ~ 10 Myr. This is younger than the previous estimate of Pecaut et al. 2012, but supports the hypothesis that there is an age distribution among stars kinematically consistent with Upper-Scorpius membership stretching from < 5 Myr up to $\sim$10 Myr. We propose that the current evidence for the age of Upper-Scorpius is consistent with the existence of two populations of stars in this part of Sco-Cen; one of $\sim$15 Myr, which formed with the rest of greater Sco-Cen, and a younger population of age $\sim$5 Myr, including the clearly young stars τ-Sco and ω-Sco, which formed through supernova triggered star formation from a separate molecular cloud.

Contents

List of Figures

List of Tables

1

Introduction and Background

Young stellar associations provide a glimpse into the state of a group of stars directly after formation, and are a unique “age-calibrated” sample of stars used as astrophysical laboratories. This makes young stellar associations prime locations for studying stellar properties such as the multiplicity output of star formation, and circumstellar disk evolution, as well as searching for exoplanets. In order for young associations to provide the key astrophysical statistics to required to make real distinctions between models in these areas, detailed characterisation of the membership, multiplicity and group stellar properties, including age, substructure and motion is required.

1.1 The Scorpius-Centaurus-Lupus-Crux Association

O and B-type stars are hot, massive stars, generally larger than two solar masses, which can form in a number or ways. One such way is in a gravitationally unbound, loosely organised group, which is termed an OB association. The Scorpius-Centaurus-Lupus-Crux association (Sco-Cen, Sco OB2) is the nearest OB association to the Sun, and features many of the familiar stars of the Australian southern winter sky. Sco-Cen is extraordinarily young, with star formation occurring only 5-20 Myr ago (de Geus, 1992), young compared to, for example, our Sun at 4600 Myr. The young age and proximity of Sco-Cen makes it a useful probe into the conditions of a group of stars just after formation. For this reason, Sco-Cen is considered one of the best testing grounds for new star formation models which, among other things, predict proportions of single, double and triple stars and the angular momentum loss mechanism for single, massive stars. However, in order for Sco-Cen to be a useful test sample, both its membership and multiplicity must be well characterised.

Sco-Cen was first recognised as a moving group by Kapteyn (1914) during an investigation of the parallaxes of 319 bright OB stars in the region of sky occupied by Sco-Cen. Following this, other kinematic studies confirmed that Sco-Cen is indeed a moving group (Plaskett (1928), Blaauw (1946), Bertiau (1958), Petrie (1962), Jones (1971), de Zeeuw et al. (1999)). Since its discovery, Sco-Cen has been classically divided into three distinct sub-groups (see Figure 1.1): Upper-Scorpius (US), Upper-Centaurus-Lupus (UCL), and Lower-Centaurus-Crux (LCC) (Blaauw, 1946), with mean parallaxes of 6.9, 7.1 and 8.5 milli-arcseconds, respectively, or distances of 145, 143 and 118 pc (de Zeeuw et al., 1999). UCL and LCC have little interstellar material associated with them, whereas filamentary material can be observed towards US which is connected to the Ophiuchus cloud complex, a region of ongoing star formation (de Geus, 1992). Photometry has demonstrated that the Ophiuchus cloud complex is on the near side of US at approximately 125 pc, and isochrone fitting gives ages for the sub-groups as 5 Myr for US, 13 Myr for UCL and 10 Myr for LCC (de Geus et al., 1989). Within the moving group, there is a common velocity among members inherent to the original forming cloud (Jones, 1971), however there is also a velocity dispersion around this common motion. A study of the spatial distributions of young stars by Kraus and Hillenbrand (2008) estimates the internal velocity dispersion for Upper-Scorpius to be $\sim 3.0\,\mathrm{km/s}$ and it is expected that the corresponding value for the older subgroups is larger (Larson, 1995).

UCL and LCC have received significantly less attention than US over the last half century. This is primarily due to their relative lack of concentration on the sky and the closer overlap with the Galactic plane, which makes separation of members and field stars more difficult. Moreover, large portions of UCL and LCC are not observable from the northern hemisphere, where many early investigations were conducted. Additionally, early investigation into pre-main sequence stars focused on dark and reflection nebulae, which are less frequent in UCL and LCC (Preibisch and Mamajek, 2008). Only in the last two decades have true high quality measurements of star motions on the sky become available, which have allowed separation of UCL and LCC members from the field (de Zeeuw et al., 1999, Rizzuto et al., 2011)[1].

The latest high-mass membership study of Sco-Cen was done by Rizzuto et al. (2011), who used modern Bayesian techniques, with proper motions, radial velocities and spatial positions, to provide the most complete membership of the association for stars bluer than $B-V<0.6$. This latest membership selects 531 members with probability of membership greater than 50%, and demonstrated that the velocity structure of Sco-Cen can in fact be modelled as roughly linear in Galactic longitude, rather than with discrete values for each subgroup. The Rizzuto et al. (2011) membership study builds on the previous membership by de Zeeuw et al. (1999), rejecting many members from the latter and including a number of important bright, blue stars such as α-Cru and β-Cru in the membership which had previously been considered separated from Sco-Cen despite their apparent position and clear young age. The latest high-mass membership for Sco-Cen is shown in Figure 1.1.

At this stage, the high mass (B, A and F-type) membership of Sco-Cen, which is

[1] The study Rizzuto et al. (2011) was based on the honours project work of the author of this thesis.

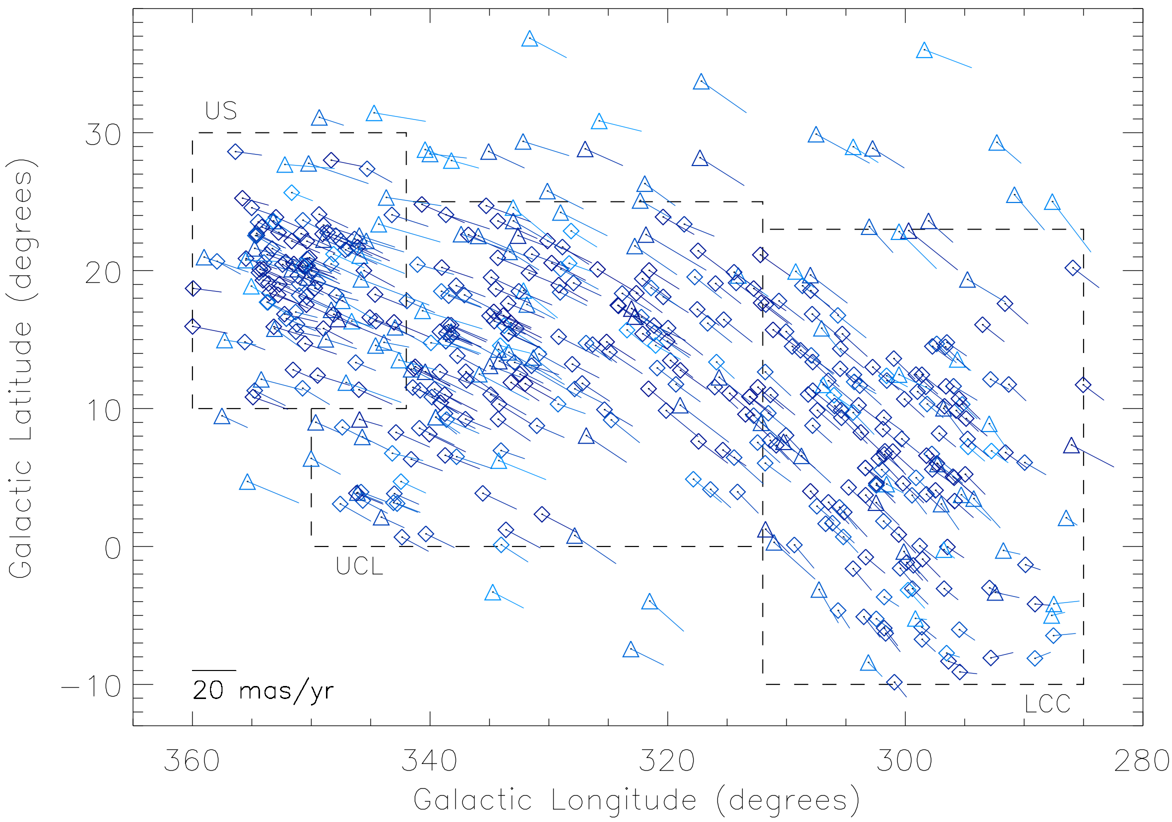

Figure 1.1: The latest (Rizzuto et al., 2011) high-mass membership of the Sco-Cen OB association. The lines indicate proper motion vectors. Higher membership probability is indicated by darker blue symbols, with 50% being the lightest symbol plotted and 100% the darkest. Members in common with the older de Zeeuw et al. (1999) membership are shown as diamonds while new members are plotted as triangles.

certainly still contaminated by interlopers due to poor radial velocities, is significantly more complete than the late-type membership, though some G to M-type members, particularly in Upper-Scorpius, have been identified and used extensively in studies of various stellar properties. Initial Mass Function (IMF) extrapolation from the high-mass membership, using any reasonable IMF law, produces an estimate of $\sim 10^4$ unidentified Sco-Cen G, K and M-type members, making the G to M-type spectral range the new frontier in Sco-Cen membership.

1.1.1 Upper Scorpius

Upper-Scorpius is the most heavily studied sub-group of Sco-Cen, due to its clear concentration and large separation from the Galactic plane ($b = 20$ degrees), making it the easiest subgroup to observe. The age of this subgroup has recently been subject to some interesting debate; the classical age of the subgroup ($\sim$5 Myr) determined from the average position of the main sequence turn-off of the most massive stars in the association has recently been revised to $\sim$11 Myr (Pecaut et al., 2012). This new age uses the PMS turn-on in the F-type stars region as well as a revised main-sequence turn-off age to approximate the age of the subgroup. The presence of unresolved multiplicity in the stars used to produce the age, combined with uncertain distances and photometric errors all contribute to the difficulty of age estimation with photometry alone. A much more reliable method is via the determination of the dynamical mass of a binary system known to be a member of a stellar population, which adds a third dimension with which to determine an age.

Despite the potentially very young age (5-11 Myr) and close proximity to the ρ-Ophiuchi molecular cloud, there are no indications of ongoing star formation in US. The majority of US members are concentrated in a small region of sky closely centered around $l = 352°$ and $b = 20°$, which is approximately 15° in extent. The distance to US was determined using photometry to be 160 ± 40 pc (de Geus et al., 1989) and this is in agreement with the mean Hipparcos distance of the Rizzuto et al. (2011) and de Zeeuw et al. (1999) members, which is 145 ± 2 pc. However, the errors on the parallaxes provided by Hipparcos are simply too large to resolve internal structure. The only conclusion drawn from the Hipparcos parallaxes is that the line of sight depth of US cannot be much greater than 70 pc (de Zeeuw et al., 1999).

A number of studies have attempted to reveal the low-mass population of US, though primarily they have been focused on small subsections of the subgroup and do not present a complete picture of the membership. An example of such work is Meyer et al. (1993), which identified 4 young objects from IRAS sources in a 80 by 80 arcsecond field near the known Upper Scorpius member σ-Sco. Pointed ROSAT X-ray studies (Martin et al., 1998, Sciortino et al., 1998) found several PMS candidates and spectroscopically confirmed PMS stars in the US and ρ-Ophiuchi star forming region.

Systematic, wide field searches for low-mass US members began with Walter et al. (1994). The authors obtained photometry and spectroscopy for the optical counterparts of detected X-ray sources. This resulted in the classification of 28 low-mass PMS stars. These new PMS stars, when placed on the HR-diagram, showed a extraordinarily small age dispersion, which was taken as an indication that the formation of these PMS stars was triggered by some external event (as is the currently accepted star formation scenario for the high-mass US stars (Preibisch and Mamajek, 2008)). Another X-Ray based study (Preibisch et al., 1998) identified 32 ROSAT All Sky Survey (RASS) optical counterparts in US which can be classified as low-mass members of the subgroup, this survey was contained to a region which intentionally excluded the ρ-Oph region. Ardila et al. (2000) presented a deep search for sub-solar mass US members. They photometrically surveyed a 14 square degree area and identified $\sim$100 possible members. When combined with low-resolution spectroscopy for a subset of these candidates, 20 stars were classified as being likely association members due to their strong H-α emission. Eleven of these candidates were later confirmed with high-resolution follow-up spectroscopy (Mohanty et al., 2004b,a), which revealed five objects with masses $< 0.1\mathrm{M}_\odot$. Martín et al. (2004) presented low-resolution spectra of some further candidates and identified 28 likely US members ranging as late as spectral type M9. In more recent years, Argiroffi et al. (2006) used *XMM-Newton* X-Ray observations and identified 22 stars as photometric member candidates, 13 of which were previously unassociated with US. Wide-field optical and near-infrared photometric survey work by Slesnick et al. (2006) led to the spectroscopic selection of 43 new low-mass members with masses less than $0.2\,\mathrm{M}_\odot$. Finally, Lodieu et al. (2007) used the UKIDSS Early Data Release and HR diagram fitting to identify $\sim$ 12 new low-mass US candidates in a $9.3\,\mathrm{deg}^2$ region. This was continued using UKIDSS Galactic Cluster Survey data (Lodieu et al., 2007) revealing 129 photometric and proper motion members with estimated masses in the 0.3-0.007 $\mathrm{M}_\odot$ range.

One very important search for PMS Sco-Cen members was done by Preibisch

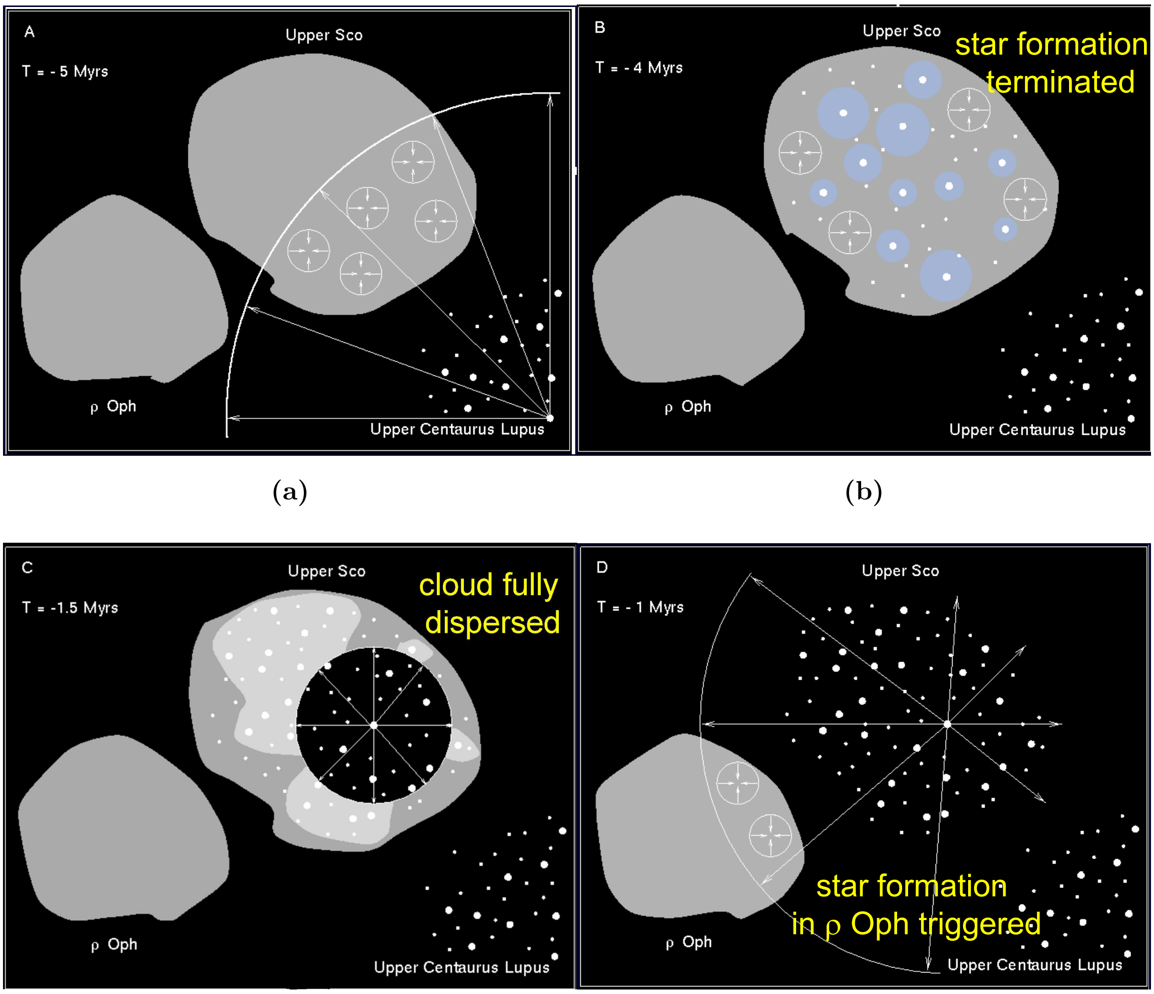

(a) (b) (c) (d)

Figure 1.2: Triggered star formation for Upper-Scorpius and the nearby star forming region ρ-Oph (Preibisch and Mamajek, 2008). The current paradigm for the Upper Scorpius star formation history revolves around the idea that the Upper Scorpius subgroup underwent triggered star formation, caused by a passing supernova shock originating in UCL. A subsequent supernova from Upper Scorpius is then thought to have triggered star formation in the ρ-Oph clouds. While this picture way be generally correct, there are outstanding issues including the possible superposition of Upper Scorpius and UCL stars and the details of the preceding star formation in greater Sco-Cen.

et al. (2002) using the 2dF (two degree field) multi-object spectrograph on the Anglo-Australian Telescope (AAT). This survey revealed 166 PMS, low-mass members, most of which are likely to be M-type dwarfs with unusually low surface gravities due to their young age. Preibisch et al. (2002) found the low mass members to be spatially consistent with the high-mass members, with ages corresponding to ∼5 Myr, agreeing with the original high-mass star age (Preibisch and Mamajek, 2008). This suggests that the low-mass members do not have an origin involving ejection from high mass multiples. Furthermore, there is no evidence for any significant age dispersion among the current US members, implying that these stars formed almost simultaneously. It has been suggested that star formation in Sco-Cen was triggered by the impact of the inner spiral arm shockwave with a large molecular cloud (Fernández et al., 2008), while the star formation process in US has thus been considered to be triggered process driven by shocks from older part of Sco Cen (Preibisch and Mamajek, 2008, Vanhala and Cameron, 1998). The triggering effect has been hypothesised to be the shockwave created by several supernova explosions in UCL which occurred approximately 12 Myr ago, compressing molecular cloud material to the critical density required for collapse. Figure 1.2 provides a graphical overview of the proposed mechanism. Observations of the kinematics of the large HI loops surrounding Sco-Cen suggest that the shockwaves passed US approximately 5 Myr ago, triggering star formation and subsequent dispersal of the cloud material. This triggered star formation is also thought to have created the young groups η-Cha, TW-Hydra, and CrA, which all show space motions indicative of an origin near UCL 12 Myr years ago (Mamajek and Feigelson, 2001b). A further sequence of Upper-Scorpius supernovae is then thought to have triggered star formation in the ρ-Oph star forming region and the Lupus clouds. The approximate time of crossing of the UCL supernovae shockwaves agrees with the youngest possible stellar age of Upper-Scorpius (de Geus, 1992), but shows a distinct difference to the newest age based on modern isochrones and photometry of B and F-type members (Pecaut et al., 2012).

1.1.2 Upper-Centaurus-Lupus and Lower-Centaurus-Crux

UCL is a much larger subgroup, both in number and extent on the sky, than its more northern sibling US, and it shows a greater level of diffusion of its members on the sky. UCL is the oldest subgroup in the association with an age of ∼18 Myr and is spread across the large region of sky ($312° < l < 342°$). The selected members have a mean distance of 140 ± 2 pc, with an important feature of UCL being the clumping seen within the subgroup around $(l, b) = (338, 15), (334, 16)$ and $(338, 10)$ degrees. Furthermore, there is a clear area completely absent of high-mass members between longitudes $(152° < l < 330°)$ and latitudes $(0° < b < 10°)$. This non-uniform distribution of members may suggest UCL has substructure, although no further elaboration has been made regarding this feature.

As mentioned above, UCL has been recognised as a potential site for the triggering of star formation in the younger subgroup US; de Geus (1992) calculated that the number of supernova explosions that have taken place in UCL is $6{\pm}3$, and demonstrated that energy imparted by the supernovae is consistent with the kinematics of the 100 pc expanding HI loops centered on UCL. This result was in agreement with the suggestion that massive UCL members destroyed the original Sco-Cen molecular cloud complex and dispersed the remaining gas not involved in star formation into what are now observed to be the large HI loops around Sco-Cen (Weaver, 1979).

The low-mass star population has only been the primary target of a single survey, by Mamajek et al. (2002), which identified 56 UCL (1.1 - 1.4 solar mass of GK-type) members by cross referencing proper-motion selected stars from Hoogerwerf (2000) with ROSAT X-ray sources from the All-Sky-Survey. The stars from this survey were classified as pre-main sequence by the strength of their Li lines. Mamajek et al. (2002) also measured the spectra of 18 GK-type stars selected from the Hipparcos catalogue by de Zeeuw et al. (1999), and confirmed 12 of these 18 as UCL members. There are likely to be ~2000 sub-solar mass stars still to be found in UCL (Mamajek et al., 2002), regardless of the choice of IMF used to make the prediction.

LCC is the nearest Sco-Cen subgroup to the Sun, with members showing a mean distance of 118 ± 2 pc, which is significantly closer than UCL and US. LCC has an estimated age of ~ 17 Myr (Carpenter et al., 2009), which places it at approximately the same age as UCL. This closest subgroup is located almost entirely on the Galactic Plane, resulting in a more difficult velocity distinction from field stars. As with UCL, there is a non-uniformity in member distribution, suggesting an as yet unresolved substructure is present in the subgroup. The latest high-mass membership (Rizzuto et al., 2011) included the previously rejected stars β-Cru and HIP 59449, both of which are thought to be binaries with ≥ 10 yr periods, and so Hipparcos proper motions may not be representative of the true photocentre motion. Finally, the open cluster IC 2602, which can be seen at (l, b) $(290, -5)$, has been suggested as belonging to LCC (Blaauw, 1964); however, the combined search method of de Zeeuw et al. (1999) has identified IC 2602 as an entirely separate group, agreeing with the analysis of Rizzuto et al. (2011), which finds very low membership probability for IC 2602 members.

The star formation history of these two older Sco-Cen subgroups is considerably more complex than the supernovae-triggered mechanism proposed for Upper-Scorpius. Both subgroups appear to be of similar age $(15 - 18)$ Myr, which agrees with the orbital age of the double lined spectroscopic binary β-Cen (Ausseloos et al., 2006), with possible substructure visible in the high-mass membership of the subgroups (Rizzuto et al., 2011, de Zeeuw et al., 1999). A potential formation scenario involves sequential star formation triggering through expanding HII regions surrounding O and B-type stars (Elmegreen and Lada, 1977). A more complete membership of these subgroups, extending down into the M-type regime, will further illuminate the star formation history of the bulk of Sco-Cen.

1.1.3 Low-Mass Stars in UCL and LCC

The majority of searches for low-mass and PMS stars in the older two subgroups of Sco-Cen were often conducted together and hence, for brevity and to reduce repetition I describe the state of knowledge in these two subgroups in one section.

As was historically the case for the search for high-mass members of the association population, UCL and LCC have received significantly less attention that US in the low-mass regime. There is some justification for this; the daunting difference in scope when moving from the relatively compact US to the great expanse of UCL and LCC on the sky requires a larger survey effort to produce results of similar significance to the age and star formation history when compared to US. In addition, there is definite substructure within the older two subgroups, with no definite "centre" at which to begin a series of observations.

Prior to the commencement of ROSAT pointed observations and the ROSAT All-Sky-Survey (RASS) there were very few known G-type and later members of UCL, and no known late-type members of LCC. The first UCL late-type member was HD 113703B (Catchpole, 1971), followed by HD 12979B and HD 143939B (Lindroos, 1986, Huélamo et al., 2000).

The Lupus dark clouds, a region of ongoing star formation and the target of many ROSAT PMS surveys, are located within the same region of sky as the UCL subgroup near $(l, b) = (335, 12)$. This has led to the indirect identification of a number of UCL candidate PMS members. Krautter et al. (1997) conducted a wide field survey for X-ray luminous stars in a 230 square-degree section of sky around the Lupus dark clouds, resulting in the identification of 136 candidate T-Tauri stars. 89 of these objects were found scattered around a wide region with RASS. These "off-cloud" PMS objects were found to be significantly older than the age of the Lupus cloud members (∼10 Myr vs. ∼2 Myr) (Wichmann et al., 1997a). A spectroscopic follow-up of a number of these objects identified 48 Li-rich stars, spatially consistent with UCL on the sky (Wichmann et al., 1997b). It was surmised that these objects were either ejected from the Lupus dark clouds, or part of the Gould Belt, with ages <∼60 Myr. It is important to note that the Gould Belt, in this region of sky, is essentially defined by the high-mass members of the subgroups of Sco-Cen and the gas associated with the Lupus and Rho-Ophiuci clouds. The vast majority of the Krautter et al. (1997) stars are spatially consistent with λ-Lup and ϕ^2-Lup, two B-type UCL members, and substructure within the high-mass population of UCL, and hence it is commonly believed that these stars are likely to be UCL members based on a simple comparison of UCAC2 proper motions and the expected association velocity (some have been confirmed, while others have not). The Wichmann et al. (1997b) stars display a large range of inferred cluster parallaxes (90 pc to 200 pc) which is consistent with the high-mass population distance measurements from Hipparcos (Rizzuto et al., 2011).

Park and Finley (1996) identified 6 X-ray variable sources near β-Crucis in a ROSAT pointing. Based on X-ray to optical flux ratios and spectral fits, it was hypothesised that these objects were T Tauri stars. Low resolution spectroscopy confirmed that these stars were in fact Li-rich, and were thus the first identified late-type stars in the LCC subgroup of Sco-Cen (Feigelson and Lawson, 1997). Following this, Zuckerman et al. (2001), in an attempt to spectroscopically identify new members of the TW Hya association (which shares a region of the sky with LCC), found a population of 8 new T Tauri stars with optical and infrared fluxes inconsistent with the TW Hya association. Mamajek and Feigelson (2001a), Mamajek (2005) surmised after a kinematic investigation that these objects are very likely to be PMS LCC members.

The first wide-field spectroscopic survey with the explicit purpose of identifying new UCL and LCC PMS members was conducted by Mamajek et al. (2002). They selected candidates by cross referencing proper motions with X-ray sources from the RASS Bright Star Catalog, as well as 18 late-type candidates from the de Zeeuw et al. (1999) Hipparcos membership. Using the spectroscopic absorption features Li 6708 Å to assign youth and Sr 4077 Å to separate giants and subgiants, they identified 88 G and K-type PMS members of UCL and LCC. Mamajek et al. (2002) used these new members to produce the age estimates of ∼16 and ∼17 Myr for UCL and LCC respectively.

1.1.4 Binary Systems in Sco-Cen

The resulting multiplicity properties of star formation are an interesting tool for probing the star formation process, and are uniquely explorable in large, unbound, nearby associations such as Sco-Cen, and can provide valuable insight for our understanding of star formation mechanisms (Blaauw, 1991). For more than a decade it has been widely accepted that at least half of all stars form in binary pairs (Mathieu, 1994, Raghavan et al., 2010), though they are still a relatively poorly understood mode of star formation. One particular unknown aspect is the role of multiplicity in the redistribution of angular momentum during star formation (Larson, 2010). Observations have also revealed that $70 - 90\%$ of stars form in clusters (Lada and Lada, 2003). This all points to the importance of a complete understanding of the star formation mechanisms, including multiplicity properties, of stars in young associations.

To test model predictions and to inspire further work into star formation, a detailed knowledge of the multiplicity of a primordial stellar population would be the ideal. This would be a population of stars whose formation processes have finished and which have stopped accreting gas from their surroundings, but before dynamical interactions have altered the multiplicity distribution in any significant way. Young stellar OB associations, such as Sco-Cen, are the closest objects to these conditions and provide a large sample of young, newly formed stars for multiplicity studies.

A complete picture of the multiplicity properties of the Sco-Cen association is not currently well known, though there are a number of studies which reveal the multiplicity of certain mass-ratio and separation regimes for different parts of the association. Simulation of selection effects in observations of moving-groups has produced an estimate for the binary population of Sco-Cen which is approximately 70 percent for late B and A-type stars (Kouwenhoven et al., 2007).

In our first paper concerning the Sco-Cen OB association (Rizzuto et al., 2011), we produced an improved high-mass membership which included 436 stars bluer than $B - V = 0.6$. This is a large sample of stars which are as young as 5 Myrs to survey for multiplicity information. The past decade has shown significant progress being made in characterising the binary population of the Sco-Cen association. A survey of 199 A and late B-type stars in Sco-Cen was done by Kouwenhoven et al. (2005) using the ESO 3.6 meter telescope at La Silla, Chile with the ADONIS/SHARPII+ instrument. They detected 74 candidate physical companions around primaries fainter than $V \sim 6$ magnitudes and with angular separations of 0.22" to 12.4". Of these, 41 were previously unseen. Another study by Shatsky and Tokovinin (2002) examined 115 B-type stars in the Sco-Cen association for visual companions using the ADONIS near-infrared coronograph, revealing 37 physical companions to Sco-Cen stars at separations of 50-900 AU, 10 of which were new detections, and provided a mass ratio distribution estimate of $q^{-0.5}$. A more recent study, which compiled observational data of Sco-Cen binary systems in a wide mass range covering both spectroscopic and wide imaging, has produced a binary fraction estimate of $> 70\%$, and a mass ratio distribution of $q^{-0.4}$ by simulating selection effects in moving group observations (Kouwenhoven et al., 2007).

There is some work still being done to identify companions to Sco-Cen stars in the spectroscopic regime; Jilinski et al. (2006) identified three new B-type Sco-Cen spectroscopic binaries among 56 targets using the FEROS echelle spectrograph. Most B-type Sco-Cen members have historically been observed spectroscopically with the intention of identifying companions. The study of Levato et al. (1987) contains an excellent summary of many of the known spectroscopic binaries among the highest mass objects in Sco-Cen. For intermediate mass spectroscopic binaries, Kouwenhoven et al. (2007) contains a full list of observational references regarding detected companions.

The general result that Sco-Cen intermediate and high-mass members have a large multiplicity fraction is indeed interesting, and considering that solar mass stars do not share this property (∼50% multiplicity), has important implications for stars formation in the high-mass regime which have not yet been fully elucidated. Improved knowledge of the primordial multiplicity distribution of stars in all mass ranges will be crucial to our understanding star formation history in young associations, and in constraining and guiding future star-formation models.

Between the imaging and spectroscopic companion separation regimes, there is a relatively understudied range of separations, approximately 7-100 mas which has been neglected due to the relatively small number of instruments capable of making such observations. For the Sco-Cen association, this corresponds to separations of 1-10 AU, an important range in constraining the multiplicity distribution of the association. Interferometry is ideal for conducting survey work in this key range, and the Sydney University Stellar Interferometer (SUSI) is placed ideally to carry out a survey of B-type stars with the goal of identifying new companions to Sco-Cen stars.

1.1.5 Interferometry

Interferometry makes use of the principle of superposition to recombine light from the same source in a way which will provide additional information about the source. A basic interferometer requires two apertures (such as telescopes or mirrors), a variable path length of delay line, and a beam combination system, which combines the light from the two apertures (see Figure 1.3). Young's double slit experiment is a simple example of a basic interferometer.

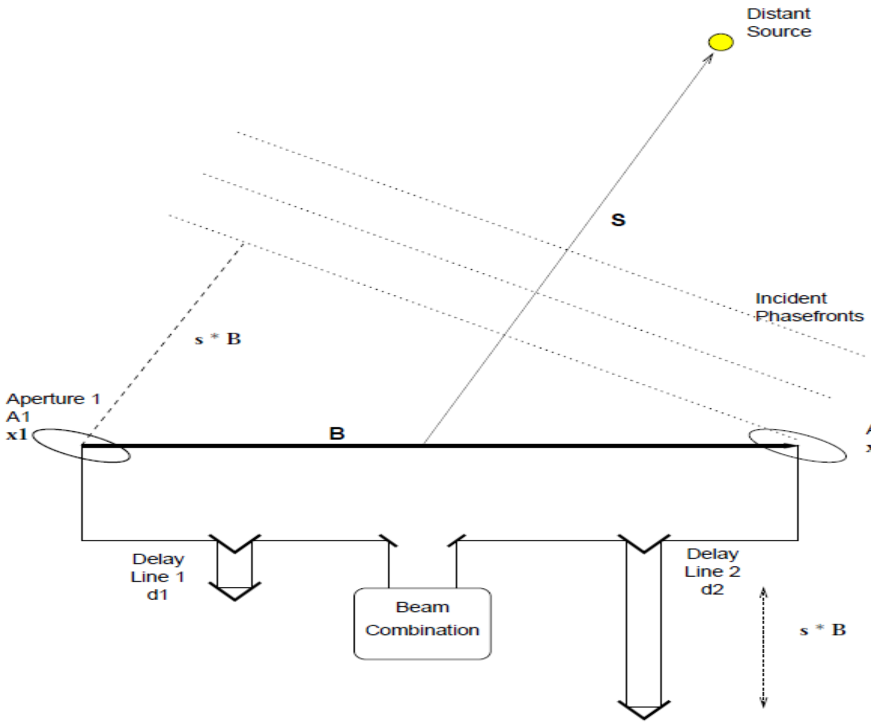

Figure 1.3: A simple interferometer

An interferometer measures finite components of the spatial frequency spectrum of a source brightness distribution on the sky and the coherence of the light at the given spatial frequency. The observable is the squared fringe visibility (V^2), which is a measure of the contrast of an interference fringe. In the most simple form, the squared fringe visibility can be defined as:

$$V^2 = \left(\frac{I_{max} - I_{min}}{I_{max} + I_{min}} \right)^2, \tag{1.1}$$

where I_{max} and I_{min} are the maximum and minimum intensities of an interference pattern (Michelson, 1891). From Equation (1.1), it is clear that the fringe visibility is a dimensionless quantity which can take values between zero and one, with totally coherent light producing a visibility of one and incoherent light zero. Figure 1.4 gives a clear example of this. More importantly, the fringe visibility seen by the interferometer depends on the distance between the apertures (called the baseline), and the wavelength of observation. This is expressed in the van Cittert-Zernike theorem:

$$Q(\vec{B}) = \frac{\int I(\vec{\alpha}) e^{-ik\vec{B}\cdot\vec{\alpha}} d\vec{\alpha}}{\int I(\vec{\alpha}) d\vec{\alpha}}, \tag{1.2}$$

where $I(\vec{\alpha})$ is the intensity distribution of a source on the sky, $\vec{\alpha}$ is a two dimensional sky coordinate, k is $\frac{2\pi}{\lambda}$ (wavenumber) and $\vec{B}$ is the baseline vector. Q is the complex visibility, and is related to the measured fringe visibility by $V = |Q|S$ where S is the system visibility measured using a calibrator star (Lawson, 2000). What the van Cittert-Zernike theorem means is that the complex visibility is in fact the Fourier transform of the image source.

For application to the work in this thesis, namely, detecting binarity in members of the Sco-Cen association, it is important to know the expected squared visibility from two close sources. This can be calculated from the sum of two uniform disk sources with a separation between them (Hanbury Brown et al., 1967):

$$V_{binary}^2 = \frac{V_1^2 + r^2 V_2^2 + 2r|V_1||V_2|\cos(k\vec{B}\cdot \vec{s_{binary}})}{(1+r)^2}, \tag{1.3}$$

where V_1 and V_2 are the visibilities of the two component stars of the binary system, $\vec{s_{binary}}$ is the separation of the binaries on the sky (for example, 15 milliarc-seconds for SUSI targets), and r is the brightness ratio of the two stars. To illustrate how Equation (1.3) is useful to an astronomer looking for binarity, it is helpful to take the example of two point sources of equal brightness. In this case $r = V_1 = V_2 = 1$, which reduces Equation (1.3) to a sinusoidal oscillation of visibility against wavelength, with period dependent on the separation of the two point sources on the sky (see Figure 1.4). Hence, if the squared visibility of a source is measured over a range of wavelengths, and the source is resolved, then binarity can be detected and characterised based on the oscillations around the single-source curve.

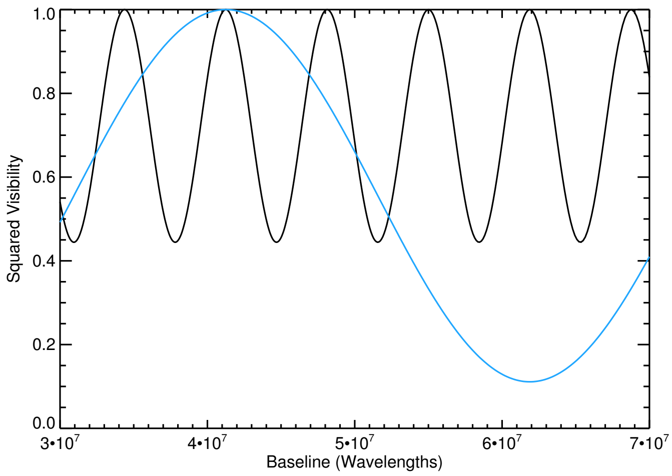

Figure 1.4: The wavelength behaviour of the squared visibility of two equally bright point sources at two separations and brightness ratios as seen by a two element interferometer of baseline 30 m. The black curve is for two point sources with angular separation of 30 mas and brightness ratio 1:5, while the blue curve is for angular separation 10 mas and contrast of 1:2. The presence of oscillations differentiates between the presence of one point source and two point sources: In this picture, a single point source would display squared visibility of one for all wavelengths.

1.2 Youth Indicators for Low-Mass Stars

There are a number of useful youth diagnostics or indicators that have been employed in identifying members of young associations such as Sco-Cen. A number of these have been mentioned above, and we will now expand on some of these methods with a focus on identification of G, K and M-type members of Sco-Cen. As such, a discussion of kinematic based selection, for which astrometry of sufficient accuracy for definitive membership selection is only available for B, A and F-type stars, will be best left to the works of de Zeeuw et al. (1999) and more recently Rizzuto et al. (2011), which both provide the starting point for the kinematic work described below in Chapter 3.1. The most widely and definitively used indicator of youth for late-type stars is the presence of lithium absorption features, often in conjunction with chromospheric and accretion produced H-α emission in the stellar spectrum. In addition to lithium, X-ray emission and chromospheric activity are often used as indicators of youth, although only X-ray emission has been used to identify PMS Sco-Cen members thus far. Figure 1.5

diagrammatically displays the spectral-type and age ranges over which these different techniques can be used.

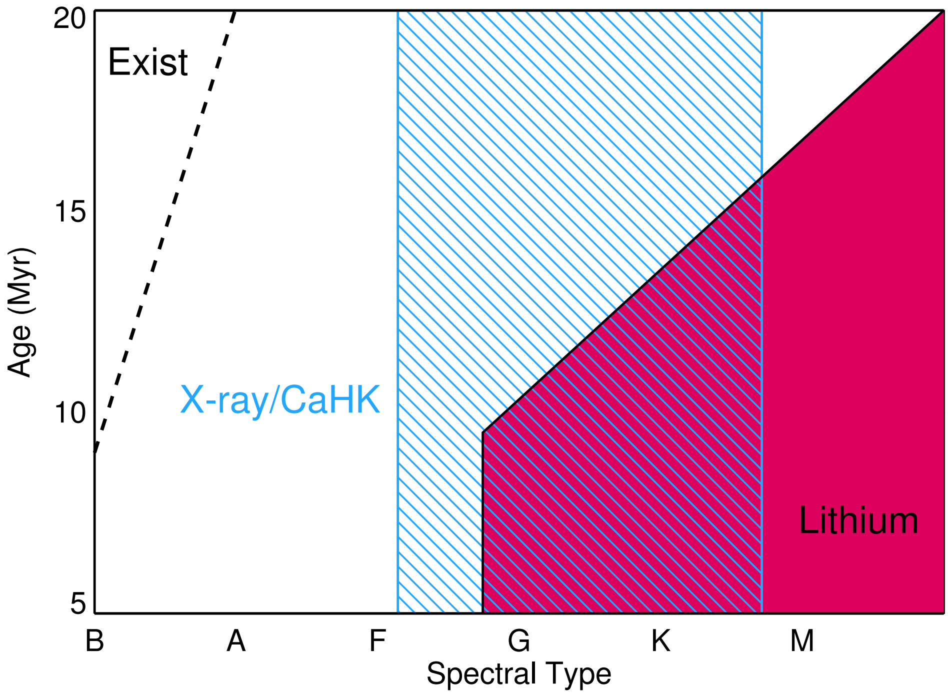

Figure 1.5: The spectral-type and age ranges over which the commonly used age indicators for identification of young stars in associations like Sco-Cen function. For the most massive stars, their existence alone provides an upper age limit. For F to late K-type stars, X-ray emission and the Ca HK doublet provide youth information, while Lithium presence provide the most robust youth diagnostic for stars later than G-type. Note the gap in age indicating techniques in the A to early F-type star range.

1.2.1 X-Ray Emission

It is well documented that stellar rotation based emission, including X-ray emission, decays with age (Henry et al., 1996), according to empirical rotation-age-activity relations that are underpinned by stellar magnetic dynamo theory. X-ray emission is often used as a tracer for stellar surface magnetic fields, and for any given late spectral-type, a large proportion of pre-main sequence stars emit X-rays at luminosities $\sim 2-3$ orders of magnitude greater than stars on the main sequence, making this property a useful youth indicator (Montmerle et al., 1983, Walter et al., 1988, Wichmann et al., 1997a, Neuhaeuser et al., 1997)

Typically, PMS stars in the age range of $\sim 1 - 100$ Myr show a slow decline in fractional X-ray luminosity (Preibisch and Feigelson, 2005), meaning that X-ray activity is a broad-stroke indicator for youth, and cannot be used to distinguish Upper-Scorpius (5-10 Myr) members from older $\sim$ 20 Myr members of UCL or LCC, or even significantly younger members of ρ-Ophiucus ($\sim$2 Myr).

In Sco-Cen, other than a small number of EINSTEIN pointed fields (Walter et al., 1994) the majority of X-ray candidate member selection was done using the ROSAT All Sky (RASS) data, and as mentioned above, the majority of this work was focussed on Upper-Scorpius. In the Upper-Scorpius region, the RASS count rate detection limit is approximately 0.02 counts/sec, which corresponds to an X-ray luminosity of $\sim 10^{30}$ ergs/sec at the typical distance of Upper-Scorpius stars (>100 pc), and for a typical plasma temperature for a PMS star (Preibisch et al., 1998). Preibisch et al. (1998) estimate that only $\sim$30% of Upper-Scorpius PMS stars would be detectable at this limit, and indeed, pointed, deep ROSAT observation of other regions reveal further X-ray sources with smaller X-ray luminosity (Preibisch, 1997).

What is clear is that the detection of an X-ray counterpart to a potential PMS star is an indicator of youth that often requires spectroscopic follow-up, because activity and rotation indicators such as X-ray emission or chromospheric Ca HK emission are not clear diagnostics of youth; some $\sim$50-100 Myr young stars, such as the Pleiades members, are indistinguishable from $5 - 20$ Myr Sco-Cen members in terms of X-ray luminosity or chromospheric activity (Mamajek and Hillenbrand, 2008). Given the evidence that the Sco-Cen subgroups have undergone mixing over several degrees on the sky (Rizzuto et al., 2011), caution must be applied in using X-ray selected (or for that matter, Li selected) samples of Upper-Scorpius members to determine bulk physical properties of the subgroup.

Currently, the available X-ray data for Upper-Scorpius and most of Sco-Cen are published (Preibisch et al., 1998, Mamajek et al., 2002), and the collection of further X-ray data is significantly less promising than collecting spectra of vast numbers of candidate Sco-Cen members.

1.2.2 The Calcium HK Doublet

The Calcium II H and K lines (3968.5 and 3933.7 Å) have been used extensively as a chromospheric emission indicator for quite some time (Vaughan et al., 1978b), and has been used historically, in the form of the R'_{HK} index, as an age estimator for field stars of approximately solar mass. The stellar magnetic dynamo is the generating source of chromospheric emission, the strength of which observationally scales with stellar rotational velocity (Noyes et al., 1984). Stellar rotation and chromospheric emission are both empirically constrained to decay as a star ages (Wilson, 1963, Skumanich, 1972, Soderblom et al., 1991, Henry et al., 1996). The primary Ca II observable is the Mount Wilson index S_{MW}, which is measured as the ratio of Ca HK core emission to continuum emission around the Ca II spectral region. This system was defined at Mount Wilson by Vaughan et al. (1978a) and has since been the standard system with which Ca HK emission is measured, and is a measurement of the Ca HK emission to total luminosity ratio. The S_{MW} index is calculated as the band ratio measurement of two triangular bandpasses centred on the Ca HK line cores (traditionally with FWHM of 1.09 Å, though in practical use this width should be no smaller than the resolution in a given spectrum) and two 25 Å wide red and violet continuum bands centred on 4000 Å and 3900 Å:

$$S_{MW} = \frac{H + K}{R + V}. \tag{1.4}$$

The S_{MW} index is strongly dependent on stellar temperature or spectral type and thus in itself is not a valid age indicator without further information (Noyes et al., 1984). Several studies have determined empirical conversions between S_{MW} and the "chromospheric activity index" R_{HK}, all of which are based on a $B - V$ colour (Middelkoop, 1982);

$$R_{HK} = 1.340 \times 10^{-4} C_{cf}(B - V) S_{MW}, \tag{1.5}$$

where the numerical factor absorbs both the Stefan-Boltzmann constant and a normalisation factor. The Middelkoop (1982) conversion factor, $C_{cf}(B-V)$, is given by;

$$\log C_{cf} = 1.13(B-V)^3 - 3.91(B-V)^2 + 2.84(B-V) - 0.47. \tag{1.6}$$

Noyes et al. (1984) produced a correction to this conversion factor (C'_{cf}) by setting $\log C'_{cf} = \log c_{cf} + \Delta \log C$ where;

$$\Delta \log C = \begin{cases} 0 & B-V > 0.63 \\ 0.135x - 0.814x^2 + 6.03x^3 & B-V < 0.63 \end{cases} \tag{1.7}$$

with $x = 0.63 - (B-V)$.

The R_{HK} index contains both the chromospheric and photospheric components of the stellar Ca II emission, and this is accounted for via a further colour-dependent conversion, which was empirically determined by Hartmann et al. (1984),

$$R_{phot} = -4.898 + 1.918(B-V)^2 - 2.893(B-V)^3, \tag{1.8}$$

to use in the correction

$$R'_{HK} = R_{HK} - R_{phot}. \tag{1.9}$$

It is important to note that the above conversions are constrained only for stars with colour $B-V > 0.4$. Note that with a properly calibrated spectrophotometer such as that which was used originally at Mouth Wilson, and a bolometric correction, this process of calibration with spectral measurements would be unnecessary.

Mamajek and Hillenbrand (2008) calibrated an empirical Ca HK activity-age relation, valid for stars with colour $0.5 < B-V < 0.9$ which corresponds to stars later than approximately spectral type F5. The colour range $0.42 < B-V < 0.5$ appears to be a transition region in which rotation-activity correlation breaks down, chromospheric activity diminishes and magnetic breaking becomes inefficient (Wolff et al., 1985, Garcia-Lopez et al., 1993). This corresponds to spectral types of approximately F3-F6. Previous Ca II activity surveys, particularly those which contain large numbers of field stars in the southern sky and known Scorpius-Centaurus association members, have an early limit of approximately F5, and extend down to early M-type stars (Henry et al., 1996, Wright et al., 2004, Gray et al., 2006, White et al., 2007). Only a small number (<10) of early F-type stars have a published R'_{HK} value (Noyes et al., 1984) and no A-type stars have measured Ca II activities.

1.2.3 The Relation Between Chromospheric Calcium II and X-Ray Activity

X-ray luminosity, or more specifically, the fractional X-ray luminosity ($\log(L_X/L_{bol})$) has been shown to be quite well correlated with the Ca HK activity index ($\log R'_{HK}$) over a wide range of masses and ages for solar-type dwarfs (Sterzik and Schmitt, 1997). Studies of the solar-type dwarfs (the Sun included) show that coronal activity traces chromospheric activity over time. It is important to note that R'_{HK} varies by approximately a factor of ten from stars of T Tauri age (<10 Myr) to field stars older than 4 Gyr, while the equivalent X-ray activity index R_X varies by approximately a factor of 30 (Mamajek and Hillenbrand, 2008). This implies that if available, the X-ray activity is a more appropriate age diagnostic than the chromospheric activity index, as it provides higher effective age resolution.

1.2.4 Lithium Depletion

The presence of lithium in a star, identified by the lithium 6708Å absorption feature in a stellar spectrum, is a decisive indicator of youth or PMS nature (D'Antona and Mazzitelli, 1994). The initial lithium content of low-mass PMS stars is depleted on a timescale of ~ 100 Myr, meaning that members of young OB associations such as Sco-Cen, with ages < 30 Myr, still posseses the majority of their initial lithium, and this can be identified in their strong lithium line, while older field stars show no lithium absorption.

In Figure 1.6, we have plotted the lithium abundance as a function of $B-V$ colour from the Siess et al. (2000) PMS models for ages indicative of Sco-Cen and older

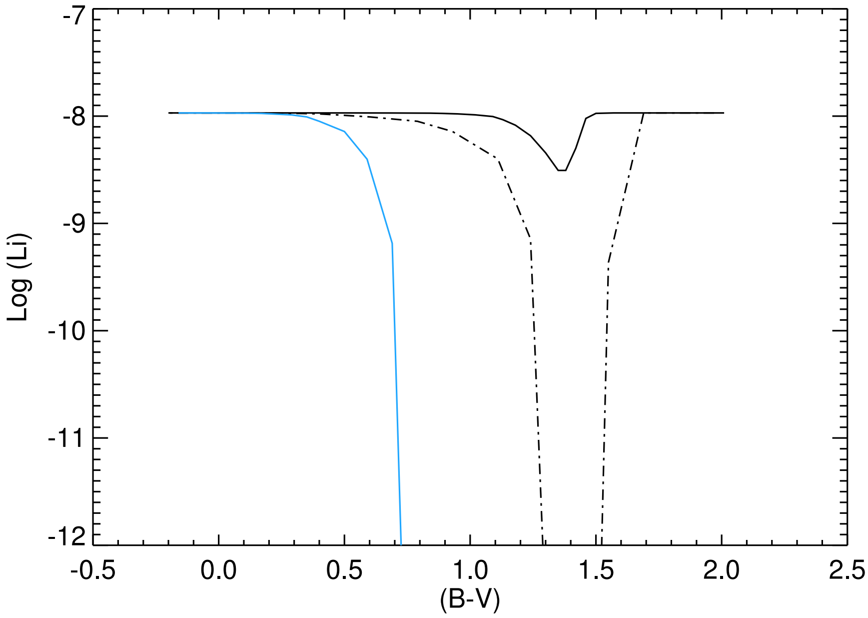

Figure 1.6: Lithium abundance for the Siess et al. (2000) models as a function of $B-V$ colour for ages 5 Myr (solid), 20 Myr (dot-dashed) and 100 Myr (blue). The figure illustrates that the presence of lithium for late F to mid M-type stars is a reliable indicator of youth, with the strongest diagnostic use being for early M-type stars.

stars. From the figure it is clear that lithium depletion occurs for a large range of spectral types, spanning late ~M5 stars to late F-type stars, and is strongest as an age diagnostic at spectral type M1. The study of Chen et al. (2011) illustrates this point further using empirical Li line strength measurements in Upper Scorpius. For stars earlier than mid F-type ($B-V > 0.5$ in Figure 1.6), Lithium ceases to function as a youth indicator due to the lack of a convective zone for stars of these temperatures.

Lithium 6708 Å is significantly easier to use as a spectral age indicator for PMS stars when compared to the need for accurate flux calibrations, complicated conversions and empirical systems that are required for Ca-HK measurements. To utilise the lithium 6708Å line as an age diagnostic, one only needs to measure the equivalent width of the spectral line. Typically for Sco-Cen aged stars (<30 Myr), a lithium 6708Å equivalent width of more than ~0.1Å would place a stars as pre-main sequence; hence, mid-resolution spectroscopy (R>1000) is required to obtain sufficient sampling of the line, and sufficient signal-to-noise is needed to obtain an accuracy of at least 0.1 Å, to resolve the Li 6708Å line of the more depleted stars.

1.3 Bayesian Statistics

Bayesian statistics is an extremely useful tool which can be exploited to make better or more complete use of available data, and an invaluable aid in hypothesis testing. The potential applications for this type of analysis are quite diverse, however, the general approach is the same in all cases. A general description of the theory behind Bayesian analysis is given below.

The core of Bayesian statistics is Bayes' Theorem, (e.g. Sivia and Skilling (2007));

$$P(M|D) = \frac{P(D|M)P(M)}{P(D)}, \tag{1.10}$$

where M and D are two events which can either be true or false. In the context of astronomy and data analysis these might represent Data and a Model. The general theme of Bayesian analysis is that given some starting point, (the prior, P(M)), which is informed by previous evidence, we can then use the observed data to modify the prior and produce the posterior distribution ($P(M|D)$). This process can involve a large set of observed data, all of which serially modify the prior in turn. The power of Bayes' theorem lies in the fact that it directly relates the quantity of interest to other quantities which are much easier to assign or calculate. In (1.10), $P(M|D)$ is called the "posterior distribution" and $P(M)$ is called the "prior distribution" or simply "prior". Using Bayes' Theorem, the probability of a particular model can be calculated, or, for a large set of models (e.g. Gaussians with different means), the most probable model can be found by calculating $P(M|D)$ for every possible model.

In some real-world cases, the probability that the data (D) is true given a model (M) is not directly known, but instead the model will produce a set of one or more parameters which can be related to the data. This means that the calculation of $P(D|M)$ is not a straightforward process. This issue is resolved by applying marginalisation and the product rule to the $P(D|M)$ term in Bayes' Theorem:

$$P(D|M) = \int P(D, \boldsymbol{\phi}|M) d\boldsymbol{\phi}, \tag{1.11}$$

$$P(D|M) = \int P(D|\boldsymbol{\phi}, M) P(\boldsymbol{\phi}|M) d\boldsymbol{\phi} \tag{1.12}$$

where $\boldsymbol{\phi}$ is a parameter or set of parameters produced from the model (M). Inserting the above equation back into Bayes' Theorem (1.10) would allow, for example, the calculation of a probability that a model is true for a given range of model parameters and data. Note that these are not to be confused with parameters that define the model, but rather outputs from the model which can be compared to the data. An example of this can be taken from counting statistics: Assume that the expected number of counts is 5 (M), then given this model, you can generate a parameter ($\boldsymbol{\phi}$) which is the number of counts with an associated probability ($P(\boldsymbol{\phi}|M)$). This can then be compared to an observed number of counts which is 4 (D) to determine the probability that the model is true. Integrating over all possible values of $\boldsymbol{\phi}$ will then return the posterior probability ($P(M|D)$). This process would produce the probability that the model stating that the mean number of counts is 5 is true given the observation of 4 counts. Repeating the process for a different model, e.g. with mean of 3 counts, would yield a different probability and allow the inference of the most likely situation given the observed data.

In carrying out the sort of analysis described above, it is important to ensure that the choice of model really does appear to match the data that you are attempting to evaluate. In the above example, there is no real ambiguity as to the form the model should take, however, in more complex situations, a model may appear to reproduce the data but have no physical connection to the situation. The choice of model is in fact a "prior" in the Bayesian analysis: by choosing a particular type of model, you are assigning a probability of zero to all other types of model, which is equivalent to choosing a prior $P(M) = 0$ for all models of a different form. Therefore, it is extremely important that some inspection of the data informs the choice of model before the analysis is carried out. Once a specific model form, or set of forms, is chosen, they can all have different prior values $P(M)$ depending on their parameters and the specifics of their use. The prior value is then modified using the observed data to produce the posterior distribution ($P(M|D)$).

1.3.1 Hypothesis Testing and Model Likelihood Ratios

In some cases it is useful to use Bayes' Theorem to calculate the value of $P(M|D)$ for a large set of models (e.g. Gaussians with different means and standard deviations); however, in other cases, there is not a large set of models but only two mutually exclusive models (M_1 and M_2). This might be a situation such as deciding whether or not a star is young, or in relation to the work described later in this text, whether or not a star is part of an association. In this case, Bayes' Theorem gives the following:

$$R = \frac{P(M_1|D)}{P(M_2|D)} = \frac{P(D|M_1)P(M_1)}{P(D|M_2)P(M_2)} = \frac{P(M_1)}{P(M_2)}K, \tag{1.13}$$

where K is called the Bayes' Factor for simplicity, and R is the model likelihood ratio. Note that $P(D|M_{1,2})$ can both be marginalised as in equation (1.12):

$$K = \frac{\int P(D|\boldsymbol{\phi_1}, M_1)P(\boldsymbol{\phi_1}|M_1)\mathrm{d}\boldsymbol{\phi_1}}{\int P(D|\boldsymbol{\phi_2}, M_2)P(\boldsymbol{\phi_2}|M_2)\mathrm{d}\boldsymbol{\phi_2}}, \tag{1.14}$$

for the case where the model yields some parameters which are compared to the data. This approach can be used to describe model probabilities relative to another specific model and completely removes the dependance on the often difficult to define $P(D)$ which can be extremely useful in a wide variety of applications. Additionally, this allows the issue of an appropriate choice of priors to be approached in a potentially simpler fashion, as the prior is now given by $P(M_1)/P(M_2)$ and is now the prior ratio. In some cases it may not be easy to define $P(M_{1,2})$, but it may be easy to define the ratio of priors for the two models. The value of $P(M_1)/P(M_2)$ is then modified by the data to produce the posterior model likelihood ratio (R) [2].

[2] I have taken the liberty of applying the terminology used for the simple formulation of Bayes' Theorem to describe the ratios in the hypothesis testing formulation. Despite potential confusion, the analogy holds true.

Once the model likelihood is found, the probability that either model holds true is straightforward to calculate. For M_1 it is given by $R/(R+1)$. Similarly, for M_2, replacing R with its inverse will provide the corresponding probability.

2

WISE Debris Disks in the Young Sco-Cen Association

In this Chapter we present an analysis of the WISE photometric data for 829 stars in the Sco-Cen OB2 association, using the latest high-mass membership probabilities. We detect debris disks associated with 134 Sco-Cen BAF-type stars. There is a clear increase in IR excess fraction with membership probability, which can be fitted linearly. 41±5% of Sco-Cen OB2 BAF stars have excesses, compared to 1±4% of field stars. This is the first time that the probability of non-membership has been used in the calculation of IR excess fractions for young stars. We do not see any significant change in excess fraction for the older Sco-Cen subgroups (16, 17 Myr) when compared to the youngest subgroup Upper-Scorpius (5 Myr). Within our sample, we have observed that B-type association members have a significantly smaller excess fraction than A and F-type association members. This work was published as Rizzuto et al. (2012), which can be obtained in electronic format online.

2.1 Introduction

Many young ($\sim$1 Myr) objects of all types, ranging from tens of solar masses down to the smallest brown dwarves, and in all environments, are surrounded by circumstellar accretion disks (Strom et al., 1989, Lada et al., 2000, Carpenter et al., 2006). The current understanding is that debris disks arise through the grinding of planetesimals to grains under gravitational collision. These dusty debris disks are an indicator and potential diagnostic of planetary systems.

A variety of observations have provided us with an overall timeline of disk evolution. The inner portion of the disk ($\leq$ 1 AU) dissipates by the age of 10 Myr in all but a small fraction of stars (Mamajek et al., 2004, Silverstone et al., 2006). From the age of 10 Myr onwards, there is an observed decline in the 24 μm excess relative to the photosphere for stars of B to K type (Carpenter et al., 2009). It has been postulated that planetesimal stirring though stellar ages of 5 to 20 Myr could produce an increase in the strength of the $\sim$ 24 μm excess with age (Kenyon and Bromley, 2008), however the current data do not show a statistically significant increase (Carpenter et al., 2009).

The Sco-Cen association and its three subgroups - Upper Scorpius (US), Upper Centaurus Lupus (UCL) and Lower Centaurus Crux (LCC) - provide three important constant-age samples within which to study debris disks around young stars. The subgroups have ages of 5, 16, and 17 Myr respectively, and are located less than 150 pc from the Sun (de Zeeuw et al., 1999). Previous studies (Carpenter et al., 2006, 2009) have investigated IRAC, IRS and Spitzer photometric data ranging from 4.5 to 70 μm in the US subgroup. They identified 54 stars with 24 μm excesses in their sample of 205 targets and found that disks around BAF-type stars appear to be comprised of dusty debris, while disks associated with K and M-type stars are likely optically thick primordial disks which are remnants of the star formation process. The older Sco-Cen subgroups, UCL and LCC, have received considerably less attention; only a handful of studies have observed small numbers of UCL and LCC stars (summarised in Carpenter et al. (2009)). The recent study by Chen et al. (2011) reports the detection of 41 new disks around F and G-type Sco-Cen stars, increasing the late-type sample size.

New Bayesian membership probabilities for the high mass members (B to F-type) of the Sco-Cen association are now available (Rizzuto et al., 2011), and preliminary photometric data from the WISE mission have been released (Wright et al., 2010). Here we present an analysis of the WISE photometry for Sco-Cen members to search for debris disks in three constant-age samples.

2.2 Data Sample

In this study we take our sample from the Hipparcos Sco-Cen membership study of Rizzuto et al. (2011). All stars with membership probabilities of 5% and greater were cross-referenced with the WISE preliminary data release. This resulted in a sample of 829 stars with spectral types ranging from early B to late F (B-V≤0.6), brighter than 9^{th} visual magnitude and within the area of sky bounded by $(285 \leq l \leq 360)$ and $(-10 \leq b \leq 60)$. Membership as described in Rizzuto et al. (2011), is based purely on kinematic and positional properties of the targets, and hence the selection is believed to be unbiased with regard to the presence of debris disks. Note that in previous papers, stars with membership probability >50% were termed members. We have chosen to include the low membership probability stars in this study in order to determine if there is a relationship between membership probability and excess fraction, and hence to identify potential additional Sco-Cen stars by disk presence.

2.3 WISE Excesses

The WISE mission data provide photometry in four bands, W_1, W_2, W_3 and W_4, with central wavelengths of 3, 4.5, 12 and 22 μm respectively (Wright et al., 2010). In this study we present an analysis of three WISE colours: W_1-W_2, W_1-W_3, and W_1-W_4. Inspection of the WISE photometry for band W_2 shows a clear bias at the bluest end of our membership sample towards poorly fitted point-spread-functions, resulting in untrustworthy W_2 photometry. For this reason the long wavelength colours were constructed with W_1, which shows a uniform distribution over spectral type of poor photometry fits. Analysis of these three colours will provide three different classes of detected excesses: (1) excesses in all colours, (2) excesses in only the short wavelength filters, and (3) excess in only the longer or longest wavelengths. Since the aim of this study is to identify dusty debris disks, it is expected that a disk-produced excess detected at bluer colours will also be detected at longer colours. Hence, excesses in only the blue colours indicate contaminated photometry and will provide a valuable diagnostic in the identification of debris disks.

For stars without debris disks the three WISE colours are expected to vary linearly with the 2MASS (J-K_s) colour, and this line represents the photospheric emission in the particular filter. To determine the photospheric colours, we have applied an iterative fitting procedure. Objects which were clear outliers in the particular WISE colour were first removed and then the software package MPFIT was used to fit a line to the sample. Stars which were separated from the fitted line by more than twice the dispersion of the residuals were then identified as outliers and removed. The process was then repeated until no further objects were removed. This fitting procedure was carried out using only the stars with greater than 60% membership probability in order to ensure that the fitted photosphere line was that of the young Sco-Cen stars. During this fitting procedure, objects with a WISE photometric fit reduced χ^2 greater than 4 in the relevant bands were excluded, as they are likely to be extended sources with poor photometry.

The criterion adopted for excess detection in the three colours was 8%, for W_1-W_2 and 30% for W_1-W_3 and W_1-W_4 above the expected photosphere line, plus the error on the WISE photometry. These detection thresholds were chosen conservatively such that the detections are likely to be significant even if the photosphere fit is underestimated by 10%. Note that as mentioned previously, objects with photometric fit reduced χ^2 greater than 4 in the relevant bands were not assigned an excess, irrespective of WISE colours. The colour-colour diagrams for the three WISE colours and the fits can be seen in Figure 2.1.

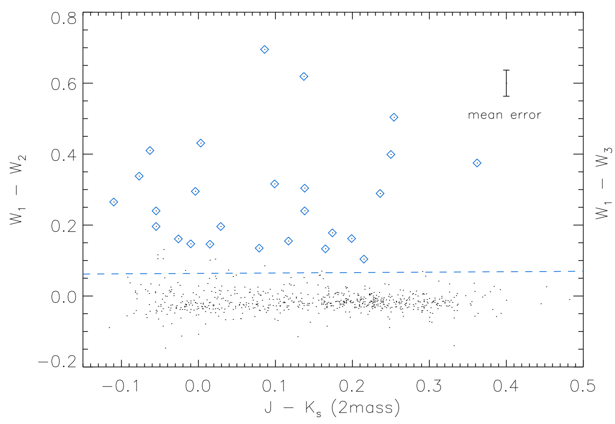

(a) W_1-W_2

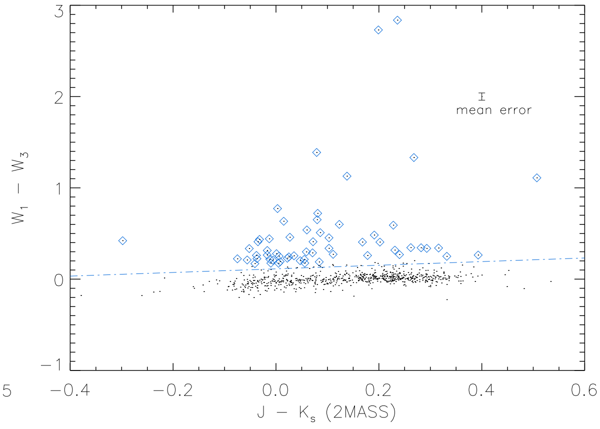

(b) W_1-W_3

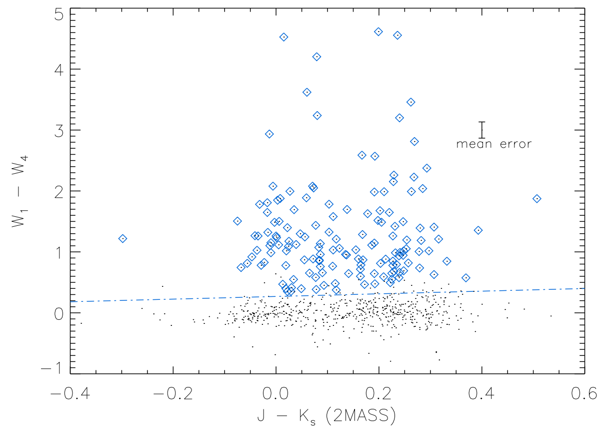

(c) W_1-W_4

Figure 2.1: The colour-colour diagrams for the three WISE colours defined above. The blue line represents the corresponding excess detection threshold above which objects are considered to have a detectable excess. The photosphere grouping is clearly seen in each colour with fitted slopes and intercepts of (0.012,-0.18), (0.019,-0.018) and (0.22,-0.016) respectively. Blue diamonds indicate stars with detectable excesses and black dots indicate stars without a detectable excess.

Given excess detections in the three WISE colours we can remove from the sample those stars with suspect photometry. There were 19 objects with a detected excess in W_1-W_2 only, 3 in W_1-W_3 only, and 3 in W_1-W_2 and W_1-W_4 only. The 19 objects which show an excess only in the W_1-W_2 colour are likely caused by the saturation behaviour of the WISE photometry fits. When partial saturation occurs in band W_2 (brighter than 6.5 mags), the WISE photometry fitting procedure produces a systematic over-estimation of the flux, which produces a smaller magnitude (Cutri et al., 2011). All 19 of these objects are in the W_2 magnitude range where flux over-estimation is expected and hence we have included these objects in our sample as having no detectable excess. In addition, we remove those objects with poor photometry fits ($\chi^2 > 4$) in the W_1 and W_4 bands, as the remainder of the analysis makes use of the W_1-W_4 excess only, there were 95 such objects. HIP 77562 and 81891, which only show an excess in W_1-W_3 both have poor photometry fits in band W_4, and so are removed from the sample.

The WISE images of the 173 objects with detected excesses were then visually inspected for the presence of close, unresolved companions and contamination from excess-producing nebulosity. This yielded 27 objects with excesses not likely to be caused by a disk. HIP 68413 ,79098 and 76063, which have detectable excess in W_1-W_2 and W_1-W_4, but not W_1-W_3, are included in the sample based on the image inspection. The lack of W_1-W_3 excess associated with HIP 68413 is most likely due to a large error on W_1-W_3 and the detected W_1-W_2 excess associated with HIP 79098 was found to be caused by a clearly visible diffraction spike in the W_2 image. HIP 76063 has a W_2 magnitude of 5.6, and so the W_1-W_2 excess associated with this star is most likely also due to saturation. Finally, HIP 80897 shows a nebulous excess in W_1-W_3 only, and so was removed from the sample. In total, we observe reliable excesses associated with 134 objects: 27 stars in US, 53 in UCL and 54 in LCC. Table A.1 in Appendix A contains all the colour and WISE photometry for our sample, with the excess detections marked.

2.4 Discussion

The sources investigated in this study are BAF-type stars and hence the detected excesses are expected to be produced by dusty debris disks rather than primordial gaseous disks (Carpenter et al., 2009). A clear outcome of our analysis is that the excess fraction in the three subgroups is not uniform with respect to membership probability (p). We have investigated the excess properties of Sco-Cen stars in discrete membership probability bins. Figure 2.2 displays the excess fraction in 10% membership probability bins with p > 20%. We have fitted linear trends to these data, which are indicated by the blue lines in Figure 2.2. Extrapolation to 100% membership probability (i.e. certain members) along the linear fits result in excess fractions of 0.36±0.1, 0.33±0.08 and 0.46±0.13 for the three subgroups US, UCL and LCC respectively. The extrapolated excess fraction for US is significantly larger than observations have previously suggested. The 24 μm excess fraction for B7-A9 stars in the US sample used by Carpenter et al. (2009) was found to be ∼0.3, and ∼0.15 for F-type stars. For associations at the age of UCL and LCC (16, 17 Myr), Chen et al. (2005) reported a 24 μm excess fraction lower-bound of ∼0.35, which is consistent with the results of our analysis. In our sample, the extrapolated 22 μm excess fraction was not found to be larger in the older subgroups (UCL, LCC) compared to the young US subgroup. Previous observations have provided some evidence for a peak in the excess fraction as stars age from <10 Myr to the 10-30 Myr age range (Currie et al., 2008). However, the statistical significance of the peak remains an open question (Carpenter et al., 2009). Our analysis reveals that in the Sco-Cen association, the excess fraction does not increase as stars age from ∼5 Myr to the 10-30 Myr age range.

Given the lack of statistically significant differences in excess fraction between the three Sco-Cen subgroups, the association as a whole can be explored. Figure 2.2d displays the linear excess fraction trend for the combined sample. Linear fitting to the data resulted in an extrapolated excess fraction of 41±5% for certain members, and 1±4% for field stars with 0% Sco-Cen membership probability, with a χ^2 of 0.82 for the fit.

The aim of this study is to compare the disk properties of young association stars with those of older main-sequence stars. An important issue to address is the possibility of contamination in the sample from, for example, bright, distant giants which appear to be spatially consistent with the Sco-Cen association. Such a star, with an incorrect parallax placing it within the Sco-Cen area of space, would have small proper motions. The Rizzuto et al. (2011) membership classification scheme, which is based

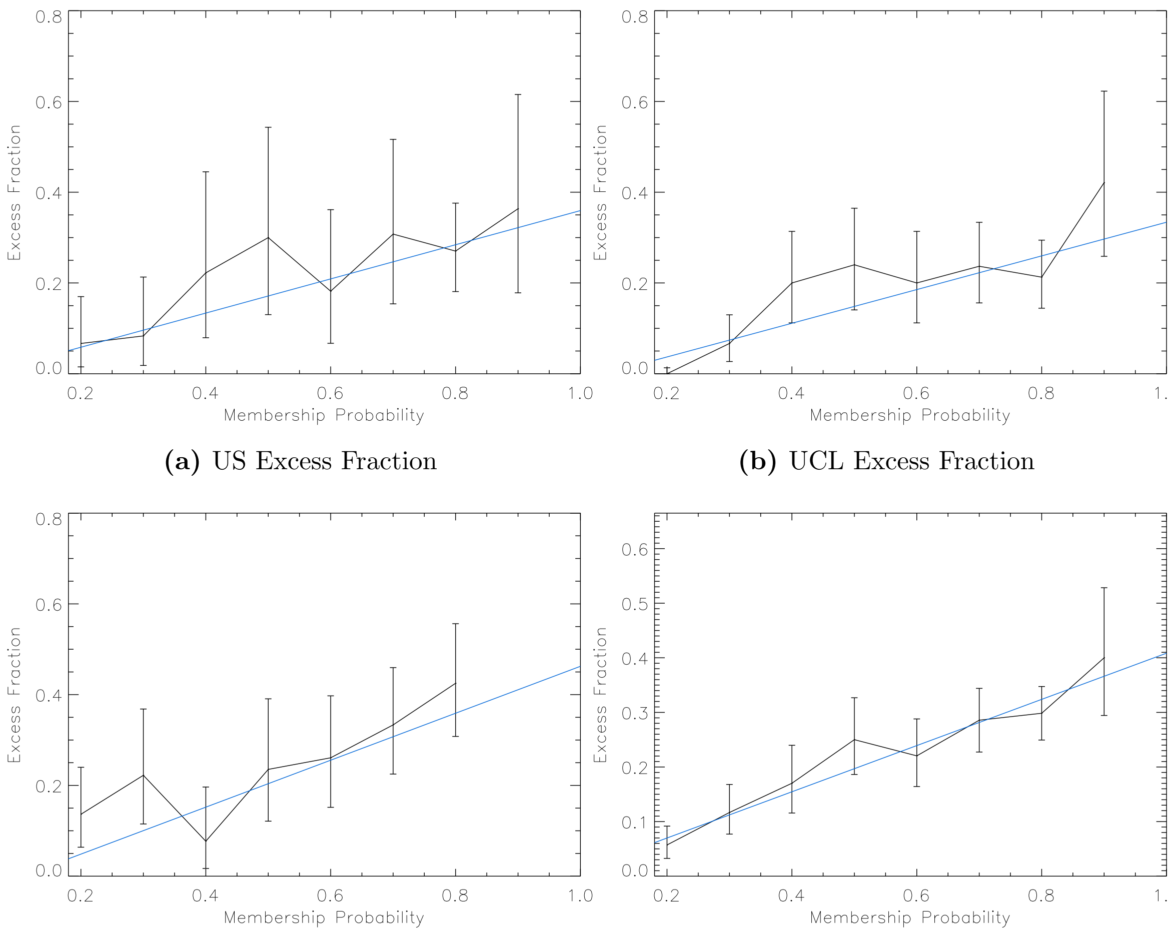

(a) US Excess Fraction

(b) UCL Excess Fraction

(c) LCC Excess Fraction

(d) Sco-Cen Excess Fraction

Figure 2.2: Excess fraction as a function of membership probability for the three subgroups and the entire association.

on kinematics and distance, would select strongly against association membership in this situation on the basis of inconsistent proper motion, making a 20% membership probability extremely unlikely. Hence our 20% membership probability cut-off ensures that the sample used provides an accurate comparison between young stars and older main-sequence stars.

The correlation between the presence of a debris disk and membership of the Sco-Cen association is clearly demonstrated in this analysis. It is thus important to consider stars with a detectable 22 μm excess which have lower membership probabilities (p<50%). In the latest Sco-Cen membership study (Rizzuto et al., 2011) a number

HIP						
51169	51203	53524	55616	55978	60183	62482
62488	63236	63395	72099	72685	75843	76223
76782	77315	77366	77523	78198	78357	78826
78943	80019	80458	80557	80921	81316	81639
81791	82154	82250	83232	84881	86853	

Table 2.1: The 34 new members based on IR excess detections.

Figure	a	b	χ^2
US	0.36±0.10	-0.02±0.09	0.4
UCL	0.33±0.08	-0.04±0.06	1.6
LCC	0.46±0.13	-0.05±0.11	3.5
All	0.41±0.05	0.01±0.04	0.8
B	0.18±0.08	0.09±0.10	0.1
A	0.45±0.11	0.05±0.09	4.1
F	0.47±0.09	-0.08±0.04	4.0

Table 2.2: The excess fraction fits for the seven graphs. The fitting was done to the equation $y = (a - b)p_{mem} + b$, where a and b are the excess fractions at $p_{mem} = 0$ and 1.0 respectively.

of de Zeeuw et al. (1999) member stars were assigned low membership probabilities due to inconclusive proper motion data and the lack of a radial velocity measurement. Unresolved multiplicity has long been recognised as an important pitfall in kinematics-based association membership selection methods (de Zeeuw et al., 1999). An equal mass binary system at the distance of Sco-Cen can produce a proper-motion offset on the order of ∼2 mas from the true centre-of-mass motion. An offset of this size is roughly on the order of the uncertainties in the proper motion (van Leeuwen, 2007), indicating that binary association members can possibly be overlooked. The presence of a debris disk can then be used to indicate membership for stars spatially and photometrically consistent, but kinematically inconsistent, with the Sco-Cen subgroups. We thus propose that stars with membership probabilities between 10 and 50% which have a detectable excess can confidently be considered association members (see Tab.

2.1).

The subgroup LCC has an anomalous concentration of stars with detectable excess in the 5-10% membership probability range. Three of these stars, HIP 50612, 52867 and 53992, are known members of the young open cluster IC2602, which is on the far side of LCC (Robichon et al., 1999), and are thus expected to have low Sco-Cen membership probabilities. Confusion with young background sources for this subgroup, which is on the Galactic plane, further contributes to the anomalous high excess fraction.

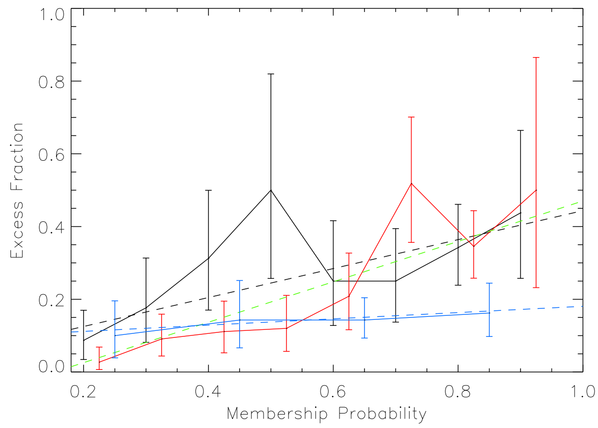

Figure 2.3: Excess fraction against membership probability for A-type (Black), F-type (Red) and B-type (Blue) stars in our sample. The dashed lines represent the linear fits.

We have examined the excess fraction properties of our sample in three colour ranges: ($-0.3 <$B-V< 0), ($0 <$B-V< 0.3) and ($0.3 <$B-V< 0.6). These groupings correspond approximately to B, A and F-type stars according to the colour tables of Allen and Cox (2000). Figure 2.3 displays plots of the excess fraction against membership probability for the three spectral type ranges. We find the extrapolated excess fractions for the A and F-type stars to be 45±11% and 47±9%, while the B-type stars in our sample show no evidence of a trend in excess fraction with membership probability. The study of Carpenter et al. (2009) also found that A and F-type stars have similar excess fractions at the age of Sco-Cen, with a small increase in excess fraction for the earlier spectral types. However, the earliest type star included in the Carpenter et al. (2009) sample is B7, and so no direct comparison can be made to the bluest end of our sample. Note that the lack of a clear trend for the B-type members could imply that most of these stars are in fact young Sco-Cen members despite their kinematics. Further investigation is required to shed additional light on the excess properties of the bluest Sco-Cen stars.

2.5 Summary and Conclusions

We have analysed the available preliminary WISE photometry for the Sco-Cen stars of the Rizzuto et al. (2011) membership list and detected 134 22 μm excesses above the expected photosphere emission. We have used Sco-Cen membership probabilities to extrapolate an excess fraction for certain members, and observe that there is no clear increase in disk fraction between the young US subgroup and the older UCL and LCC subgroups. However, we report a significantly larger disk fraction than previously observed in the youngest subgroup US. These results agree with those of previous studies (Carpenter et al., 2009). Importantly we find that the excess fraction is significantly lower for the B-type stars in our sample compared to A and F-type association members, which is contrary to the trend seen by Carpenter et al. (2009). One possible explanation relates to multiplicity. B-type stars have a significantly higher multiplicity fraction compared to later type stars (Kouwenhoven et al., 2005). The presence of a companion can potentially truncate the inner regions of the debris disk through resonances (Artymowicz and Lubow, 1994), producing a smaller disk fraction. This has been observed in a recent study of binaries in Taurus-Auriga, particularly with close (<40AU) companions (Kraus et al., 2011a). Among the highest probability members in our sample (>90%) there are six close (<100 AU) multiple systems without disk detections and one close multiple system with a detected excess. A more comprehensive, comparison between disk presence and multiplicity information for the Sco-Cen B-type stars may shed light on this issue, but is beyond the scope of this study.

3

New Low-Mass Sco-Cen Members

As mentioned previously, young OB associations like Sco-Cen provide an incredible laboratory, in the form of a primordial group of stars directly after formation, which can be exploited in the study of the output of star formation. The obvious prerequisite for such study is a level of completeness in the identification of association members that is currently not yet attained in Sco-Cen in any mass regime other than the most massive B-type stars. Sco-Cen contains approximately 150 B-type stars which are spatially concentrated into three subgroups: Upper-Scorpius, Upper-Centaurus-Lupus (UCL) and Lower-Centaurus-Crux (LCC) with only the B, A and F-type membership of Sco-Cen being considered relatively complete with some 800 members. Even in this high-mass regime, there is expected to be a $\sim$30% contamination by interlopers in the kinematic membership selections, mainly due to the lack of precision radial velocity measurements for these objects (Rizzuto et al., 2011). Additionally, in light of the upcoming high-precision GAIA proper motions and parallaxes, a well characterised spectroscopically confirmed Sco-Cen membership will be instrumental in illuminating the substructure of the association.

Unfortunately, Sco-Cen is poorly characterised for its proximity, the reason for which is the enormous area of sky the association inhabits at low Galactic latitudes ($\sim 80^\circ \times 25^\circ$ or $\sim 150 \times 50$ pc). IMF extrapolation from the high-mass members implies, with any choice of IMF law, the Sco-Cen is expected to have $\sim 10^4$ PMS G, K and M-type members, most of which are, as yet, undiscovered. This implies that the vast majority of PMS (<20 Myr) stars in the solar neighbourhood are in Sco-Cen (Preibisch et al., 2002), making Sco-Cen an ideal place to search for young, massive planetary companions. Although, as described in Chapter 1, some work has been done in illuminating the lower-mass population of Sco-Cen, the late-type membership of Sco-Cen cannot be considered complete in any spectral-type or colour band. A more complete picture of the late-type membership of Sco-Cen is the primary requirement for determining the age spread, structure, and star formation history of the association, for illuminating the properties of star formation, and for embarking on further searches for young exoplanets.

A particular point is the contentious age of the Sco-Cen subgroups. Upper Scorpius has long been considered to be ∼5 Myr old, however recent work has shown that it may be as old as 11 Myr (de Geus, 1992, Pecaut et al., 2012). Similarly, B, A and F-type UCL and LCC members have main-sequence turn off/on ages of $\sim 16 - 18$ Myr, while studies of the incomplete sample of lithium-rich G, K and M-type members show a variety of mass-dependent age estimates. The HR-diagram age for the known K-type stars in UCL and LCC is ∼12 Myr, the few known M-type stars indicate a significantly younger age of ∼4 Myr, most likely due to a bias produced by a magnitude limited sample, and the G-type members have an age of ∼17 Myr, which is consistent with the more massive stars (Preibisch and Mamajek, 2008, Song et al., 2012). There is also a positional trend in the age of the PMS stars of the older subgroups, with stars closer to the Galactic Plane appearing significantly younger than objects further north. This is almost certainly the result of as yet undiscovered and un-clarified substructure within the older subgroups, which have a very complex star-formation history. These uncertainties and questions can be addressed with a more complete picture of the membership of Sco-Cen on an association-wide scale.

The above is clear motivation for the identification of the full population of the Sco-Cen association, a task that will require significant observational and computational effort to complete. In this section, we describe our spectroscopic search for new PMS members of the Upper-Scorpius region of the Sco-Cen association, which is currently underway and continuing beyond the scope of this thesis. This involved developing a new Bayesian kinematic selection algorithm to identify high probability candidate members of the association for spectroscopic followup, and spectral analysis of youth indicating features such as Li 6708Å and H-α. This work was published as Rizzuto et al. (2015), which can be obtained in electronic format online.

3.1 Bayesian Membership Selection

Bayesian statistics is incredibly useful in distinguishing between members of a stellar association with a distinct kinematic profile and background interlopers. We have employed a new Bayesian selection algorithm to identify potential Sco-Cen low-mass members from the vast multitude of interlopers in the Sco-Cen field of sky, using the UCAC4 proper-motion catalogue, and RAVE radial velocities where possible. Both the 2MASS NIR J,H, and K magnitudes as well as APASS visible magnitudes were available for the majority of the candidate Sco-Cen members we have addressed. Using these data, the basic framework is that of the hypothesis testing-scenario involving two mutually exclusive models, which is described earlier in Section 1.3.1.

For application to moving groups and stellar associations, we consider the following two models: (1) A star is a member of the association (M_g) and (2) A star is not a member of the association, but rather from the field (M_f). Both of these models provide a variety of information, namely, position, distance, velocities, and a model isochrone;

$$M_{g,f}(l, C_x) = \{l, b, r, U, V, W, M_x\}, \tag{3.1}$$

where l and b are Galactic longitude and latitude, r is distance, U, V and W are the three components of a star's Galactic velocity [1], C_x is some colour and M_x is an absolute magnitude in some filter. The model values of distance and velocity are dependent on the Galactic longitude of a candidate star, while the model absolute magnitude is dependent on the star's colour. For the application to PMS stars in the Sco-Cen subgroups, we have used Siess isochrones (Siess et al., 2000) of 6 Myr for US and 16 Myr for UCL and LCC for the group models (M_g) and an older 1 Gyr isochrone for the field model (M_f).

3.1.1 Kinematic Models

Sco-Cen Association Kinematic Model (M_g)

The Sco-Cen association is a complex group of comoving objects, with both distinct and interspersed subgroups and hidden substructures. Despite this, the association is quite well described by a linear kinematic model in the three Galactic velocity components, with respect to Galactic longitude. This trend also holds true for the mean Galactic latitude of the association members, and the spread of association members about this mean Galactic latitude;

$$(U, V, W, b, \sigma_b) = Al + B, \tag{3.2}$$

where A and B are different coefficients for each of the velocity components and latitude components, b is the Galactic latitude, and σ_b is the Galactic latitude spread of the association members. Similarly, the association mean distance is well described

[1] U is the component of the Galactic velocity pointing out of the galactic centre, W is the component pointing perpendicular to the Galactic Plane, and V is the component in the direction of Galactic rotation.

by a linear model in space;

$$r = (A\cos l + B\sin l)^{-1} \tag{3.3}$$

where again A and B are the linear coefficients and r is the model association mean distance. This, combined with a characteristic distance spread of 25 pc, produces a complete model of the Sco-Cen association kinematics which can be used in the selection algorithm to determine association membership. These linear kinematic trends were first described in a membership selection of the high mass B, A and F-type stars in the Sco-Cen association (Rizzuto et al., 2011). The values for the linear parameters are given in Table 3.1.

	A	B ($l = 0$)
U_g	0.13	50.9
V_g	0.009	-20.8
W_g	0.019	-12.3
b_g	0.21	-55.0
σ_{b_g}	-0.1	45.6
r_g	0.0059	-0.0072
	Distance	
σ_{r_g}	25 pc	
σ_{int}	3.0 km s^{-1}	

Table 3.1: The Sco-Cen association kinematic model parameters. The Galactic velocity component parameters (U_g, V_g, W_g) are given in km s^{-1}, the Galactic latitude mean and standard deviation (b_g and σ_{b_g})is given in degrees, and the distance parameters in parsecs. The final two numbers are the standard deviations of the association model distance taken directly from the Rizzuto et al. (2011) membership, and the internal velocity dispersion (σ_{int}) of the association, taken from Kraus and Hillenbrand (2007a).

The group kinematic models are normal distributions in each Galactic velocity component, the mean of which is dependent on the Galactic longitude of the particular object in the way described by the linear models above. The model distance distribution for Sco-Cen is treated in a very similar way, with model distance defined as a normal distribution with mean given by a linear trend in Galactic longitude and a standard deviation which is constant across the association. Similarly, the model Galactic latitude is also treated as a normal distribution with both mean and standard deviation dependent on the Galactic longitude of the particular object of intrest, This produces a decreasing mean and widening range of possible latitudes going from the younger Upper-Sco association to the more dispersed older subgroups (from high to low Galactic longitude). Included in the model is also a pre-main sequence isochrone, taken from the Siess models (Siess et al., 2000), which will be used to convert photometry into distances.

Parameter	Value (km/s)
U_f	9.0
V_f	-6.9
W_f	-7.0
σ_{U_f}	19.8
σ_{V_f}	12.8
σ_{W_f}	8.0
Galactic Latitude°	
b_f	0
σ_{b_f}	60

Table 3.2: The field model Galactic velocity mean and dispersion for each component, taken from the Galactic Thin Disk of Robin et al. (2003), and the field Galactic latitude normal distribution parameters in degrees.

Field Star Kinematic Model (M_f)

In the selection algorithm that will be described below, the Sco-Cen association model will be directly compared to a kinematic model describing non-association members, or field stars. The parameters of this model are taken from the Galactic Thin Disk model of Robin et al. (2003), and describe a normal distribution for each Galactic velocity component, with significantly larger standard deviations than those described in the Sco-Cen association model. Spatially, we treat the field as a very wide normal distribution in Galactic latitude, with highest probability at the Galactic Plane. As with the association model, the field model includes a field main sequence isochrone, for converting between photometry and distance.

3.1.2 The Bayesian Algorithm

Once the field and association models are defined, it is then possible to evaluate the available data using a Bayesian framework. In this application, we use the hypothesis testing version of Bayes' Theorem, presented in Equation (1.12), with a marginalised Bayes' factor as in Equation (1.14);

$$R = \frac{P(M_g|D)}{P(M_f|D)} = \frac{P(M_g)}{P(M_f)} \frac{\int P(D|\boldsymbol{\phi}_g, M_g) P(\boldsymbol{\phi}_g|M_g) \mathrm{d}\boldsymbol{\phi}_g}{\int P(D|\boldsymbol{\phi}_f, M_f) P(\boldsymbol{\phi}_f|M_f) \mathrm{d}\boldsymbol{\phi}_f}, \tag{3.4}$$

where again, $M_{g,f}$ represents the association and field models, and $\phi_{g,f}$ represents the set of parameters, or a parameter vector derived from the models, which can be directly compared to the data D. The data are compiled from positions and proper motions taken from the UCAC4 catalog (Zacharias et al., 2013), and a photometric distance calculated from the APASS B and V band photometry (Henden et al., 2012) and 2MASS J,H and K photometry (Skrutskie et al., 2006), using the model isochrones. The first step in the analysis is to define a coordinate transform which will allow simple comparison of the models with the astrometric data.

The Convergent Point Coordinate System

To determine the parameters in the model parameter vectors $\phi_{g,f}$ we must convert the Galactic velocities and distances taken from the model into proper motions. Rather than using the conventional Equatorial proper motion coordinates, we will use a new proper motion coordinate system defined by the "Convergent Point", i.e. the point on the sky at which a star will appear to recede to due to its proper motion, given sufficient time. The actual position of the convergent point can be easily calculated from the Galactic velocity components:

$$\begin{aligned} \tan(l_{cp}) &= \tfrac{V}{-U}, \\ \tan(b_{cp}) &= \tfrac{W}{\sqrt{(U^2+V^2)}}. \end{aligned} \tag{3.5}$$

The benefit of using this coordinate system is that it is the natural coordinate system of a group of objects with a common velocity, with proper motion along the great circle joining a star and the Convergent Point ($\mu_{\|}$) containing all the on-sky motion of a perfect group member, a proper motion in the direction perpendicular to this ($\mu_{\perp}$) being equal to zero for the perfect group member. Figure 3.1 provides a schematic explanation of this new coordinate system.

Conversion of the Equatorial proper motions available in the UCAC4 catalogue for candidate Sco-Cen members is done via a simple rotation by the angle between the North Pole (Equatorial) and the Convergent Point great circle, namely, the angle analogous to γ in Figure 3.1 if the figure were displayed in Equatorial, rather than Galactic Coordinates. Calculating the new proper motions and radial velocity from the association and field Galactic velocities and distances is slightly more involved, and requires the definition of some new unit vectors:

$$\begin{aligned} \hat{\mathbf{p}} &= \cos(\gamma)\hat{\mathbf{b}} + \sin(\gamma)\hat{\mathbf{l}}, \\ \hat{\mathbf{r}} &= (\cos(l)\sin(b), \sin(l)\sin(b), \cos(l)), \end{aligned} \tag{3.6}$$

where $\hat{\mathbf{p}}$ and $\hat{\mathbf{r}}$ are the unit vectors in the direction of $\mu_{parallel}$ and radial velocity (ν_r), which depend on the position of the particular star on the sky, with $\hat{\mathbf{l}}$ and $\hat{\mathbf{b}}$ representing the Galactic longitude and latitude unit vectors, respectively. The angle

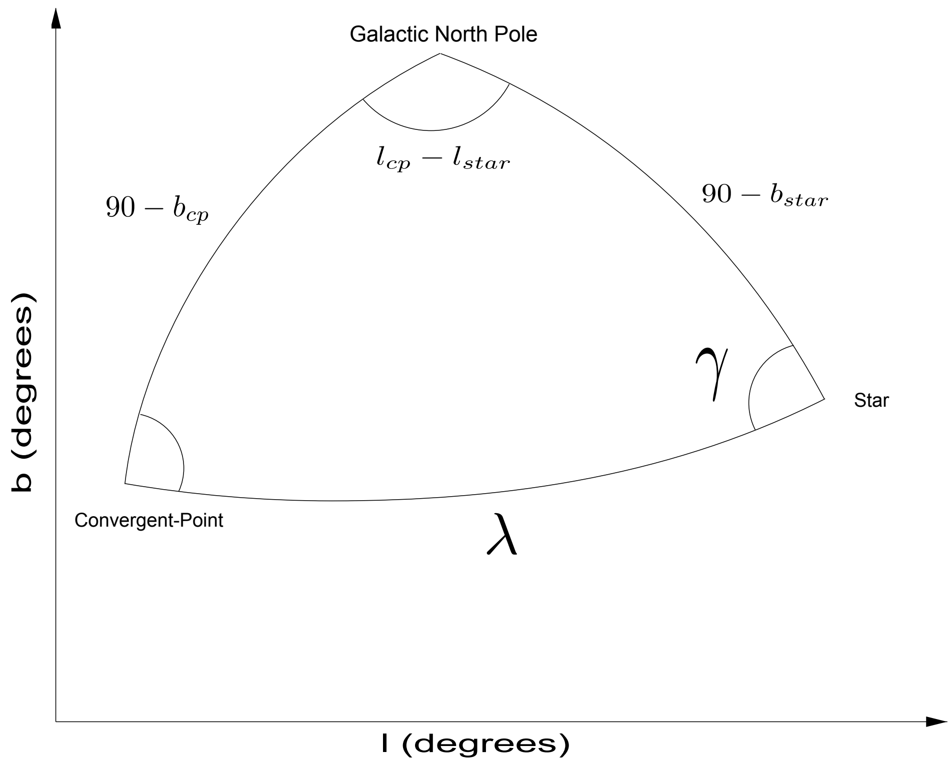

Figure 3.1: Diagramatic representation of the Convergent Point and the new coordinate system based upon it. λ is the great circle angle joining the star and the Convergent Point, (l_{cp}, b_{cp}) is the position of the Convergent Point on the sky, (l_{star}, b_{star}) is the position of the star, and γ is the angle between the Convergent Point great circle and the great circle joining the Galactic North Pole and the Star. The new proper motions based on this coordinate system will be $\mu_{\|}$, which points along the great circle λ, and $\mu_{\perp}$, which points perpendicular to this direction. With basic trigonometric identities, conventional proper motions can be directly converted to this system based on the angles γ and λ.

γ is given by;

$$\begin{aligned} \sin(\gamma) &= \tfrac{\sin(l - l_{cp})\cos(b_{cp})}{\sin(\lambda)}, \\ \cos(\gamma) &= \tfrac{(\sin(b_{cp}) - \cos(\lambda)\sin(b))}{\cos(b)\sin(\lambda)}, \end{aligned} \tag{3.7}$$

where (l_{cp}, b_{cp}) are the Galactic coordinates of the Convergent Point, λ is the angular distance between the Convergent Point and the star, and (l, b) are the stellar coordinates. Using the new unit vectors described in equation (3.6), model values of new velocity components can be calculated from any given set of velocity components derived from a model $\mathbf{U}_{g,f} = (U_{g,f}, V_{g,f}, W_{g,f})$:

$$\begin{aligned} U_{\parallel} &= \mathbf{U}_{g,f} \cdot \hat{\mathbf{p}}, \\ U_{\perp} &= 0, \\ \nu_r &= \mathbf{U}_{g,f} \cdot \hat{\mathbf{r}}, \end{aligned} \tag{3.8}$$

where $U_{\parallel}$ is the model velocity towards the Convergent Point, which can be converted to proper motion units using a distance measure which is described below, and $U_{\perp}$ is the velocity perpendicular to the Convergent Point, which is by construction of the coordinate system equal to zero. Combining this new coordinate system with a distance measure will allow direct comparison of the association and field models with stellar data.

Photometric Distance Measure

Using kinematic methods to identify low-mass stars in Sco-Cen presents a further challenge compared to the high-mass membership due to simply poorer quality measurements, namely, the absence of a directly measured parallax for candidate members. The only real distance measurement that can be made is to use photometry combined with appropriate isochrones to estimate the distance to candidate Sco-Cen stars. We have done this by comparing APASS B and V, and 2MASS J and K, and producing photometric distances using Siess pre-main sequence isochrones (Siess et al., 2000) in accordance with the association (M_g) and field (M_f) models which are defined above.

Included in our distance estimate was a multiplicity photometric bias correction. This estimate was based on the expected multiplicity statistics of G, K and M-type stars, taken from Kraus et al. (2011b), which indicates $\sim 50\%$ of solar type stars have a companion. Combined with a standard initial mass function for the companion, this produces an average multiplicity bias of 0.2 magnitudes. Our photometric distances are thus calculated by adjusting the measured photometry by 0.2 magnitudes and then calculating a distance based on an interpolated isochrone magnitude. We define the uncertainty on the photometric distance to be 20%, or ± 0.4 magnitudes. This calculation is done for every star in our sample for both the association and field models.

Calculating Bayes' Factors

We now describe the calculation of the probabilities of membership using equation (3.4), which makes up the bulk of the selection algorithm. This will rely on the conversions and calculation described in the previous sections of this chapter. The calculation of the Bayes' factor from equation (3.4) involves multi-dimensional integrals over all possible values of the different model parameters U, V, W, Galactic latitude b and distance r. Here, we can de-couple Galactic latitude from the integral, as it is completely independent from the other components, because it is not used in any conversions to new coordinate systems, and can hence be directly compared to the stellar data;

$$\begin{aligned} P(D|M_{f,g}) &= \textstyle\int_{-\infty}^{+\infty} P(b|M_{g,f})P(D|b)\mathrm{d}b \\ & \textstyle\int_{-\infty}^{+\infty} P(\boldsymbol{\theta}|M_{g,f})P(D|\boldsymbol{\theta})\mathrm{d}\boldsymbol{\theta}, \end{aligned} \tag{3.9}$$

where $\boldsymbol{\theta} = \{U, V, W, r\}$ represents the remaining model parameters once Galactic latitude (b) is removed. Given the level of precision of the stellar positions, $P(D|b)$ is set to unity when Galactic latitude is equal to the stellar Galactic latitude ($b = b_{\star}$), and zero otherwise. This leaves the remaining term describing the model Galactic latitudes, which as described above, is treated as a normal distribution:

$$P(b|M_{g,f}) = \frac{1}{\sqrt{2\pi\sigma^2_{b_{g,f}}}} \exp\left(-\frac{(b - b_{g,f})^2}{2\sigma^2_{b_{g,f}}}\right). \tag{3.10}$$

The parameters of this normal distribution for the group and field models are described above in Tables 3.1 and 3.2. The four remaining parameters in the integral are coupled and are hence treated together. $P(\boldsymbol{\theta}|M_{g,f})$ is a further set of distributions. The Galactic velocity components are treated as normal distributions for both the field and the association, though with different parameters (see section 3.1.1):

$$P(U|M_{g,f}) = \frac{1}{2\pi\sigma^2_{U_{g,f}}} \exp\left(-\frac{(U-U_{g,f})^2}{2\sigma^2_{U_{g,f}}}\right),$$

$$P(V|M_{g,f}) = \frac{1}{2\pi\sigma^2_{V_{g,f}}} \exp\left(-\frac{(V-V_{g,f})^2}{2\sigma^2_{V_{g,f}}}\right), \tag{3.11}$$

$$P(W|M_{g,f}) = \frac{1}{2\pi\sigma^2_{W_{g,f}}} \exp\left(-\frac{(W-W_{g,f})^2}{2\sigma^2_{W_{g,f}}}\right),$$

where for the association kinematic model, the parameters describing the model are linearly dependent on the Galactic longitude of each star of intrest, and will thus vary across the association. The association distance is also treated as a normal distribution with its mean dependent on stellar Galactic longitude;

$$P(r|M_g) = \frac{1}{2\pi\sigma^2_{r_g}} \exp\left(-\frac{(r-r_g(l))^2}{2\sigma^2_{r_g}}\right). \tag{3.12}$$

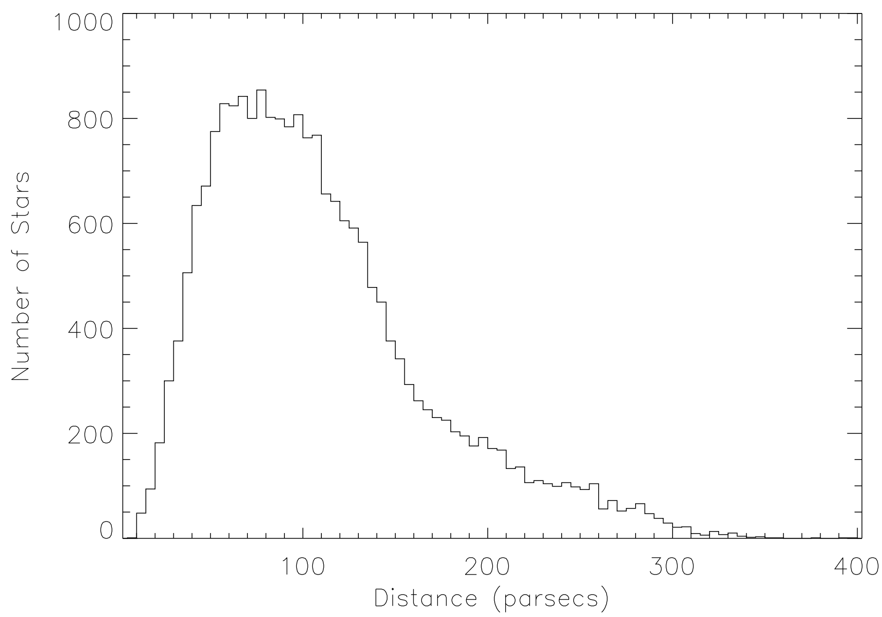

Figure 3.2: Field photometric distance distribution, showing features of the input catalog magnitude and colour cuts in the distance peak and tail, and the isochrone used in estimation of the distances.

The distance distribution for the field model is treated in a significantly different manner as it cannot be described with a simple normal distribution. Instead, we take the set of all photometric distances generated using the stellar photometry and field main-sequence, and use this to describe the field distance distribution; an example is shown in figure 3.2.

With these definitions of the model distributions, and the numerically generated field distance model, we generate 10^5 random (U, V, W, r) samples for the group integral in equation (3.4), and 10^6 samples for the field integral. These values were chosen empirically such that the uncertainty on the resultant probabilities was typically 1%. More samples are required for the field integral due to the significantly wider range of probable values for both the Galactic velocity components, and the field model distance. Sampling of the normal distributions for the Galactic velocity and group distance was done using inbuilt functions in IDL to generate random normal distributions. The field distance distribution is not analytically determined, and so sampling was done with the rejection sampling method (Neal, 2003), which samples an arbitrary random variable by uniformly sampling on the region described by its probability density function.

Using the randomly generated values, we then calculate the final terms in the Bayes' factor integrals. These remaining terms are those relating model parameters to the data, and are expressed in terms of the "Convergent Point" coordinates described above;

$$P(D|\boldsymbol{\theta}_g) \propto \exp\left(-\frac{\mu_\perp^2}{2\sigma_{\mu_\perp}^2} - \frac{(\mu_\parallel - \frac{A\nu_{\parallel g}}{r})^2}{2(\sigma_{\mu_\parallel}^2 + [A\nu_{\parallel g}\sigma_{\frac{1}{r}}]^2)} - \frac{(\nu_r - \nu_{r_g})^2}{2\sigma_{\nu_r}^2} - \frac{(\frac{1}{r} - \frac{1}{r_g})^2}{2\sigma_{\frac{1}{r}}^2}\right), \quad (3.13)$$

where $A = 4.740470466\,\mathrm{km\ yr\ s^{-1}}$ is a constant used for unit conversion of absolute velocities to distance-relative proper motions, the value of which is given by the ratio of kilometres in one AU and seconds in one Julian year. With the addition of the above equations, the integrals in (3.4) can now be fully calculated, yielding a Bayes' Factor (K) for each candidate member. Determining a model likelihood ratio (R) from the Bayes' Factor requires additional prior information, which we describe in the following section

Determining a Suitable Prior and Membership Probabilities

The prior probability $P_0 = P(M_g)/P(M_f)$, which is defined for our case in (3.4), represents starting information about the models which will be altered by the application of observed data (the Bayes' Factors). The choice of prior is extremely important in determining robust membership probabilities. A uniform prior, which would state that, initially, a star is as likely to be a member of the Sco-Cen association as it is to be a field star, is an overly simple prior, and will grossly overestimate membership probabilities because the field distributions described above are so much broader than the group distribution.

A logical way to express the prior is as the expected ratio of Sco-Cen association members to field stars in the area of sky occupied by Sco-Cen, and in the particular magnitude and colour range being examined. Given the sparse nature of the current Sco-Cen low-mass star membership, it is difficult to determine this number directly. Instead, we first use an extrapolated initial mass function (IMF) fit to the B, A and F-type membership of the most recent high-mass membership of Sco-Cen (Rizzuto et al., 2011). A simple extrapolated Salpeter IMF fit to the high mass membership produces a prior of $P_0 = 0.015^{+0.004}_{-0.008}$, when compared with the field density in the UCAC4 catalogue. This is smaller than the prior of 0.08 used in the high-mass membership selection (Rizzuto et al., 2011), which is not surprising considering the increasing field contamination expected for the cooler stars. Using the prior we can then compute model likelihood ratios (R) for each candidate member, and then determine robust membership probabilities directly from these ratios $P(M_g|D) = R/(R+1)$.

In summary, the general procedure is as follows:

1. Remove stars with colours or magnitudes outside the range in which a G, K or M-type Sco-Cen member is expected to fall.

2. Remove stars with suspect photometry and proper motions as described in the UCAC4, 2MASS and APASS catalogues.

3. Using APASS and 2MASS photometry, calculate association and field model distances for each star in the sample.

4. Generate a random sample of 10^5 association model velocity and distance values, and 10^6 field model values.

5. For each random value, use the conversions described above to calculate values of $\mu_{\|,m}$, $\nu_{r,m}$ and to rotate the measured stellar proper motions.

6. Compare the model proper motions to the stellar values using equation (3.4) to calculate a Bayes' factor.

7. Using the prior, calculate model likelihood ratios, and then membership probabilities.

3.1.3 Results of the Selection Algorithm

Here we discuss some characteristics of the membership probabilities produced by the Bayesian selection algorithm. We applied the selection to an input portion of the UCAC4 catalogue, which spanned the Upper-Scorpius subgroup of the Sco-Cen association, with a magnitude range of $10 < V < 14$ and a colour span of $0.3 < B-V < 1.3$. This colour-magnitude range encompasses young (<10 Myr) stars in the late G-type to early M-type range, or a mass spread of 0.5 to 1.8 $M_\odot$. This spectral type range represents the current frontier of membership completeness for Sco-Cen, which currently ends at the limit of the HIPPARCOS astrometry at approximately the early G-type members.

To determine the validity of the membership selection, we have compiled a list of previously known Sco-Cen members in the spectral type range used in our selection. These objects were compiled from the studies of Walter et al. (1994), Preibisch et al. (1998), Preibisch and Zinnecker (1999), Preibisch et al. (2001) and Preibisch et al. (2002), and comprise 87 objects which were included in our selection sample. We cross-matched the coordinates of these objects with the UCAC4 catalogue, and plot a histogram of their membership probabilities in Figure 3.3. We find that the vast majority of the known pre-main sequence members of Upper Scorpius included in our selection sample have membership probabilities $P_{mem} > 0.7$, with the smallest probability for a known member being 28%. There were also 19 known non-members included in our Bayesian selection. Combining the known members and non-members (total 106 objects), the Bayesian probabilities predict that there will be 90 members, and 16 non-members. These estimates agree within the Poisson counting error of the actual number of members and non-members, and hence we are confident our analysis is producing meaningful probabilities.

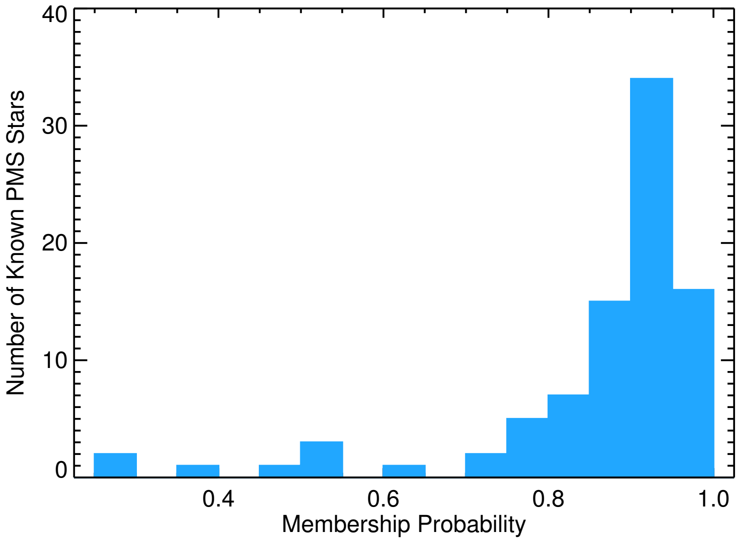

Figure 3.3: Histogram of the Membership probability of the 87 known pre-main sequence Upper-Scorpius members included in our selection sample. Note the significant portion of the known members with membership probabilities larger than 70 %, indicating that the selection algorithm is providing a high-confidence prioritisation of potential Upper Scorpius candidate members.

Taking objects with greater than 30% probability of Sco-Cen membership according to our selection, we expect an interloper fraction of 30-40%, depending on the choice of prior, which is unsurprising given the quality of astrometry that is available for these objects. Despite this, and given the high recovery rate of previously discovered Upper Scorpius members, we expect the membership selection described above to provide a robust prioritisation of candidate members for targeting with spectroscopic followup observations.

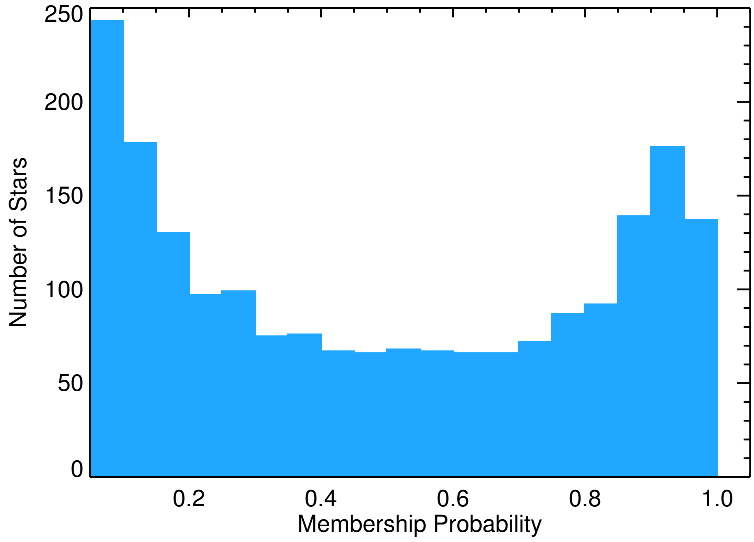

Figure 3.4: Histogram of membership probabilities produced by our Bayesian selection algorithm for the entire selection sample. For ease of viewing, we have omitted the smallest probability bin of the histogram ($0 < P_{men} < 0.05$), which contains the largest number of objects.

3.2 Spectroscopic Membership Confirmation of Sco-Cen Low-Mass Stars

A purely kinematic selection of the low-mass members of Sco-Cen is not sufficient to assign membership to G,K and M-type stars because the quality of the astrometric data available would produce an interloper contamination much higher than would be acceptable for future studies using Sco-Cen as an age benchmark. In order to determine membership beyond any doubt, spectroscopic follow-up of the candidate members is needed to identify stellar youth indicators, which would place candidate members in the Sco-Cen association. Sco-Cen is a vast association, spanning thousands of square degrees, and hence, determining the compete low-mass membership of the association requires a large observing campaign. Our Bayesian selection algorithm provides a means of reducing the overall time required per identified association member, and in this section, we describe follow-up observations we undertook to identify new Sco-Cen members on the G, K and M-type mass range. Over the course of the last three years, we have been awarded 8 nights using the 6dF spectrograph on the UK Schmidt telescope at Siding Spring Observatory; unfortunately none of these nights were useable due to poor weather. This instrumental setup would have been capable of observing 150 stars simultaneously, but was decommissioned in preparation for the FunnelWeb and TAIPAN surveys. We were also awarded 18 nights using the WiFeS integral field spectrograph on the ANU 2.3 m telescope, also at Siding Springs. Unfortunately, due again to poor weather, only 8 nights on the ANU 2.3 m had clear and usable time, most of them in 2014.

3.2.1 Young Stars and Gas Giants with WiFeS

The WiFeS (Wide Field Spectrograph) instrument on the ANU 2.3m telescope is an integral field, or imaging, spectrograph, which provides a spectrum for a number of spatial pixels across the field of view using an image slicing configuration. The field of view of the instrument is 38×25 arcseconds, and is made up of 25 slitlets which are each one arc second in width, and 38 arcseconds in length. The slitlets feed two 4096×4096 pixel detectors, one for the blue part of the spectrum and the other for the red, providing a total wavelength coverage of 330 - 900 μm, which is dependent on the specific gratings used for the spectroscopy. Each 15 micron pixel corresponds to 1×0.5 arcseconds on sky.

There are a number of gratings offered to observers for use with WiFeS. For identification of Upper-Scorpius members, we required intermediate-resolution spectra of our candidate members, with a minimum resolution of ∼3000 at the Li 6708 Å line, and so selected the R7000 grating for the red arm and the B3000 grating for the blue arm, which was used solely for spectral-typing. This provided $\lambda/\Delta\lambda \sim 7000$ spectra covering the lithium 6708Å and H-α spectroscopic youth indicators. The blue spectra provided additional SED information and allow temperature, gravity, metallicity and spectral type fitting of the new members. To properly identify members, we required a 3σ-detection of a 0.1Å equivalent width lithium line, which corresponds to a signal-to-noise ratio of at least 30 per pixel. In order to achieve this, we took exposures of 5 minutes for R=13 stars (approximately type M3 in Upper-Scorpius), and binned by 2 pixels in the y-axis, to create 1×1" spatial pixels and reduce overheads. With overheads we were able to observe 12 targets an hour in bright time, or ~80-90 targets per completely clear night.

In conjunction with identifying new Sco-Cen members, we also searched for GSC 06214-00210b analogs by making use of the WiFeS imaging capabilities and spectroastrometry. As mentioned above, these are wide (>100 AU), roughly planetary mass (~10 M_{Jup}) companions to approximately 4% of young stars, the majority of which are accreting (Ireland et al., 2011a). These accreting exoplanets are expected to be found most often around the youngest stars, making Sco-Cen and extremely important hunting ground for these objects.

Detection of these wide orbit gas giants with WiFeS is possible due to the relative brightness in H-α emission of these planetary companions compared to other wavelengths. Figure 3.5 displays Hubble Space Telescope (HST) observations of GSC 06214-00210 in both narrow-band H-α and broad band filters. The stark difference in the star to planet contrast in the accretion-produced H-α compared to the broadband filter is clear from the image; in the H-α, the star to planet contrast is 5:1, while in the broadband visible it is ~10,000:1 (Zhou et al., 2014).

Although there are no published visible spectra of these objects, we used 2M1207A (~10 times smaller accretion luminosity' Bowler et al. (2011), Herczeg and Hillenbrand (2008)) as a proxy for basic calculation of the expected detectability of these types of objects with the WiFeS spectrograph. The H-α luminosities quoted here are consistent with recently published HST measurements of several young accreting wide planetary-mass companions (Kraus et al., 2014), and hence provided a reasonable estimate of detection possibilities for our WiFeS survey.

2M1207A has an average H-alpha flux of approximately 2×10^{-14} erg s^{-1} cm^{-2} (Herczeg and Hillenbrand, 2008) in a ~200 km s^{-1} width emission line at a distance of 52 pc (Ducourant et al., 2008). Such an object at the distance of the Sco-Cen association (~150 pc) will have a flux in H-α of approximately 2×10^{-15} erg s^{-1}. We searched for companions with fluxes down to 10^{-15} erg s^{-1}, which thus included objects two times fainter than 2M1207 or ~20 times fainter than GSC 06214-00210b. Assuming 2" seeing,

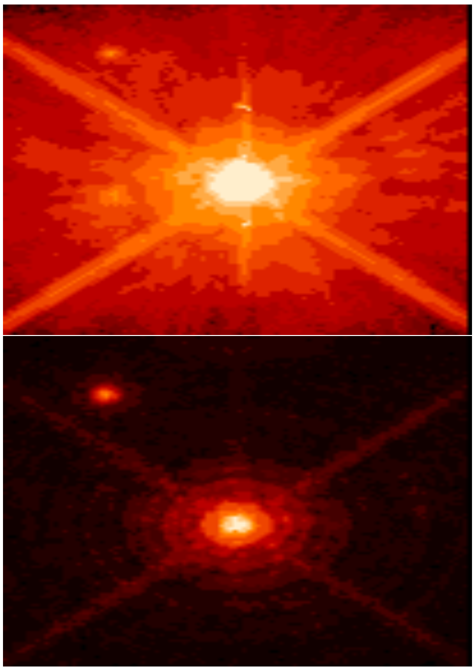

Figure 3.5: Hubble Space Telescope images of GSC 06214-00210 and its massive gas giant companion in both the F625W wide filter (top) and the narrow band H$-\alpha$ filter (bottom). In the H-α the star to planet contrast is 5:1, making the planet extremely bright for a substellar object.

our survey was expected to detect GSC 06214-00210b analogues down to separations of $\sim$1", using a spectroastrometric analysis which we will discuss below.

3.2.2 Sample Construction and Observations

The Bayesian membership selection method described above provides reliable membership probabilities, which can be used to separate mid and high-confidence Sco-Cen candidate members from the background and foreground interlopers which confuse the Sco-Cen area of sky and make observational identification of Sco-Cen members difficult.

WISE IR Excesses as Youth Flags

In addition to the Bayesian selection of candidate members, we further catalogued WISE 22, 12 and 4.5 μm excess emission for our candidates. As described above in Chapter 2, and in the study by Rizzuto et al. (2012), observed mid-IR emission in excess of the expected photosphere levels is often indicative of either a debris or gaseous primordial disk. In the case of the G, K and M-type Sco-Cen candidates of interest in this section, IR excesses point to the presence of a gaseous hydrogen disk remaining after formation and actively accreting onto the central star, which is often associated with H-α emission (Carpenter et al., 2009). The timescale over which such a disk is expected to produce mid-IR emission above the stellar photosphere is very short, with excess emission strength, and hence the number of stars with observable IR excess reducing by a factor of $\sim$5 by 100 Myr (Rieke et al., 2005).

Using HIPPARCOS based membership probabilities, we showed in Chapter 2 that $\sim$41% of B, A and F-type stars in Sco-Cen exhibit a mid IR excess in at least the 22 μm band, with the corresponding percentage of older field stars being consistent with 0% (Rizzuto et al., 2012). Other studies of lower mass Sco-Cen stars indicate a similar level of disk prevalence for K and M-type stars: Chen et al. (2011) determine that 32$\pm$5% of F and G-type Sco-Cen members have either debris or primordial gas disks, and Carpenter et al. (2009) conclude that $\sim$25-35% of Sco-Cen G and K-type members have excesses greater than 15% above the photosphere level, with only $\sim$5% of older, >200 Myr field G and K-type stars exhibiting a similar excess. The important point is that the presence of a mid-IR excess above the expected stellar photosphere is a strong indicator of the youth of the host stars, and can be used in conduction with the Bayesian kinematic selection to identify the high likelihood candidate Sco-Cen members for priority follow-up and confirmation.

The detection of excesses was done using public WISE mission data (Wright et al., 2010) which are available in an online database. The analysis was done in a way similar to that described in Rizzuto et al. (2012), which is presented above as part of this thesis. The WISE mission data consist of magnitudes in four bands, W_1, W_2, W_3 and W_4, centred on wavelengths 3, 4.5, 12 and 22 μm respectively (Cutri et al., 2011). As in Chapter 2 we construct three colours from the WISE photometry and compare them to the expected linear relationship of the photospheric emission with $J-K$ colour (Carpenter et al., 2006). We fit to this photosphere emission in colour-colour space for each WISE colour described above, removing outliers, which presumably are stars with potential mid IR excesses, in an iterative method (see Chapter 2). Once the photosphere emission is determined we select those objects in each WISE colour which are more than one-sigma above the photosphere level as displaying an excess. Although the infrared excesses were not deliberately used to prioritise observations, they were available in the observation table when choices were made as to which star to observe, so the excess fraction amongst the incompletely observed sample may not be a robust observable.

Target Sample and Observations

We drew our targets from our Bayesian selection in a square region of Upper Scorpius bounded by $(l, b) = (343, 10)$ and $(360, 30)$, which covers the classical extent of the Upper Scorpius subgroup. We selected targets in this region of sky between 10th and 14th magnitude in the APASS V-band, in order to include late G-type to early M-type (M3) Upper Scorpius members. Finally, we excluded all objects with a Bayesian membership probability of $P_{mem} < 5\%$. This resulted in 2043 objects, with 207 displaying excesses in the mid-IR after the WISE excess analysis was applied. Our target sample table is displayed in Appendix B.

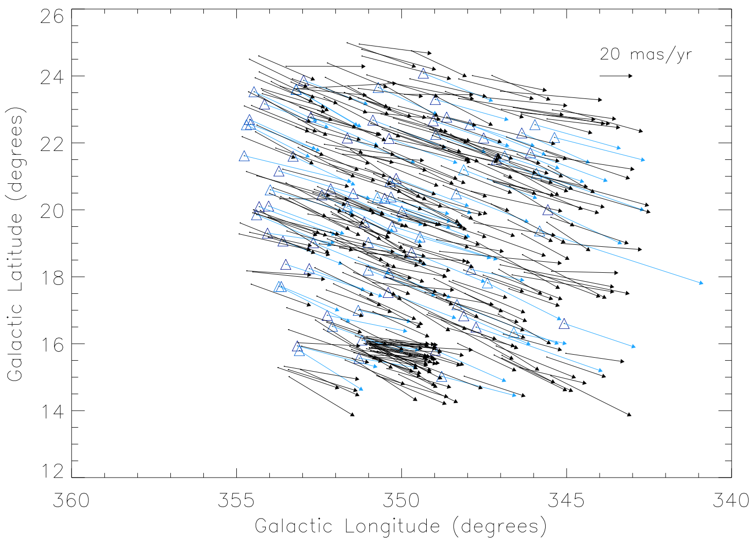

Figure 3.6: Proper motion plot of G, K and M-type potential members selected using our Bayesian selection algorithm. The blue points represent high-mass members taken from Rizzuto et al. (2011) (triangles), while the black arrows represent low-mass stars in our sample.

The initial intention for our survey was to observe Upper Scorpius member candidates with WiFeS, which would confirm membership, while simultaneously identifying wide-orbit gas giant companions; however, due to the increased likelihood of a prolonged period of poor weather on the afternoon of the first observing night in June 2013, we decided to include in the sample some objects already identified as pre-main sequence Sco-Cen members, so as to allow a better characterisation of the selection method and increase the probability of detecting a wide-orbit gas giant. In total, we observed 75 targets in our sample over the course of the first two half-nights of our observing time (19/06/2013 and 09/04/2014). These objects included GSC 6214-0210, GQ-Lup and 1RXSJ1609, the prototypical wide gas giant host, and known accretors.

The Kepler K2-Field Sample

In early 2014, a collaboration, including Dr. Michael Ireland, Dr. Adam Kraus and the author, submitted a proposal to observe candidate Upper-Scorpius members in the K2 campaign. The proposed candidate members spanned spectral types ranging from A5 to M5, and were chosen from both the Bayesian selection described above, and a complementary selection method developed by Dr. Kraus using a combination of kinematic and photometric distance estimates derived from multiple all-sky catalogues, based on a similar method used previously for the Coma-Ber cluster (Kraus and Hillenbrand, 2007b). In that selection, if a candidate is placed above the main sequence based on the distance estimates, then it is deemed likely to be an Upper-Scorpius member. In the magnitude range where this new sample overlaps with the Bayesian sample described above, we typically have >90% of the Bayesian selected stars included in the sample, although this selection method is more conservative and includes a larger number of candidates. The final sample was constructed from both selection methods.

For the second group of observations, spanning the dates 16/06/2014 to 23/06/2014, we used the combined sample, containing stars selected by the Bayesian process, as well as stars submitted in the Kepler K2 proposal, in order to obtain membership-confirming spectra of as many of these objects as possible. We expected the new Galactic Archeology with HERMES (GALAH) survey, currently being carried out with the new HERMES multi-object spectrograph at the Anglo Australian Telescope, to observe a large number of the 11<V< 14 candidates, and so we deferred observing any of these targets until a clear picture of which are left unobserved is available. We thus observed as many targets as possible from the K2 sample with Kepler interpolated V_{JK} magnitudes between 13.5 and 14.5.

In periods of marginal weather conditions, such as thin or intermittent cloud cover, we observed targets with Kepler magnitudes brighter than 11th magnitude, and kinematically selected high-mass (B, A, F and G-type) candidates that have poor or absent radial velocity measurements, with the goal of excluding any interlopers from the current high-mass membership. Table C.1 in Appendix C provides a summary of our spectroscopic observations of candidate G,K and M-type Upper Scorpius members. Analysis of the high-mass member observations is currently ongoing and so discussion of these objects will be left to a later publication.

After learning about 2.3 m telescope operations from the two poor-weather runs at Siding Springs Observatory, the successful WiFeS observations were done remotely from Macquarie University using the TAROS remote user software for the 2.3 m telescope. This allows full control of the telescope systems from a distant location. We took a single 5 minute exposure of each target, using the "stellar" field of view option, which only reads out one half of the CCD for each arm of the WiFeS spectrograph. We also binned every two pixels in the Y-direction, which produces a spatial resolution of 1×1 arcsecond, as opposed to the standard 1×0.5 arcsecond resolution. The binning and field of view restriction reduced readout overheads by a factor of four, allowing a single exposure to be read out in less than 20 seconds. This yielded an extremely fast cadence for our observations, and ensuring that we always slewed to nearby targets, we were able to complete observations of a single target in ∼6-7 minutes. We began our observations with 10 bias frames, a flat field, and an arc exposure (NeCd), and then continued to take one arc frame every hour throughout the night. In total, we observed 406 G,K and M-type candidate members. The full sample of ∼700 candidate members can be completely observed with spectroscopy over the course of 2015 with moderate time allocation and continued operation of the HERMES (GALAH) survey.

3.2.3 Data Reduction

The raw WiFeS data was initially reduced with a pre-existing Python data reduction software package called the "WiFeS PyPeline", which is provided to WiFeS observers. The purpose of the software is to transform the CCD image, which consists of a linear spectrum for each spatial pixel of the WiFeS field of view, into a data cube. This involves bias subtraction, flat-fielding, bad pixel and cosmic ray removal, sky subtraction, wavelength calibration, flux calibration, reformatting into the cube structure, and interpolation across each pixel to produce a single wavelength scale for the entire image. Once this process is complete, the user is left with a single cube for each object observed, with dimensions 25"×38"×3650 wavelength units. For the grating resolutions and angles used in our observations, we obtained spectral coverage from 3200 – 5500 Å in increments of 1.3 Å in the blue arm, and 5400 – 7000 Å in increments of 0.78 Å in the red arm.

Following the standard WiFeS reduction procedure, we continued with a further custom reduction, the aim of which was to measure the centroid position of the target object in each wavelength, such that the presence of an H-α-bright planetary mass companion could be detected by the measurement of a wavelength-dependent centroid shift. This consisted of determining a best fit point spread function (PSF) model for the spatial image in a clean section of the spectrum, and then measuring the centroid shift of this PSF at each wavelength along the spectrum. An additional benefit of this is a more accurate sky subtraction, and an integrated spectrum of each object, which can be used to measure equivalent widths of key spectral lines.

We first cut out a 10" by 10" wide window (10×10 pixels), centred on the target. The vast majority of the stellar flux is contained within the central 3" by 3" region of the windowed image, and so the adopted width of 10" allows a clear region of background around the target; Figure 3.7b provides an illustration of the data. We then fit a Moffat point spread function (Racine, 1996) to a region of the spectral continuum which does not include any spectral features, but is close to the H-α line. This region consisted of 400 spectral units, spanning 6368 – 6544 Å. Figure 3.7a displays the spectral region used for the initial PSF fit, as well as the H-α and Li 6708 Å lines for one target in our sample, 1RXS J153910.3-264633, which shows strong indications of youth.

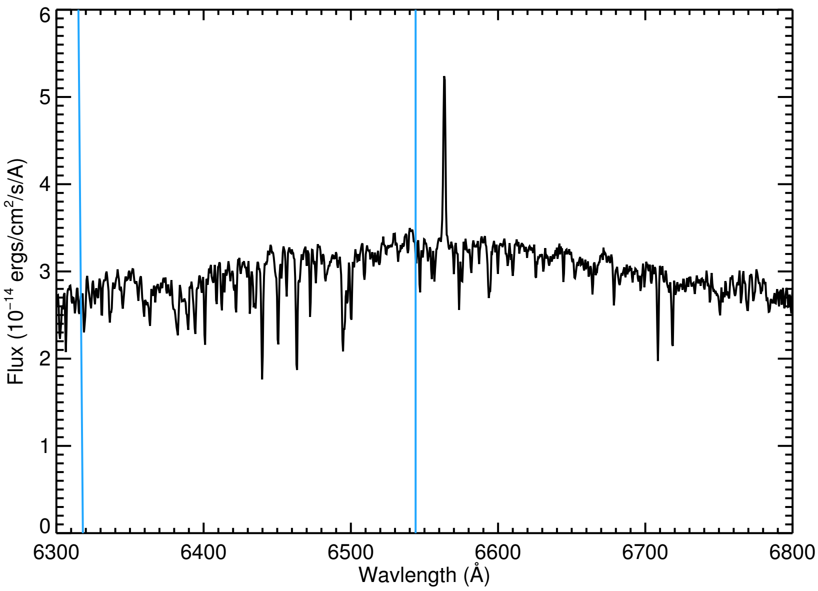

(a)

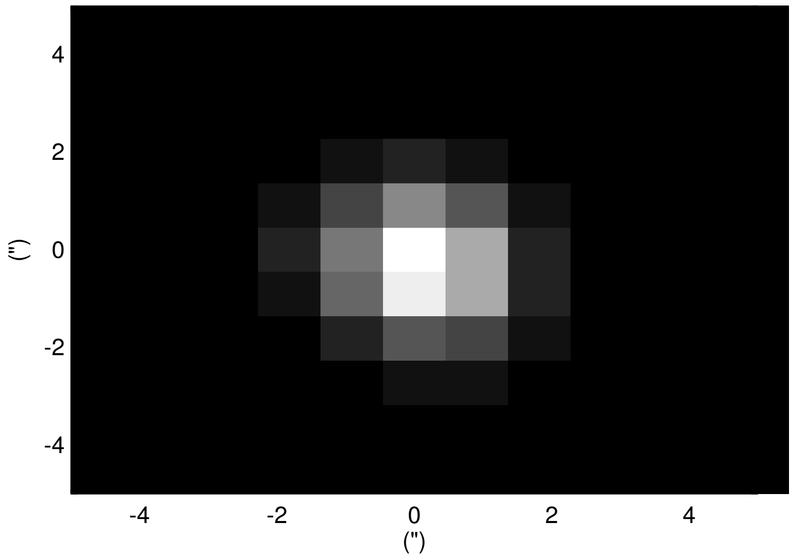

(b)

Figure 3.7: (a) Example spectrum for object 1RXS J153910.3-264633, a high priority target in our observation sample, which shows signs of youth such as H-α emission and Li 6708Å absorption. The region of the continuum used for the initial PSF fitting is bounded by blue lines. (b) Spatial image created for 1RXS J153910.3-264633 by adding the images at each wavelength of the PSF fitting region of the continuum.

The precise model that we fit to the spatial image is given by;

$$\mathrm{PSF} = \mathrm{S} + \mathrm{F}\frac{(2^{\frac{1}{\beta}}-1)(\beta-1)}{\pi w^2(1+(2^{\frac{1}{\beta}}-1)(\theta/w)^2)^{\beta}}, \tag{3.14}$$

where S indicates the sky contribution to the flux, β is an integer parameter that determines the strength of the wings of the Moffat PSF, θ is the distance from the centre of the profile, w is the half width of the Moffat PSF, and F is the stellar flux. Given that we have a two dimensional PSF, and that each dimension has a different Moffat function half width, we require two different values of w. We create this two dimensional Moffat profile by scaling θ appropriately;

$$\theta = w_x^2(x-x_0)^2 + w_y^2(y-y_0)^2, \tag{3.15}$$

where w_x and w_y are the PSF width parameters in each dimension, (x, y) is the position of a given point on the image, and (x_0, y_0) is the image centroid. Inputting this value of θ into a Moffat function with width $w = 1$ will thus produce the desired asymmetric two dimensional profile.

We found that $\beta = 4$, a value which describes most telescope PSFs, yielded the closest fit to our data. We also attempted to fit a Gaussian profile to the spatial images, in the same format as the Moffat profile described in equation 3.14; however the Gaussian model produced consistently poorer fits to the data than the Moffat model, particularly in the wings of the PSF, with typical values of $\chi_r^2 \sim 4$ for the Gaussian model fit and $\chi_r^2 \sim 2$ for the Moffat model. On the basis of the goodness of fit difference, we adopted the Moffat model exclusively in our analysis. For each target observed, we used the continuum spectral region between $6368-6544$Å to determine the parameters of the Moffat PSF that most closely reproduced the spatial images. We then fixed the half width parameters in each dimension, and fit our PSF model to each individual wavelength element image along the spectrum to determine S, F and the centroid position for each wavelength. This process provides two useful characteristics, the first of which is the integrated spectrum (F) of the target (see Figure 3.8), with the sky component (S) subtracted out, and secondly the centroid position (x_0, y_0), for

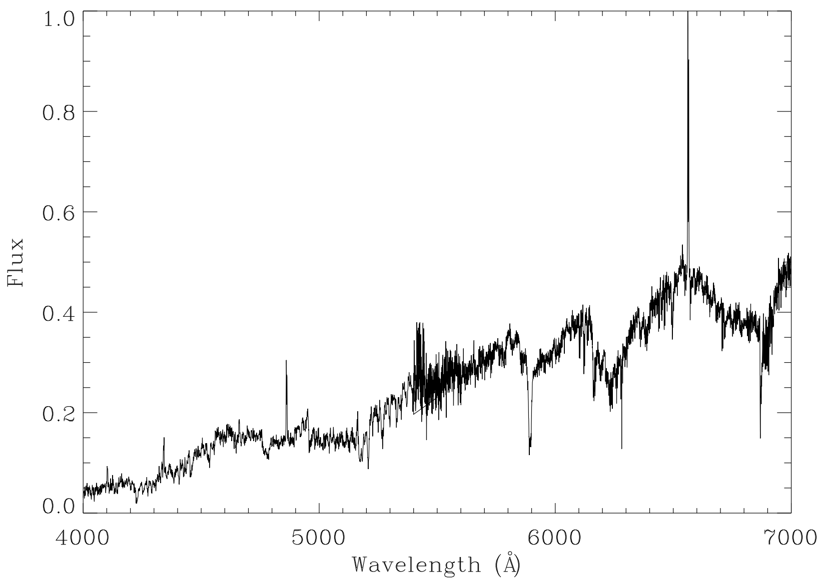

Figure 3.8: The full WiFeS integrated spectrum produced by first processing with the WiFeS Pypeline, and then our spectro-astrometric analysis for the star USco 48, a known member of the Upper Scorpius subgroup.

each wavelength, which will be used to search for H-α bright companions.

Equivalent Widths and Spectral Typing

Using the integrated spectrum of the object F, we calculate the equivalent widths of the H-α and Li 6708 Å lines in the usual way, namely, by first fitting a continuum flux level F_c to the line, and then integration across the spectral line;

$$EW = \sum_{i=1}^{n_\lambda}(1 - (F_i/F)_c^2)\Delta\lambda, \tag{3.16}$$

where F_i is the flux in a given wavelength element, $\Delta\lambda$ is the spectral resolution, and $1 < i < n$ runs over the extent of the spectral line. The uncertainty on this measurement is given by;

$$\sigma_{EW}^2 = \sum_{n=i}^{n_\lambda} \Delta\lambda^2(\sigma_{F_i}^2(\frac{1}{F_c})^2 + \sigma_{F_c}^2(\frac{F_i}{F_c})^2), \tag{3.17}$$

where σ_{F_i} is the uncertainty in the spectrum, and σ_{F_c} is the continuum fit uncertainty, which we take to be equal to the signal to noise ratio of the continuum on either side of the spectral line.

We also fit spectral types to our reduced spectra, using the Pickles (1998) spectral library as reference. This library contains low resolution spectra (5Å) for each spectral type and luminosity class, with spectra spanning a wavelength range of $1150-25000$Å. We initially cut the library spectra at the wavelength limits of our observations (4000-7000)Å, removing the bluest part of each of our spectra, which is often significantly noisier than the rest of the data. The library spectrum is then interpolated onto the same wavelength scale as the data for comparison. We compare the library spectra to the data by calculating the normalised cross-correlation of the library and data spectra, and repeating the process for each library spectrum. The cross-correlation for a single spectrum is given by:

$$C_r = \frac{1}{n}\sum_{\lambda}\frac{(D(\lambda)-\bar{D})(L(\lambda)-\bar{L})}{\sigma_D\sigma_L} \tag{3.18}$$

where $D(\lambda)$ and $L(\lambda)$ are the data and library spectra, σ_D and σ_L are the standard deviations of the two spectra, and $\bar{D}$ and $\bar{L}$ are the average values of the spectra. When calculating the cross-correlation, we introduce a wavelength shift varying from -5 to 5 Å, and take the largest calculated cross-correlation for each library spectrum. We manually check that the maximum shifts for the output fits were at most 1 and 2 WiFeS pixels in the blue and red spectra, respectively. Through visual inspection of the estimated spectra, the spectral types listed here are accurate to within one spectral subtype. Table 3.3 lists both the Li 6708Å and Hα equivalent widths, and the estimated spectral types of the young stars observed in our survey.

3.2.4 Survey Results

We display the Li 6708 Å line equivalent widths for those stars with a lithium line in the 406 stars observed in our survey in Figure 3.9a and the colour magnitude diagram of the new members in Figure 3.9b. As mentioned above, due to the short timescale over which Li is depleted (D'Antona and Mazzitelli, 1994), the presence of a strong Li line can robustly identify a star as young, and hence part of a young association. We defined any star with a Li 6708 Å equivalent width greater than 0.1 Å to be a young star. This low, but significantly above field, Li threshold is in general keeping with previous surveys, and is justified given the effects of episodic accretion on Li depletion in the latest models (Baraffe and Chabrier, 2010). In total we identify 252 stars as members based on their Li 6708 Å absorption, 232 of which are new.

Table 3.3: Stars with measured Lithium absorption in our survey for new Upper Scorpius members. The first column lists either the UCAC4 catalogue unique source identifier if the object was taken from the Bayesian sample, or the adopted name if the target was taken from the Kepler sample. We also list the the spectral type fits, EW(Li), and EW(Hα), the equivalent widths of the Li 6708Å and Hα lines respectively. For the object UCAC4-415856526, the spectral type could not be accurately determined due to the poor quality of the data.

Name	R.A. (J2000.0)	Decl. (J2000.0)	EW(Li) (Å)	$\sigma_{EW(Li)}$ (Å)	EW(Hα) (Å)	$\sigma_{\mathrm{EW(Li)}}$ (Å)	SpT
UCAC-365072173	15 39 06.96	-26 46 32.1	0.46	0.02	-1.22	0.03	K7
UCAC-408484365	15 41 31.21	-25 20 36.3	0.40	0.01	-2.70	0.04	G8
UCAC-4549054	16 02 00.39	-22 21 23.9	0.66	0.04	-4.23	0.05	M2
UCAC-4550645	16 02 08.45	-22 54 59.1	0.67	0.03	-3.50	0.05	K7
UCAC-404499023	16 00 42.76	-21 27 38.0	0.55	0.02	-2.37	0.04	K5
UCAC-404500621	16 00 40.56	-22 00 32.2	0.42	0.01	0.28	0.02	K3
UCAC-404425413	15 58 12.70	-23 28 36.4	0.25	0.01	0.89	0.02	G8
UCAC-404477376	15 59 59.95	-22 20 36.8	0.59	0.03	-4.64	0.05	K7
UCAC-27473795	16 00 13.30	-24 18 10.7	0.59	0.03	-2.14	0.04	K7
UCAC-408765529	15 49 21.00	-26 00 06.3	0.44	0.02	-0.09	0.02	K4
UCAC-1285895575	15 53 06.83	-22 47 17.4	0.66	0.03	-4.28	0.06	M1
UCAC-70157647	15 55 02.14	-21 49 43.5	0.48	0.02	-0.46	0.03	K5
UCAC-1010064430	15 57 34.31	-23 21 12.3	0.58	0.02	-6.37	0.06	M1
UCAC-426546698	15 57 16.74	-25 29 19.3	0.67	0.04	-2.44	0.07	K5
UCAC-404411726	15 56 55.46	-22 58 40.4	0.58	0.04	-3.10	0.15	M0
UCAC-415911029	16 09 30.31	-21 04 58.9	0.49	0.02	-0.76	0.03	K7
UCAC-4644043	16 05 21.57	-18 21 41.2	0.47	0.02	-37.96	0.15	K7
UCAC-415797428	16 05 38.16	-20 39 47.0	0.59	0.02	-1.09	0.03	K5

Continued on next page

UCAC-50927093	16 06 43.86	-19 08 05.5	0.59	0.02	-8.57	0.07	K7
UCAC-50925875	16 06 47.94	-18 41 43.8	0.49	0.02	-0.92	0.04	K5
UCAC-415856526	16 08 01.41	-20 27 41.6	0.33	0.11	0.00	0.00	F2
UCAC-416412009	16 21 54.67	-20 43 09.1	0.38	0.02	-0.67	0.03	K4
UCAC-415852329	16 07 40.06	-21 48 42.7	0.51	0.02	-2.06	0.05	K4
UCAC-39419158	16 12 06.68	-30 10 27.1	0.55	0.03	-33.77	0.14	M0
UCAC-28097463	16 15 33.11	-27 07 58.8	0.58	0.03	-2.55	0.06	K5
UCAC-28091657	16 15 35.86	-25 29 01.0	0.41	0.02	-0.13	0.02	K3
UCAC-416165104	16 15 59.86	-23 25 04.5	0.49	0.03	-0.80	0.04	K4
UCAC-160814997	16 16 51.30	-24 33 27.7	0.14	0.02	3.59	0.06	K1
UCAC-416241839	16 17 31.38	-23 03 36.0	0.24	0.02	1.05	0.03	G8
UCAC-416272798	16 18 19.98	-20 05 34.9	0.33	0.03	1.24	0.04	G8
UCAC-1312371465	15 42 26.21	-22 47 46.0	0.46	0.04	-3.08	0.07	K7
UCAC-408606874	15 45 09.71	-25 12 43.0	0.61	0.02	-2.02	0.04	K7
UCAC-1233680087	15 47 10.64	-17 36 24.3	0.52	0.05	-4.20	0.08	K7
UCAC-30182208	15 47 43.31	-18 19 15.4	0.55	0.02	-1.82	0.04	K7
UCAC-408774136	15 49 25.09	-28 43 52.8	0.54	0.03	-2.39	0.05	M1
UCAC-408935154	15 54 03.58	-29 20 15.5	0.46	0.03	-1.75	0.04	K7
UCAC-416412009	16 21 54.67	-20 43 09.1	0.36	0.02	-0.43	0.02	K5
UCAC-404419461	15 56 47.69	-19 50 07.6	0.60	0.02	-3.12	0.03	M1
UCAC-4548058	16 02 24.61	-22 00 24.8	0.72	0.04	-3.92	0.07	K7
UCAC-160764955	16 16 02.92	-24 30 54.8	0.47	0.05	-1.92	0.07	M0
UCAC-160759135	16 16 17.20	-26 09 10.2	0.71	0.05	-2.24	0.06	K5
UCAC-416235767	16 17 22.98	-21 21 11.9	0.60	0.02	-1.45	0.05	K7
UCAC-160911080	16 19 14.74	-25 32 31.3	0.34	0.02	0.59	0.02	K4
UCAC-160921648	16 19 31.39	-25 18 12.8	0.40	0.03	0.45	0.04	M0
UCAC-416333148	16 19 45.38	-21 47 57.8	0.35	0.03	-2.56	0.05	M1
UCAC-416355975	16 20 27.24	-21 26 06.9	0.52	0.04	-2.51	0.05	M1
UCAC-977055474	16 20 45.79	-28 49 20.1	0.66	0.07	-5.67	0.11	M0
US-07477	16 23 59.02	-27 36 03.8	0.47	0.02	-6.44	0.04	M3
US-02400	15 55 41.41	-20 43 15.1	0.64	0.01	-6.10	0.04	M2
US-02644	15 58 06.95	-26 23 46.6	0.44	0.02	-5.24	0.04	M2
US-05370	16 17 16.50	-23 27 57.1	0.61	0.02	-8.59	0.05	M3
US-07557	16 24 11.77	-19 55 58.3	0.51	0.01	-4.78	0.04	M3
US-04997	16 15 27.51	-26 27 28.1	0.46	0.04	-4.09	0.06	M5

Continued on next page

US-05416	16 17 29.95	-24 51 03.0	0.34	0.02	-6.97	0.04	M3
US-07049	16 22 54.79	-21 38 09.2	0.31	0.01	-5.52	0.04	M3
US-06595	16 21 48.53	-25 17 26.6	0.48	0.01	-1.21	0.03	M2
US-06214	16 20 32.46	-22 57 45.3	0.51	0.01	-7.12	0.04	M3
UCAC-27777972	16 07 29.43	-25 46 15.7	0.44	0.01	-2.82	0.03	M2
US-04100	16 09 49.55	-24 44 46.8	0.55	0.01	-4.75	0.11	M2
US-06707	16 22 05.88	-21 21 55.7	0.30	0.01	-2.57	0.02	M2
US-08856	16 27 33.21	-28 21 09.7	0.13	0.01	-4.93	0.05	M3
US-02540	15 57 03.68	-23 04 48.4	0.68	0.02	-9.64	0.05	M5
US-02575	15 57 23.92	-20 51 45.4	0.60	0.02	-5.06	0.05	M2
US-03279	16 03 38.30	-18 54 07.7	0.55	0.02	-4.37	0.04	M2
US-02451	15 56 20.60	-23 36 10.0	0.45	0.02	-4.63	0.05	M3
US-04880	16 14 49.89	-21 39 32.1	0.56	0.02	-2.61	0.03	M2
US-05791	16 19 02.15	-21 38 09.8	0.43	0.02	-6.13	0.05	M3
US-04767	16 14 03.80	-24 53 08.8	0.42	0.02	-2.48	0.06	M2
US-04066	16 09 35.75	-21 38 05.7	0.55	0.01	-3.66	0.03	M3
US-02343	15 55 05.13	-20 26 07.7	0.40	0.02	-6.85	0.05	M2
US-02461	15 56 24.92	-25 41 20.3	0.27	0.02	-5.67	0.04	M3
US-02355	15 55 08.53	-23 18 51.1	0.55	0.01	-8.07	0.04	M2
US-04053	16 09 31.09	-20 41 46.0	0.53	0.03	-9.06	0.06	M4
US-06008	16 19 48.37	-22 12 51.9	0.43	0.03	-16.57	0.14	M3
US-06712	16 22 06.58	-21 27 08.9	0.53	0.02	-7.31	0.05	M3
US-07459	16 23 57.24	-26 20 24.5	0.33	0.02	-7.36	0.05	M4
US-08026	16 25 23.28	-27 27 31.5	0.49	0.03	-8.88	0.06	M4
US-05868	16 19 16.09	-29 15 12.6	0.52	0.02	-4.94	0.04	M3
US-06638	16 21 55.94	-27 05 03.4	0.61	0.04	-7.69	0.07	M5
US-02999	16 01 13.99	-25 16 28.2	0.48	0.04	-5.88	0.15	M3
US-06011	16 19 48.80	-22 24 47.2	0.88	0.06	-15.55	0.10	M5
US-04746	16 13 56.63	-24 57 56.7	0.36	0.02	-5.08	0.04	M3
US-04329	16 11 17.45	-24 41 20.3	0.63	0.02	-5.77	0.04	M3
US-08522	16 26 34.95	-25 11 40.9	0.48	0.01	-1.01	0.02	M2
US-02989	16 01 08.97	-26 45 10.5	0.47	0.05	-5.38	0.19	M3
US-06482	16 21 29.53	-25 29 43.1	0.29	0.02	-4.29	0.06	M3
US-05034	16 15 36.43	-26 22 09.1	0.36	0.03	-4.29	0.08	M2
US-04172	16 10 14.45	-19 51 37.7	0.63	0.02	-4.90	0.04	M4

Continued on next page

US-04613	16 13 09.79	-20 44 59.1	0.57	0.03	-6.11	0.04	M4
US-04655	16 13 21.91	-21 36 13.6	0.53	0.03	-21.99	0.20	M2
US-02889	16 00 12.17	-21 57 03.3	0.43	0.03	-4.37	0.14	M1
US-02395	15 55 39.28	-20 53 07.2	0.81	0.04	-6.91	0.07	M5
US-04682	16 13 32.79	-20 44 41.4	0.48	0.02	-1.96	0.03	M3
US-04721	16 13 44.90	-24 34 14.4	0.47	0.02	-7.23	0.05	M3
US-05405	16 17 26.15	-24 50 59.3	0.45	0.02	-5.71	0.04	M3
US-06004	16 19 47.11	-22 03 11.3	0.49	0.04	-8.67	0.07	M4
US-02611	15 57 42.47	-25 51 35.5	0.59	0.06	-9.58	0.10	M4
US-02576	15 57 24.55	-20 38 38.2	0.52	0.04	-3.48	0.09	M1
US-09976	16 31 05.80	-27 25 46.0	0.38	0.04	-9.05	0.11	M4
US-10272	16 31 56.69	-28 46 12.7	0.17	0.04	-9.99	0.10	M4
US-09628	16 29 56.63	-26 59 18.2	0.52	0.03	-8.00	0.08	M4
US-06412	16 21 15.84	-22 40 04.6	0.52	0.03	-4.73	0.08	M2
US-08259	16 25 57.91	-26 00 37.4	0.21	0.11	-0.12	0.14	K3
US-08259	16 25 57.91	-26 00 37.4	0.37	0.03	-0.08	0.04	M0
US-04527	16 12 36.05	-27 23 03.2	0.38	0.07	0.99	0.06	K7
UCAC-416412009	16 21 54.67	-20 43 09.1	0.32	0.05	-0.67	0.11	K4
US-07978	16 25 16.90	-23 22 03.1	0.74	0.07	-3.75	0.19	M2
UCAC-415960223	16 11 04.80	-23 33 16.6	0.43	0.06	-1.80	0.17	K7
US-03844	16 08 04.11	-26 40 44.9	0.33	0.10	-7.58	0.77	K7
UCAC-27848808	16 08 56.96	-28 35 57.4	0.47	0.15	-10.31	0.31	M5
UCAC-27470462	15 59 52.70	-25 26 29.2	0.38	0.03	-1.63	0.10	M1
US-04973	16 15 19.49	-25 40 12.0	0.51	0.07	-6.57	0.33	M2
US-04771	16 14 07.34	-22 17 32.1	0.51	0.07	-4.84	0.25	M1
US-07545	16 24 09.43	-21 34 07.6	0.49	0.27	-5.02	0.70	M3
US-03292	16 03 46.95	-22 45 24.7	0.38	0.06	-3.48	0.17	M2
US-04455	16 12 05.05	-20 43 40.5	0.58	0.07	-12.04	0.36	M2
UCAC-416027053	16 12 35.31	-20 34 34.0	0.51	0.06	-2.39	0.12	M1
UCAC-1014105644	16 11 26.03	-26 31 55.9	0.46	0.10	-3.02	0.35	M1
UCAC-415927254	16 09 39.70	-22 00 46.6	0.57	0.07	-3.23	0.18	M1
UCAC-27567164	16 03 01.77	-26 26 21.9	0.48	0.05	-3.03	0.23	K3
US-04914	16 15 00.60	-29 19 34.9	0.49	0.07	-3.57	0.15	M3
US-04956	16 15 12.40	-23 18 45.3	0.34	0.05	-1.25	0.10	M1
US-04055	16 09 31.65	-22 29 22.4	0.46	0.07	-4.88	0.17	M2

Continued on next page

US-06727	16 22 08.58	-29 15 06.3	0.56	0.05	-3.24	0.14	M2
US-08117	16 25 35.04	-23 32 55.0	0.67	0.06	-2.62	0.13	M0
UCAC-450863417	16 26 19.98	-22 33 02.5	0.48	0.03	-1.24	0.04	M2
UCAC-379516528	16 27 27.66	-28 21 50.4	0.56	0.03	-5.38	0.15	M2
US-08204	16 25 49.26	-25 54 37.2	0.47	0.02	-1.40	0.03	K7
UCAC-160960929	16 25 28.81	-26 07 53.8	0.55	0.02	-2.86	0.04	M3
US-07894	16 25 02.37	-23 21 44.8	0.65	0.03	-3.08	0.05	M2
US-02956	16 00 49.73	-23 38 43.2	0.60	0.02	-4.16	0.04	M2
US-03015	16 01 22.34	-19 37 22.3	0.45	0.02	-2.59	0.03	M2
US-06168	16 20 21.64	-20 05 34.8	1.07	0.25	-5.90	0.28	M4
US-03964	16 08 56.29	-21 48 48.9	0.56	0.02	-3.71	0.03	M2
UCAC-27638513	16 04 06.71	-26 37 07.1	0.52	0.03	-4.27	0.04	M2
UCAC-416412009	16 21 54.67	-20 43 09.1	0.37	0.01	-0.64	0.01	K4
US-07577	16 24 15.52	-25 44 34.5	0.31	0.02	-0.04	0.02	M1
US-05419	16 17 30.32	-24 38 39.0	0.58	0.03	-1.72	0.05	M2
US-06291	16 20 50.96	-22 53 39.9	0.49	0.02	-1.52	0.04	M2
US-04951	16 15 11.05	-23 22 42.6	0.56	0.03	-3.39	0.03	M2
US-04862	16 14 41.25	-25 56 05.2	0.67	0.02	-3.99	0.05	M2
UCAC-1264986286	16 07 51.37	-17 18 23.2	0.54	0.03	-4.09	0.04	M2
US-02441	15 56 12.17	-23 54 07.6	0.36	0.08	-8.44	0.08	M5
US-02826	15 59 38.07	-26 03 23.3	0.81	0.08	-16.24	0.11	M5
US-05231	16 16 33.46	-25 52 36.8	0.53	0.02	-2.84	0.04	M2
UCAC-416124883	16 14 52.70	-23 08 02.7	0.42	0.03	-4.23	0.04	M3
US-10798	16 33 34.97	-18 32 54.0	0.17	0.05	-8.47	0.21	M3
UCAC-60508355	16 34 38.27	-28 35 50.5	0.22	0.02	-3.31	0.04	M2
UCAC-1253739312	16 23 57.91	-26 02 29.9	0.39	0.02	-1.01	0.03	K7
US-07114	16 23 04.74	-27 59 25.3	0.37	0.01	-1.83	0.02	K7
UCAC-450721096	16 22 44.07	-21 42 22.2	0.53	0.04	-3.36	0.05	M4
UCAC-70205421	15 56 25.11	-20 16 15.8	0.61	0.07	-10.16	0.08	M5
US-04782	16 14 10.11	-22 17 23.6	0.62	0.04	-3.09	0.04	M4
US-06824	16 22 20.93	-27 47 09.5	0.58	0.02	-3.88	0.04	M2
US-05510	16 17 55.02	-27 11 30.4	0.46	0.02	-2.95	0.04	M2
US-04793	16 14 12.59	-24 54 28.8	0.49	0.02	-2.06	0.03	K7
US-08483	16 26 28.04	-25 26 47.8	0.52	0.02	-2.00	0.03	M2
US-04690	16 13 36.45	-23 26 27.0	0.36	0.02	-5.87	0.04	M2

Continued on next page

UCAC-416355791	16 20 36.41	-21 23 12.0	0.65	0.04	-13.01	0.09	M5
US-04482	16 12 13.69	-24 31 36.9	0.31	0.03	-4.25	0.05	M3
US-04198	16 10 26.25	-22 09 10.5	0.60	0.03	-7.54	0.05	M3
US-04046	16 09 29.70	-22 00 58.0	0.59	0.02	-3.34	0.03	M2
US-04292	16 11 05.67	-21 44 03.3	0.63	0.02	-6.01	0.04	M2
UCAC-1253766409	16 24 18.60	-28 54 47.5	0.37	0.02	0.85	0.03	K3
US-02963	16 00 52.72	-25 23 42.6	0.46	0.07	-4.11	0.10	M2
UCAC-1253727753	16 23 32.34	-25 23 48.5	0.31	0.01	0.22	0.01	K5
US-03277	16 03 37.77	-18 45 08.3	0.56	0.04	-4.65	0.08	M2
US-06412	16 21 15.84	-22 40 04.6	0.53	0.02	-5.35	0.06	M2
US-04466	16 12 08.14	-25 47 57.9	0.66	0.03	-6.59	0.07	M3
US-08507	16 26 32.77	-26 22 59.0	0.58	0.12	-4.48	0.15	M5
US-03251	16 03 25.99	-26 27 32.0	0.83	0.07	-9.27	0.11	M4
US-04705	16 13 38.40	-24 43 31.0	0.33	0.02	-10.56	0.07	M3
US-05320	16 16 59.84	-21 54 27.3	0.17	0.02	-4.22	0.05	M3
US-02674	15 58 18.85	-19 15 44.9	0.53	0.02	-3.81	0.04	M2
US-04524	16 12 33.53	-25 43 28.1	0.69	0.06	-8.52	0.22	M4
US-06729	16 22 08.94	-21 40 37.2	0.39	0.03	-4.48	0.06	M3
US-02774	15 59 08.65	-26 00 54.5	0.49	0.05	-7.27	0.35	M3
US-02878	16 00 07.05	-23 40 48.7	0.61	0.04	-20.54	0.16	M5
US-08727	16 27 09.51	-26 18 54.9	0.48	0.04	-8.58	0.10	M5
US-05144	16 16 09.47	-22 43 43.8	0.39	0.02	-4.15	0.04	M2
US-04604	16 13 06.28	-26 06 10.8	0.38	0.03	-6.11	0.07	M3
UCAC-426463797	15 55 29.81	-25 44 50.0	0.53	0.02	-1.79	0.04	M2
US-02757	15 58 58.21	-23 04 35.2	0.60	0.03	-7.71	0.19	M2
US-02957	16 00 49.89	-19 28 00.4	0.61	0.06	-5.38	0.18	M2
US-03362	16 04 18.93	-24 30 39.3	0.57	0.02	-24.08	0.37	M2
UCAC-415950434	16 10 05.02	-21 32 31.9	0.43	0.02	-54.01	1.71	M0
US-04024	16 09 20.63	-22 22 05.7	0.56	0.08	-16.49	0.39	M5
US-05179	16 16 18.94	-25 42 28.7	0.61	0.04	-7.34	0.14	M2
US-08419	16 26 19.64	-21 37 20.8	0.43	0.02	-1.07	0.03	M2
US-07232	16 23 24.54	-17 17 27.1	0.59	0.02	-5.29	0.09	M2
US-08986	16 27 57.94	-25 24 18.7	0.32	0.03	-6.06	0.13	M3
US-11299	16 35 06.26	-20 25 28.3	0.61	0.04	-11.45	0.14	M4
UCAC-496677275	16 30 02.76	-27 27 00.5	0.42	0.04	-3.65	0.19	M2

Continued on next page

UCAC-160980130	16 25 55.41	-27 21 24.3	0.73	0.04	-8.91	0.23	M5
US-08560	16 26 41.21	-22 00 09.5	0.35	0.02	-2.80	0.08	M2
US-10821	16 33 38.82	-21 50 26.3	0.73	0.02	-1.70	0.03	M2
UCAC-416396644	16 21 41.27	-22 12 05.6	0.54	0.04	-7.42	0.15	M5
US-04648	16 13 20.54	-22 29 15.9	0.38	0.02	-4.18	0.07	M2
US-06179	16 20 24.98	-21 50 24.1	0.47	0.02	-4.61	0.09	M2
US-02699	15 58 28.56	-23 34 19.1	0.42	0.02	-5.07	0.13	M3
US-02412	15 55 50.98	-25 19 39.4	0.60	0.03	-5.05	0.11	M3
US-10031	16 31 15.42	-26 57 15.1	0.45	0.02	-2.12	0.06	M2
US-03282	16 03 39.22	-18 51 29.4	0.59	0.03	-2.28	0.14	M3
US-03080	16 01 59.88	-18 43 45.7	0.36	0.02	-4.25	0.10	M3
US-02947	16 00 43.10	-24 30 50.3	0.38	0.06	-10.46	1.23	M4
US-04841	16 14 33.64	-20 04 29.9	0.55	0.02	-4.44	0.08	M3
US-03305	16 03 51.75	-21 40 15.5	0.55	0.04	-14.20	0.64	M6
US-11110	16 34 35.14	-26 58 03.0	0.54	0.05	-27.10	0.70	M5
US-06090	16 20 06.16	-22 12 38.5	0.60	0.03	-2.49	0.06	M3
US-05108	16 16 00.81	-22 14 19.3	0.51	0.04	-9.47	0.33	M5
US-02492	15 56 42.45	-20 39 34.0	0.54	0.02	-3.76	0.10	M3
US-05410	16 17 27.69	-24 21 02.6	0.55	0.04	-7.42	0.66	M4
US-06012	16 19 48.86	-21 40 36.0	0.57	0.04	-4.93	0.13	M3
US-08744	16 27 12.74	-25 04 01.8	0.53	0.02	-9.14	0.12	M2
US-05390	16 17 21.62	-23 25 00.4	0.64	0.03	-2.00	0.07	M3
US-07184	16 23 17.42	-21 59 06.8	0.61	0.03	-5.03	0.35	M3
US-05359	16 17 13.81	-22 51 58.4	0.58	0.04	-7.15	0.20	M4
US-03235	16 03 14.91	-22 34 45.5	0.48	0.05	-15.50	9.06	M5
US-02642	15 58 06.40	-23 40 41.8	0.44	0.03	-3.46	0.11	M4
US-03877	16 08 20.79	-21 31 23.5	0.70	0.04	-5.62	0.19	M4
US-02762	15 59 01.93	-26 16 33.0	0.57	0.08	-10.57	0.61	M5
US-02719	15 58 36.20	-19 46 13.6	0.70	0.04	-4.02	0.10	M4
US-02666	15 58 15.71	-20 21 36.9	0.35	0.07	-9.36	0.31	M5
US-02479	15 56 34.26	-20 03 33.3	0.63	0.06	-12.93	0.35	M5
US-03031	16 01 29.03	-25 09 06.9	0.34	0.03	-129.46	13.94	M4
US-03718	16 07 14.03	-17 02 42.5	0.71	0.04	-3.70	0.09	M4
US-03131	16 02 23.57	-22 59 33.3	0.49	0.09	-13.91	1.23	M6
US-04892	16 14 52.45	-25 13 52.3	0.16	0.03	-6.54	0.50	M3

Continued on next page

US-04326	16 11 16.87	-26 39 33.1	0.60	0.05	-5.85	0.20	M5
UCAC-27891415	16 10 03.12	-27 28 39.7	0.64	0.05	-7.64	0.19	M5
US-04109	16 09 52.88	-24 41 53.6	0.51	0.06	-15.07	0.44	M5
US-05135	16 16 08.56	-20 41 51.4	0.56	0.03	-3.81	0.10	M4
US-04491	16 12 17.24	-28 39 08.2	0.61	0.06	-7.14	0.58	M3
US-06094	16 20 06.86	-22 47 32.1	0.52	0.04	-8.63	0.21	M5
UCAC-450863417	16 26 19.98	-22 33 02.5	0.34	0.04	-4.53	0.09	M4
US-04317	16 11 13.95	-20 19 18.8	0.65	0.04	-12.08	0.36	M4
US-08100	16 25 32.74	-26 11 38.6	0.72	0.06	-8.74	0.34	M5
US-10489	16 32 35.87	-16 12 57.8	0.13	0.01	0.90	0.02	M2
US-08420	16 26 19.96	-22 58 09.8	0.60	0.03	-3.06	0.07	M3
US-04235	16 10 39.78	-20 37 09.4	0.63	0.02	-4.87	0.35	M3
US-05067	16 15 47.33	-19 11 18.5	0.57	0.02	-5.08	0.12	M2
US-04704	16 13 38.34	-21 58 51.9	0.43	0.04	-4.62	0.12	M4
US-04930	16 15 06.21	-25 00 46.0	0.56	0.05	-8.56	0.47	M5
US-07445	16 23 55.09	-23 30 39.7	0.53	0.02	-3.48	0.08	M3
US-09249	16 28 46.05	-27 11 57.5	0.33	0.02	-2.52	0.08	M2
US-05018	16 15 32.20	-20 10 23.7	0.60	0.02	-11.06	0.15	M2
US-10799	16 33 35.04	-27 15 44.8	0.35	0.03	-3.86	0.25	M3
US-05992	16 19 43.10	-22 16 17.6	0.69	0.05	-2.78	0.10	M4
US-05338	16 17 06.06	-22 25 41.5	0.31	0.04	-4.78	0.18	M5
US-06668	16 21 59.76	-27 06 36.6	0.51	0.06	-5.34	0.18	M5
US-08198	16 25 48.09	-21 54 19.5	0.42	0.06	-4.53	0.42	M3
US-03116	16 02 14.89	-24 38 32.6	0.66	0.09	-15.33	0.46	M5
US-03311	16 03 54.05	-25 09 39.4	0.59	0.06	-7.55	0.32	M5
US-03161	16 02 44.48	-25 43 32.3	0.45	0.04	-8.79	1.50	M3
US-06485	16 21 29.62	-21 29 03.8	0.93	0.09	-13.95	0.47	M5
US-04616	16 13 10.09	-24 35 24.8	0.65	0.06	-7.67	0.33	M4
US-03977	16 09 00.52	-27 45 19.4	0.80	0.18	-11.25	0.62	M5
US-11534	16 35 45.74	-27 11 16.6	0.26	0.02	-8.03	2.47	M2

Table 3.3 lists the measured equivalent widths and estimated spectral types for the young stars identified. Given the number of new members discovered, we estimate a conservative member identification rate of ~50%. Of the targets observed for which

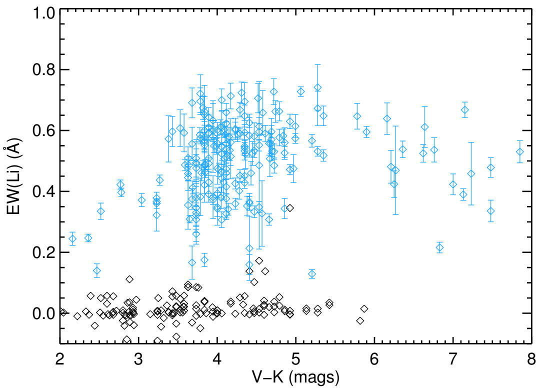

(a)

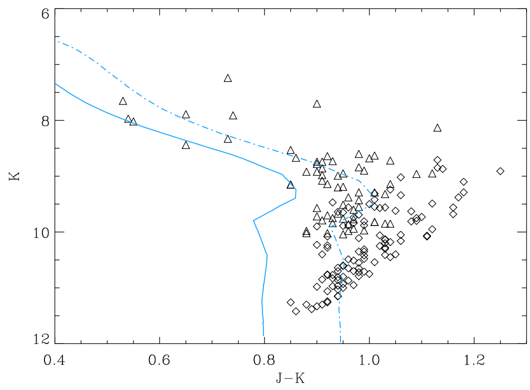

(b)

Figure 3.9: (a) This plot displays the equivalent width of the Li 6708 Å line against V-K colour for the stars observed in our survey. Those stars with measured Li 6708 Å equivalent widths more than 1-σ above a threshold value of 0.1 Å were deemed to be young association members, and are plotted in blue. (b) The (J-K,K) colour-magnitude diagram for the Upper Scorpius members identified among the potential members observed in our survey. The solid line represent a 6 Myr Padova isochrone (Girardi et al., 2002) at the mean distance of the Upper Scorpius subgroup (∼130 pc), the dashed blue line is the same isochrone reddened to $E(B-V) = 0.2$ using the Savage and Mathis (1979) extinction law.

we calculated Bayesian membership probabilities (103 in total), 68 were classified as members of Upper-Scorpius based on Lithium 6708 Å line strength. Based on the Bayesian probabilities, we expected 76 members among the 103 observed stars. These numbers do not completely agree and have a spread of ~ 1 times the Poisson counting error. This is likely due to an over-estimated prior. We explained above that the prior used was $0.015^{+0.004}_{-0.008}$; using an adjusted prior of 0.012, which is within the error on our prior estimation, produces complete agreement between the Bayesian selection and the observed number of members. The list of membership probabilities in Appendix B provides the corrected probabilities computed with the adjusted prior.

3.2.5 Spectro-astrometric Companion Detection

In addition to computing an integrated spectrum of each object observed with WiFeS, we also determine the spectro-astrometric centroid position of the image in each wavelength along the spectrum. Figure 3.10 displays an example centroid position shift as a function of wavelength for the region around the H-α line for the star UCAC4-404477376 (USco 48), a star without a detected companion. If a star hosts an accreting companion, including both stellar and planetary companions, we would expect the spatial image centroid position to shift in Hα when compared to the surrounding wavelengths. As mention above, based on contrast ratios of massive gas giant planets ($\sim$10 M_{Jup}) orbiting young stars at wide orbits (>100 AU), we expected to be able to detect, using spectro-astrometry, the companion of stars like GSC 6214-0210, the companion of which is a massive accreting gas giant with a H-α contrast of $\sim$5:1 and an orbital separation of > 2 arcseconds.

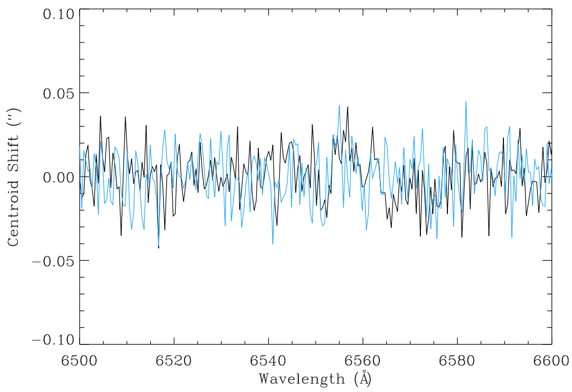

Figure 3.10: Centroid position shift in X and Y directions on the WiFeS detector at wavelengths surrounding the H-α line, for the star UCAC4-404477376. The black/blue lines are the X and Y positions respectively. Note that there is no significant centroid shift at any wavelength for this object.

Name	R.A. (J2000.0)	Decl. (J2000.0)	EW(H-α)	X (")	Y (")	P.A. (°)	ρ r	(")	
US-10798	16 33 34.97	-18 32 54.0	-8.47±0.21	-0.02±0.1	-0.14±0.05	180±5	0.18±0.10	3.0±0.5	PC
US-07477	16 23 59.02	-27 36 03.8	-6.44±0.04	-0.066±0.007	-0.03±0.1	30±15	...	...	PC
US-05179	16 16 18.94	-25 42 28.7	-7.34±0.14	0.08±0.01	-0.104±0.004	233±16	...	...	PC
US-02492	15 56 42.45	-20 39 34.0	-3.76 ±0.10	0.115±0.005	0.11±0.02	136±5	0.4±0.1	1.4±0.7	PC
US-03031	16 01 29.03	-25 09 06.9	-129.46±13.94	-0.20 ±0.01	0.004±0.005	1±5	...	1±0.5	S
US-03362	16 04 18.93	-24 30 39.3	-24.08±0.37	0.035±0.008	0.085±0.006	122±12	...	...	S
US-03187	16 02 58.45	-25 45 29.8	-5.48±0.05	0.07±0.01	-0.032±0.006	199±15	...	...	S
UCAC4-50927093	16 6 43.86	-19 8 5.55	-8.57±0.07	-0.108±0.012	-0.082 ±0.013	217.5±5.5	...	...	S

Table 3.4: Stars in our WiFeS membership survey sample for which a significant spectro-astrometric centroid shift was measured in the H-α line. We tabulate the centroid shifts in X and Y, as well as the resultant companion position angle. Where detection of the companion is possible in the H-α spatial image, we also fit separations (ρ) and contrast ratios (r). The final column indicates whether the companion is a planetary-mass candidate in need of follow-up confirmation (PC) or a stellar companion (S).

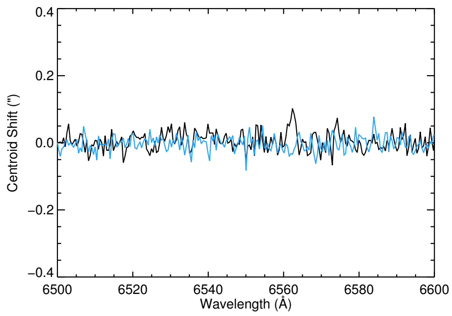

(a) US-03187

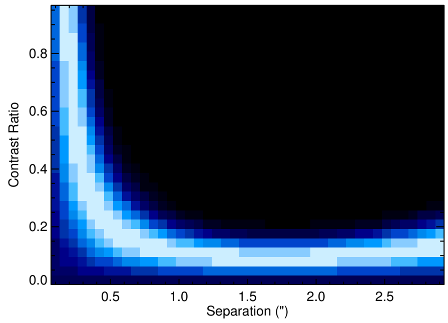

(b) US-03187

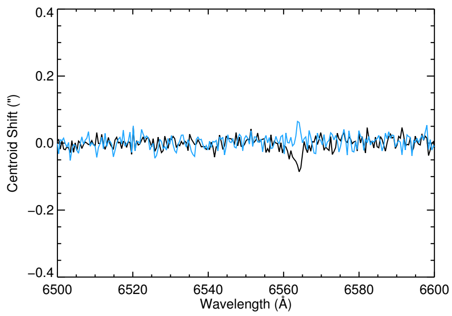

(c) US-07477

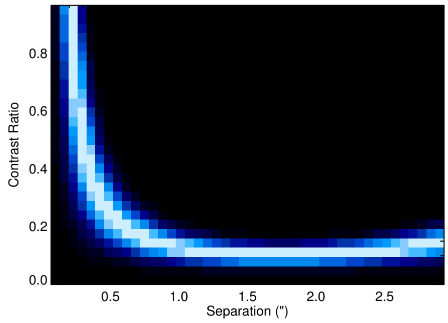

(d) US-07477

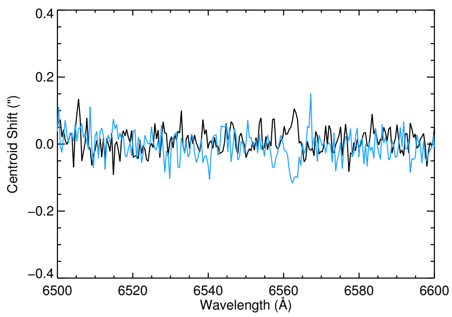

(e) US-05179

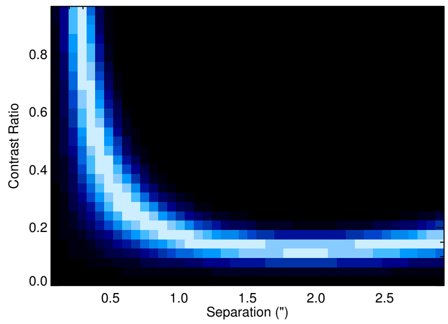

(f) US-05179

Figure 3.11: Centroid shifts and grids of possible contrast-separation values for three low-mass candidate companions to new Upper-Scorpius members US-03187, US-07477, and US-5179. Given the lack of any lithium absorption for US-03187, the companion is expected to be stellar.

When identifying a significant centroid shift, we first fit a linear function to the systematic centroid position as a function of wavelength, to remove any drift in the

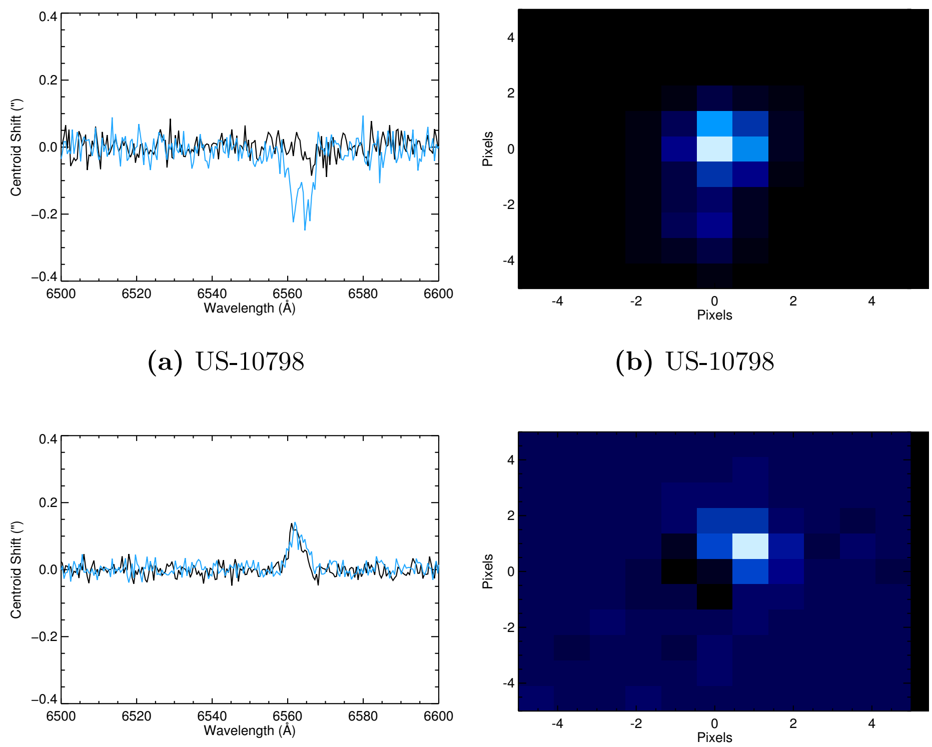

(a) US-10798 **(b)** US-10798

(c) US-02492 **(d)** US-02492

Figure 3.12: Centroid shifts and H-α images for two spatially resolvable planetary mass candidate companions to new Upper-Scorpius members US-10798 and US-02492. (a), (c): The centred position shifts for the two stars respectively. (b): The centroid shift, and the WiFeS spatial image for US-10798 in a 5 spectral element band centred on the H-α line. The companion is clearly seen 3" below the primary on the image. (d): The corresponding H-α image for US-02492 with the fitted PSF of the primary subtracted away to reveal the companion.

centroid position that may be caused by chromatic instrumental behaviour. We then calculate the RMS noise in the centroid position for both the X and Y directions. For the star given as an example in Figure 3.10, the RMS noise was 0.014 pixels and 0.017 pixels in the X and Y directions respectively. We then identify centroid shifts as a shift greater than twice the measured noise in a 10 Å bandpass around the H-α line. In our sample of stars, we detected companions associated with 8 of the targets in our sample on the basis of significant spectro-astrometric centroid shifts in the H-α line. These objects, the corresponding centroid shifts, and any estimated companion parameters are tabulated in Table 3.4.

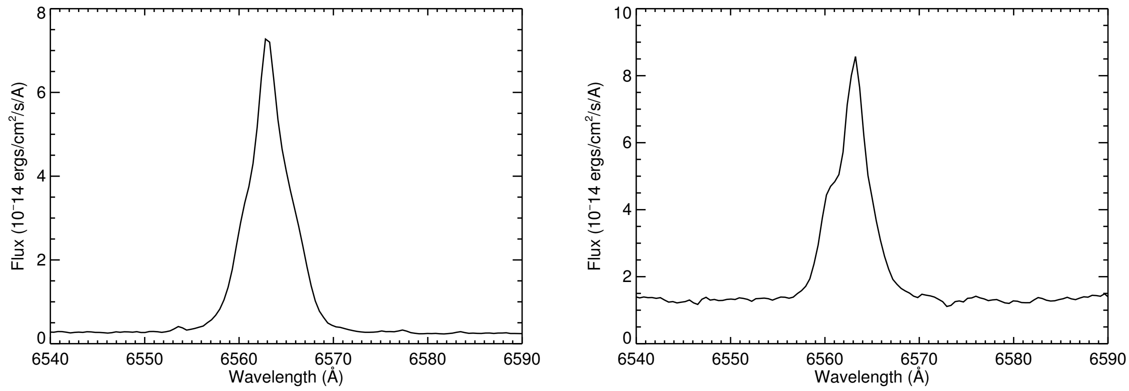

(a) US-03031 **(b)** US-03362

Figure 3.13: Spectro-astrometrically detected companions to US-03031 and US-03362 which were determined to be stellar companions due to their H-α line profiles, which show evidence of superposition of two similar brightness sources, or complexity due to winds and jets.

We further analyse the companion detections by applying the image PSF for each star, produced previously, during the spectro-astrometric analysis as a template star image. The general procedure involves creating a series of synthetic images at the calculated position angle, and at different separations and contrasts. We then apply the centroid fitting procedure detailed above and compare the centroid shifts of the synthetic images to the measured shifts from the data.

The first step is to determine a noise model for the spatial images, which can be used to construct the noise for the synthetic images. We do this by fitting a linear model to the noise array of the spatial image as a function of image pixel counts:

$$N = Sa + c, \tag{3.19}$$

where a and c are the fitted parameters, N is the noise array, and S is the image array. Typically, the noise model produces synthetic uncertainties within 5% of the expected values. Figure 3.16 displays the data and model noise spatial values for the star UCAC4-50927093.

With the noise model determined, we then build synthetic images by adding shifted and scaled Moffat PSF's at different separation and contrast. For each point on the contrast-separation grid, the primary PSF is first placed at the centre of the synthetic image, and then the secondary is scaled by the contrast ratio and shifted by the separation value in the direction of the position angle. Note that the background term in the fitted PSF is only added once. We use a separation grid of $0.2 - 3$" in steps of 0.066", and contrast ratios of $0 - 1$ in steps of 0.03. We display grids of the most likely values of contrast and separation computed as described above for our companion detections in Figure 3.11 for US-03187, US-07477 and US-05179. In addition to producing a measurable centroid shift, the companion to US-10798 was clearly resolvable in the spatial images. We coadded spatial images for a 5 spectral-element band centred on the H-α line, and then fitted separation and contrast ratio to the image. Figure 3.12b displays the H-α image. Similarly, for US-02492, we coadded spectral-elements and then subtracted the primary PSF determined in the original spectro-astrometric analysis to reveal the companion. The result of this can be seen in Figure 3.12d. The companions to US-03031 and US-03362 display clearly complex H-α lines, implying multiple stellar objects with significant accretion or complex winds and jets, and hence we designate them as stellar companions. Figure 3.13 displays the H-α region spectra for these object. Finally, we discuss UCAC-50927093 individually below, because the companion has been observed previously in the literature and hence it provides a useful test case for the analysis.

To definitively determine whether or not these companions are in the planetary-mass range, high-resolution follow-up observations with, for example, adaptive optics and aperture masking observations on 8 m class telescopes is required. This is because the centroid shift could also be produced by a close stellar companion, or a stellar companion orbiting an accreting primary. The star US-03187 did not display any measurable Li absorption, and so the centroid shift is expected to be caused by the latter scenario.

UCAC4-50927093

UCAC4-50927093 (USco J160643.8-190805) is a known late-type member of Upper-Scorpius, with a Li 6708 equivalent width of 0.59±0.01Å and a Hα equivalent width of ∼8.6 Å. Figure 3.14 displays the centroid position shift for this Sco-Cen member and the spectrum. We measured centroid shifts in (X,Y) to be (-0.108,-0.082) pixels, with RMS noise of (0.012 and 0.013).

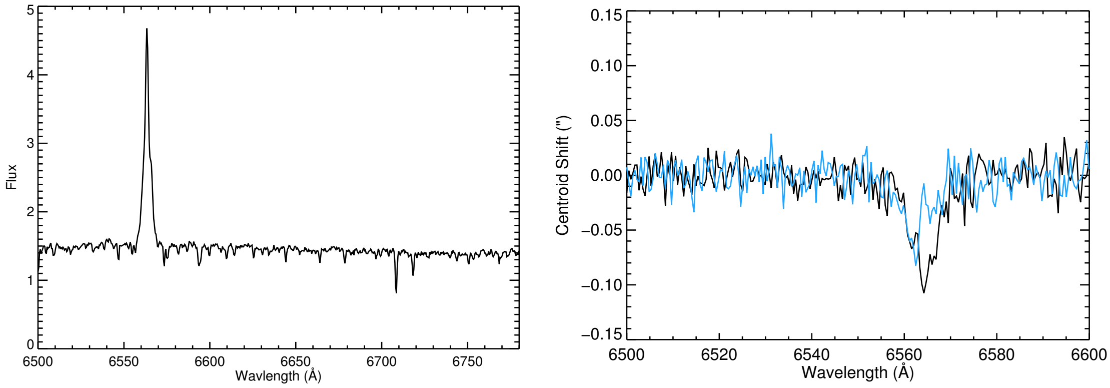

(a) **(b)**

Figure 3.14: (a) Spectrum of UCAC4-50927093 in the H-α and Li 6708 Å region. (b) Centroid position shift in X and Y directions on the WiFeS detector at wavelengths surrounding the H-α line, for the star UCAC4-50927093. The black/blue lines are the X and Y positions respectively. The estimated noise in the X and Y directions is 0.012 pixels and 0.013 pixels respectively, and the centroid shift at the H-α line is -0.108 and -0.082 pixels in X and Y.

The star has previously been observed with adaptive optics and aperture masking, with no companion detections between 0.3-1.0 arcseconds (Kraus et al., 2008, Ireland et al., 2011b). This indicates that the companion detected here is most likely a very close stellar companion closer than ∼500 mas. Furthermore, we searched the Gemini archives and discovered observations of this source with the Gemini Near-IR Imager (NIRI); the image is shown in Figure 3.15. While this thesis was in preparation, a publication presenting this companion, and others was released which quoted a separation of 247±1 mas and position angle of 222.68±0.12 degrees for this system (Lafrenière et al., 2014).

The position angle of the companion can be directly calculated from the H-α centroid shift in X and Y, and is found to be 217.5±5.5 degrees, which agrees with the NIRI imaging value from mid-2008 within $1-\sigma$. While the position angle of the binary

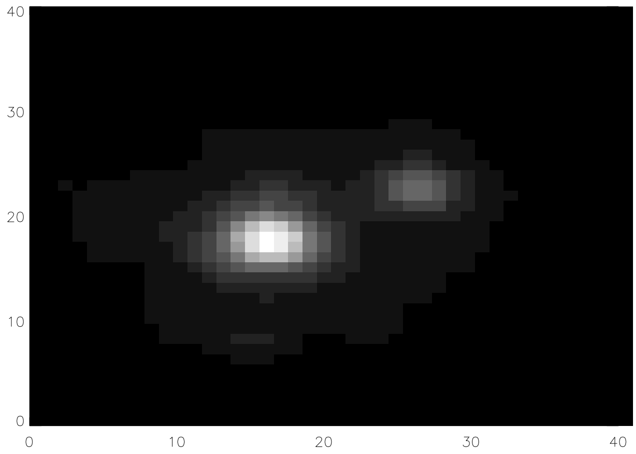

Figure 3.15: NIRI@Gemini image of UCAC4-50927093 taken in July 2008. The measured separation and position angle are 247±1 mas and 222.67±0.12 degrees respectively. The system had a K-band contrast of 0.22 or K magnitude difference of ∼1.7 (Lafrenière et al., 2014).

system can be directly calculated from the centroid shift, the separation and contrast ratio are highly degenerate. This is because multiple combinations of contrast r, and angular separation ρ, can produce the observed X and Y pixel centroid shifts. This degeneracy precludes definitive estimation of these parameters; however we can produce a set of possible values of contrast and angular separation by modelling the centroid shift behaviour of the data as a function of these parameters.

Figure 3.16c presents the most likely values of contrast and separation calculated from the synthetic images. We find a large span of possible contrast and separation values. Separations consistent with the previously measured values of 247±1 mas are possible, and exhibit large H$-\alpha$ contrast ratios greater than 0.6 (secondary to primary).

The Planetary Companion to GSC-6214-0210

GSC-6214-00210 (GSC-6214), as explained above, is the prototype host for the wide, massive gas-giant planets that we intend to study with WiFeS. We observed GSC-6214-0210 with the WiFeS IFU on four dates, 19/06/2013, 09/04/2014, 16/06/2014 and 17/06/2014, during our observing campaign to identify new Upper Scorpius members. The companion, GSC-6214-0210b, is expected to be detected in H-alpha due to its wide

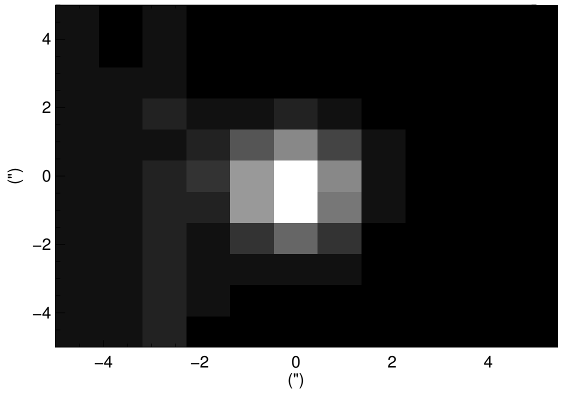

(a) Real Noise

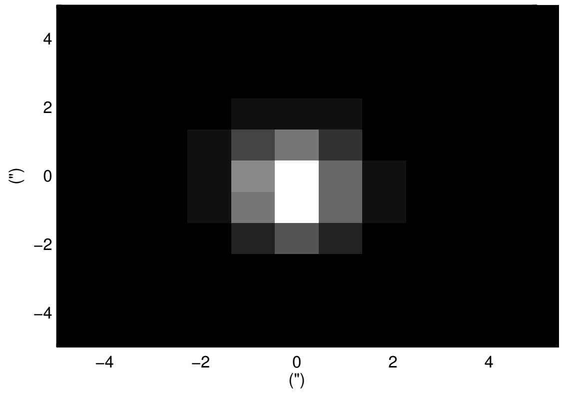

(b) Synthetic Noise

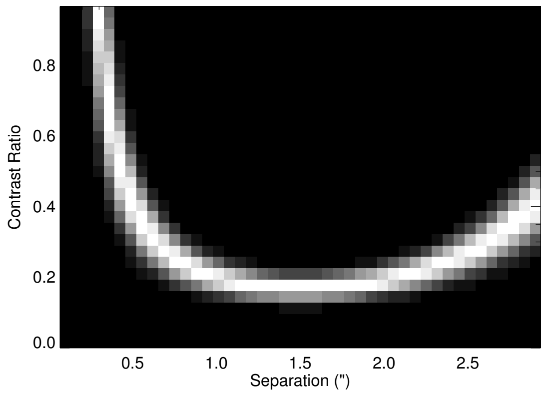

(c) Grid Value Results

Figure 3.16: (a,b) The uncertainty in the spatial image array taken from the data (a) and the generated uncertainty built from the fitted noise model (b). Both images are unscaled. Grid of contrast and separation for the UCAC4-50927093 primary and secondary. (c) Grid of contrast and separation for the UCAC4-50927093 primary and secondary. Brighter colour indicates that the synthetic centroid shifts at a given contrast-separation point more closely match the measured centroid shifts. The contrast ratios here are listed as secondary to primary.

orbit of $\sim$ 2". Interestingly, we do not detect GSC-6214-0210b in the H-α spectro-astrometry at any level, and we measure a significantly lower than expected, and variable, equivalent width of H-α for the system. The single previous H-α equivalent width was -1.51 Å (Preibisch et al., 1998). Table 3.5 lists the Li 6708 Å and H-α equivalent widths for our four observations. Over the four observations, the measured Li 6708 Å equivalent width was measured to be 0.37±0.01 Å , and showed a very small scatter of less than one sigma. These measurements agree with the discovery measurement of ∼0.38 Å (Preibisch et al., 1998).

Date	EW(Li)	EW(H-α)
19/06/2013	0.38±0.01	-0.64±0.02
09/04/2014	0.36±0.02	-0.43±0.02
16/06/2014	0.32±0.05	-0.67±0.10
17/06/2014	0.38±0.01	-0.63±0.02

Table 3.5: Equivalent width measurements for the four observations of GSC-6214. The Li 6708 Å equivalent widths are all consistent and agree with the discovery values of 0.38 Å of Preibisch et al. (1998); however the H-α equivalent widths vary significantly over the four nights. Note that the observations on the night of 16/06/2014 was taken in poor weather conditions, which is reflected in the uncertainty.

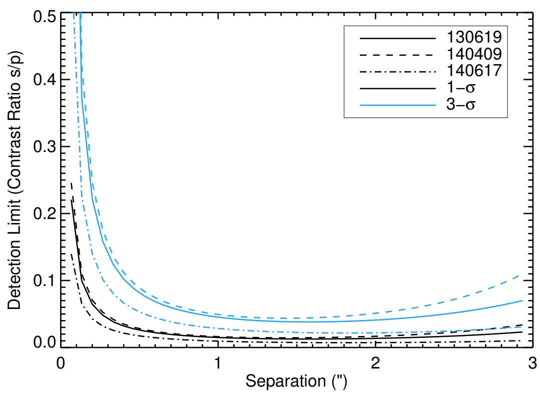

Figure 3.17: Spectro-astrometric companion detection limits (1 and 3-σ) for the three observations of GSC-6214 which were not in poor weather conditions, determined using synthetic PSFs and noise models to compute model centroid shifts. The detection limits in this figure are computed for the expected position angle of the companion of $\sim 176°$ (Ireland et al., 2011b).

We also compute companion detection limits based on the spatial image centroid position and using the PSF and noise model described above. These are presented in Figure 3.17. We find that at the expected $\sim$ 2" separation and position angle of 176° (Ireland et al., 2011b), the $3-\sigma$ detection contrast limits are all better than 10:1, and typically better than 20:1, which is significantly lower than the expected contrast of

5-10:1 observed in previous studies.

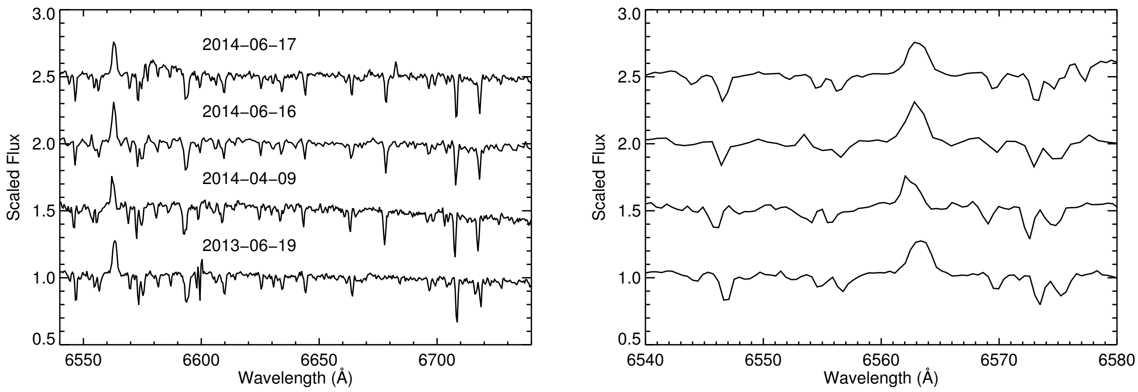

(a) **(b)**

Figure 3.18: The four spectra of GSC-6214 that we have taken in 2013-2014 focussing on the H-α and Li 6708 Å region in (a) and more closely focussed on H-α in (b). Note that the region between 6675-6680 Å has been masked out in the 2013-06-19 spectrum to remove a data reduction artefact resulting from non-ideal atmospheric conditions during observation.

As seen in Table 3.5, there is significant variation in the H-α line equivalent widths, which is accompanied by a slight change in the H-α line profile. This can be seen in the stacked spectra in Figure 3.18. The original and last observations show a distinct difference to the second observation in H-α.

Near-IR adaptive optics observations of GSC-6214b in 2011 have revealed multiple signs of youth and strong Paschen-β emission (1282 nm), indicating the presence of, and accretion from, a circumplanetary disk surrounding the companion planet with a luminosity of $\log L_{Pa_\beta}/L_\odot = -6.14 \pm 0.08$ (Bowler et al., 2011). More recently Zhou et al. (2014) used HST photometry and PSF subtraction to measure a H-α luminosity of $\log L_{H_\alpha}/L_\odot = -5.03$ for the companion GSC 6214-0210b. Applying the relations between accretion and line luminosity of Rigliaco et al. (2012), these measurements produce an accretion luminosity of $\log L_{acc}/L_\odot = -4.56 \pm 0.31$ and 4.6 ± 0.5 respectively.

The lack of a significant centroid shift in the spectro-astrometry we present, combined with the decrease in measured H-α equivalent width from -1.51 Å to < 0.65 Å , suggests the possibility that the rate of accretion of material from the circumplanetary disk onto the companion GSC-6214b has significantly slowed since the previous observations. To produce similar H-α and accretion luminosities as the above studies, we would require a change in H-α equivalent width of at least 0.4 Å. When compared to the original H-α measurement by Preibisch et al. (1998), we see that from July 1997 to June 2014, there has been a decline in H-α equivalent width of 0.9 ± 0.1 Å. This also indicates that during the period of 2011-2012, accretion onto GSC 6214-0210b was most likely declining. Table 3.6 provides an overview of the accretion measurements over time.

GSC 6214-0210b Accretion Timescale		
Date	Observation	Accretion?
July 1997	Preibisch et al. (1998)	Y
July 2010	Bowler et al. (2011)	Y
Feb 2012	Zhou et al. (2014)	Y
June 2013	This Thesis	N
June 2014	This Thesis	N

Table 3.6: Accretion measurements over time for GSC 6214-0210b.

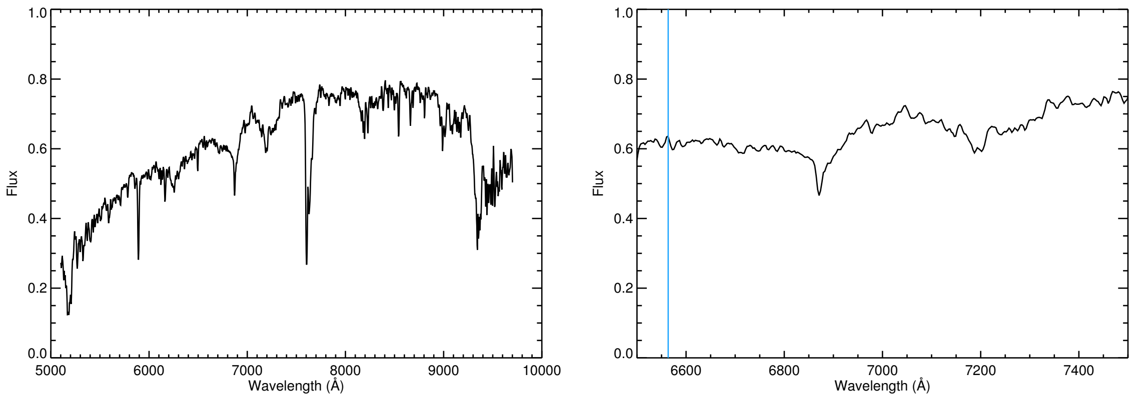

(a) **(b)**

Figure 3.19: SNIFS spectrum of the primary GSC 6214-0210a. Panel (a) shows the full wavelength range, while (b) shows the Hα line for GSC 6214-0210. Despite the low spectral resolution (2.93 Å), an H-α equivalent width of the primary can be calculated (0.6 ± 0.2), which agrees with our measurement for the system, and is consistent with termination of accretion onto the companion GSC 6214-0210b.

We have also obtained the SNIFS spectrum of the primary GCS 6214-0210a from Bowler et al. (2011), which can be seen in Figure 3.19. From this low resolution spectrum, we find that the H-α equivalent width of the primary is 0.6 ± 0.2 Å. This is consistent with our WiFeS measurements, and provides further evidence that the secondary GSC 6214-0210b has stopped accreting.

4

Long-Baseline Interferometric Multiplicity Survey of Sco-Cen

In this chapter, we present the first multiplicity-dedicated long baseline optical interferometric survey of the Sco-Cen association, using the Sydney University Stellar Interferometer (SUSI). This work was published in MNRAS as Rizzuto et al. (2013b), the electronic version of which can be found online. Since the publication of this paper, the analysis has been updated, additional SUSI, and PIONIER data from VLTI have been taken on many of the targets, and the data have been re-calibrated. One of the closest, high contrast detections (τ-Sco) was subsequently determined to be an artefact of calibration, and follow-up observations are described as part of a following chapter (Chapter 5) to be submitted as a refereed paper. We have also removed the detection limits for additional companions for those systems with detected companions from Table 4.1, as the methodology for this was not described in the original paper and was over-optimistic.

4.1 Introduction

Multiplicity properties of recently formed stars can provide valuable insight into the understanding of star formation mechanisms (Blaauw, 1991). For more than a decade it has been widely accepted that at least half of all solar-type stars form in pairs (Mathieu, 1994, Raghavan et al., 2010), though multiple systems are still a relatively poorly understood part of star formation. One particular unknown aspect is the role of multiplicity in the redistribution of angular momentum during star formation (Larson, 2010). Observations have also revealed that $70-90\%$ of stars form in clusters (Lada and Lada, 2003).

Detailed knowledge of the multiplicity of a primordial stellar population would be the ideal. This would be a population of stars whose formation precesses have finished and which have stopped accreting gas from their surroundings, but before dynamical interactions and stellar evolution have altered the multiplicity distribution. Stellar OB associations are the closest match to these conditions, by virtue of their low density and youth, and provide a large sample of young, newly formed stars for multiplicity study.

We discussed in Chapter 1 that there has been significant progress in characterising the Sco-Cen binary population in both the visual binary range (28-1500 AU) (Shatsky and Tokovinin, 2002, Kouwenhoven et al., 2005) and in the spectroscopic regime (Levato et al., 1987, Brown and Verschueren, 1997, Jilinski et al., 2006). Between these two separation ranges, there is the understudied 1-10 AU separation range, spanning a regime where radial velocity measurements are not possible with current instrumentation. Binary systems with these separations include rapidly rotating and possibly pulsating B-type stars, and cover a regime in which radial velocity measurements are not possible with current instrumentation. The purpose of this Chapter is to present a survey of the Sco-Cen association for binary separations within this niche using the

Sydney University Stellar Interferometer, and to use our new observations, in conjunction with the knowledge in the literature, to determine the multiplicity properties of the young B-type stars in Sco-Cen. This will address the question of whether B-type stars form alone or as part of a double or multiple system.

4.2 Observations and Data Reduction

4.2.1 Target Sample

Our aim was to observe all stars within the area of sky occupied by Sco-Cen which were brighter than 5^{th} apparent visual magnitude and bluer than $B - V = -0.1$ magnitudes. There are 75 stars which fit these criteria, and of these we observed 58. The spatial distribution and proper motion of our observed targets, in relation to the Rizzuto et al. (2011) membership, is shown in Figure 4.1. The decision to observe all stars within the given colour and magnitude range, rather than just the 52 members in the Rizzuto et al. (2011) selection, was motivated in two ways. Firstly, the presence of undetected binarity can affect the *Hipparcos* proper motions upon which the membership determination was based (de Zeeuw et al., 1999). *Hipparcos* measurements were carried out over a period of 3.3 years. Hence, unresolved binary systems, especially those with periods greater than 3.3 years, can affect the observed centre of motion. The typical magnitude of this error has been shown to be $\sim 2\,\mathrm{mas\,yr}^{-1}$ (Wielen et al., 1997), which is larger than the average *Hipparcos* proper motion uncertainty. Secondly, bright, blue high-mass stars in the region of space which is considered to be Sco-Cen are young and almost certainly formed as part of the association and have since undergone dynamical changes which affect a kinematic based membership. Indeed, applying our above magnitude and colour filter to the *Hipparcos* catalog bounded by $(285^\circ < l < 360^\circ)$ and $(-10^\circ < b < 40^\circ)$ clearly depicts a concentration of the bluest stars in the Sco-Cen subgroups and a paucity outside of these regions (Fig 4.1a). Similarly, Figure 4.1b demonstrates that none of the high-mass stars in the Sco-Cen region of the sky have large offsets from the expected member proper motions. Table

4.1 lists all stars observed with SUSI and the corresponding detection limits.

Table 4.1: List of observed stars and detection limits (Δm) in different angular separation ranges. The spectral types are taken from the Henry Draper catalogue. We have omitted detection limits for those objects with a detected companion.

Star	HIP	HR	SpT	7-10 (mags)	10-13 (mags)	13-17 (mags)	17-20 (mags)	20-80 (mags)	80-100 (mags)	100-150 (mags)	150-200 (mags)
13-Sco	79404	6028	B3	1.53	2.92	2.98	2.96	2.73	2.21	1.62	0.84
3-Cen	67669	5210	B5	2.54	3.67	3.71	3.69	3.45	2.97	2.29	1.70
4-Cen	67786	5221	B5	1.98	3.19	3.21	3.13	2.95	2.44	1.86	1.18
4-Lup	76945	5839	B5								
δ-Sco	78401	5953	B0								
G-Cen	60710	4732	B3	2.68	3.22	2.90	3.29	3.06	2.66	2.17	1.45
a-Cen	70300	5378	B5	2.20	3.14	3.11	3.11	2.91	2.48	1.86	1.30
α-Lup	71860	5469	B2	2.86	2.42	2.94	3.19	3.01	2.68	2.24	1.45
α-Mus	61585	4798	B3								
b-Cen	71865	5471	B3								
β-Cru	62434	4853	B1	2.29	1.97	2.33	2.61	2.47	2.12	1.60	0.85
β-Lup	73273	5571	B2p	3.08	4.05	4.04	4.09	3.79	3.24	2.65	2.11
β-Mus	62322	4844	B3								
χ-Cen	68862	5285	B3	2.11	3.10	3.20	3.08	2.91	2.41	1.79	1.21
δ-Cen	59196	4618	B5								
δ-Cru	59747	4656	B3	3.38	3.03	3.44	3.68	3.52	3.12	2.69	1.90
δ-Lup	75141	5695	B2	2.44	3.37	3.35	3.27	3.15	2.70	2.01	1.53
d-Lup	76371	5781	B3	2.19	3.15	3.12	2.99	2.93	2.47	1.82	1.31
e-Lup	74449	5651	B3	1.96	3.04	3.01	2.94	2.83	2.30	1.73	1.12
ϵ-Cen	66657	5132	B1								
ϵ-Lup	75264	5708	B3								
η-Cen	71352	5440	B3p	3.12	4.14	4.22	4.28	3.86	3.35	2.76	2.10
η-Lup	78384	5948	B3	3.24	3.96	4.01	4.04	3.76	3.20	2.64	1.98
f-Cen	63945	4940	B3								
γ-Lup	76297	5776	B3								
γ-Mus	61199	4773	B5	2.48	1.81	2.98	2.18	2.92	2.61	2.29	1.66
...	57851	4549	B5	2.67	1.54	3.29	2.90	3.34	2.98	2.53	1.88
...	59173	4618	B5	3.22	3.41	3.11	3.65	3.46	3.02	2.56	1.90
...	62327	4848	B3	2.92	2.59	2.98	3.23	3.09	2.70	2.28	1.56
...	72800	5543	B8	1.47	2.77	2.77	2.77	2.53	2.03	1.42	0.65
...	78655	5967	B5	1.71	2.98	3.01	3.00	2.78	2.25	1.65	0.88
ι-Lup	69996	5354	B3	3.13	4.06	4.04	3.98	3.88	3.29	2.68	2.06
j-Cen	57669	4537	B5								
κ-Cen	73334	5576	B3								
κ-Sco	86670	6580	B2								
ξ^2-Cen	64004	4942	B3	3.04	3.50	3.27	3.58	3.36	2.99	2.43	1.77
λ-Cru	63007	4897	B3	2.99	2.55	3.08	3.33	3.18	2.85	2.32	1.55

λ-Lup	74117	5626	B3								
μ01-Cru	63003	4898	B3	2.46	1.32	2.70	2.75	2.65	2.29	1.84	1.19
μ02-Sco	82545	6252	B2	2.53	3.53	3.60	3.59	3.49	3.13	2.81	2.32
μ-Cen	67472	5193	B2p								
ν-Cen	67464	5190	B2	1.37	2.85	2.91	2.85	2.65	2.14	1.54	0.00
o-Lup	72683	5528	B5								
ϕ^2-Lup	75304	5712	B3								
ϕ-Cen	68245	5248	B3	2.12	3.04	2.90	2.79	2.90	2.34	1.82	1.15
π-Cen	55425	4390	B5								
π-Sco	78265	5944	B2	2.93	3.35	3.41	3.58	3.62	3.39	3.09	2.52
ρ-Cen	59449	4638	B3								
ρ-Lup	71536	5453	B5								
ρ-Sco	78104	5928	B3	1.95	3.24	3.31	3.35	3.08	2.59	1.93	1.33
σ-Cen	60823	4743	B3								
σ-Lup	71121	5425	B2	3.04	3.76	3.68	3.60	3.58	3.11	2.54	1.74
τ^1-Lup	70574	5395	B3								
τ-Lib	76600	5812	B3								
τ-Sco	81266	6165	B0	2.26	2.67	3.31	3.09	3.63	3.65	3.62	3.63
θ-Lup	78918	5987	B3	1.04	2.57	2.62	2.60	2.38	1.88	1.24	0.00
υ^1-Cen	68282	5249	B3	2.13	3.11	3.00	2.83	2.88	2.42	1.75	1.17
ζ-Cru	60009	4679	B3	2.64	2.96	2.97	3.08	2.88	2.50	1.97	1.19

4.2.2 Observations

The observations were performed with the Sydney University Stellar Interferometer (SUSI) on a 15 m baseline, using the PAVO beam combiner (Ireland et al., 2008). SUSI operates in 25 optical wavelength channels between 550 and 800 nm, and on the 15 m baseline has an angular resolution of 7 mas. The coherence length of each spectral channel of the PAVO beam combiner is 30 μm, which gives a detectable separation range of ∼7-200 mas.

The observations were carried out over six half-nights between July 14^{th} and August 6^{th} 2010. Target stars which were in close proximity to each other on the sky were sectioned into groups of four or five stars. This was done in order to keep constant air mass and seeing conditions between the targets so that later calibration would be made more accurate. This also reduced the time taken to slew between stars during the observation nights. Furthermore, each group of stars was observed twice, with

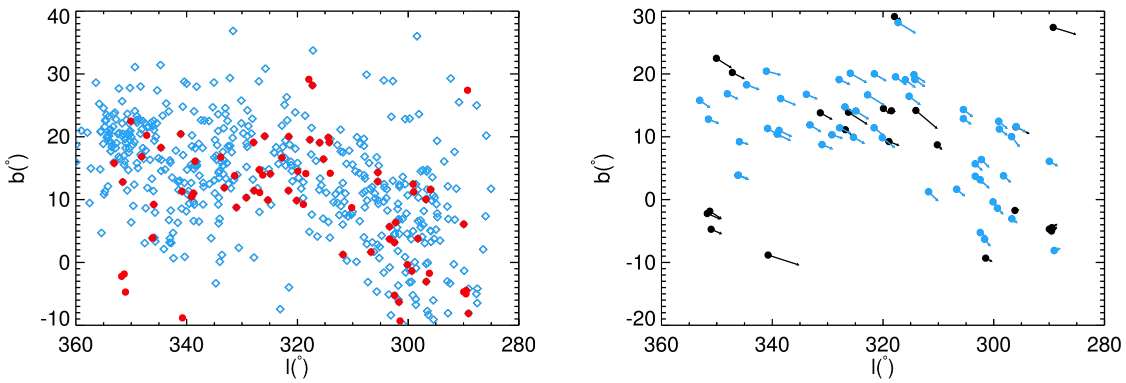

(a) Sample Sky Positions

(b) Sample Proper Motions

Figure 4.1: The on-sky locations of the Sco-Cen region high-mass stars observed in our survey. Blue squares indicate the Rizzuto et al. (2011) members and red circles indicate the stars in our sample. Note the lack of high-mass stars (blue circles) outside of the Sco-Cen regions. The second figure illustrates the proper motion vectors of the stars in our sample. Blue objects once again represent members in the Rizzuto et al. (2011) selection with greater than 50% membership probability. The lack of highly deviant proper motions highlights the possibility that multiplicity induced proper motion offsets might explain the exclusions.

sufficient time between them to allow the Earth's spin to rotate the baseline with respect to the targets and provide a new position angle for the second observation. This allowed a separation on the sky to be found rather than a projection along an individual baseline position angle. Given that we expect to observe new companions with periods of ∼1 year and with orbital motions on the order of ∼1° of position angle per day, we have ensured observations are either on the same night or neighbouring nights where orbital motion is insignificant compared to position angle uncertainties. Each observation consisted of recording 100 seconds worth of 3.5 ms exposures while an interference fringe pattern was locked on the camera.

4.2.3 Data Reduction and Calibration

Data Reduction

The raw image frames recorded by the PAVO camera were reduced into squared visibility values for each of the 25 wavelength channels using a number of IDL programs written by the SUSI group. The pupil image frame was sectioned into an image for each wavelength channel, and these were used to calculate the squared visibility V^2. Without going into the fine detail or complexities of SUSI data reduction, the method of calculation is given by Equation (4.1). The pupil is Fourier transformed to yield the power spectrum, and the power of the fringe is totalled and divided by the total flux squared.

$$V^2 = \frac{\text{Fringe Power}}{(\text{Flux})^2} \tag{4.1}$$

Individual frames taken during observations of single targets which showed anomalously low visibilities were rejected based on manual inspection. This is most important for nights where seeing was particularly bad (greater than ∼2.5"; ten Brummelaar et al. (1994)), intermittent clouds were present, or technical problems were encountered. The result of the data reduction is a squared visibility in 49 wavelength bands which are interpolated from the 25 wavelength channels observed by the PAVO beam combiner.

Calibration

The visibility profiles provided by SUSI include the influence of various systematics, such as seeing effects, air turbulence in the beam combination enclosure, dust on optical surfaces and the response of detectors. These can be removed through calibration against another star which is assumed to have a well-characterised point-source-like visibility profile. This is often a star of small angular diameter. The basic assumption is the following:

$$V^2_{\text{measured}} = V^2_{\text{true}} V^2_{\text{system}}, \tag{4.2}$$

where V^2_{true} is the true squared visibility of the target star, V^2_{measured} is the measured squared visibility obtained from SUSI observations and V^2_{system} is the system response factor (different for each wavelength channel) which must be removed from the data. The calibration is done by taking a star which is assumed to be described by a uniformly bright disk with a diameter that can be predicted by $B-V$ colour and V magnitude. This calibrator star must also be within a few degrees of the target it will calibrate, in order to calibrate for seeing effects. The error in this prediction due to the B-V uncertainty is inherently small because the calibrator diameters are very small (below the resolution limit of the instrument). A uniform disk model is then fitted to the predicted diameter, producing squared visibilities for each wavelength channel. This predicted visibility profile is taken to be the V^2_{true} for the calibrator star, and using Equation (4.2) the system response V^2_{system} is found. Hence, to calibrate a target, the measured visibility profile is divided by the system response found using the calibrator.

In usual SUSI observing, one or preferably more than one specific calibrator would usually be chosen prior to observation for each science target. However, for the purpose of detecting Sco-Cen binary companions, we have simply used those stars which did not display the characteristic signal of a binary star as calibrators for those that did. This worked well as the observations were done in groups of stars nearby in the sky, and calibrators were hence available nearby on the sky and at a very small time difference (often less than ten minutes). Observed targets with a clear oscillatory squared-visibility profile in the uncalibrated data were set aside and labelled as companion detections. For the remaining observations, many cross-calibrations were manually performed and inspected, allowing subtle detections, good calibrator observations, and suspect data to be identified among the observations.

Once good calibrators were identified, they were cross-checked with the available literature as a final precaution to ensure that they were not binary or multiple systems, or that they were multiple systems with companions well outside the SUSI coherence length limit or much fainter than the SUSI detection limits. In general, if a star has a companion with an angular separation greater than $1-2$ arcseconds, it can still be a valid calibrator. A binary system with the secondary at an angular separation of ∼200 mas has an optical path difference between central fringes which is just beyond the 30 μm coherence length of the SUSI/PAVO beam combiner and thus is not a suitable calibrator. Such a binary system will produce a systematically lower visibility than a corresponding single star. A uniform decrease in visibility across all wavelength channels in the calibrator can be problematic depending on what it is used to calibrate. There is no issue when calibrating an obvious binary which displays more than one visibility oscillation with wavelength, as the astrometry is not affected by a slight mis-calibration, however, in the case of a very-narrow binary (<20 mas separation) a slight shift in V^2 up or down can affect the determination of the brightness-ratio of the system. In both cases, the measured separation is not affected. On average, each star with an identified companion had two calibrators with similar airmass, with some having more than two. In a small number of cases only one calibrator was available, though a reliable determination of the system parameters can still be obtained.

4.3 Companion Detections

Fitting to the Data

Once the data have been calibrated a model binary system visibility is fitted to the data. In the fitting, each component in the binary system is treated as a point source. This approach is justified given the colour and magnitude constraints on our sample: we have only selected stars bluer than $B - V = -0.1$ and brighter than 5^{th} magnitude in V, placing all our objects firmly in the B-type range. This means that the bluest object β-Crucis, which has an angular diameter of ~ 0.7 mas (Hanbury Brown et al., 1974), is representative of the largest objects observed. This is well below the resolution limit of 7 mas of the 15 metre baseline at SUSI and hence the binary systems will be observed as two point sources. The equation that was fitted to the visibility profiles was the following;

$$V^2 = \frac{V_p^2 + r^2 V_s^2 + 2rV_pV_s\cos\left(\frac{2\pi\vec{B}\cdot\vec{s_b}}{\lambda}\right)}{(1+r)^2}, \tag{4.3}$$

where r is the secondary to primary brightness flux ratio, $\vec{B}$ is the baseline vector projected onto the sky, $\vec{s_b}$ is the separation of the binary system on the sky and λ is the wavelength of observation (Lawson, 2000). V_p and V_s are the primary and secondary star visibility profiles respectively. In the case of perfect system alignment and focus, these would both be equal to unity at all wavelengths (as is the case with point-sources). In order to remove the effects of any de-focus in the beam combination system, we modelled the primary and secondary visibility profiles as Gaussians;

$$V_{p,s} = \exp\left(-a\left(\frac{\vec{B}\cdot s_{p,s}}{\lambda}\right)^2\right) \tag{4.4}$$

where $s_{p,s}$ is the separation on the sky of the primary or secondary from the stellar photo-centre, and a is a coefficient to be determined. This adequately models coherence length degradation due to de-focus in the system, leaving close companion observations relatively unaffected and wide separation companions more difficult to detect. To determine the value of a for our system we calibrated against the well characterised κ-Cen system, which has a $\Delta m = 1.4$ magnitude companion at $\sim$100 milliarcseconds separation. We find a value of $a = 9.5 \times 10^{-3}$.

The fitting process yields both the brightness ratio and the baseline-separation product ($\vec{B}\cdot\vec{s_b}$), which is the true separation of the binary system projected onto the direction of the SUSI baseline. Figure 4.2 presents some typical binary visibility profiles and corresponding fits, and all the fitted visibility profiles can be found in Appendix D.

With two observations separated by sufficient time, the sky rotates with respect to the baseline and so it is possible to find the true separation of the binary system on the sky at the epoch of observation. The observed separations fitted as described above are in fact the true separations in the north and east directions on the sky under a

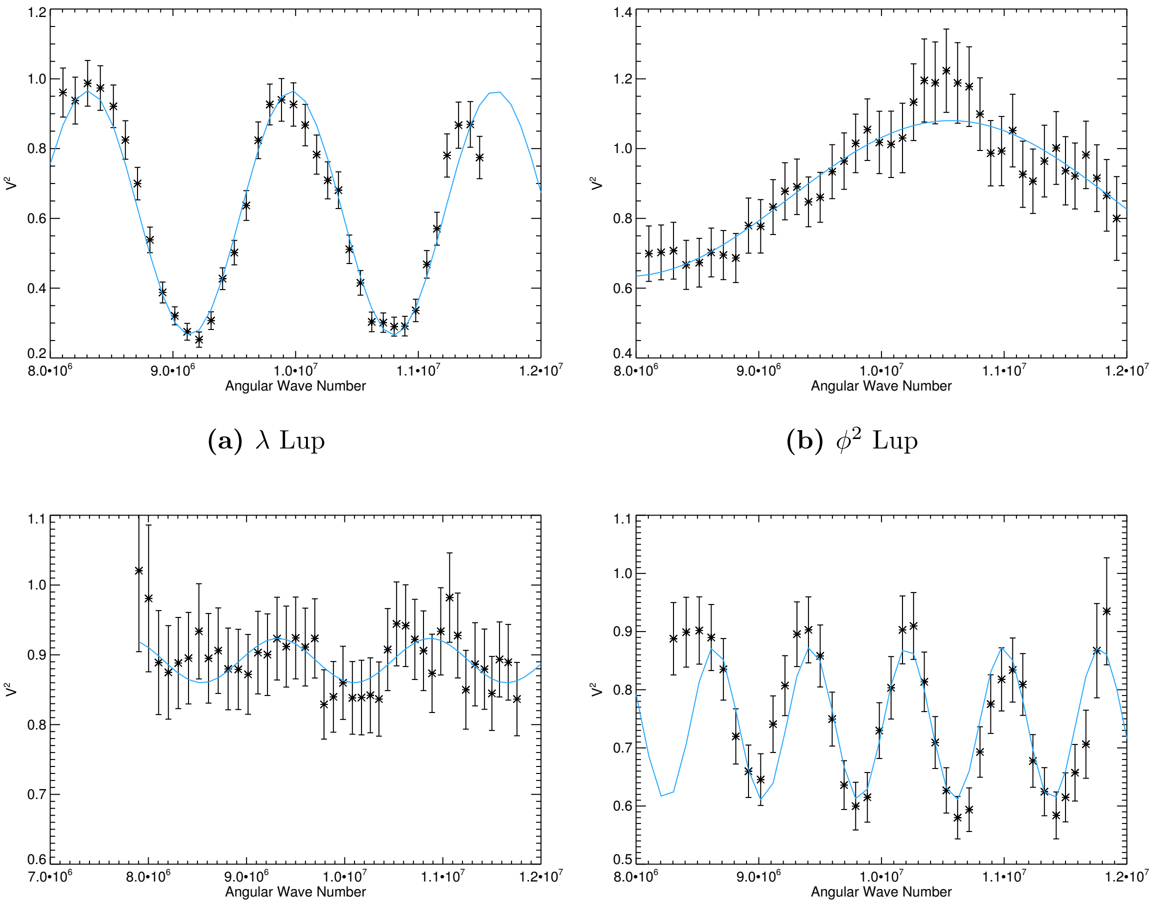

(a) λ Lup **(b)** ϕ^2 Lup

(c) τ Sco **(d)** κ Cen

Figure 4.2: Examples illustrating the typical characteristics of the survey data and the closeness of the binary fits. Figure 4.2d displays the wide companion against which we calibrated for de-focus. The other three visibility profiles are detections of companions to the stars ϕ^2-Cen and γ-Lup, and the non-detection of a companion to the star τ-Sco. In these figures, the horizontal axis is the angular wavenumber.

simple rotation defined by the position angles of observation baseline:

$$R \begin{pmatrix} \rho_N \\ \rho_E \end{pmatrix} = \begin{pmatrix} \cos\theta_1 & \sin\theta_1 \\ \cos\theta_2 & \sin\theta_2 \end{pmatrix} \begin{pmatrix} \rho_N \\ \rho_E \end{pmatrix} = \begin{pmatrix} \rho_1 \\ \rho_2 \end{pmatrix}, \tag{4.5}$$

where θ_1 and θ_2 are the position angles, measured North through East, of the two observations, ρ_1 and ρ_2 are the observed separations and ρ_N and ρ_E are the true separations in the north and east directions on the sky at the epoch of observation.

Inverting the matrix R and multiplying on the left gives ρ_N and ρ_E. It is important to note that there is a 180° uncertainty in the position angle of an observed binary system detected using SUSI; this is because a particular binary squared-visibility profile is independent of which star is the brighter component of the system. This means that a position angle of 0° could in fact be 180°, or that ρ_N and ρ_E could actually be of the opposite sign. The uncertainty on these two separations can be calculated by transforming the covariance matrix in the standard way:

$$\mathrm{COV}(\rho_N, \rho_E) = R^{-1} \begin{pmatrix} \sigma^2_{\rho_1} & 0 \\ 0 & \sigma^2_{\rho_2} \end{pmatrix} (R^{-1})^t, \tag{4.6}$$

where $(R^{-1})^t$ is the transpose of R^{-1} and noting that the covariances between the two observed separations are zero because they are completely independent observations. In the cases where more than two observations of a target were done, we used least-squares fitting to calculate the true separation. The observations used in the fits were generally taken on the same night, or over two nearby nights, so that even in the case of the closest and fastest moving companions detected, any orbital motion is insignificant. In the case of the close α-Mus companion, which was observed twice in mid July and twice in early August of 2010, we have treated the two nights individually. We also note that the detection of previously known companions to targets 4-Lup and δ-Cen are somewhat marginal (in particular 4-Lup), however the fitted binary parameters are consistent with the literature.

4.4 Detected Companions and Detection Limits

Among the 58 Sco-Cen targets we observed, companions were found to be associated with 23 of them, 13 of which are new detections. The fitted parameters, as well as the final combined contrast ratios and separations for each companion can be seen in Table. 4.2.

The completeness of this survey is dependent on two parameters, the resolvable range of companion separations and the largest detectable primary to secondary brightness ratio. An upper bound for the former is given by the coherence length of the interferometer as discussed above, and is ∼200 mas; however, this will be reduced by any de-focus in the system. The latter is not obvious directly from the data. Hence we have used a Monte-Carlo scheme to determine detection limits in different binary separation bands.

This was done by creating a sample of synthetic companions to each observed primary, with random contrast ratio and a random separation within the separation band. The faintest synthetic companion detectable at a three-σ level (where σ is the typical uncertainty in the calibrated squared-visibility profile) is taken as the detection limit.

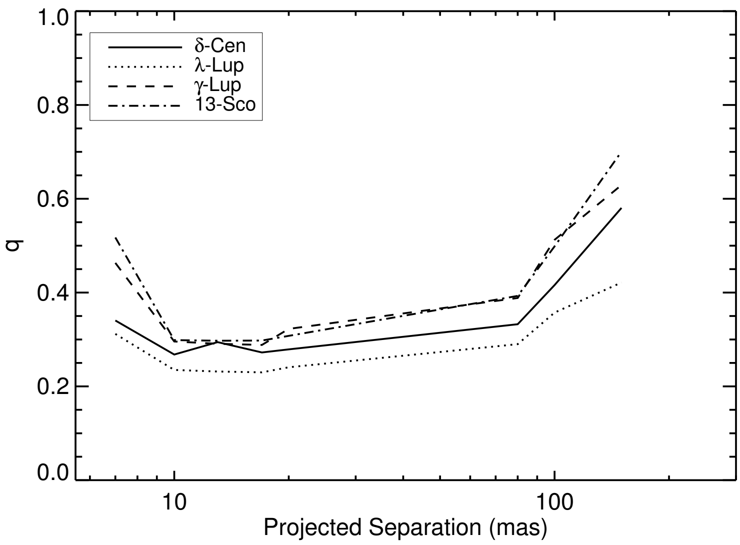

Figure 4.3: Detection limits for four stars observed in our survey.

These limits are then converted into mass ratios using isochrones of the mean subgroup ages. Typical detection limits are shown in Figure 4.3. From the diagram, companions with mass ratios down to typically $q = 0.3$ can be detected at separations of ∼7-100 milliarcseconds, at which point the defocus in the system makes wider detections impossible at the smaller mass ratios.

Table 4.2: The table of observed companion details. Contrast ratios (Δm) are in magnitudes, separations (ρ) are in milliarcseconds, Obs refers to observation number, baseline position angles (PA_B) are in degrees and ^{n} following a star name indicates a new companion. For each target, if more than one useable observation was taken we also provide a final contrast ratio (Δm_f) and the separations in the North and East direction (ρ_N,ρ_N) with their full covariance matrix (the final column is the correlation between the two separations), as well as a final, combined separation (ρ_f) and position angle (PA_f). The high correlations are due to the fact that the position angles differ by much less than 90°. Note that the position angles listed have a 180° uncertainty, hence, we have chosen to provide all position angles in the ($0 \leq PA < 180$) range.

Name	Date	Obs	PA_B (°)	Δm (mag)	$\sigma_{\Delta m}$ (mag)	ρ (mas)	σ_ρ (mas)	PA_f (°)	σ_{PA_f} (°)	Δm_f (mag)	$\sigma_{\Delta m_f}$ (mag)	ρ_f (mas)	σ_{ρ_f} (mas)	ρ_N (mas)	σ_{ρ_N} (mas)	ρ_E (mas)	σ_{ρ_E} (mas)	$\mathrm{COR}_{N,E}$
4-Lup	15/07/2010	1	14.50	0.00	0.23	2.77	1.18											
δ-Sco	15/07/2010	1	179.98	2.11	0.89	87.87	0.11											
	15/07/2010	2	176.67	2.11	1.04	86.61	0.17	12.34	2.22	2.11	0.02	89.95	0.80	87.87	0.11	19.23	3.57	0.54
α-Mus^n	14/07/2010	1	5.07	2.8	0.74	10.12	0.6											
	06/08/2010	1	30.7	2.7	0.15	15.7	0.5											
b-Cen^n	14/07/2010	1	5.67	1.06	0.18	9.22	0.05											
β-Mus^n	14/07/2010	1	6.95	3.48	0.23	18.29	0.07											
	14/07/2010	2	13.78	3.72	0.88	13.19	0.58	120.58	3.49	3.50	0.12	45.62	4.37	23.21	0.61	-39.27	4.89	-0.99
δ-Cen	15/07/2010	1	18.23	3.45	0.87	11.63	0.89											
ϵ-Cen^n	15/07/2010	1	11.62	2.59	0.33	109.11	0.20											
	15/07/2010	2	10.50	2.54	0.30	106.53	0.18	61.83	1.86	2.56	0.03	170.50	11.22	80.48	2.60	150.31	13.37	-1.0
ϵ-Lup	14/07/2010	1	8.71	1.69	0.15	49.25	0.09											
	14/07/2010	2	39.54	1.23	0.11	49.49	0.09	24.63	0.21	1.53	0.23	51.22	0.11	46.55	0.11	21.35	0.22	-0.77
f-Cen^n	26/07/2010	1	24.34	2.34	0.56	8.44	0.37											
	26/07/2010	2	28.62	1.24	0.27	8.61	0.22	41.69	21.29	2.10	0.55	8.84	2.94	6.60	2.65	5.88	5.07	-0.99
γ-Lup	26/07/2010	1	9.35	32.86	0.36	62.84	0.13											
	14/07/2010	2	8.77	1.37	0.16	59.13	0.09	89.61	0.38	2.63	0.98	371.48	15.95	2.53	2.52	371.47	15.96	-1.0
j-Cen^n	15/07/2010	1	30.64	2.38	0.35	40.40	0.20											
	26/07/2010	2	26.67	3.24	0.55	45.72	0.27											
	26/07/2010	3	32.25	3.43	0.80	36.64	0.36	145.38	7.18	3.14	0.32	95.61	10.53	78.68	6.69	-54.32	11.69	-1.0

Continued on next page

κ-Cen	14/07/2010	1	10.14	1.56	0.20	113.63	0.17											
	14/07/2010	2	5.85	1.25	0.12	110.01	0.12	31.33	1.05	1.40	0.16	121.88	1.29	104.10	0.36	63.38	2.70	-0.96
κ-Sco	06/08/2010	1	170.36	4.23	0.65	14.61	0.22											
λ-Lup	26/07/2010	1	18.36	0.93	0.06	55.14	0.04											
	27/07/2010	2	177.07	1.73	0.06	16.94	0.04											
	27/07/2010	3	3.53	1.25	0.04	28.75	0.02	78.31	0.14	1.49	0.23	109.87	1.21	22.25	0.17	107.60	1.24	-0.56
μ-Cen^n	14/07/2010	1	8.50	3.15	0.37	33.13	0.14											
	14/07/2010	2	2.99	3.22	0.53	23.36	0.19	80.20	0.21	3.17	0.04	105.55	2.40	17.96	0.30	104.01	2.46	-0.92
o-Lup	15/07/2010	1	16.25	0.28	0.06	42.62	0.03											
ϕ^2-Lup^n	15/07/2010	1	15.74	2.56	0.53	16.84	0.19											
	15/07/2010	2	18.81	2.05	0.17	16.72	0.08	9.94	11.77	2.17	0.26	16.92	1.03	16.67	1.21	2.92	3.63	-1.0
π-Cen	14/07/2010	1	6.12	1.35	0.13	26.64	0.08											
	14/07/2010	2	11.19	0.56	0.12	34.16	0.09	78.94	0.16	1.29	0.48	90.22	1.33	17.31	0.21	88.54	1.38	-0.96
ρ-Cen^n	15/07/2010	1	19.72	1.10	0.20	54.12	0.13											
ρ-Lup^n	14/07/2010	1	7.28	1.28	0.07	15.40	0.07											
	14/07/2010	2	6.21	1.98	0.10	15.99	0.08	123.33	5.61	1.82	0.35	35.07	4.94	19.27	0.69	-29.30	5.67	-1.0
σ-Cen^n	14/07/2010	1	14.33	2.59	0.58	88.11	0.37											
τ^1-Lup^n	26/07/2010	1	21.88	2.60	0.32	18.84	0.11											
	27/07/2010	2	1.18	2.97	0.36	18.04	0.11											
	27/07/2010	3	7.67	2.82	0.65	18.58	0.21	18.30	0.15	2.83	0.11	18.88	0.02	17.93	0.01	5.93	0.06	-0.74
τ-Lib^n	14/07/2010	1	5.58	2.85	0.58	12.10	0.19											

4.5 Wide Companions with All-Sky Data

A primary goal of our study is to create the best possible picture of the multiplicity of the highest-mass stars in the Sco-Cen association. We have moved closer to this goal in the close companion regime with our interferometric survey described above. Conventional and coronagraphic imaging studies complement our work by producing a very complete picture out to ~6 arcseconds. Beyond these separations, proximity to the primary becomes a rather poor indicator of physical association with the primary. Indeed, any detection beyond $\sim 10^3$ AU is likely to be a background or foreground contamination. This means the multiplicity catalogs such as the Washington Double Star catalog (Mason et al., 2011) are not strictly reliable for separations beyond ~5 arcseconds. With the availability of all-sky photometry catalogs in numerous bands, such as 2MASS and APASS, it is possible to produce a clearer picture of the wide-separation companion regime.

We undertook a search about our 58 survey targets in the 2MASS (Skrutskie et al., 2006) point source catalog out to a maximum separation of 10^4 AU. The 2MASS point source catalog has a resolution of ~5 arcseconds, meaning that there will be no overlap between our closer companions and the new companions found here. This search yielded 670 such possible companions brighter than the $K = 14$ 2MASS completeness limit with sufficient near-infrared photometry to allow placement on a colour-colour diagram. We then cross-matched these objects with the APASS (Henden et al., 2012) catalog to obtain B and V band magnitudes for the brighter candidates in the sample, and UCAC4 (Zacharias et al., 2013) to obtain proper motions. We found 55 of the objects had UCAC4 proper-motions and APASS photometry.

We then calculated photometric distances to our companions assuming that they are members of the Sco-Cen association. This was done using Siess isochrones (Siess et al., 2000) of age 6 Myr for US members and 16 Myr for members of UCL and LCC. For the brightest candidates, which are expected to fall on the main sequence, we used a Padova main sequence (Girardi et al., 2002) to calculate the photometric distances. Distances were calculated for for $(J-K,K)$,$(H-K,K)$ and $(B-V,V)$ where available, and averaged. Photometric distance uncertainties were conservatively estimated to be ∼10%. If a *Hipparcos* parallax measurement was available, this was of course used in place of the photometric distances and uncertainties. A candidate was then deemed a true companion only if the photometric distance and available proper motions showed agreement with the *Hipparcos* proper motion and distance of the primary at the 3σ level.

We have identified 15 companions in this way, 7 of which had proper-motions, and exclude the other 655 potential companions. The new companions are presented in Table 4.3. We note that due to the fact that there are potentially nearby Sco-Cen members to all of the primary stars in our sample, combined with the uncertainty of the photometric distances, there is some chance that association members have been identified as companions. The frequency of spurious companions increases dramatically with the separation, and so we consider companions out to 10^4 AU to be reliable, while beyond this limit there is almost certainly significant contamination from other Sco-Cen association members as well as background and foreground objects.

4.6 The Multiplicity Distribution of the Sco-Cen High-Mass Stars

With the addition of our survey results to the literature, it is possible to study the outcome of multiple star formation among high-mass stars. First we compile all available multiplicity information on the stars in our survey sample from the literature and combine them with our own observations. We then recast the data in terms of separation in astronomical units binary mass ratio, rather than angular separations and magnitude differences. We then inspect the distributions of these parameters as a starting-point for a Bayesian analysis of the data, which will provide the most robust determination of the parameters which describe the multiplicity distribution of our Sco-Cen sample. In the Bayesian analysis of the multiplicity distribution which follows, we combine these detection limits with those of Shatsky and Tokovinin (2002).

Primary	Sep (")	δK	PA (°)	Secondary
α-Lup	25.68	6.97	-127.72	CD-46 9501B
β-Cru	42.56	7.45	-34.12	HD 111123B
β-Mus	94.78	6.87	35.36	
ϵ-Lup	26.29	3.85	168.70	CD-44 10066C
	40.02	7.72	-170.03	
f-Cen	37.84	5.85	31.22	
	11.53	3.43	77.82	HD 113703B
γ-Lup	53.42	10.11	-67.59	
	39.10	10.57	-150.46	
J-Cen	61.53	6.93	-74.63	
κ-Sco	52.84	9.75	-168.68	
	55.34	8.96	17.97	
μ^1-Cru	35.02	0.78	17.03	μ^2-Cru
μ^2-Sco	25.38	7.92	16.17	
σ-Lup	26.27	6.11	-156.49	

Table 4.3: Companions to our target sample identified from 2MASS and APASS all-sky data.

Table 4.4: Mass ratios and separations for our sample. Typical uncertainty of the mass ratios is better than 10%, and the separations in AU for the SUSI companions is typically 10%. For the wider companions, the uncertainy is of the order of the uncertainty of the 2MASS positions, which are typically 1% . The source references are (1) this work, (2) Shatsky and Tokovinin (2002), (3) Mason et al. (2011), (4) this work, all-sky search (5), wide spectroscopic companion, see Table 4.5, (6) the SUSI study of Tango et al. (2009)

Primary	q	ρ(AU)	Source
3-Cen	0.49	693.43	2
4-Lup	0.95	0.3	1, 5
δ-Sco	0.45	11.08	6
α-Lup	0.08	4316.02	4
α-Mus	0.01	459.23	2
	0.35	2.64	1
b-Cen	0.65	1.0	1
β-Cru	0.06	4601.61	4

Continued on next page

β-Mus	0.86	95.42	3
	0.03	9044.19	4
	0.29	4.35	1
δ-Cen	0.31	12.12	1,3
d-Lup	0.49	279.63	3
ϵ-Cen	0.46	19.64	1
ϵ-Lup	0.65	46.37	3
	0.19	4062.64	4
	0.02	6185.01	4
	0.64	7.92	1
f-Cen	0.21	196.83	2
	0.05	4801.44	4
	0.21	1463.15	4
	0.43	1.12	1
γ-Lup	0.72	139.13	3
	0.01	9289.89	4
	0.01	6799.89	4
	0.39	64.61	3
HR 4549	0.44	165.98	3
HR 4848	0.03	850.24	2
HR 5543	0.13	123.20	2
j-Cen	0.03	8666.47	4
	0.32	13.47	1
κ-Cen	0.02	661.16	2
	0.71	20.14	3
κ-Sco	0.01	7516.23	4
	0.01	7871.50	4
	0.26	2.08	1
λ-Lup	0.03	82.29	3
	0.57	13.70	1
μ^1-Cru	0.71	4052.72	4
μ^2-Sco	0.02	4022.14	4
μ-Cen	0.08	749.11	2
	0.33	17.05	1
o-Lup	0.91	5.33	1

Continued on next page

ϕ^2-Lup	0.45	3.15	1
π-Cen	0.59	8.89	1
ρ-Cen	0.65	5.68	1
ρ-Lup	0.49	3.34	1
σ-Lup	0.06	4624.80	4
τ^1-Lup	0.41	5.99	1
τ-Lib	0.35	1.65	1

4.6.1 Compilation of the Sample Data

In order to produce the most accurate determination of the Sco-Cen multiplicity distribution we have compiled data from a number of sources in the literature. The Bayesian analysis presented below is most easily implemented in terms of mass ratios and physical separations rather than angular separations and magnitude differences. Hence we determined physical separations using the *Hipparcos* parallax measurements (van Leeuwen, 2007) and the mass ratios using isochrones for the corresponding subgroup ages and the magnitude band used in the original observation. The primary mass was determined using the *Tycho* (Perryman and ESA, 1997) V magnitude and the Padova isochrone of the age of the subgroup which each star is found in (Girardi et al., 2002). The secondary mass was then found by moving fainter along the appropriate magnitude band from the value of the primary. In the case of a small magnitude difference which would not place the secondary in a spectral-type range expected to exhibit premain-sequence (PMS) behaviour the same Padova isochrone was used. For larger contrast ratios which would result in a PMS companion the corresponding Siess PMS isochrone was used (Siess et al., 2000). The Padova and Siess isochrones show very close overlap (on the order of a tenth of a magnitude) in the higher-mass region of the isochrone in which all Sco-Cen stars observed are past their PMS phase. Any error introduced by this slight difference is, in general, expected to be much smaller than the errors associated with reddening and the measurements of the contrast ratios used to determine the mass ratios, and will not significantly contribute to the outcome of the analysis. The uncertainty of the mass ratios calculated in this way are expected to be typically better than 10%, which is more than accurate enough for the Bayesian analysis which follows. Similarly, the uncertainty on the physical separations for the SUSI companions are also typically 10%, while the wider companions in the arcsecond and greater separation regimes are expected to be accurate to $\sim 1\%$. Table 4.4 provides a list of the calculated physical separations and mass ratios for the non-spectroscopic companions.

For completeness we must also include all spectroscopic companions to the stars in our sample. They provide important information on the smallest separation range of companions and are vital in determining the properties of the multiplicity in the association. We include information on both double and single line companions to our sample stars in two different ways. For the double lined companions there is a directly measured mass ratio for the system, and so the separation can be directly calculated via the orbital period. We have taken the semimajor axes of the binary system and used them along-side the projected separations of our wider companion data. This is justifiable in light of the bin sizes we have used in separation in our analysis and the conversion factors of Dupuy and Liu (2011), which are close to unity for solar-type stars. The single line binary companions are not directly useable. The mass ratio and separation of the system cannot be directly determined from the measurements provided by the observation of a single line binary; however they do place useful constraints on the possible values of mass ratio and inclination, and hence also separation, that the systems can have. Table 4.5 lists the full information from the literature for the spectroscopic systems in our sample for both the single and double lined systems.

We deal with the unknown mass ratio and separation of the single lined systems in the following way: Firstly, we use the observed mass function $f(M_1)$ of the system to determine the distribution of possible values of mass ratio and inclination, based on a primary mass taken from the spectral type and colour of the stars and the corresponding Padova isochrone. Bayes' theorem states the following for the case of a single lined

Table 4.5: Spectroscopic companions to stars in our sample, with period (P) and mass function ($f(M_1)$. Mass ratios (q) are provided for the double lined spectroscopic binaries. The final column lists the literature sources from which the data was taken:(1) Levato et al. (1987), (2) Thackeray and Hutchings (1965), (3) Thackeray (1970),(4) Neubauer (1931), (5) Uytterhoeven et al. (2005), (6) Aerts et al. (1998), (7) Cohen et al. (2008), (8) this work, (9) Buscombe and Kennedy (1962)

Star	q	P (days)	$f(M_1)$	$\sigma_{f(M_1)}$	
3-Cen		17.42800	0.00830	0.00157	1
4-Lup	0.954	12.26000	0.30680	0.03633	1,2
ν-Cen		2.62528	0.00230	0.00031	1
ϵ-Lup	0.865	4.55959			3,4
γ-Lup		2.80895	0.0065	0.00225	1
τ-Lib	0.5	3.29066	0.12626	0.04604	1
ρ-Sco		4.00331	0.00164	0.00050	1
π-Sco	0.78	1.57010	0.27634	0.03574	1
ξ^2-Cen		7.64965	0.03800	0.00322	5
β-Cru	0.625	1828.0000			6,7,8
13-Sco		5.78053	0.01760	0.00410	1
4-Cen		6.930137	0.00598	0.00143	1
e-Lup		0.901407	0.001	0.0002	9

binary system;

$$P(q,i|f(M_1)) = \frac{P(f(M_1)|q,i)P(q,i)}{P(f(M_1))}, \tag{4.7}$$

where M_1 and q are the mass of the primary and the secondary to primary mass ratio respectively, and $P()$ denotes probability. We interpret this by first treating the probability of the observed mass function value as unity, $(P(f(M_1)) = 1)$, because we will use the uncertainty in the measurement in the calculations of $P(f(M_1)|q,i)$. $P(q,i)$ is the prior probability distribution of mass ratio and inclination of the orbit. The mass distribution of the companions is unknown, and is one of the properties we wish to determine, hence we define it as uniform up to a mass ratio of 1, and zero beyond it. The distribution of inclinations (i), for purely geometric reasons, follows a sinusoidal distribution between 0 and $\pi/2$ radians, if the handedness of the orbit is not considered. For our purposes, treating clockwise and anticlockwise orbits as identical will not affect the outcome of our analysis, as we only require masses and separations. Hence it is defined as $P(q,i) = \sin i$. Finally, we define $P(f(M_1)|q,i)$ to be a Gaussian with mean given by the observed mass function of the system and standard deviation defined by the uncertainty in the mass function measurement:

$$P(q,i|f(M_1)) = \frac{\sin i}{\sqrt{2\pi}\sigma_f} \exp\Big(-\frac{(f(M_1) - f_{mod}(M_1))^2}{2\sigma_f^2}\Big), \tag{4.8}$$

where $f_{mod}(M_1)$ is the "model" mass function calculated from a given value of mass ratio (q) and inclination (i). This produces a probability distribution similar to Figure 4.4. The distribution shows that for each mass ratio q there is a clear range of allowable inclinations which can produce a mass function which agrees with that given by the observations. The position of the allowable mass ratio-inclination pairs is determined by the observed mass ratio and the estimated primary mass. Historically, at this point an expected value of inclination can be chosen; however, this would not represent the observations as closely as possible. The optimal approach is to generate a sample of "virtual" systems for each observation based on the described probability density functions (PDFs). We do this by sampling from the described PDF for each system using rejection sampling, which maps a random uniform distribution onto an arbitrary PDF. We take 30 samples for each single lined binary system and include all of these "virtual" systems in our sample.

It is important to note that, while the above method of dealing with single lined spectroscopic binaries is an improvement on simply choosing an expected value of $\sin i$ such as 0.8, it is nevertheless still invariably tangled with prior assumptions. Primarily, we have used a range of allowed values as a substitute for the true value, and this has the potential to bias further results. Despite this, our analysis will still produce a robust estimate of the multiplicity properties of Sco-Cen.

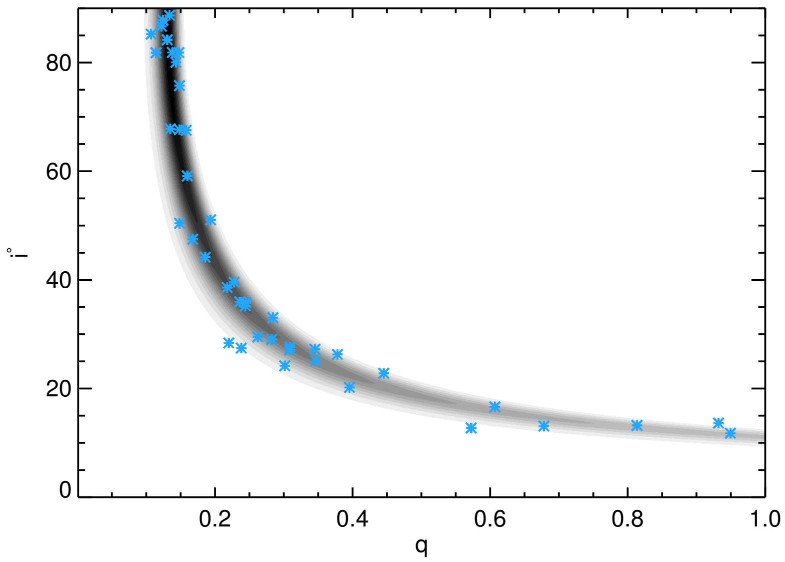

Figure 4.4: An example of the mass ratio-inclination distribution described in equation 4.8, for the single lined spectroscopic binary system 13-Sco (Levato et al., 1987). The position of the most probable mass ratio and inclination is determined by the observed mass function ($f(M_1)$) of the spectroscopic binary system, while the width of the distribution for any given mass ratio or inclination is determined by the uncertainty in this measurement. The blue points represent a random sampling from the distribution used to represent the "virtual" systems used in our analysis.

Combining both the visual and spectroscopic companions we have a complete picture of the state of knowledge on the multiplicity of the stars in our sample. With this we can determine the multiplicity characteristics of the population of the highest mass stars in Sco-Cen.

4.6.2 Bayesian Analysis

Classically, the standard method of illustrating binary population statistics is to create histograms of the important quantities, such as separation and mass ratio within the completeness limits of the available data. A model is then fit to the histograms to derive the population parameters. This approach is most useful when the functional forms of the distributions are completely unknown. When a functional form can be determined, a more direct and complete method for working with the data is to use Bayesian statistics, where each observation influences a prior PDF. Bayesian statistics,

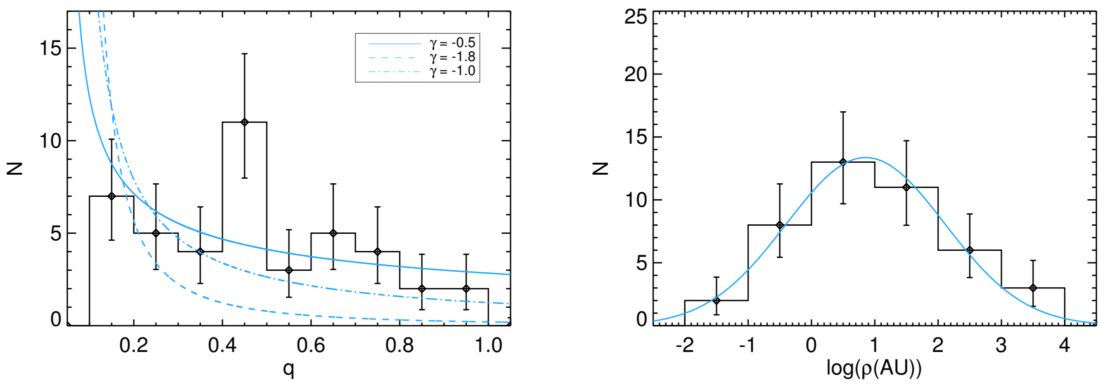

(a) **(b)**

Figure 4.5: Simple histograms displaying the mass ratio and separation (AU) of the companions for the stars in our sample with $q > 0.1$. The most likely values of the spectroscopic binary parameters from the PDF's were taken for inclusion in this plot. The mass ratio in the first figure appears to follow a negative power-law distribution with exponent of approximately -0.5, and the separation of the companions in the second follows a log-normal distribution with mean of ~ 0.9 and spread of ~ 1.28. The blue lines in the first figure illustrate mass ratio distributions with different power-law exponents, and in the second figure represent the best fit log-normal Gaussian distribution.

as opposed to histogram fitting procedures, takes into account all available data in an optimal way, which inherently avoids the need for completeness corrections. Bayesian statistics bypasses the step of fitting a distribution to observations by directly yielding the PDF for the model parameters, which is helpful in showing a study's population measurements, and their uncertainty. As stated above, the important requirement in the use of Bayesian statistics is that the analysis can only be used in the presence of some assumed functional forms of the population distributions, meaning that some inspection of the data (usually with histograms) is required as a starting-point for any Bayesian analysis.

Firstly, we present simple histograms to motivate our choice of prior distributions in the Bayesian analysis; these are shown in Figure 4.5. Figure 4.5a displays the histogram of mass ratios of the companions in our sample with $q > 0.1$ and the best fit to the data is shown in blue. We avoid the $q < 0.1$ range of mass ratios due to significant unquantified incompleteness which may bias our distribution. In the Bayesian analysis which follows, we treat the $q < 0.1$ regime of mass-ratio as unconstrained. Our plot appears to fit a power-law, and fitting to the histogram gives a best fit exponent of -0.38 ± 0.24, which agrees with the value of -0.4 which Shatsky and Tokovinin (2002) determined to be the most likely distribution based on their K-band imaging data (much of which is included in our sample and analysis below). The distribution of companion separations in our sample ($q > 0.1$) is displayed in Figure 4.5b. The data appears to fit a log-normal distribution in separation quite closely, with a mean log-separation in AU of 0.9 ± 0.2 and standard deviation of 1.29 ± 0.18. We know there is incompleteness within the sample, in particular, we expect incompleteness in the SUSI separation range (1-10 AU) below $q \sim 0.2 - 0.3$ where companions were not always detectable. Beyond 100 AU the sample can be considered highly complete down to $q = 0.1$ with the addition of our all-sky search, and the spectroscopic binary regime is most likely complete, although it is possible that some SB2's were mistaken for SB1's by the early observers.

Given these observed prior distributions, we can use Bayesian statistics to derive the multiplicity parameters of our sample. We again make use of Bayes' theorem;

$$P(M|D) \propto P(D|M)P(M), \tag{4.9}$$

where D represents the observations or data, M represents some model, namely some set of parameters and assumed functional forms, which may or may not describe the data, $P(D|M)$ is the probability of obtaining a given observation or data as a function of the model, $P(M|D)$ is called the posterior PDF of the model given the data and P(M) is the prior PDF for the model. Note that both $P(D|M)$ and $P(M|D)$ depend on the model parameters. This framework is applied by starting with the prior PDF and modifying it with an observation, producing a new prior PDF. This new PDF is then used with a subsequent observation to produce a further modified prior PDF, the process is then continued for all available observations.

The formalism for the application of the above Bayesian statistics to the analysis of multiplicity populations was first introduced by Allen (2007), though we present it in a similar way to Kraus et al. (2011b). The Allen (2007) method makes use of four parameters: a companion frequency F, a power-law distribution exponent γ, a mean of a lognormal separation distribution $\log \rho_m$ and a standard deviation for the same distribution $\sigma_{\log \rho}$. These parameters describe the PDF of the multiplicity population which describes our sample. Each parameter is assigned a prior and the observations are used to modify the priors to yield the population distribution as described above. In our work, we use a similar modification to the companion frequency F as Kraus et al. (2011b): in our analysis F can be greater than unity, representing the fact that we are dealing with higher order multiple systems and not solely binaries, which is the case in the Allen (2007) study.

Rather than the observations individually modifying the prior PDF, we group the data into discrete bins of log-separation and mass ratio and compile a function which describes the number of observed companions in each bin, $N_{comp}(q, \log \rho)$, which is combined with a detection function $N_{obs}(q, \log \rho)$, which describes the number of observations sensitive to a given bin of q and $\log \rho$. The detection function is built based on the detection limits of each observation we took, combined with those of Shatsky and Tokovinin (2002). We then use each set of grouped data as a single "observation" in the Bayesian sense to modify the prior PDF as described above.

The expected frequency of a companion existing in a particular bin of q and $\log \rho$ can be easily calculated from the above functional forms using the four parameters;

$$R(q, \log \rho | M) = \Delta q \Delta \log \rho \frac{F q^{\gamma}(\gamma + 1)}{\sqrt{2\pi}\sigma_{\log \rho}} \exp\left(\frac{-(\log \rho - \log \rho_m)^2}{2\sigma^2_{\log \rho}}\right), \tag{4.10}$$

where we have written $M = (F, \gamma, \log \rho_m, \sigma_{\log \rho})$, the set of model parameters, for brevity. Hence, for a given number of observations sensitive to a particular $(q, \log \rho)$ bin, the number of expected companions detected is given by $RN_{obs}(q, \log \rho)$. From this the value of $P(D|M)$ is described by a Poisson distribution;

$$P(N_{obs}, N_{comp} | M) = \frac{(RN_{obs})^{N_{comp}}\, e^{-RN_{obs}}}{N_{comp}!}, \tag{4.11}$$

where M once again represents the four parameters describing the expected distributions. We calculate the value of $P(D|M)$ for values of q between 0 and 1 in bins of width 0.1, and for values of $\log \rho$ between -2.0 and 4.0 dex, with all bins having width 0.5 dex. We then use the SUSI detection limits to create a map of N_{obs} in different separation and mass-ratio bins. For the spectroscopic binary separation bins, the number of observations (N_{obs}) has been scaled to match the number of random samples we took from the single lined spectroscopic binary systems. In our analysis, we treat the mass ratio range of $0-0.1$ as unconstrained to avoid bias due to unknown incompleteness in this regime where detections are often difficult. The results of this analysis will allow quantification of how many stars are missed in this range. Once the probability of each set of parameters in each bin is calculated, we let each value modify the prior distribution as explained above, yielding the posterior PDF.

Given that all of our prior knowledge went into the determination of the expected distribution shapes, we would like to choose priors for our four parameters which reflect a maximum level of ignorance. The companion frequency, F, is a scale independent parameter, and so the most ignorant choice of prior is given by $1/F$ (Sivia and Skilling, 2007). Similarly the prior for the spread of the separation distribution is given by $1/\sigma_{\log \rho}$, as this parameter is also scale independent. Both $\log \rho$ and γ are completely unconstrained and so we assign uniform priors to them.

The Bayesian analysis we have described here produces a PDF for all possible combinations of the four model parameters and is thus a four-dimensional matrix. To allow presentation of the results, we marginalise the PDF over different sets of parameters and present surfaces and curves for different parameters. The most illuminating results are seen when uncorrelated parameters are shown and others marginalised away. We find that both the companion frequency (F) and the mass ratio exponent (γ) are not correlated with any other parameters, while the $\log \rho_m$ and $\sigma_{\log \rho}$ are strongly correlated. In Figure 4.6 we have plotted the most useful presentations of the results.

Figures 4.6c and 4.6d show very clearly defined peaks for the companion frequency and mass ratio exponent, with values of $F = 1.25^{+0.27}_{-0.20}$ and $\gamma = -0.46 \pm 0.13$. These results make qualitative sense: The total number of observed companions ($q > 0.1$) was 43, hence the vanishing probability of a companion frequency below $\sim$0.8 in Figure

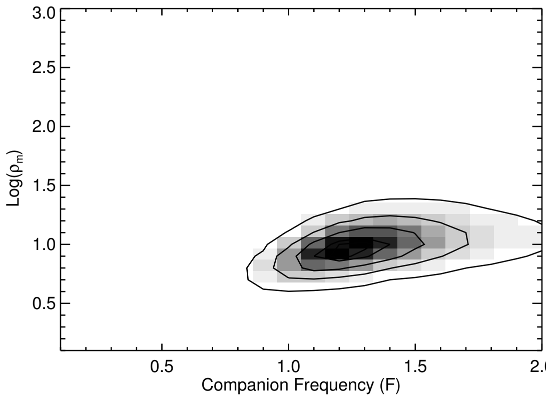

(a)

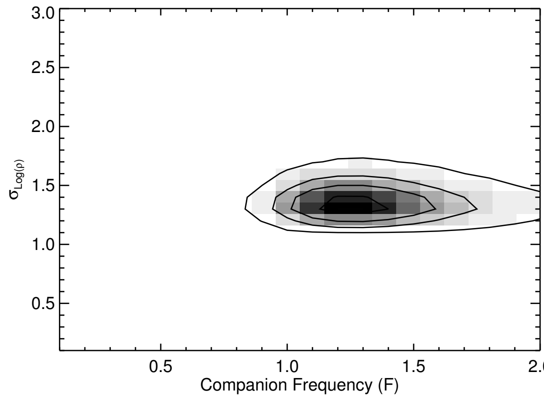

(b)

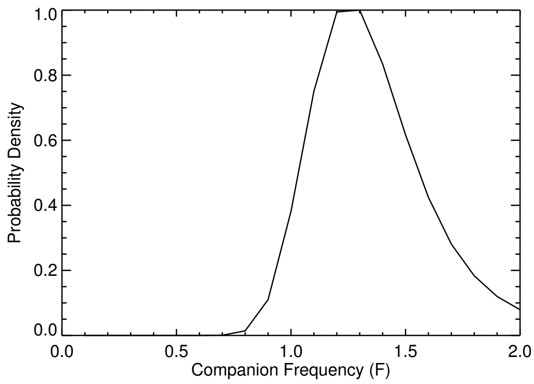

(c)

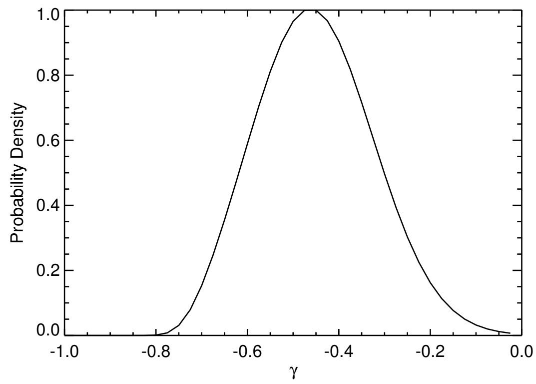

(d)

Figure 4.6: The marginalised probability density functions produced from our Bayesian analysis in selected correlated dimensions. The figures are as follows: (a) displays the PDF for F and $\log \rho_m$ in AU, (b) displays the PDF for F and $\sigma_{\log \rho}$; both have contours drawn at 10, 25, 68, 80 and 95% confidence levels. Figures (c) and (d) display the PDFs for F and γ respectively, marginalised over all other parameters and rescaled for ease of display.

4.6c. Our determination of γ agrees with the estimated value of -0.5 from the Shatsky and Tokovinin (2002) study, although a wider range of possible values is indicated here. The slight difference is not unexpected, as Shatsky and Tokovinin (2002) used only imaging data in their analysis. Note that the value of the mass ratio exponent γ is significantly different for the Sco-Cen high-mass stars compared to that which was determined for lower mass stars in other star-forming regions. The study of Kraus et al. (2011b) found γ to be ~ 0 for 0.25-0.7 $M_\odot$ primaries in the Tau-Aur star forming region, and Allen (2007) determined a value of ~ 1.8 for ultra-cool dwarfs. This highlights a potential mass-dependence of the multiplicity outcome of star formation. A further study, using a sample of multiplicity data for the full primary mass range within a single association would further indicate whether this mass trend is present or whether it is related to the specific star-forming regions or associations.

In Figures 4.6a and 4.6b we present surface plots of the $F - \log \rho_m$ and $F - \sigma_{\log \rho}$ PDFs. Both show a clear peak in the PDF at values of $\log \rho_m = 0.95^{+0.25}_{-0.15}$ and $\sigma_{\log \rho} = 1.35^{+0.35}_{-0.25}$. Note the correlation between $\log \rho_m$, $\sigma_{\log \rho}$ and F; a larger value of $\log \rho_m$ requires larger values of F and $\sigma_{\log \rho}$ to account for the number of small separation companion detections.

4.6.3 Single Stars

The formation of binary or higher order multiple systems is considered as a possible requirement for the conservation of angular momentum in high-mass star formation. Hence, we attempt to ascertain the overall frequency of single stars in our sample. Note that our general result of a companion frequency larger than one, and the large number of companions to stars in our sample are, at least, broadly consistent with the notion that all high-mass stars form with one or more companions. In our sample, there are 18 stars which do not have an observed companion. These stars are listed in Table 4.6.

The 18 apparently single stars put a hard upper limit of 31% on the single star fraction among Sco-Cen high mass stars. Using our probability distribution with the most likely parameters determined from the Bayesian analysis, we can estimate the number of single stars which in fact have a companion which was outside of our detection limits by integrating over appropriate separation and mass-ratio regions. We find the most probable number of missed companions among the 18 single stars to be 4 ± 1 companions. We then note that two of the single stars β-Lup and η-Lup were not observed by Shatsky and Tokovinin (2002), leaving the 0.3-5" arcsecond regime unobserved. From our multiplicity distribution, we expect that 1 ± 1 of these can have a companion in this separation range. Combining these estimates, this corresponds to

Single Stars
G-Cen
A-Cen
β-Lup
χ-Cen
δ-Cru
δ-Lup
η-Cen
η-Lup
γ-Mus
HR 4618
HR 5967
ι-Lup
λ-Cru
ϕ-Cen
θ-Lup
υ^1-Cen
ζ-Cru
τ-Sco

Table 4.6: The single Sco-Cen stars in the survey sample.

an inferred single stars fraction of approximately 19-27% of the sample. A very simple comparison can be made to our Bayesian model by treating the probability of a star having a certain number of companions as a Poisson function with a mean given by our most likely value of companion frequency $F = 1.25 \pm 0.25$. This produces a single stars fraction of 22-37%, and a fraction of quadruple or higher order multiples of 8-19%, which is consistent with our single stars fraction and the 8 (12%) higher order multiples in our sample. The combination of our survey results and the literature indicates that a number of young high-mass B-type stars which have formed alone, and not as a part of a multiple system.

4.6.4 The Effects of Multiplicity on Kinematics

The effect of multiplicity on kinematics is a significant issue, not just for determining accurate astrometry, but also for understanding how these effects will impact studies using the astrometry. As an example we have calculated a centre of mass (CoM) proper motion for the binary system defined by α-Cru A and B. The separations and position angles used to do the calculation were taken from the Washington Double Star catalogue (Mason et al., 2011). α-Cru is a wider binary than those observed in our survey; the two measured separations from the catalogue were 5.4 and 4.0 arcseconds. The position angles were 114 and 112 degrees. From the separation and position angle change, the mean motion of the secondary was calculated relative to the primary. This motion was then subtracted from the measured proper motion of the secondary, leaving the CoM proper motion. Our calculated CoM proper motion was (-36.3,-11.8) mas yr^{-1} in right ascension and declination respectively. This is significantly different to the proper motion of the system provided by *Hipparcos* which is $(-35.53, -14.89) \pm (0.45, 0.42)$ mas yr^{-1} (van Leeuwen, 2007). Discrepancies such as this which are larger than the typical *Hipparcos* proper motion errors can certainly affect the outcome of, for example, membership selection surveys for moving groups such as Sco-Cen. It is evident that this issue needs to be addressed for a larger sample of wide binaries.

4.7 Conclusion

Our survey of the highest-mass B-type stars in the young Sco-Cen association has determined constraining parameters of 23 companions, and discovered 13 new companions to these stars.

We used Bayesian statistics and all available multiplicity information to determine the most likely parameters of the multiplicity population of our sample, the results of which agree with previous, less complete analyses. We find that the multiplicity distribution of the stars in our sample to be best described by a log-normal distribution in separation, with a mean of $0.95^{+0.25}_{-0.15}$ and a standard deviation of $1.35^{+0.35}_{-0.25}$, while the mass-ratio follows a power law distribution with exponent $\gamma = -0.46 \pm 0.13$.

In addition, the frequency of companions was determined to be $F = 1.25^{+0.27}_{-0.20}$. The multiplicity literature, and our survey results, both point to a very large multiple fraction among high-mass stars in young associations, with only $\sim 19 - 27\,\%$ being single stars according to our statistics. This broadly agrees with the idea that companion formation and companion related mechanisms are the primary angular momentum redistribution method among high-mass stars (Larson, 2010). However, the data suggests a significant number of single stars among our sample, which according to our Bayesian analysis, are unlikely to fall under the umbrella of missed companions outside of the current detection limits.

Given that the role of magnetic fields in angular momentum loss for high-mass stars is most likely less important, e.g., the lack of collimated jets often associated with lower-mass stars (Arce et al., 2007), some mechanism must be present in the star forming environment which creates single stars. This implies that these stars are either part of a very large-scale wide system, were ejected from a multiple system early in their lifetime, or formed as single stars. Models have suggested that disruptive interactions can shape the formation of high-mass stars in dense clusters (Bonnell et al., 2003), but ejection in Sco-Cen is much less likely because OB associations are in general sparse environments. With velocity dispersion on the order of 1° per Myr, it is difficult to observationally test ejection hypotheses without GAIA-quality astrometry. The large scale behaviour of Sco-Cen is not completely unknown. It has been shown, using lower-mass members in the Preibisch et al. (2002) survey of US that two degrees is the approximate wide-scale binarity limit in US Kraus and Hillenbrand (2008). Assuming that UCL and LCC have similar structures, there is some chance that a small number of the single stars in our sample could be part of a very wide multiple system with one or more other high mass stars. However, this is unlikely to account for all of the potential single stars in our sample. A further possibility is the merger of two lower-mass members of a binary system to form an apparently single, B-type star. While this has been modelled extensively for the case of dense clusters, it is unclear what the frequency of such interactions is in the context of OB associations (Zinnecker and Yorke, 2007, Bonnell et al., 1998). In all likelihood, the stellar density in Sco-Cen is insufficient to induce binary mergers (Bonnell and Bate, 2005).

5

Age Dating the Upper-Scorpius Association using Close Binary Systems

5.1 Introduction

The coeval Sco-Cen populations are often used as "age-calibrated" samples of objects in the study of a number of different science goals, such as circumstellar disk evolution (Carpenter et al., 2009, Chen et al., 2011, Rizzuto et al., 2012), exoplanet identification and evolution (Kraus and Ireland, 2012, Ireland et al., 2011b) and multiplicity studies (Kouwenhoven et al., 2007, Kraus et al., 2011b, Rizzuto et al., 2013a). Furthermore, mass estimation from models of very low mass companions to K and M-type association members is highly dependant on the assumed age. Thus, it is critical that the age estimation for young associations is both highly accurate, and unbiased.

As mentioned in Chapter 1 the ages of the Sco-Cen subgroups are contentious; the youngest and most compact subgroup, Upper-Scorpius, was first age-dated using the main sequence turn-off, and was estimated to be ∼5-7 Myr old (de Geus, 1992). This was then supported by a spectroscopic survey for low-mass association members by Preibisch et al. (2002), which also determined a population age of ∼5 Myr, with a very narrow age spread. More recent work utilising new spectral-typing and photometry of F-type members has shown that Upper-Scorpius may have a median age of ∼11 Myr, which is significantly different from any previous work (Pecaut et al., 2012). The older and larger Sco-Cen subgroups, UCL and LCC, due to undoubtedly more complex star formation history and substructure, display variations in age estimates with both position and spectral type (Mamajek et al., 2002, Preibisch et al., 2002, 1998, Song et al., 2012).

A currently unexplored improvement for age-dating Sco-Cen is the inclusion of orbital elements of well characterised Sco-Cen member binary system. An accurate orbit can provide a direct measurement of the total system dynamical mass, which can then be used as an additional orthogonal dimension in model fitting. Paired with a contrast ratio between the primary and the secondary companion, this provides a vast improvement in estimating the age of individual stars, which then provide an age estimate for the association region in which they are found.

In this chapter, we present orbits for seven low-mass Upper Scorpius stars monitored with Sparse Aperture Masking (SAM) techniques with the NIRC2 Camera on the Keck 2 telescope. Using these seven orbits we estimate an age for the Sco-Cen subgroups using a Bayesian model fitting procedure.

5.2 Target Sample, Observations, and Data Analysis

Our low-mass target members of Upper Scorpius were selected from a multiplicity and planet-search survey of the Upper-Scorpius subgroup of Sco-Cen (Kraus et al., 2008), the targets for which were compiled in Kraus and Hillenbrand (2007a) from a number of recent membership surveys of the Upper-Scorpius region (Preibisch et al., 1998, 2001, 2002, Slesnick et al., 2006, Ardila et al., 2000, Walter et al., 1994, Martín et al., 2004). The Kraus et al. (2008) survey identified 12 new binary companions to Upper-Scorpius G/K/M-type stars, and we have been continually monitoring 8 of these systems using NIRC2 aperture masking in natural guide star AO mode, over a time-scale of five years. All NIRC2 AO observations were taken using the smallest available pixel scale of 10 mas pixel^{-1} and either a two or four location dither pattern (diagonal). The majority of the observations were done using the 9-hole aperture mask and the narrow-band CH_4S filter, with some observations in J,K$'$ and L$'$. Table 5.1 lists the full target sample, with basic stellar properties.

Aperture masking data reduction utilises the complex triple product or closure-phase, in addition to squared interferometric visibilities, in order to remove non-common path errors and variable optical aberrations. Binary system profiles can then be fit to the visibilities and closure phases to produce separations and position angles. For this work we used the aperture masking reduction pipeline created by Dr. Michael Ireland, further explanation of which is given in the appendix of Kraus et al. (2008). In Table 5.2 we list the individual aperture masking observational details, including observation filter, fitted separations and position angle.

Name	SpT	m_V
GSC 6209-735	K2	11.4
GSC 6794-156	G6	9.8
USco J160517.9-202420	M3	14.2
ScoPMS 017	M1	13.8
RX J1550.0-2312	M2	14.1
RX J1601.9-2008	G5	10.4
ROXs 47A	K4	13.6
GSC 6209-735	K2	11.4

Table 5.1: Basic information for the stars in our orbit monitoring sample. Spectral types are taken from Preibisch et al. (2001).

Our targets were also observed with the Hubble Space Telescope Wide Field Camera (WFC3) in mid-2012, in a number of visible filters ranging from $275 - 850$ nm.

Table 5.2: The full list of Keck NIRC2 observations of our low-mass aperture masking sample in the Upper Scorpius subgroup of Sco-Cen. The data provided are: angular separation (ρ), uncertainty on separation (σ_ρ), companion position angle (θ), position angle uncertainty (σ_θ), magnitude difference (Δm), and magnitude difference uncertainty ($\sigma_{\Delta m}$). The original observation of ROXs 47a (labelled [a]), was taken from the discovery paper of Barsony et al. (2003), which used the Hale 200 inch telescope, this measurement was not included in the orbital fit. The HST PSF fitting astromentry was determined using the PSF fitting procedure described in Liu et al. (2008), and was included in the orbital fit.

Date	MJD	Filter	ρ (mas)	σ_ρ (mas)	θ (°)	σ_θ (°)	Δm (mag)	$\sigma_{\Delta m}$ (mag)
				GSC6209-735				
30/07/14	56868	CH4S	17.20	1.66	175.82	6.38	3.05	Fixed
29/07/14	56511	K	22.23	13.04	180.44	3.38	3.68	1.60
7/08/13	56511.50	CH4S	16.36	2.48	72.47	1.201	2.93	0.45
4/04/12	56021.50	CH4S	33.10	0.60	31.8	0.7	3.09	0.03
22/06/11	55734.50	CH4S	26.83	0.95	11.62	0.93	2.99	0.05
5/04/10	55291.50	CH4S	12.70	1.0	243.5	5.8	3.1	0.01
1/06/09	54983.50	CH4S	26.1	1.6	195.5	1.1	3.5	0.10
30/05/07	54250.50	CH4S	31.0	2.0	42.5	3.6	3.15	0.01
				GSC6794-156				
6/08/13	56510.50	Kc	70.51	0.11	93.49	0.06	0.46	0.01
15/04/12	56032	HST	71.50	0.50	115.30	0.60	...	...
5/06/11	55717.50	L’	70.47	0.11	129.76	0.09	0.45	0.01
4/04/10	55290.50	Jc	65.99	0.06	150.12	0.05	0.532	0.01
1/06/09	54983.50	CH4S	60.59	0.12	167.46	0.12	0.504	0.01
6/06/07	54257.50	K’	44.30	0.07	230.74	0.08	0.45	0.01
				USco J160517.9-202420				
30/07/14	56868	CH4S	25.09	0.23	303.84	0.57	0.387	0.022
4/04/12	56021.50	CH4S	31.73	0.04	271.19	0.08	0.44	0.01
22/06/11	55734.50	CH4S	37.20	0.08	278.57	0.14	0.46	0.01
5/04/10	55291.50	CH4S	38.28	0.07	287.6	0.08	0.391	0.01
1/06/09	54983.50	CH4S	33.61	0.11	294.32	0.16	0.41	0.01
17/06/08	54634.50	CH4S	21.40	0.09	309.21	0.47	0.517	0.02
6/06/07	54257.50	K’	16.15	0.59	251.12	1.11	0.4	0.07
				ScoPMS 17				
29/08/14	56867	K	34.27	0.08	117.76	0.14	0.708	0.006
7/08/13	56511.50	CH4S	27.10	0.04	132.5	0.08	0.79	0.01
4/04/12	56021.50	CH4S	11.65	0.34	198.1	3.5	0.79	0.01
22/06/11	55734.50	CH4S	22.54	0.10	32.72	0.2	0.79	0.02
5/04/10	55291.50	CH4S	39.74	0.10	50.49	0.14	0.761	0.01

Continued on next page

5/06/07	54256.50	K'	53.86	0.19	68.93	0.2	0.78	0.01
				RXJ1550.0-2312				
30/07/14	56868	CH4S	42.35	2.25	136.66	2.95	1.19	0.21
4/04/12	56021.50	CH4S	66.96	0.20	89.02	0.13	0.863	0.01
14/04/12	56030	HST	64.10	0.20	89.56	0.27	...	...
22/06/11	55734.50	CH4S	66.80	0.30	77.5	0.3	0.87	0.03
5/04/10	55291.50	CH4S	58.66	0.15	56.71	0.12	0.893	0.01
1/06/09	54983.50	CH4S	46.33	0.12	35.96	0.13	0.82	0.01
17/06/08	54634.50	CH4S	26.88	0.17	344	0.31	0.81	0.01
6/06/07	54257.50	K'	26.93	0.04	222.07	0.11	0.76	0.01
5/06/07	54256.50	K'	26.95	0.05	222.13	0.13	0.76	0.01
				RXJ1601.9-2008				
29/07/14	56867	K	32.829	0.39	206.09	0.34	1.84	0.02
4/04/12	56021.50	CH4S	17.50	1.70	100.45	1.22	2.28	0.32
22/06/11	55734.50	CH4S	25.50	0.30	67.6	0.3	2.04	0.02
5/04/10	55291.50	CH4S	28.47	0.36	43.83	0.34	2.08	0.02
17/06/08	54634.50	CH4S	24.40	0.70	231.5	0.8	2.08	0.05
31/05/07	54251.50	CH4S	39.31	1.57	217.67	0.59	2.14	0.13
				ROXs 47A				
29/07/14	56867	K	52.31	0.15	73.08	0.21	0.094	0.007
7/08/13	56511.50	CH4S	42.39	0.04	62.2	0.05	0.372	0.002
02/06/12	56445.0	HST	39.9	1.4	58.9	1.0	...	...
22/06/11	55734.50	J	21.20	0.30	141.1	1.6	0.21	0.02
5/04/10	55291.50	CH4S	43.43	0.18	108.5	0.2	0.221	0.01
1/06/09	54983.50	CH4S	51.76	0.19	98.73	0.22	0.171	0.01
24/05/02[a]	52418.50	K	40.0	30.0	107	20	0.1	1.60

5.2.1 Orbital Parameters

From a series of at least four separations and position angles, spanning a temporal baseline which is a sizeable portion of the binary system orbital period, it is possible to extract the seven orbital parameters without a distance measurement. These seven parameters are periastron passage epoch (T), orbital period (P), angular semi-major axis (a), orbital eccentricity (ϵ), longitude of the ascending node (Ω), argument of periapsis (ω), and orbital inclination (i). The primary requirement for extracting the orbital parameters is a relationship between the parameters and an observation time to astrometry. This process is described below, and can be found in full in Smart (1931).

Keplerian Orbits

The normal two-body scenario is used to parameterise the location of the companion relative to the host star at a given time (t) based on the seven orbital elements. The starting point is the mean anomaly (M);

$$M(t) = \frac{2\pi}{P}(t - T), \tag{5.1}$$

where P is the orbital period and T is the periastron passage epoch. The mean anomaly is a convenient angle that does not represent any real geometric quantity, but rather is the angle between the direction of periastron and the position of the companion, if it were in a circular orbit. This means the mean anomaly varies linearly with time. This can be expressed in terms of another angle, called the eccentric anomaly (E), which is the angle between the direction of periastron and the companions position measured from the centre of mass, projected onto a circle circumscribing the orbital ellipse. This is called Kepler's equation:

$$M(E) = E - \epsilon \sin E, \tag{5.2}$$

where ϵ is the orbital eccentricity. This is then solved numerically to determine E. The eccentric anomaly is then related to the true anomaly (ν), the corresponding angle to E measured from the focus rather than the centre of the ellipse by:

$$\tan\frac{\nu}{2} = \sqrt{\frac{1+\epsilon}{1-\epsilon}}\tan\frac{E}{2}. \tag{5.3}$$

Given the true anomaly, calculation of the observed separation (ρ) and position angle of the companions (θ) is done using basic properties of the ellipse and projection into the frame of reference of the observer:

$$\rho = \frac{a(1-\epsilon^2)}{1+\epsilon\cos v}\sqrt{\cos^2\alpha + \sin^2\alpha\cos^2 i}, \tag{5.4}$$

$$\tan\theta - \Omega = \sin\alpha\cos i/\cos\alpha, \tag{5.5}$$

where $\alpha = (\nu + \omega)$. This provides both angular separation and position angle for a given set of parameters and a given observational time, and allows an orbital solution to be fitted to the astrometry obtained in our monitoring program.

Fitting to the Astrometry

The astrometric measurements taken in our orbit monitoring program were used to determine orbital solutions using a χ^2 minimisation on a grid of orbital parameters, applying the method described above to compare orbital parameters to the observations. Table 5.3 lists the orbital solutions for the stars in our program, while the corresponding orbital plots can be found in Figures 5.1 to 5.7. Typically, the semi-major axis (in angular units) and the period, the two important parameters for estimation of the system dynamical mass, are determined to better than ∼2–3 %. In the last two columns of Table 5.3, we list the system dynamical masses at a fixed parallax of 7.5 mas, chosen to represent the mean distance to the Upper Scorpius subgroup. These system masses can then be appropriately scaled to alternate parallax π_n through multiplication by $(7.5/\pi_n)^3$, with appropriately adjusted uncertainties.

5.2.2 HST observations

In addition to AO imaging of the low-mass targets, we have obtained single-epoch observations of these binary systems with the Hubble Space Telescope (HST) Wide Field Camera 3 (WFC3) in a variety of visible filters spanning wavelengths of $225 - 900$ nm. Three exposures in each filter were taken, to which was applied the standard HST reduction, calibration and cosmic ray rejection procedure (Rajan, 2010). We calculated binary system combined magnitudes for each WFC3 filter using aperture photometry on the combined images with a 0.4" radius star aperture and a sky annulus of $4 - 6$". Given the orbital solutions we have determined for these systems,

Star	T (JD)	P (days)	a (mas)	ϵ	Ω (°)	ω (°)	i (°)	M_T ($M_\odot$)
GSC6209-735	2455160±4	1998.4±18.3	27.79±0.53	0.219±0.014	208.0±1.6	22.5±2.6	63.9±1.3	2.18±0.17(±0.42)
GSC 6794-156	2453993±1	5506.2±33.3	64.15±0.46	0.230±0.003	334.3±1.0	74.0±1.2	209.4±1.1	3.54±0.12(±0.63)
J160517.9-202420	2456554±0	2146.2±3.4	21.88±0.38	0.907±0.004	160.4±5.7	59.3±5.8	154.8±2.0	0.92±0.05(±0.17)
ScoPMS 17	2455945±1	5471.5±47.1	47.58±0.37	0.880±0.002	199.6±0.3	286.1±0.3	236.0±0.3	1.46±0.06(±0.26)
RX J1550.0-2312	2454410±0	3128.5±11.6	46.26±0.05	0.481±0.001	241.1±0.7	30.0±0.9	329.6±0.5	4.11±0.04(±0.72)
RX J1601.9-2008	2454970±3	2936.6±24.7	35.70±0.36	0.348±0.013	223.7±0.5	105.5±0.8	287.8±0.4	2.15±0.10(±0.39)
ROXs 47A	2455930±2	3010.2±43.3	32.70±0.33	0.818±0.009	27.2±11.7	239.9±11.7	343.4±1.7	1.57±0.09(±0.29)

Table 5.3: List of orbital elements and corresponding uncertainties fitted to the astrometric data for the objects monitored in our program. The final columns contain the total system masses for our targets, derived from the orbital parameters at a fixed distance of 145 pc (6.9 mas parallax), chosen to represent the mean distance of Upper Scorpius. The uncertainties provided are solely taken from the uncertainty in the orbital parameters, and the bracketed uncertainties include an uncertainty of ±0.7 mas on the parallax. Note that the large system mass for RXJ1550.0-2312 (M-type) implies that the star is very likely to be in the foreground with respect to Upper-Scorpius, with a parallax greater than ~10 mas.

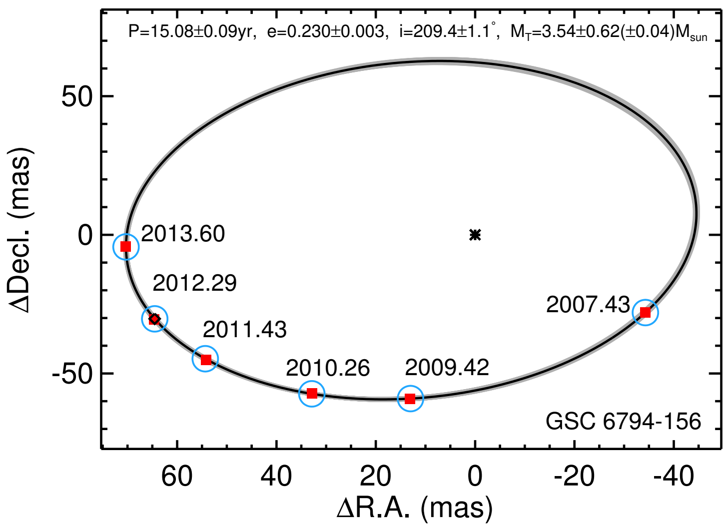

Figure 5.1: Orbital solution for GSC 6794-156 from NIRC2 AO aperture masking. The data is shown as red squares, with corresponding model fits shown as blue circles. We show the best fit orbit in black, with a 1-σ region shaded in grey. The black diamond shows the orbital position of the secondary at the time of the corresponding HST observations. We also display the orbital period, semimajor axis, eccentricity and system mass at 145 pc.

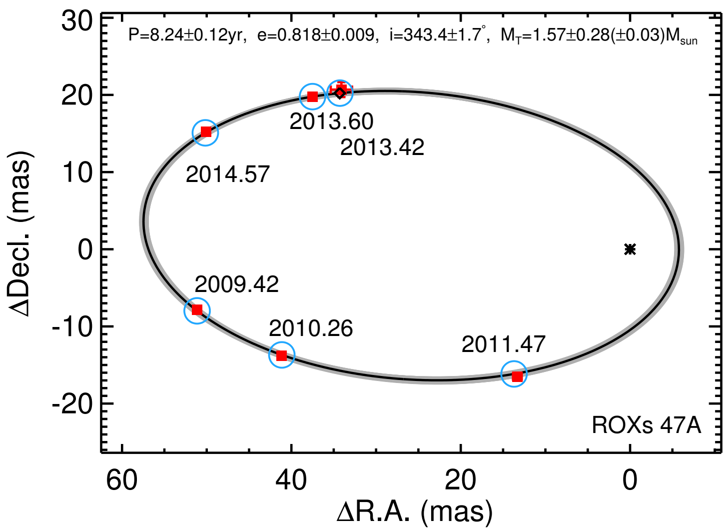

Figure 5.2: Orbital solution for ROXs 47Aab from NIRC2 AO aperture masking, with equivalent colors and symbols as Figure 5.1.

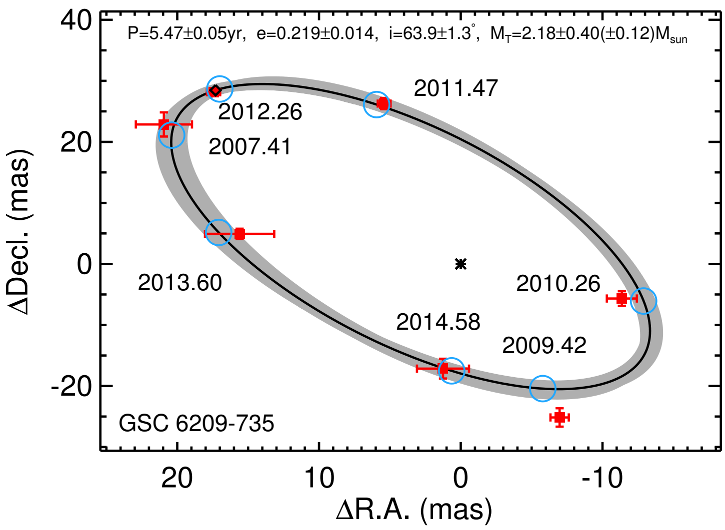

Figure 5.3: Orbital solution for GSC 6209-735 from NIRC2 AO aperture masking, with equivalent colors and symbols as Figure 5.1.

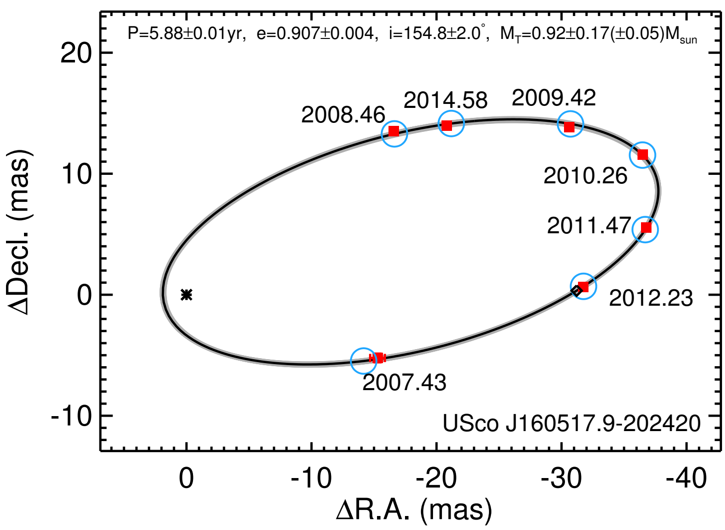

Figure 5.4: Orbital solution for USco J160517.9-202420 from NIRC2 AO aperture masking, with equivalent colors and symbols as Figure 5.1.

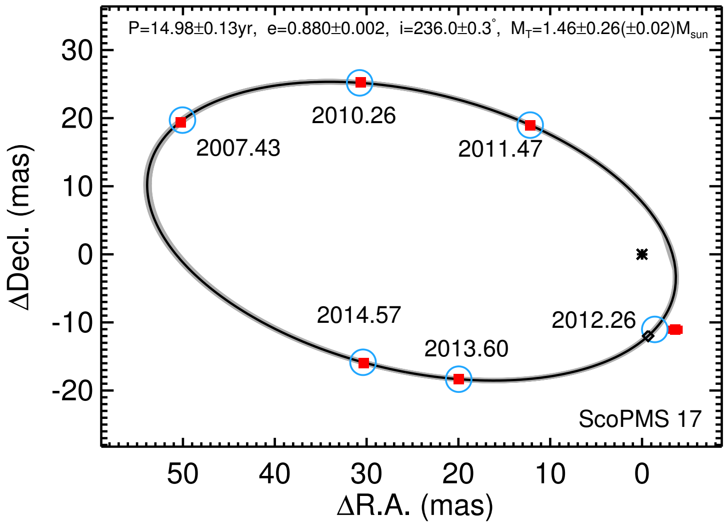

Figure 5.5: Orbital solution for ScoPMS 17 from NIRC2 AO aperture masking, with equivalent colors and symbols as Figure 5.1.

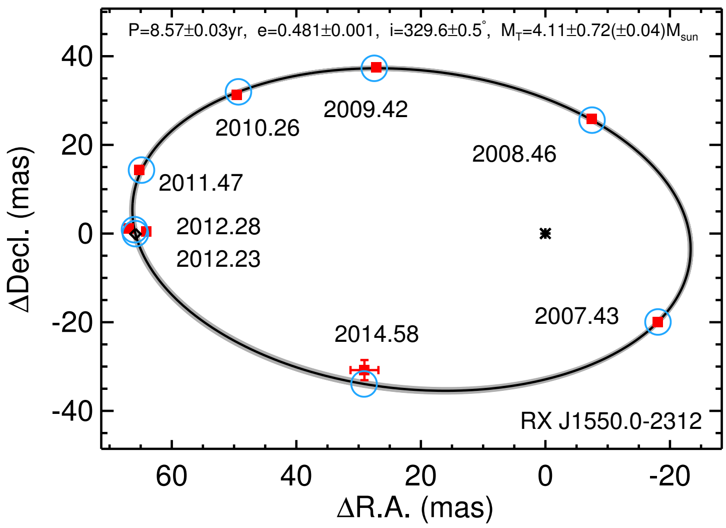

Figure 5.6: Orbital solution for RX J1550.0-2312 from NIRC2 AO aperture masking, with equivalent colors and symbols as Figure 5.1.

Table 5.4: Hubble Space Telescope, Wide Field Camera 3 photometry, and differential photometry for the G, K and M-type binary systems in our orbit monitoring program.

Filter	RXJ1550...	RXJ1601...	USco J1605...	GSC6209-735	GSC6794-156	ROXs47A	ScoPMS017
F225W	...	14.96±0.04	...	...	14.34±0.03	...	...
	...	...	...	...	1.58±0.19	...	...
F275W	18.43±0.14	13.48±0.03	18.19±0.12	15.43±0.04	12.88±0.02	18.99±0.18	18.08±0.12
	1.37±0.31	...	...	...	1.35±0.19	0.40±0.36	...
F336W	17.05±0.05	11.77±0.02	17.16±0.06	13.20±0.02	11.15±0.02	17.29±0.06	16.66±0.05
	1.21±0.24	0.06±0.11	0.84±0.38	...	0.89±0.26	0.10±0.84	1.03±0.42
F390W	16.47±0.03	11.68±0.02	16.60±0.03	13.01±0.02	11.07±0.02	16.48±0.03	16.17±0.03
	1.57±0.17	0.17±0.31	0.64±0.41	...	0.43±0.43	0.42±0.43	1.06±0.18
F395N	16.67±0.06	12.15±0.02	16.77±0.06	13.50±0.03	11.54±0.02	16.90±0.07	16.41±0.06
	...	...	...	...	...	...	...
F438W	15.88±0.03	11.41±0.02	15.98±0.03	12.58±0.02	10.77±0.02	15.72±0.03	15.56±0.03
	1.69±0.14	0.24±0.40	0.09±0.56	4.16±2.35	0.62±0.33	0.04±0.47	0.14±0.45
F467M	...	11.07±0.02	...	...	10.39±0.02	...	...
	...	...	...	...	...	...	...
F475W	15.03±0.02	...	15.14±0.02	12.05±0.02	...	14.80±0.02	14.81±0.02
	1.57±0.09	...	0.12±0.30	...	...	0.33±0.38	0.32±0.15
F547M	...	10.43±0.02	...	...	9.76±0.02	...	...
	...	...	...	...	...	...	...
F555W	14.28±0.02	...	14.35±0.02	11.62±0.02	...	13.91±0.02	14.05±0.02
	1.21±0.31	...	0.22±0.24	...	...	0.04±0.10	0.64±0.47
F625W	13.25±0.02	...	13.34±0.02	10.87±0.02	...	12.83±0.02	13.06±0.02
	1.39±0.21	...	0.32±0.19	...	...	0.17±0.07	0.19±0.10
F631N	...	9.96±0.02	...	...	9.30±0.02	...	...
	...	...	...	...	...	...	...
F656N	12.04±0.03	9.39±0.02	12.13±0.03	10.30±0.02	8.67±0.02	11.71±0.03	11.86±0.03
	...	...	...	...	...	...	...
F673N	...	9.73±0.02	...	...	9.09±0.02	...	...
	...	...	...	...	...	...	...
F775W	11.69±0.02	9.38±0.02	11.95±0.02	10.25±0.02	8.82±0.02	11.47±0.02	11.73±0.02
	0.89±0.10	-0.07±0.21	0.25±0.07	...	0.36±0.04	0.16±0.09	1.04±0.58
F850LP	10.85±0.02	8.98±0.02	11.14±0.02	9.85±0.02	8.36±0.02	10.56±0.02	10.92±0.02
	0.86±0.04	1.03±0.84	0.22±0.09	...	0.34±0.09	0.18±0.06	0.53±0.71

we can accurately predict the separation and position angle of each binary system at the epoch of observation with the HST, to within a few milli-arcseconds. Combined with the stability of the HST point spread function (PSF), we can derive differential photometry from our observations even though the binary separations are typically

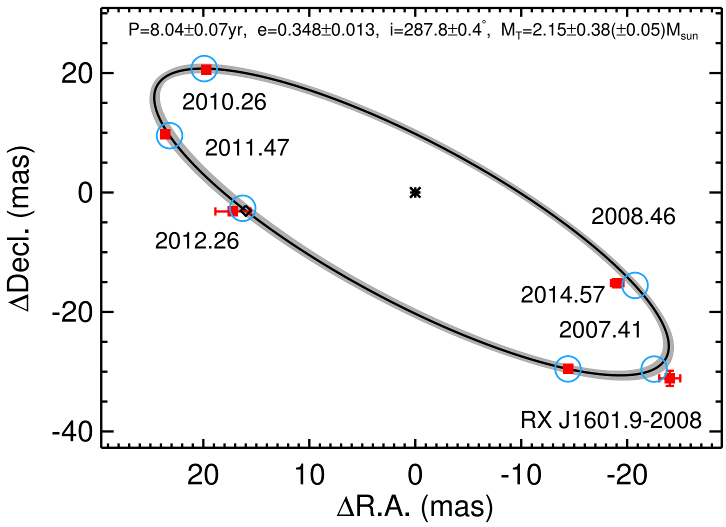

Figure 5.7: Orbital solution for RX J1601.9-2008 from NIRC2 AO aperture masking, with equivalent colors and symbols as Figure 5.1.

< 60 mas. Using the Tiny Tim software (Krist et al., 2011), our collaborator Trent Dupuy created PSF models for the WFC3 wide-band filters. These were then fitted to the images of our binary systems, with the separation and position angle fixed to the values determined by the orbit. This PSF fitting procedure was carried out by Trent Dupuy and is described in further detail in a previous publication (Liu et al., 2008). The resulting photometry is presented in Table 5.4.

5.3 τ-Scorpii Follow-Up Observations

Over the course of 2012 - 2014, we have continued to observe the B-type Upper Scorpius member τ-Sco with the goal of definitively ruling out the existence of a companion, this included additional SUSI observations, Keck aperture-masking, and interferometry with PIONIER/VLTI. Table 5.5 summarises the observations.

The SUSI observations, which can be found in Appendix E, show no significant detection on any of the six nights on which the target was observed. Similarly the Keck aperture-masking does not indicate the presence of a companion out to 200 mas.

Table 5.5: Summary of follow-up observations of τ-Sco

Date	Instrument	Note
20/07/2012	SUSI	40 m
26/08/2012	SUSI	40 m
05/07/2013	SUSI	60 m
26/07/2013	SUSI	60 m
15/08/2013	SUSI	80 m
04/04/2012	NIRC2	Hc filter, 18-hole mask
03/07/2014	PIONIER	H-free

The PIONIER observations are also consistent with the result that τ-Sco is a single star, with both closure-phases and square-visibilities consistent with an unresolved object. These can be seen in Figure 5.8.

The VLTI observations provide a broad UV-coverage, with spatial resolution as small as 4 mas in both the North and East directions (Figure 5.8c). From the combined data, we conclude that τ-Sco is almost certainly a single star.

5.4 Age Estimation

The goal is to produce a method for determining the age and masses of the stars in a binary system of known orbit from the orbital parameters and measured magnitudes in a number of filters, as well as a contrast ratio in one or more filters. We phrase the problem in terms of Bayes' Theorem:

$$P(\Phi|D) \propto P(\Phi)P(D|\Phi), \tag{5.6}$$

where Φ represents a model and D represents the data. The model Φ consists of an age, model parallax (π_m), primary and secondary masses (M_p and M_s), a reddening parameter ($E(B-V)$), and a set of isochrones, which map mass, reddening and age to magnitudes in different filters, T_{eff} and $\log{(g)}$, which can be compared to the data.

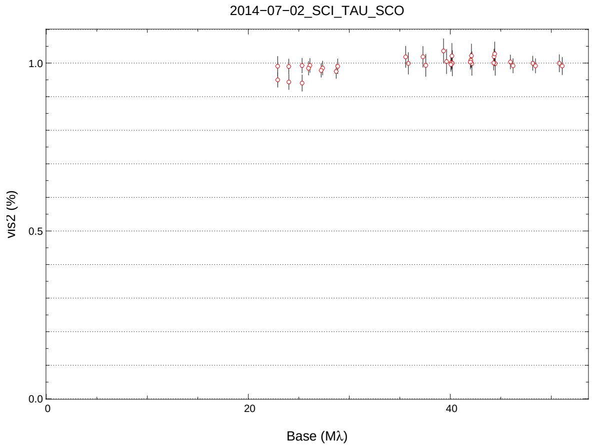

(a) Squared Visibility

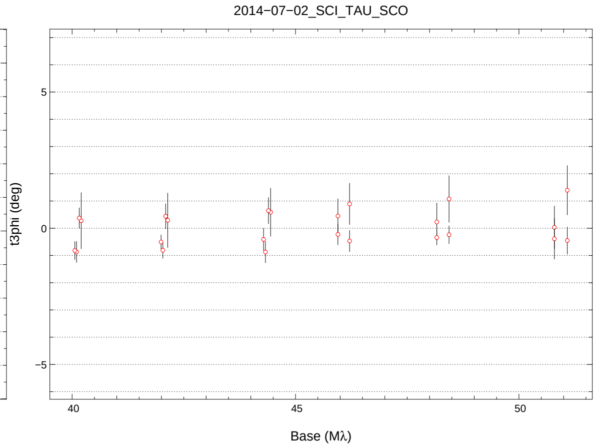

(b) Closure-Phase

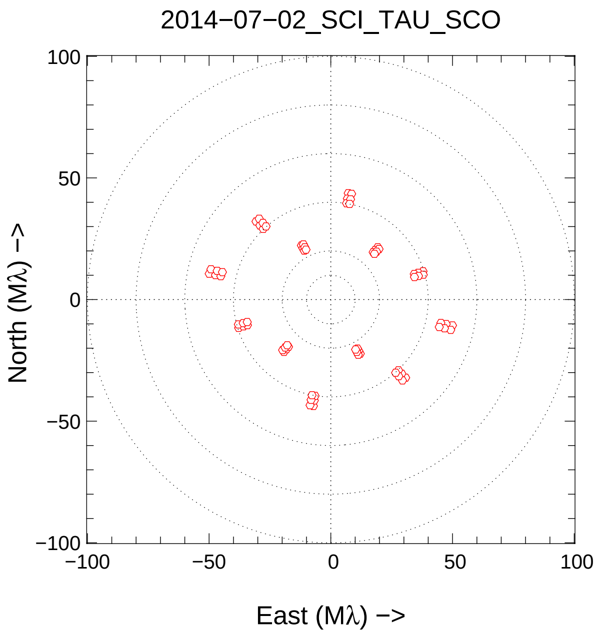

(c) UV-Coverage

Figure 5.8: Calibrated PIONIER data for τ-Sco from 03/07/2014. Both the squared visibility and closure phase are consistent with an unresolved object, indicating that τ-Sco is very likely to be a single star.

The data, D, consist of an association parallax in the absence of a directly measured distance (6.9 ± 1.7 mas, taken from Rizzuto et al. (2011)), the total mass observable ($M_T \pi^3$) calculated from the orbital period and semi-major axis, the magnitude difference in one or more filters (Δm_i), taken from our AO aperture masking observations, and a set of combined magnitudes in available catalog filters $\{m_{\star,i}\}$, including *APASS*

BVgri filters, 2MASS J,H and K, as well as combined and differential photometry in a number of HST WFC3 filters.

Firstly, the model is expressed in terms of the more directly comparable parameters such as magnitude difference and combined magnitude using marginalisation:

$$P(D|\Phi) = P(D|\phi)P(\phi|\Phi), \tag{5.7}$$

where $\Phi = \{\mathrm{Age}, \mathrm{ß_m}, \mathrm{M_p}, \mathrm{M_s}, \mathrm{m_{p,i}}, \mathrm{m_{s,i}}\}$, $\phi = \{\pi_m, m_{s+p,i}, \Delta m_i, (M_p + M_s)\pi_m^3\}$, and Δm_i is the magnitude difference between secondary and primary in filter i for the given primary and secondary masses, reddened according to the Savage and Mathis (1979) extinction law and the model reddening parameter. $m_{s+p,i}$ is the combined magnitude in filter i of the primary and secondary for the given masses and at the given parallax and also reddened as above.

Note that this transformation is simple because the new parameters are directly given by the original model and so $P(\phi|\Phi) = 1$, leaving the following:

$$P(\phi|D) = \frac{P(D|\phi)P(\Phi)}{P(D)}. \tag{5.8}$$

For the prior probability distribution $P(\Phi)$, we have chosen a uniform distribution, the most ignorant prior, meaning that all values of the model parameters are initially treated as being equally likely. For each set of model parameters, we then calculate $P(D|\phi)$, which takes the following form when separated into individual variables:

$$\begin{gathered} P(D|\phi) = P(\pi_\star|\pi_m)P(M_t\pi^3|(M_{p+s})\pi_m^3) \\ \textstyle\prod_i P(m_{\star,i}|m_{s+p,i}) \prod_j P(\Delta m_{\star,j}|\Delta m_j), \end{gathered} \tag{5.9}$$

where i and j indicate multiplication over all available magnitude filters. The probabilities in the above equations are modeled as normal distributions, with standard deviationd given by the uncertainties in the data:

$$\begin{aligned} P(\pi_\star|\pi_m) &\propto \exp -\tfrac{(\pi_\star - \pi_m)^2}{2\sigma_{\pi_\star}}, \\ P(M_t\pi^3|(M_{p+s})\pi_m^3) &\propto \exp -\tfrac{(M_t\pi^3 - (M_p+M_s)\pi_m^3)^2}{2\sigma^2_{M_t\pi^3}}, \\ P(m_{\star,i}|m_{s+p,i}) &\propto \exp -\tfrac{(m_{\star,i} - m_{s+p,i})^2}{2\sigma^2_{m_{\star,i}}}, \\ P(\Delta m_{\star,j}|\Delta m_j) &\propto \exp -\tfrac{(\Delta m_{\star,j} - \Delta m_j)^2}{2\sigma^2_{\Delta m_{\star,j}}}, \end{aligned} \tag{5.10}$$

where we have omitted the usual normalisation factors for the purpose of brevity. We then calculate the probability of a grid of model parameter sets using equations (5.9) and (5.10) to determine the most likely value of age, component masses and parallax. This was done with age ranging from $1 - 25$ Myr in steps of 1 Myr, and primary and secondary mass ranging from a minimum of $0.5\mathrm{M}_\odot$ to 2 Msun in steps of $0.02\mathrm{M}_\odot$. The model parallax was varied from $2 - 15$ mas in steps of 0.1 mas, and the reddening parameter $E(B - V)$ was varied from $0 - 1$ in steps of 0.05 magnitudes. Once a fit was found, we decreased the step size and sampling range to fully sample the probability distribution. We also added in quadrature an error of 0.05 magnitudes to all non-simultaneous photometric measurements to account for the average variability of PMS dwarfs (Herbst et al., 2007)

To reduce the dependence of the results of our age estimation on the characteristics of any one particular set of model isochrones, or at least to illuminate the model dependence, we use both the Padova (Girardi et al., 2002) and the Dartmouth PMS models (Dotter et al., 2008) to determine the age of the binary systems in our Upper Scorpius sample. The photometry available to us for fitting varies between objects; for the most part, B,V, g, r, and i magnitudes from the APASS survey, and 2MASS near-IR magnitudes are available for most of the target systems. ROXs47A is a hierarchical triple system (Barsony et al., 2003), of which we are examining the inner dynamical system. The third component of the system, which is of comparable brightness to the primary, is at a separation of 0.79", which means that the 2MASS and APASS photometry are contaminated and are unusable. Table 5.6 tabulates all publicly available photometry for the stars in our sample. For completeness we include ROXs 47A in the table, though we do not use this photometry in the fitting procedure described below. As mentioned above, we also incorporated our HST WFC3 wide band photometry and differential photometry obtained in 2012. We excluded the filters F225W, F275W, and F336W, because this wavelength range is highly sensitive to the activity of the PMS star in question, and so cannot be reliably fit using the models.

5.4.1 Estimated Stellar Properties

Computation of the posterior probability for our Bayesian models yields a five dimensional space of probabilities, one dimension for each model parameter, which can be reduced to lower dimensions by marginalising over uncorrelated model parameters. We found none of our model parameters were strongly correlated, though the reddening parameter showing some correlation with the other parameters for some of the stars in our sample. This produced a possibility of multiple solutions with different but comparable probabilities, which can then be evaluated individually by inspection.

Name	J	H	K	B	V	g	r	i
RXJ1550.0-2312	9.885±0.024	9.215±0.023	8.930±0.023	15.613±0.479	14.065±0.054	14.760±0.337	13.342±0.196	12.059±0.102
RXJ1601.9-2008	8.350±0.020	7.808±0.026	7.672±0.020	11.333±0.043	10.380±0.030	10.985±0.187	10.086±0.004	9.637±0.011
USco J160517.9-202420	10.154±0.022	9.349±0.024	9.143±0.019	15.858±0.052	14.224±0.035	15.059±0.042	13.497±0.036	12.400±0.140
GSC6209-735	9.158±0.030	8.603±0.042	8.426±0.020	12.514±0.058	11.403±0.049	11.917±0.033	11.012±0.053	10.626±0.095
GSC6794-156	7.779±0.027	7.280±0.027	7.084±0.018	10.673±0.015	9.775±0.085	10.321±0.150	9.499±0.201	8.980±0.144
ROXs47A	9.245±0.024	8.351±0.031	7.929±0.061	15.381±0.098	13.611±0.095	14.510±0.119	12.835±0.092	11.615±0.051
ScoPMS017	9.932±0.024	9.235±0.026	8.992±0.021	15.571±0.366	13.833±0.095	...	...	12.058±0.086

Table 5.6: Available photometry of the binary systems observed. The IR JHK magnitudes are taken from 2MASS and the BVgri magnitudes are taken from the latest APASS data release.

We produce one-dimensional probability densities for the parameters of our model, and then determined the intervals which contain the most likely values of each parameter. Figure 5.9 displays the probability of each model parameter for the star USco J160517.9-202420.

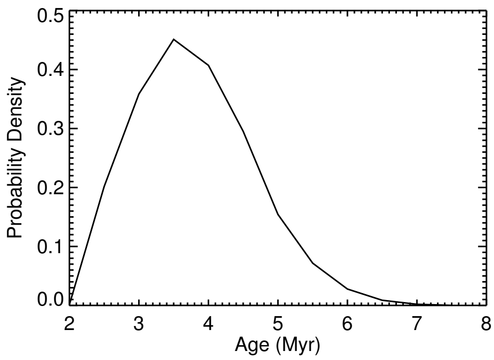

(a) Age

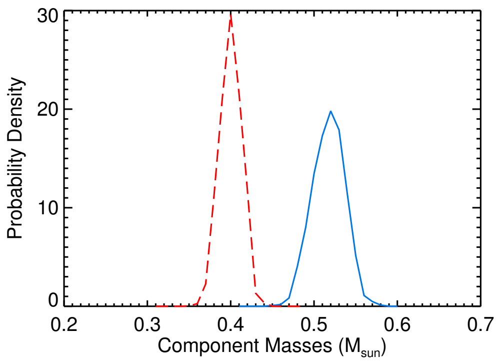

(b) Component Masses

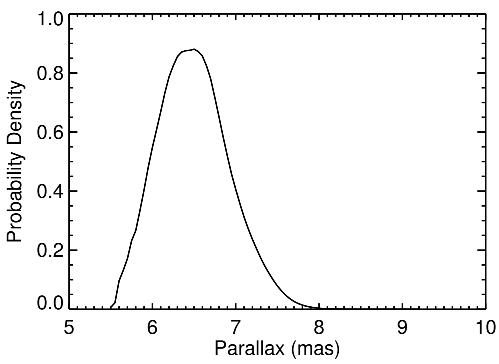

(c) Parallax

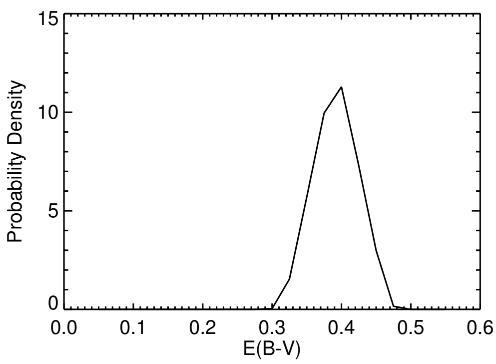

(d) $E(B-V)$

Figure 5.9: The probability of each model parameter for the star USco J160517.9-202420. Note that the two peaks in (b) are the primary (blue) and secondary (red) mass, which are placed on a single figure for ease of viewing, but are treated separately in the analysis.

Given these output distributions, we then calculate 1-σ Bayesian "credible" intervals for each parameter, which can be found in Table 5.7. We also provide the corresponding estimated model photometry for the binary components in Tables 5.8 and 5.9 for the Padova and Dartmouth isochrones respectively.

Name		Age (Myr)	M_p ($M_\odot$)	M_s ($M_\odot$)	π (mas)	$E(B-V)$ (mag)	χ^2_r
GSC6209-735	P	$17.0^{+3.2}_{-3.0}$	1.17±0.06	0.25±0.02	7.9±0.5	0.41±0.06	5.0
	D	$19.7^{+5.0}_{-5.7}$	1.17±0.09	0.32±0.04	7.5±1.0	0.50±0.07	7.4
GSC6794-156	P	$9.9^{+1.2}_{-0.8}$	1.52±0.04	1.42±0.03	7.3±0.1	0.38±0.03	12.4
	D	$11.1^{+0.8}_{-0.5}$	1.45±0.01	1.36±0.01	7.4±0.1	0.39±0.02	15.0
USco J1605...	P	$3.8^{+0.8}_{-1.0}$	0.52±0.02	0.40±0.01	6.5±0.4	0.39±0.03	2.2
	D	$6.0^{+0.9}_{-1.1}$	0.59±0.03	0.45±0.02	6.9±0.3	0.28±0.03	3.6
ScoPMS 17	P	$5.3^{+0.6}_{-0.5}$	0.47±0.01	0.29±0.01	8.6±0.2	0.29±0.02	4.1
	D	$6.3^{+0.6}_{-0.6}$	0.52±0.02	0.31±0.01	8.4±0.2	0.16±0.02	8.5
RXJ1601.9-2008	P	$10.2^{+1.7}_{-1.8}$	1.51±0.06	0.73±0.07	6.8±0.2	0.40±0.06	6.2
	D	$11.2^{+1.1}_{-0.8}$	1.45±0.05	0.78±0.05	6.7±0.2	0.43±0.03	7.3
RXJ1550.0-2312	P	$10.8^{+0.9}_{-0.9}$	0.39±0.02	0.23±0.01	12.8±0.4	0.38±0.04	2.0
	D	$12.9^{+1.0}_{-1.1}$	0.47±0.04	0.27±0.02	12.2±0.4	0.24±0.03	2.7
ROXs 47A	P	$2.8^{+0.3}_{-0.3}$	0.58±0.01	0.52±0.01	7.8±0.1	0.62±0.02	11.0
	D	$3.5^{+0.3}_{-0.4}$	0.61±0.02	0.55±0.02	7.6±0.1	0.45±0.02	13.2

Table 5.7: The estimated stellar parameters for the stars in our sample. The models Padova (P) and Dartmouth (D) refer to the Girardi et al. (2002) and Dotter et al. (2008) model grids respectively. The final column lists the model best fit reduced χ^2 value.

USco J160517.9-202420

We find that the best fit model parameters for USco J160517.9-202420 indicate that it is a young binary system of age ~5 Myr, with the three model fits producing age and parallax estimates that agree within the one-sigma uncertainties. There is some difference in the best fit masses and extinction parameter between the models: The Padova model produces primary and secondary masses which are significantly smaller than the corresponding Dartmouth model fits. Similarly, the Padova fits yield a larger extinction to the system. The two solutions agree within $1.5-2$ sigma, though the Padova models fit the data more closely. The study in which this star was identified as a Sco-Cen member estimates $E(B-V) = 0.3$ and estimation using spectral type and the $J-K$ color yields $E(B-V) \sim 0.3$ using the intrinsic color tables of Bessell and Brett (1988). Both these estimations are consistent with our model fits, within a few tenths of a magnitude in $E(B-V)$. Forcing a smaller value of $E(B-V) < 0.3$ for the extinction parameter, our fitting procedure produces a younger, but consistent, age of 3.5±0.7 Myr, and a smaller primary mass of 0.44±0.01, though the overall model fit is significantly poorer in this case.

GSC6794-156

Both model fits produce a system age of ∼10 Myr for GSC 6794-156, which is consistent with the recent Pecaut et al. (2012) age estimation for Upper Scorpius. In the other four parameters the Padova and Dartmouth models agree generally, however, for the Dartmouth models, we see some degeneracy in the component masses. We quote the most probable solution in Table 5.7. Both the Padova and Dartmouth models estimate a system parallax of 7.3±0.2, and most likely reddening parameter of $E(B-V) =$ 0.4 mag. Given both the ΔJ and ΔK values from the Keck NIRC2 aperture masking (see Table 5.2), we can estimate the expected extinction for this system using standard tables of template photometry for young systems, with some uncertainty produced by the unclear spectral-type of the primary. The tables of Bessell and Brett (1988) give an intrinsic J-K color of of 0.43 mag for the approximately G6 primary of system this system. The observed color, corrected for the presence of the companion using the aperture masking contrasts is 0.617 mag, which then yields a value of $E(B-V) \sim 0.4$ for the system. Similar estimation using the intrinsic colors for young stars from Pecaut and Mamajek (2013) produces a value of $E(B-V) \sim 0.2-0.4$ mag. Both of these values are consistent with our determination for the system.

RXJ1550.0-2312

From the original orbital solution for RXJ1550.0-2312, there was clear evidence that the system was significantly closer than the median Upper-Scorpius parallax of ∼7.5 (See Table 5.3). Upon applying the Bayesian fitting method described above, we found a peak in the system parallax PDF beyond 10 mas, and so we removed the input prior system parallax of 7.5±1.6 mas and refit the data for both models. We find ages and extinctions for the models that agree within 1.5-sigma, with an expected system age of 12.6±0.7 Myr, which is consistent with the latest 11 Myr age of Upper Scorpius. The fitted component masses and system parallax also agree across the models. Our fitting estimates the reddening parameter $E(B-V)$ to be 0.38±0.04 mag from the Padova model fit and 0.24±0.03 mag from the Dartmouth models. The estimated parallax for RXJ1550.0-2312 is quite large compared to the other objects in our sample, and places it in the foreground of Upper-Scorpius at $\sim$ 12 mas parallax or $\sim$ 85 pc. This distance is more consistent with membership of the neighbouring, older Upper-Centaurus-Lupus (UCL) subgroup. This is consistent with the age estimation and the fact that RXJ1550.0-2312 is near the border region between Upper-Scorpius and UCL, we suggest that this object may be a member of UCL.

RXJ1601.9-2008

At the time of our HST observation of this object, the separation of the components on the sky was only ~17 mas, which combined with the large brightness contrast between the components of this system made it impossible to produce a meaningful differential magnitude fit for this object from the HST data. Hence we employed only the IR magnitude difference from the NIRC2 AO aperture masking observations, and the unresolved system HST and catalog magnitudes to fit the stellar parameters of this system. The model ages and extinctions for the system agree between the three models to within 1-sigma. Estimation of the extinction from the spectral type and color tables gives $E(B-V) = 0.2 - 0.4$ which agrees with the values determined from our fitting procedure.

GSC6209-735

The extreme contrast between the primary and the secondary (ΔH=3.05 mag), combined with the small angular separation of the primary and the secondary removed the possibility of a reliable differential photometric fit being produced from the HST data. As such, the only magnitude difference available was the H-band Keck masking measurement. This orbit is also the least well-constrained in our sample and hence the parameter fits for this system are highly unconstrained and show a large range of possible system ages and multiple component mass and parallax solutions. Despite this, it is possible to say that this system is most likely >10 Myr according to both all three models, with possible age solution at $\sim 15 - 20$ Myr and beyond 30 Myr. The possible age solutions for this binary system are significantly older than the other PMS binary systems in our sample, and places GSC6209-735 as a potential member of the older Upper Centaurus Lupus subgroup of Sco-Cen. However, unlike RXJ1550.0-2312, GSC6209-735 has an estimated parallax consistent with both Upper Scorpius and UCL, and is located near the centre of Upper Scorpius. With further astrometry, and differential photometry in further filters it will be possible to constrain the stellar parameters for this system.

ScoPMS 17

The results for ScoPMS 17 indicate that it is definitely a young star with age < 8 Myr. Both models produce an age consistent with ~6 Myr, with primary and secondary masses of $\sim 0.5\,M_\odot$ and $\sim 0.3\,M_\odot$ respectively. As with some of the other young stars in our sample, the models produce slightly different solutions for the extinction parameters $E(B-V)$, with the Dartmouth models indicating less extinction generally. Estimation from the colour tables gives a value of $E(B-V) \sim 0.2$, which is more consistent with the Dartmouth reddening solution, however the Padova model produces a significantly better fit to the data.

ROXs47A

We expected ROXs 47A to be the most difficult M-type system for the models to accurately reproduce, given the very young age and disk presence. The Bayesian fitting procedure produced a very young and highly reddened fit for ROXs47A, with an estimated age < 4 Myr for the Padova and Dartmouth model. The estimated parallaxes for both the Padova and Dartmouth models (7.8 mas and 7.7 mas respectively) are consistent with ROXs47A being a members of the very young ρ-Ophiuchus star forming region, which is located at $(\alpha, \delta) = (16^h28^m, -24^\circ 33'')$ and a distance of ~130 pc, i.e.,

Table 5.8: Best fit model photometry for the primary and secondary components of each modelled binary system, taken from the results of our Bayesian fitting procedure, including estimated extinction, as described above for the Padova isochrones.

	$T_{eff}(K)$	B	V	R	J	H	K	g	r	i	F225W	F390W	F438W	F475W	F555W	F625W	F775W	F850LP
									GSC6794-156									
P	5886	11.34	10.32	9.64	8.35	7.93	7.81	10.85	10.01	9.66	15.66	11.63	11.38	10.89	10.42	9.82	9.24	8.88
S	5519	12.15	11.00	10.27	8.85	8.36	8.23	11.61	10.65	10.25	17.23	12.54	12.20	11.64	11.12	10.46	9.83	9.43
									GSC6209-735									
P	5447	12.65	11.45	10.70	9.24	8.73	8.59	12.09	11.08	10.67	17.94	13.06	12.69	12.11	11.57	10.90	10.25	9.83
S	3592	18.47	16.63	15.30	12.42	11.74	11.43	17.74	15.94	14.75	26.19	19.28	18.55	17.68	16.82	15.72	14.24	13.38
									RXJ1550.0-2312									
P	3823	16.13	14.43	13.14	10.35	9.61	9.35	15.47	13.76	12.64	24.14	16.85	16.17	15.42	14.61	13.53	12.15	11.31
S	3590	17.25	15.40	14.05	11.14	10.45	10.13	16.52	14.70	13.49	25.06	18.08	17.34	16.46	15.59	14.48	12.98	12.11
									USco J160517.9-202420									
P	3857	16.34	14.68	13.44	10.75	9.95	9.72	15.69	14.03	12.98	24.28	17.06	16.38	15.64	14.86	13.81	12.49	11.69
S	3684	17.05	15.32	14.00	11.09	10.38	10.10	16.37	14.66	13.43	24.79	17.79	17.11	16.32	15.51	14.43	12.93	12.05
									RXJ1601.9-2008									
P	5902	11.44	10.42	9.74	8.45	8.03	7.91	10.95	10.11	9.76	15.74	11.72	11.47	10.99	10.52	9.92	9.34	8.98
S	4071	15.96	14.32	13.18	10.92	10.07	9.88	15.30	13.67	12.91	24.05	16.72	15.99	15.26	14.47	13.46	12.46	11.80
									ScoPMS017									
P	3791	15.91	14.34	13.13	10.43	9.71	9.49	15.30	13.73	12.62	23.33	16.56	15.94	15.25	14.51	13.50	12.12	11.32
S	3551	16.85	15.09	13.84	11.13	10.47	10.17	16.15	14.45	13.32	24.07	17.66	16.94	16.09	15.27	14.23	12.81	12.02
									ROXs47A									
P	3637	16.23	14.45	13.13	10.23	9.52	9.23	15.53	13.78	12.57	23.93	17.00	16.30	15.47	14.64	13.56	12.06	11.19
S	3536	16.55	14.69	13.36	10.48	9.80	9.48	15.81	14.00	12.80	24.18	17.41	16.65	15.75	14.88	13.78	12.29	11.44

Table 5.9: Best fit model photometry for the primary and secondary components of each modelled binary system, taken from the results of our Bayesian fitting procedure, including estimated extinction, as described above for the Dartmouth isochrones.

	$T_{eff}(K)$	B	V	R	J	H	K	g	r	i	F475W	F555W	F625W	F775W	F850LP
							GSC6794-156								
P	5972	11.35	10.29	9.59	8.21	7.81	7.68	10.80	9.92	9.53	10.97	10.39	9.78	9.19	8.78
S	5574	12.24	11.02	10.26	8.75	8.28	8.14	11.62	10.60	10.17	11.78	11.13	10.46	9.82	9.37
							GSC6209-735								
P	5760	12.45	11.30	10.58	9.14	8.70	8.56	11.87	10.91	10.50	12.03	11.41	10.77	10.15	9.73
S	3354	19.07	17.22	15.84	12.41	11.73	11.39	18.30	16.51	15.04	18.40	17.38	16.31	14.54	13.55
							RXJ1550.0-2312								
P	3521	15.98	14.41	13.26	10.32	9.63	9.36	15.32	13.82	12.58	15.42	14.53	13.62	12.10	11.28
S	3298	17.14	15.53	14.28	11.07	10.44	10.15	16.47	14.91	13.51	16.57	15.65	14.70	13.01	12.10
							USco J160517.9-202420								
P	3709	16.24	14.64	13.51	10.74	9.96	9.72	15.55	14.04	12.91	15.66	14.75	13.85	12.45	11.69
S	3527	16.93	15.35	14.17	11.11	10.38	10.11	16.26	14.76	13.45	16.36	15.48	14.56	12.96	12.11
							RXJ1601.9-2008								
P	4959	11.75	10.60	9.95	8.62	8.10	8.01	11.16	10.21	9.89	11.31	10.66	10.06	9.53	9.18
S	3504	16.40	14.95	13.84	10.85	10.14	9.90	15.78	14.42	13.12	15.88	15.06	14.22	12.63	11.81
							ScoPMS017								
P	3633	15.66	14.18	13.11	10.39	9.67	9.44	15.02	13.63	12.49	15.12	14.28	13.44	12.02	11.29
S	3370	16.79	15.31	14.15	11.07	10.43	10.17	16.17	14.75	13.40	16.27	15.42	14.54	12.91	12.05
							ROXs47A								
P	3737	16.01	14.31	13.12	10.24	9.42	9.16	15.28	13.67	12.50	15.39	14.43	13.48	12.04	11.25
S	3623	16.42	14.75	13.52	10.44	9.64	9.37	15.71	14.12	12.81	15.81	14.88	13.92	12.33	11.48

slightly closer than the Upper-Scorpius subgroup. This parallax is inconsistent with the distance to Ophiuchus, and the estimated age of 5.2±0.5 Myr is significantly older than the mean age of 2.1 Myr of the Ophiuchus PMS stars (McClure et al., 2010). All three fits produce extinction values consistent with extinction value of McClure et al. (2010) (E(B-V)=0.52 mag).

5.5 The Binary-Star Age of Upper Scorpius

A number of the members we have explored here appear to be younger than 10 Myr, and there appears to be a population of Upper-Scorpius members of age $>$ 10 Myr. The Pecaut et al. (2012) study, which used photometry for B, A, F and G-type stars, estimated the age of the Upper Scorpius subgroup to be 11±2 Myr, which is significantly different to the age determinations for the younger stars in our work, and the age estimations in previous work (Preibisch et al., 2002, de Geus, 1992). There is some indication that the PMS models can produce large age spreads for accreting stars, with observed luminosities above the ∼10 Myr isochrone being unreliable (Baraffe et al., 2009). However, there is no adequate explanation for high-luminosity non-accreting stars, the existence of which provide strong evidence for a younger population in Upper-Scorpius.

There are some key differences between the approach we have taken, and that of the Pecaut et al. (2012) study, the most important of which is that we are using photometry combined with a dynamical mass observable derived from orbital monitoring. Pecaut et al. (2012) estimate the main sequence turn-off age for the B-type stars to be 10±2 Myr. This was estimated by fitting isochrones to photometry of 6 stars using a number of models, including both rotation and non-rotation, to estimate an age. However it is difficult to fit a mean sequence turn-off age to a small number of objects with different distances and differential reddening. If a mean main-sequence turn off age is calculated by weighing the values of individual stars by their membership probability from Rizzuto et al. (2011), a much smaller value of 6.8±2.8 Myr is found, which is in close agreement with previous values. Furthermore, the effective temperature and luminosity of the star δ-Sco, a 0.45 AU binary system with an emission disk, in the Pecaut et al. (2012) study (Figures 10 and 11) does not reflect its spectral type (B0.2V), which would place it much closer to the 2-5 Myr isochrone. Furthermore, the effective temperature of this object has previously been more directly measured to be 31460±1970 K with the Narrabri Intensity Interferometer (Code et al., 1976), which is consistent with the spectral type and younger age. The difference between the Pecaut et al. (2012) value and these other measures is most likely due to the high rotation rate of the δ-Sco primary, which makes the colour-colour relations used to compute the effective temperature and luminosity unreliable (Tango et al., 2009). Additionally, the star π-Sco, which was also used by Pecaut et al. (2012), was determined to be an unlikely member of Upper-Scorpius by Rizzuto et al. (2011).

The B-type star τ-Sco has a well-determined temperature of 32000±1000 K and luminosity of $\log \mathrm{L}/\mathrm{L}_\odot = 4.47 \pm 0.13$ measured from the He and H absorption lines, and has a very slow rotation period of 43 days (Simón-Díaz et al., 2006, Strassmeier, 2009). This means that τ-Sco is certainly very young, with an age between 2 and 5 Myr. For non-rotating stellar models the most massive 15 Myr stars should be approximately 12 $\mathrm{M}_\odot$ (Ekström et al., 2012). The existence of τ-Sco and ω-Sco, a similarly massive Upper-Scorpius member, strongly argues for some star formation at 5 Myr.

The main-sequence A-type, and G-type PMS member age estimates of Pecaut et al. (2012) are 9±2 Myr and 10±3 Myr respectively, which broadly agree with our Bayesian age estimate. This leaves only the F-type members, which Pecaut et al. (2012) estimate to be 13±1 Myr, which is in clear disagreement to our age measurements of individual Upper Scorpius members. In the Pecaut et al. (2012) study, the Upper-Scorpius space velocity used to determine the kinematic association distances of the F-type stars is taken from Chen et al. (2011); this is slightly different from the Rizzuto et al. (2011) values, which are faster by approximately 1 kms^{-1} in U, the most significant direction for Upper-Scorpius. This means that for any given proper-motion, an F-type star would appear further away when compared to the motion of the association, and will have a luminosity increased by approximately 10%, or 0.05 dex. While this difference is in the correct direction, it is not significant enough to account for the above age discrepancy.

Evidence for Young Upper-Scorpius
Height above main sequence of some members
The existence of τ-Sco
The existence of ω-Sco
The existence of δ-Sco
High-luminosity, non-accreting K and M-type stars
Evidence for Old Upper-Scorpius
F-type member population age
Evolved B-type stars in Upper-Scorpius region

Table 5.10: Summarised evidence for the existence of two Upper-Scorpius populations.

There is also measured blurring in the Hipparcos Sco-Cen substructure on the order of $\sim 5°$, meaning some older UCL stars could be included in this sample (Rizzuto et al., 2011).

An alternate hypothesis is that there are two populations of stars in the Upper-Scorpius subgroup: one of age $\sim$5 Myr, including τ-Sco and other massive B-type stars, and a second population of age $\sim$15 Myr. In these two populations, F-type stars will occupy significantly different mass ranges. From the Dartmouth isochrones (Dotter et al., 2008), we find that the 5 Myr population, with $3.78 < \log T_{eft} < 3.85$ spans masses ranging from 1.87 to 2.02 $M_\odot$. Similary, for the 15 Myr population with identical temperature range, we have mass ranging from 1.23 to 1.54 $M_\odot$. Taking into consideration a reasonable IMF, such as the Kroupa IMF with exponent -2.3, we would expect a factor of 20 times more stars from the older population compared to the younger population, and hence an older age estimation from a combined sample within the specific spectral-type range.

Furthermore, we note that for a B-type population, for B3 and later the population is essentially unbiased. For the M-type stars, which are a magnitude limited sample, there is a significant bias against the older population due to the substantial luminosity difference between a 5 Myr and a 15 Myr population in the M-type regime. For the K and M-type stars, we can compare the R-band magnitude of the isochrones and assume an RMS 10% relative distance dispersion. Cutting at $3-\sigma$ above the 5 Myr isochrone gives a faint limit of 6.54 magnitudes in R, which is 0.7 magnitudes brighter than the 15 Myr population. This is consistent with the current data for Upper-Scorpius, for which the isochronal age from the magnitude limited, known M-type stars is ~5 Myr (Preibisch et al., 2002).

Combining the three spectral type ranges, a population model for Upper-Scorpius with approximately one third of the population of age ~5 Myr, and the remaining two thirds of age ~15 Myr, is consistent with the current data for Upper-Scorpius members.

A possible star formation scenario for such a population implies that the majority of Upper-Scorpius formed as part of the greater Sco-Cen association through sequentially triggered star formation in the original molecular cloud, and has an age of ~11 Myr, and proper motion in R.A. of ~ -13 mas/yr. A separate cloud, moving with a slower proper motion of ~-9 mas/yr, would then undergo star formation approximately 5 Myr ago, triggered by the known supernova explosion in UCL (de Geus, 1992). This difference in motion of the clouds means the cloud which formed the young population of Upper-Scorpius, which we will now refer to as the "τ-Scorpii" association, corresponds to ~5° of positional difference on the sky over 5 Myr, or approximately 10 pc. A 28 $M_\odot$ (or 39 $M_\odot$ for rotating models) star will end its life as a supernova at 6.3 Myr (Ekström et al., 2012) meaning that this is the minimum required time difference between the formation of one association and a second, supernova-triggered association. Our estimates here indicate that on the order of 10 Myr, and 10 pc separated the Sco-Cen association and the τ-Scorpii molecular clouds, this is both sufficient time for a supernova to occur, and sufficient distance for safety of the τ-Sco cloud from disruptive Sco-Cen B-type star cloud dispersal. Further triggered star formation then produced the even younger ρ-Oph star forming region, which is actively undergoing star formation.

In this scenario, the two Upper-Scorpius populations would be both spatially overlapping, and kinematically overlapping due to the characteristic velocity dispersion of the association. With higher precision parallaxes and proper motion from the Gaia mission data, the two Upper-Scorpius populations may be identifiable.

6

Conclusions and Future Work

Conclusions

In the first section of this thesis, we have analysed the available preliminary WISE photometry for the B, A and F-type Sco-Cen stars of the Rizzuto et al. (2011) membership list and detected 134 22 μm excesses above the expected photosphere emission. We have used Sco-Cen membership probabilities to extrapolate an excess fraction for certain members, and observe that there is no clear increase in disk fraction between the young US subgroup and the older UCL and LCC subgroups. However, we report a significantly larger disk fraction than previously observed in the youngest subgroup US. These results agree with those of previous studies (Carpenter et al., 2009). Importantly we find that the excess fraction is significantly lower for the B-type stars in our sample compared to A and F-type association members, which is contrary to the trend seen by Carpenter et al. (2009). One possible explanation relates to multiplicity.

B-type stars have a significantly higher multiplicity fraction compared to later type stars (Kouwenhoven et al., 2005). The presence of a companion can potentially truncate the inner regions of the debris disk through resonances (Artymowicz and Lubow, 1994), producing a smaller disk fraction. This has been observed in a recent study of binaries in Taurus-Auriga, particularly those with close (<40AU) companions (Kraus et al., 2011a). Among the highest probability members in our sample (>90%) there are six close (<100 AU) multiple systems without disk detections and one close multiple system with a detected excess. A closer, more comprehensive, comparison between disk presence and multiplicity information for the Sco-Cen B-type stars may shed light on this issue.

In the second section of this thesis, we developed a new kinematic selection method for identifying potential Sco-Cen member stars, which utilised a Bayesian algorithm and various all-sky astrometric and photometric data catalogs. The results of this selection have been used as a sample for spectroscopic confirmation of youth, and hence membership in Sco-Cen. Over eight nights, we observed 406 potential Upper-Scorpius stars with the Wide Field Spectrograph (WiFeS) on the ANU 2.3 m telescope, an integral field spectrograph, identifying 232 as new members. Using the spatial information, we simultaneously searched for wide orbit (∼2"), massive (∼ 10 M_Jup) gas giant planetary companions to these potential members. We identify four candidate accreting, wide gas-giant planetary companions to the new Upper-Scorpius members US-10798, US-07477, US-05179, and US-02492, which can be confirmed with adaptive optics follow-up. Additionally, we observed the prototype Sco-Cen planet host of this type, GSC-6214-0210, on four separate nights in mid-2013 to mid-2014. For this object, we measured a significant decrease in H-α equivalent width from -1.5 Å to $<$ 0.65 Å between the original observations by Preibisch et al. (1998), and our observations. Furthermore, we do not detect the presence of the companion in H-α in any of our observations. Comparison with the SNIFS spectrum of the primary indicates that our measured H-α emission is associated with the primary. The lack of a detection of the companion, combined with the reduction in H-α emission suggests that the planetary companion GSC-6214-0210b has stopped accreting from its circumplanetary disk.

In the third section of the thesis we report the results of an interferometric multiplicity survey of B-type members of Sco-Cen. This consisted of 58 stars in the Sco-Cen region of space with colour $B-V < -0.1$ and hence encompasses the most massive stars in the association. We used the Sydney University Stellar Interferometer to observe these objects and detected 23 binary companions, 13 of which were new detections.

We used Bayesian statistics and all available multiplicity information in the literature to determine the most likely parameters of the multiplicity population of our sample, the results of which agree with previous, less complete analyses. We find that the multiplicity distribution of the stars in our sample to be best described by a log-normal distribution in separation, with a mean of $0.95^{+0.25}_{-0.15}$ and a standard deviation of $1.35^{+0.35}_{-0.25}$, while the mass-ratio follows a power law distribution with exponent $\gamma = -0.46 \pm 0.13$. In addition, the frequency of companions was determined to be $F = 1.25^{+0.27}_{-0.22}$. The multiplicity literature, and our survey results, both point to a very large multiple fraction among high-mass stars in young associations, with only $\sim 19 - 27\,\%$ being single stars according to our statistics. This broadly agrees with the idea that companion formation and companion related mechanisms are the primary angular momentum redistribution method among high-mass stars (Larson, 2010). However, the data suggests a significant number of single stars among our sample, which according to our Bayesian analysis, are unlikely to fall under the umbrella of missed companions outside of the current detection limits.

Given that the role of magnetic fields in angular momentum loss for high-mass stars is most likely less important, e.g., the lack of collimated jets often associated with lower-mass stars (Arce et al., 2007), some mechanism must be present in the star forming environment which creates single stars. This implies that these stars are either part of a very large-scale wide system, were ejected from a multiple system early in their lifetime, or formed as single stars. Models have suggested that disruptive interactions can shape the formation of high-mass stars in dense clusters (Bonnell et al., 2003), but ejection in Sco-Cen is much less likely because OB associations are in general sparse environments. With velocity dispersion on the order of $1°$ per Myr, it is difficult to observationally test ejection hypotheses without GAIA quality astrometry. The large scale behaviour of Sco-Cen is not completely unknown. It has been shown, using lower-mass members in the Preibisch et al. (2002) survey of US, that two degrees is the approximate wide-scale binarity limit in US (Kraus and Hillenbrand, 2008). Assuming that UCL and LCC have similar structures, there is some chance that a small number of the single stars in our sample could be part of a very wide multiple system with one or more other high mass stars. However, this is unlikely to account for all of the potential single stars in our sample. A further possibility is the merger of two lower-mass members of a binary system to form an apparently single, B-type star. While this has been modelled extensively for the case of dense clusters, it is unclear what the frequency of such interactions is in the context of OB associations (Zinnecker and Yorke, 2007, Bonnell et al., 1998).

The final section of this thesis describes the orbit of 7 G to M-type binary members of the Upper-Scorpius subgroup of Sco-Cen. We monitored these binary systems over 5 years with Keck2 adaptive optics and aperture masking, and then fitted an orbit to the data. We have also obtained HST photometry of these binary systems in a series of filter ranging from the UV to 900 nm and applied aperture photometry and PSF fitting to determine differential photometry for these systems. Using the orbital parameters and the available photometry, we developed a new Bayesian model-fitting procedure, which fits isochrones to the binary system data to determine system age, primary and secondary mass, distance and reddening towards the objects. We find that after the fitting, these binary systems indicate a mean age of 7 ± 2 Myr for the Upper Scorpius subgroup, though there is a spread of ages in the subgroup varying from a few Myr to ages up to >10 Myr. This result differs from both the traditional age of 5 Myr with very little age spread, and the more recent result which suggests Upper-Scorpius is 11 Myr old (Pecaut et al., 2012). We analyse and summarise the available evidence for the age of the Upper-Scorpius subgroup, and present the hypothesis that the evidence is consistent with the existence of two populations, an older population that formed with the greater Sco-Cen association, of age $\sim$15 Myr, and a younger population including the clearly young massive early B-type stars, which formed via supernova-triggered star formation ∼5 Myr ago. We label the younger group the τ-Scorpii association, which, due to the velocity dispersion of Sco-Cen, overlaps the older Sco-Cen population in velocity space.

Future Work

We intend to continue the work outlined in this thesis to build a clearer picture of the group and individual stellar properties of the Sco-Cen association. The intended avenues of study include:

1. A vastly expanded spectroscopic campaign for the K2 region in Upper Scorpius to illuminate the low-mass population of Sco-Cen. This will involve further WiFeS observations of candidate members for $V > 14$, and incorporation of the ongoing HERMES (GALAH) observations, which will cover the K2 region in the $10 < V < 14$ magnitude range.

2. In conjunction with this, we will use the results of the UK-Schmidt telescope FunnelWeb survey using the TAIPAN spectrograph. Data from this survey are planned to be released in 2016 and will include R∼2500 spectra of every star brighter than 12^{th} magnitude in R-band. This will provide radial velocities and and Ca-HK measurements which can be used to distinguish members and non-members.

3. Detailed modelling of the interesting high-mass Sco-Cen stars, including τ-Sco, π-Sco, δ-Sco and σ-Sco, combining interferometry, spectroscopy, and rotation modelling, as described in the Ph.D thesis of Maestro (2014).

4. Adaptive optics follow-up, with aperture masking, of the four candidate accreting gas-giant planetary companions to US-10798, US-07477, US-05179, and US-02492, and the other new members of Upper-Scorpius we have discovered.

A

WISE Data and Excess Detection for the B, A and F-type Sco-Cen Members

Here we provide a summary list of the WISE colours and excess detections for the B, A and F-type stars in our WISE search for circumstellar disks.

Table A.1: The (J-K_s) and WISE colours with errors for our sample. [a] This column indicates the detection of an excess in the three colours, and the final column indicates the subgroup in which the star is found. The superscript [1] following the excess detection label indicates that the particular star was excluded from the excess fraction analysis due to unreliable photometry.

HIP	P	(J-K_s)	W_1-W_2	$\sigma_{W_1-W_2}$	W_1-W_3	$\sigma_{W_1-W_3}$	W_1-W_4	$\sigma_{W_1-W_4}$	Ex[a]	SG
49360	6	-0.039	-0.032	0.035	-0.044	0.035	0.003	0.075	NNN	LCC
50520	62	0.043	0.146	0.055	-0.058	0.051	-0.102	0.057	NNN[1]	LCC

Continued on next page

50612	7	0.019	-0.025	0.034	0.039	0.034	0.399	0.068	NNY	LCC
50667	7	0.055	-0.005	0.033	0.216	0.031	0.870	0.072	NYY	LCC
50847	62	-0.110	0.265	0.058	-0.018	0.053	-0.006	0.058	YNN[1]	LCC
51169	22	-0.056	-0.017	0.032	0.210	0.032	0.813	0.094	NYY	LCC
51203	33	0.115	-0.028	0.033	0.068	0.033	0.482	0.085	NNY	LCC
51507	9	0.028	0.005	0.017	-0.029	0.023	-0.119	0.087	NNN	LCC
51508	6	0.033	-0.046	0.035	-0.040	0.034	0.037	0.075	NNN	LCC
52059	6	-0.054	-0.043	0.038	-0.041	0.036	-0.089	0.076	NNN	LCC
52116	7	0.057	-0.049	0.037	-0.050	0.036	-0.078	0.063	NNN	LCC
52132	13	-0.044	-0.018	0.033	-0.015	0.033	-0.046	0.096	NNN	LCC
52171	8	0.270	0.209	0.021	-0.172	0.025	-0.230	0.127	NNN[1]	LCC
52293	15	-0.011	-0.046	0.039	-0.029	0.039	-0.009	0.066	NNN	LCC
52328	7	-0.050	-0.867	0.015	-1.199	0.020	-0.944	0.063	NNN[1]	LCC
52357	82	0.112	-0.019	0.039	-0.022	0.038	-0.103	0.069	NNN	LCC
52736	25	-0.055	0.240	0.062	-0.053	0.058	0.203	0.062	YNN[1]	LCC
52867	8	0.083	-0.012	0.034	0.150	0.033	1.073	0.067	NNY	LCC
53016	7	0.142	-0.021	0.035	0.006	0.034	-0.009	0.094	NNN	LCC
53524	46	0.117	-0.038	0.040	0.059	0.039	1.210	0.046	NNY	LCC
53913	7	-0.003	0.004	0.033	0.026	0.032	0.094	0.089	NNN	LCC
53992	9	0.253	-0.011	0.033	0.048	0.035	1.052	0.083	NNY	LCC
54168	13	-0.002	-0.038	0.036	-0.037	0.035	-0.072	0.079	NNN[1]	LCC
54176	40	0.227	-0.006	0.034	0.038	0.037	0.006	0.162	NNN	LCC
54767	64	-0.004	0.295	0.057	0.046	0.051	0.042	0.057	YNN[1]	LCC
55003	6	0.082	0.077	0.047	0.021	0.045	-0.014	0.058	NNN[1]	LCC
55188	78	0.025	-0.116	0.025	0.263	0.028	2.523	0.038	NNN[1]	LCC
55205	11	0.194	-0.009	0.033	0.002	0.044	-0.300	0.348	NNN	LCC
55334	58	0.235	0.010	0.035	0.045	0.035	-0.025	0.078	NNN	LCC
55616	15	0.056	-0.033	0.030	0.176	0.030	1.246	0.060	NYY	LCC
55978	18	0.160	-0.024	0.033	-0.012	0.055	0.885	0.160	NNN[1]	LCC
56227	58	0.167	-0.033	0.033	-0.013	0.031	-0.121	0.118	NNN	LCC
56354	84	1.345	1.509	0.068	3.325	0.060	6.046	0.061	NYY	LCC
56379	83	1.007	1.022	0.054	5.163	0.053	7.695	0.054	NNN[1]	LCC
56561	24	0.025	0.821	0.059	0.000	0.061	-0.030	0.065	NNN	LCC
56673	10	0.362	0.375	0.059	0.154	0.053	0.305	0.057	YNN[1]	LCC
56943	6	0.000	-0.108	0.029	0.077	0.044	1.261	0.102	NNN[1]	LCC

Continued on next page

56993	33	-0.004	-0.019	0.036	-0.005	0.034	-0.068	0.104	NNN	LCC
57043	6	0.019	-0.037	0.033	-0.043	0.033	-0.130	0.098	NNN	LCC
57238	26	0.009	-0.079	0.027	-0.031	0.029	0.184	0.171	NNN	LCC
57273	5	0.200	-0.019	0.033	0.012	0.035	0.234	0.202	NNN	LCC
57285	46	0.305	-0.014	0.034	0.008	0.035	0.278	0.087	NNN	LCC
57375	51	0.169	0.014	0.034	0.053	0.034	0.074	0.092	NNN	LCC
57451	23	0.041	-0.018	0.039	0.126	0.038	1.274	0.050	NNN[1]	LCC
57531	7	0.194	-0.011	0.031	0.023	0.032	0.087	0.103	NNN	LCC
57644	21	-0.008	-0.026	0.039	-0.018	0.039	0.099	0.070	NNN	LCC
57669	9	0.123	0.712	0.077	0.600	0.071	1.060	0.072	NYY	LCC
57851	73	-0.060	0.185	0.061	-0.093	0.057	-0.056	0.062	NNN	LCC
57947	50	0.279	0.007	0.037	0.033	0.036	0.029	0.074	NNN	LCC
57950	76	0.191	-0.008	0.034	0.067	0.032	0.644	0.077	NNY	LCC
57953	26	0.268	-0.024	0.030	0.003	0.035	-0.226	0.440	NNN	LCC
58054	34	0.238	-0.034	0.031	0.026	0.033	0.046	0.161	NNN	LCC
58075	47	0.303	-0.074	0.025	-0.011	0.026	0.120	0.130	NNN	LCC
58146	77	0.218	-0.030	0.039	-0.023	0.040	-0.063	0.086	NNN	LCC
58167	87	0.189	-0.019	0.034	0.021	0.034	0.097	0.085	NNN	LCC
58220	88	0.282	0.004	0.035	0.344	0.033	1.188	0.054	NYY	LCC
58326	32	-0.116	-0.089	0.042	-0.008	0.042	1.106	0.052	NNN[1]	LCC
58416	87	0.216	0.028	0.039	0.038	0.038	0.117	0.067	NNN	LCC
58465	88	0.111	0.032	0.043	0.005	0.040	0.032	0.058	NNN	LCC
58528	85	0.284	-0.018	0.035	0.125	0.034	0.696	0.070	NNN[1]	LCC
58670	11	0.261	-0.022	0.032	0.019	0.032	-0.107	0.153	NNN	LCC
58680	48	0.142	-0.040	0.031	-0.019	0.033	-0.412	0.354	NNN	LCC
58720	59	-0.075	0.032	0.046	0.223	0.044	1.506	0.047	NYY	LCC
58760	21	0.326	-0.017	0.032	0.079	0.042	0.136	0.118	NNN	LCC
58859	83	-0.015	-0.014	0.041	-0.040	0.039	-0.030	0.067	NNN	LCC
58884	78	0.020	0.301	0.061	-0.002	0.055	-0.011	0.059	NNN	LCC
58899	84	0.251	-0.001	0.034	0.002	0.034	-0.175	0.106	NNN	LCC
58901	51	0.032	-0.006	0.045	-0.053	0.045	-0.192	0.112	NNN	LCC
59084	23	0.222	-0.043	0.030	-0.051	0.037	-0.794	0.420	NNN	LCC
59173	66	0.254	0.504	0.064	0.007	0.057	0.009	0.068	YNN	LCC
59184	40	0.138	0.304	0.062	-0.031	0.055	-0.008	0.062	YNN	LCC
59281	26	0.102	-0.009	0.037	-0.005	0.037	-0.055	0.073	NNN	LCC

Continued on next page

59282	88	0.084	0.013	0.036	0.189	0.035	0.865	0.052	NYY	LCC
59360	45	0.103	0.050	0.040	0.058	0.039	0.015	0.069	NNN[1]	LCC
59383	6	0.130	-0.032	0.030	-0.017	0.035	-0.088	0.352	NNN	LCC
59397	86	0.047	0.006	0.037	0.202	0.036	1.298	0.046	NYY	LCC
59413	86	0.570	-0.097	0.037	-0.082	0.037	-0.171	0.091	NNN[1]	LCC
59430	30	0.298	-0.020	0.031	0.000	0.032	-0.160	0.166	NNN	LCC
59449	60	-0.217	0.619	0.067	0.013	0.060	-0.015	0.062	NNN	LCC
59481	88	0.196	-0.045	0.034	0.006	0.034	0.012	0.129	NNN	LCC
59502	86	0.027	0.016	0.038	0.459	0.040	1.995	0.057	NYY	LCC
59505	81	0.216	0.019	0.030	0.064	0.030	-0.199	0.162	NNN	LCC
59541	33	0.113	0.001	0.034	0.021	0.034	0.079	0.087	NNN	LCC
59579	13	0.310	-0.021	0.033	0.019	0.033	-0.204	0.217	NNN	LCC
59603	82	0.266	0.016	0.036	0.032	0.035	0.144	0.093	NNN	LCC
59693	74	0.332	-0.004	0.030	0.250	0.033	0.847	0.111	NYY	LCC
59716	64	0.236	-0.029	0.034	0.033	0.034	0.192	0.090	NNN	LCC
59724	59	0.111	-0.017	0.032	0.148	0.033	1.580	0.046	NNY	LCC
59747	75	-0.204	0.546	0.076	-0.069	0.076	-0.207	0.078	NNN	LCC
59781	82	0.317	-0.039	0.034	0.265	0.068	1.215	0.447	NNN[1]	LCC
59897	28	0.015	-0.018	0.030	0.033	0.034	0.021	0.322	NNN	LCC
59898	66	-0.002	0.132	0.047	0.336	0.046	1.751	0.048	NNN[1]	LCC
59960	89	0.263	-0.011	0.039	0.110	0.039	1.991	0.044	NNY	LCC
60009	79	0.001	0.282	0.069	-0.102	0.064	-0.032	0.067	NNN	LCC
60084	42	0.075	-0.023	0.035	0.026	0.035	0.149	0.109	NNN	LCC
60183	31	-0.017	0.072	0.042	0.314	0.040	1.648	0.043	NYY	LCC
60205	62	0.293	-0.033	0.031	0.053	0.036	0.226	0.304	NNN	LCC
60245	74	0.162	0.049	0.024	0.092	0.026	0.056	0.163	NNN	LCC
60348	78	0.279	-0.008	0.032	0.103	0.033	0.737	0.082	NNY	LCC
60360	44	0.040	-0.022	0.034	0.008	0.034	0.118	0.109	NNN	LCC
60379	53	-0.045	0.131	0.119	0.016	0.105	-0.003	0.155	NNN	LCC
60459	88	0.067	0.019	0.037	0.032	0.038	0.144	0.088	NNN	LCC
60513	76	0.230	-0.008	0.033	-0.002	0.033	-0.222	0.143	NNN	LCC
60561	73	-0.037	0.011	0.039	0.224	0.039	1.027	0.045	NYY	LCC
60577	81	0.285	-0.033	0.038	0.043	0.036	0.373	0.072	NNN	LCC
60580	5	0.106	-0.029	0.033	-0.018	0.033	0.096	0.098	NNN	LCC
60629	6	-0.046	-0.036	0.031	-0.042	0.035	-0.558	0.431	NNN	LCC

Continued on next page

60710	71	-0.082	0.334	0.065	-0.057	0.061	-0.055	0.073	NNN	LCC
60718	66	0.013	0.587	0.004	0.610	0.009	0.318	0.019	NNN[1]	LCC
60823	79	-0.077	0.645	0.067	0.007	0.059	-0.014	0.061	NNN	LCC
60851	82	0.014	0.050	0.049	-0.029	0.047	0.110	0.076	NNN	LCC
60855	70	-0.026	0.161	0.059	-0.006	0.055	0.019	0.063	YNN	LCC
61049	85	0.393	-0.049	0.035	0.264	0.034	1.355	0.043	NYY	LCC
61086	20	0.183	-0.017	0.032	0.054	0.045	0.406	0.518	NNN	LCC
61087	88	0.272	0.097	0.072	1.170	0.070	2.489	0.069	NNN[1]	LCC
61098	8	0.188	-0.015	0.033	0.053	0.033	0.029	0.237	NNN	LCC
61257	84	-0.056	0.009	0.040	-0.002	0.038	0.027	0.064	NNN	LCC
61265	67	0.014	-0.019	0.036	-0.017	0.035	0.025	0.104	NNN	LCC
61268	26	0.130	-0.016	0.033	0.034	0.033	-0.231	0.209	NNN	LCC
61426	54	0.156	-0.012	0.032	0.037	0.032	0.126	0.138	NNN	LCC
61498	81	0.015	0.101	0.055	0.634	0.051	4.527	0.050	NYY	LCC
61530	24	0.203	-0.024	0.030	0.034	0.031	-0.117	0.217	NNN	LCC
61557	34	0.118	0.034	0.044	-0.019	0.043	0.023	0.063	NNN	LCC
61585	71	-0.072	0.448	0.074	-0.200	0.074	-0.236	0.085	NNN	LCC
61639	84	0.266	-0.057	0.047	-0.037	0.045	0.004	0.061	NNN	LCC
61684	73	0.205	-0.032	0.037	0.136	0.036	1.487	0.046	NNY	LCC
61691	14	0.072	0.003	0.030	0.043	0.034	-0.218	0.370	NNN	LCC
61715	8	0.103	-0.069	0.035	0.453	0.062	1.783	0.201	NYY	LCC
61717	21	0.192	-0.013	0.028	0.034	0.029	0.319	0.230	NNN	LCC
61753	13	0.337	-0.023	0.033	0.026	0.032	0.332	0.079	NNN	LCC
61782	84	0.060	-0.004	0.034	0.539	0.032	3.621	0.035	NYY	LCC
61789	15	0.095	0.438	0.079	-0.056	0.073	-0.033	0.076	NNN	LCC
61796	61	-0.046	0.007	0.043	-0.042	0.041	-0.074	0.057	NNN	LCC
61845	12	0.165	-0.024	0.033	0.005	0.035	-0.018	0.248	NNN	LCC
61906	40	0.184	-0.022	0.030	-0.015	0.032	-0.219	0.201	NNN	LCC
62002	49	0.233	0.044	0.034	0.059	0.036	0.050	0.078	NNN[1]	LCC
62026	77	0.012	0.035	0.051	0.053	0.049	0.238	0.058	NNN	LCC
62032	73	0.158	0.059	0.025	0.127	0.027	0.225	0.130	NNN	LCC
62058	80	-0.055	-0.040	0.051	-0.098	0.049	-0.055	0.064	NNN	LCC
62085	6	0.066	-0.037	0.034	0.001	0.037	0.118	0.262	NNN	LCC
62087	11	0.211	-0.048	0.034	-0.012	0.033	0.060	0.100	NNN	LCC
62134	83	0.171	-0.296	0.022	-0.353	0.025	-0.128	0.102	NNN[1]	LCC

Continued on next page

62154	39	0.210	-0.013	0.032	0.105	0.099	0.515	0.521	NNN	LCC
62171	78	0.300	-0.007	0.033	0.031	0.032	0.090	0.129	NNN	LCC
62179	64	0.042	0.002	0.043	-0.009	0.041	-0.086	0.081	NNN	LCC
62203	15	0.085	-0.037	0.033	-0.043	0.035	0.127	0.196	NNN[1]	LCC
62205	20	0.217	-0.007	0.035	-0.033	0.038	-0.135	0.093	NNN	LCC
62226	38	0.237	-0.011	0.034	0.057	0.044	0.603	0.363	NNN	LCC
62327	84	-0.059	0.279	0.062	-0.064	0.058	0.145	0.081	NNN	LCC
62427	65	0.241	-0.024	0.033	0.065	0.034	0.992	0.089	NNY	LCC
62428	81	0.124	0.030	0.046	0.052	0.047	0.325	0.073	NNN	LCC
62431	59	0.263	-0.020	0.035	0.009	0.035	-0.154	0.117	NNN	LCC
62482	23	0.073	-0.033	0.038	0.133	0.038	2.050	0.045	NNY	LCC
62488	34	0.227	-0.018	0.034	0.125	0.034	0.849	0.066	NNY	LCC
62657	83	0.285	0.000	0.031	0.124	0.032	2.040	0.045	NNY	LCC
62683	62	0.449	0.348	0.068	-0.082	0.063	-0.082	0.065	NNN	LCC
62711	7	0.110	-0.019	0.034	-0.001	0.033	0.064	0.111	NNN	LCC
62723	22	0.263	-0.038	0.034	0.014	0.036	0.181	0.238	NNN	LCC
62765	6	0.164	-0.004	0.034	0.019	0.033	0.196	0.157	NNN	LCC
62786	55	-0.067	-0.061	0.048	-0.134	0.047	0.051	0.064	NNN	LCC
62916	15	0.027	-0.023	0.038	-0.026	0.038	-0.102	0.074	NNN	LCC
62941	13	0.172	-0.021	0.032	0.039	0.034	0.008	0.223	NNN	LCC
63003	68	0.029	0.561	0.070	-0.036	0.063	0.008	0.068	NNN	LCC
63005	81	0.003	0.431	0.069	0.773	0.062	1.849	0.064	YYY	LCC
63007	83	0.297	0.343	0.064	-0.079	0.057	-0.085	0.060	NNN	LCC
63022	27	0.198	-0.019	0.032	0.004	0.037	-0.047	0.345	NNN	LCC
63036	6	-0.022	-0.113	0.030	-0.073	0.055	0.164	0.369	NNN	LCC
63041	83	0.202	0.007	0.036	0.406	0.074	1.677	0.353	NNN[1]	LCC
63085	9	0.167	-0.023	0.039	-0.006	0.038	0.039	0.067	NNN	LCC
63204	87	0.248	-0.089	0.049	-0.066	0.048	-0.052	0.057	NNN	LCC
63210	75	-0.015	0.181	0.060	-0.103	0.056	-0.011	0.060	NNN	LCC
63236	40	0.001	-0.003	0.038	0.279	0.036	1.236	0.046	NYY	LCC
63246	43	0.228	-0.011	0.032	0.030	0.033	0.217	0.125	NNN	LCC
63272	84	0.228	-0.015	0.035	0.030	0.034	0.014	0.112	NNN	LCC
63395	22	0.209	-0.029	0.031	0.095	0.038	0.592	0.150	NNY	LCC
63435	48	0.251	-0.032	0.031	0.037	0.032	0.148	0.145	NNN	LCC
63439	70	0.239	-0.015	0.033	0.117	0.034	0.936	0.091	NNY	LCC

Continued on next page

63527	32	0.195	0.013	0.039	0.031	0.038	-0.032	0.082	NNN	LCC
63540	10	0.090	-0.033	0.032	-0.007	0.034	0.258	0.229	NNN	LCC
63606	40	0.197	-0.060	0.025	-0.023	0.026	0.083	0.118	NNN	LCC
63678	8	0.059	-0.026	0.033	0.299	0.034	1.888	0.054	NYY	LCC
63819	6	0.097	-0.027	0.033	0.018	0.033	0.319	0.145	NNN	LCC
63836	85	0.222	-0.018	0.033	0.072	0.033	0.496	0.101	NNY	LCC
63839	73	-0.032	0.001	0.038	0.435	0.038	1.781	0.045	NYY	LCC
63886	75	0.164	-0.016	0.036	0.048	0.034	0.716	0.060	NNY	LCC
63935	9	0.259	0.003	0.032	0.048	0.032	0.110	0.101	NNN	LCC
63945	79	-0.024	0.250	0.064	-0.109	0.054	-0.106	0.060	NNN[1]	LCC
63975	57	0.236	0.289	0.046	2.837	0.043	4.556	0.041	YYY	LCC
64004	73	0.076	0.269	0.064	-0.148	0.060	-0.138	0.064	NNN	LCC
64033	27	0.534	0.405	0.072	-0.025	0.067	-0.053	0.068	NNN	LCC
64044	78	0.310	-0.026	0.033	0.024	0.033	0.174	0.111	NNN	LCC
64053	82	0.086	0.085	0.053	0.141	0.049	0.759	0.053	NNY	LCC
64184	81	0.240	-0.014	0.035	0.269	0.035	3.201	0.036	NYY	LCC
64204	10	0.026	-0.057	0.040	-0.068	0.040	-0.030	0.102	NNN	LCC
64264	58	0.332	-0.041	0.036	0.001	0.034	-0.187	0.138	NNN	LCC
64316	42	0.285	-0.038	0.030	-0.013	0.037	-0.054	0.421	NNN	LCC
64320	70	-0.049	-0.029	0.046	-0.091	0.044	-0.025	0.060	NNN	LCC
64322	74	0.225	-0.031	0.037	0.069	0.044	0.649	0.219	NNY	LCC
64372	30	0.293	-0.034	0.036	-0.022	0.034	-0.219	0.112	NNN	LCC
64425	54	0.062	0.338	0.064	-0.040	0.058	0.059	0.061	NNN	LCC
64515	71	-0.036	0.025	0.048	-0.069	0.046	-0.090	0.063	NNN	LCC
64560	21	0.232	-0.008	0.032	0.057	0.035	0.141	0.305	NNN	LCC
64565	16	0.127	-0.003	0.040	-0.049	0.039	-0.090	0.062	NNN	LCC
64570	35	0.353	-0.022	0.034	0.017	0.033	-0.122	0.186	NNN	LCC
64617	51	0.197	-0.016	0.036	0.005	0.035	0.021	0.095	NNN	LCC
64661	47	-0.042	0.407	0.062	-0.014	0.057	-0.057	0.061	NNN	LCC
64752	32	0.173	-0.027	0.033	0.007	0.032	0.198	0.122	NNN	LCC
64837	69	0.227	-0.018	0.035	0.146	0.034	0.778	0.061	NNY	LCC
64846	28	0.302	-0.033	0.031	0.021	0.035	-0.165	0.303	NNN	LCC
64877	61	0.214	-0.154	0.028	-0.033	0.031	1.064	0.071	NNN[1]	LCC
64891	17	0.205	-0.053	0.030	-0.064	0.030	-0.165	0.190	NNN[1]	LCC
64892	74	-0.023	-0.019	0.036	-0.035	0.036	0.085	0.075	NNN	LCC

Continued on next page

64925	80	-0.032	0.007	0.034	-0.012	0.034	-0.021	0.086	NNN	LCC
64933	8	0.007	0.015	0.048	-0.025	0.046	-0.002	0.059	NNN	LCC
64975	11	0.228	-0.005	0.032	0.053	0.038	0.421	0.316	NNN	LCC
64995	79	0.167	-0.085	0.031	0.073	0.031	2.588	0.033	NNY	LCC
65021	59	-0.024	-0.038	0.033	-0.037	0.033	-0.124	0.105	NNN	LCC
65089	84	0.135	-0.021	0.034	0.090	0.032	0.959	0.058	NNY	LCC
65112	81	-0.075	0.134	0.051	-0.021	0.048	-0.007	0.059	NNN[1]	LCC
65136	63	0.193	0.024	0.029	0.072	0.033	0.174	0.210	NNN	LCC
65178	61	0.000	-0.035	0.037	-0.043	0.036	0.053	0.074	NNN	LCC
65215	11	0.245	-0.026	0.030	0.014	0.032	-0.201	0.220	NNN	LCC
65219	78	0.096	0.031	0.039	0.045	0.039	0.011	0.073	NNN[1]	LCC
65271	62	0.359	0.461	0.066	-0.049	0.059	0.149	0.071	NNN	LCC
65348	50	0.077	-0.022	0.032	0.000	0.033	0.039	0.187	NNN	LCC
65394	67	0.004	-0.030	0.034	-0.017	0.034	-0.066	0.102	NNN	LCC
65426	76	0.055	-0.064	0.039	-0.013	0.038	0.053	0.068	NNN	LCC
65474	26	-0.233	0.704	0.002	0.710	0.005	0.462	0.013	NNN[1]	UCL
65502	7	0.223	0.003	0.033	0.029	0.032	0.017	0.104	NNN	LCC
65504	16	0.256	-0.023	0.032	0.001	0.033	0.186	0.120	NNN	UCL
65517	69	0.445	-0.022	0.032	0.048	0.032	0.054	0.174	NNN	LCC
65529	7	0.131	-0.025	0.033	-0.013	0.034	-0.304	0.203	NNN	UCL
65546	7	0.244	-0.033	0.036	0.005	0.035	-0.018	0.147	NNN	UCL
65617	64	0.282	-0.022	0.033	0.048	0.040	0.001	0.193	NNN	LCC
65822	81	0.029	0.011	0.037	0.002	0.036	-0.073	0.073	NNN[1]	LCC
65875	88	0.269	-0.021	0.039	0.202	0.037	2.812	0.039	NNY	LCC
65910	15	0.022	-0.036	0.033	-0.018	0.031	-0.080	0.147	NNN	LCC
65965	70	-0.017	-0.023	0.034	0.264	0.033	1.808	0.045	NYY	LCC
66063	11	0.112	-0.018	0.032	-0.007	0.034	0.139	0.121	NNN	UCL
66068	75	0.006	-0.036	0.037	0.251	0.037	1.502	0.047	NYY	LCC
66075	56	0.203	-0.031	0.036	0.036	0.034	0.812	0.050	NNY	LCC
66152	49	-0.044	0.051	0.042	0.044	0.041	-0.014	0.065	NNN	LCC
66160	34	0.153	-0.030	0.033	0.026	0.035	-0.028	0.314	NNN	UCL
66255	29	0.065	-0.030	0.034	-0.017	0.034	0.158	0.112	NNN	LCC
66447	93	0.084	-0.029	0.037	0.038	0.036	0.854	0.057	NNN[1]	UCL
66454	89	-0.051	0.031	0.044	-0.014	0.044	-0.016	0.062	NNN	LCC
66566	82	0.035	-0.013	0.034	0.256	0.034	1.694	0.045	NYY	LCC

Continued on next page

66642	16	0.290	-0.042	0.033	-0.022	0.032	-0.185	0.123	NNN	LCC
66651	75	0.000	0.028	0.029	0.042	0.030	0.100	0.096	NNN	LCC
66701	12	0.209	-0.024	0.030	-0.004	0.031	-0.441	0.261	NNN	LCC
66722	92	0.022	0.056	0.045	0.042	0.044	0.130	0.059	NNN	UCL
66764	8	0.326	-0.027	0.031	0.014	0.033	0.016	0.169	NNN	UCL
66821	83	-0.061	0.459	0.055	0.036	0.049	0.412	0.052	NNN[1]	LCC
66884	12	0.216	-0.023	0.033	0.030	0.036	0.268	0.227	NNN	UCL
66908	88	0.061	-0.031	0.040	-0.023	0.039	-0.081	0.075	NNN	UCL
67036	81	-0.093	-0.056	0.040	-0.083	0.039	-0.178	0.084	NNN	LCC
67068	80	0.211	-0.003	0.034	0.049	0.033	0.234	0.090	NNN	LCC
67075	49	0.290	-0.030	0.035	0.029	0.033	0.050	0.114	NNN	UCL
67114	13	0.185	-0.012	0.031	0.012	0.036	0.162	0.363	NNN	UCL
67199	86	0.059	0.063	0.045	0.045	0.043	0.021	0.057	NNN[1]	LCC
67230	65	0.248	0.005	0.040	0.085	0.050	1.017	0.110	NNY	LCC
67260	61	0.091	-0.026	0.038	-0.023	0.037	-0.115	0.078	NNN	LCC
67277	20	0.359	-0.057	0.039	-0.021	0.039	-0.090	0.099	NNN	UCL
67306	33	0.043	-0.018	0.037	-0.021	0.037	-0.013	0.082	NNN	UCL
67334	46	0.244	-0.011	0.032	0.037	0.032	0.139	0.129	NNN	UCL
67360	6	-0.002	-0.037	0.033	-0.076	0.035	-0.687	0.418	NNN	LCC
67407	7	0.336	-0.041	0.033	-0.017	0.033	-0.193	0.198	NNN	UCL
67428	73	0.307	-0.012	0.033	0.069	0.033	0.629	0.077	NNY	LCC
67440	6	0.329	-0.032	0.033	0.011	0.037	0.249	0.238	NNN	UCL
67441	8	0.312	0.042	0.028	0.086	0.030	0.028	0.152	NNN	LCC
67448	25	0.030	-0.034	0.037	-0.037	0.035	-0.204	0.150	NNN	UCL
67464	57	-0.226	0.566	0.079	-0.134	0.072	-0.117	0.076	NNN	UCL
67472	54	-0.298	0.600	0.074	0.421	0.066	1.219	0.067	NYY	UCL
67477	13	0.171	-0.021	0.034	0.048	0.038	-0.127	0.476	NNN	UCL
67497	92	0.192	-0.020	0.034	0.181	0.033	2.571	0.040	NNY	UCL
67669	66	-0.842	0.321	0.073	0.338	0.069	1.088	0.071	YYY	UCL
67703	70	-0.055	0.196	0.053	-0.026	0.049	0.036	0.057	YNN[1]	UCL
67786	7	-0.077	0.338	0.070	-0.107	0.063	-0.101	0.069	YNN[1]	UCL
67844	17	0.238	-0.018	0.035	0.034	0.043	0.308	0.150	NNN	LCC
67859	30	0.222	0.022	0.037	0.017	0.037	0.051	0.092	NNN	UCL
67916	7	0.038	-0.014	0.035	0.005	0.033	0.101	0.106	NNN	LCC
67919	66	0.192	-0.008	0.043	0.010	0.041	0.094	0.059	NNN	LCC

Continued on next page

67957	89	0.392	0.018	0.064	0.033	0.062	-0.049	0.148	NNN	UCL
67970	90	0.198	-0.013	0.032	0.173	0.032	1.517	0.055	NNY	UCL
67973	75	-0.047	0.152	0.049	0.107	0.047	0.278	0.055	NNN[1]	UCL
68080	60	0.077	0.025	0.051	-0.015	0.049	0.581	0.056	NNN[1]	UCL
68245	76	0.137	0.619	0.072	-0.031	0.064	-0.075	0.066	YNN	UCL
68282	77	0.252	0.480	0.069	-0.074	0.062	-0.104	0.064	NNN	UCL
68335	87	0.313	-0.009	0.036	0.040	0.035	0.036	0.091	NNN	UCL
68413	66	0.165	0.133	0.052	0.149	0.053	0.786	0.139	YNY	LCC
68454	7	0.123	-0.018	0.033	0.003	0.033	-0.043	0.107	NNN	UCL
68489	20	0.009	-0.037	0.031	-0.064	0.033	0.101	0.130	NNN[1]	UCL
68532	89	0.190	-0.060	0.038	-0.046	0.037	-0.108	0.073	NNN[1]	UCL
68702	22	-0.111	2.014	0.004	1.911	0.014	1.806	0.021	NNN[1]	LCC
68722	72	0.132	-0.014	0.030	-0.005	0.030	-0.066	0.187	NNN	UCL
68781	89	0.065	-0.021	0.035	0.117	0.033	0.653	0.067	NNY	UCL
68854	7	0.354	-0.026	0.030	0.038	0.032	0.264	0.151	NNN	UCL
68862	58	-0.050	0.302	0.059	-0.119	0.053	-0.127	0.058	NNN	UCL
68867	56	0.011	-0.032	0.036	-0.027	0.035	-0.005	0.114	NNN	UCL
68958	42	0.021	-0.004	0.040	-0.009	0.038	0.139	0.060	NNN	UCL
69011	77	-0.006	-0.012	0.043	0.208	0.042	2.079	0.043	NYY	UCL
69113	80	-0.035	-0.078	0.048	-0.129	0.046	-0.051	0.068	NNN	UCL
69291	88	0.183	-0.016	0.034	0.005	0.034	0.194	0.128	NNN	UCL
69300	23	0.137	-0.027	0.036	0.062	0.040	0.159	0.079	NNN	UCL
69302	82	0.184	-0.025	0.031	0.021	0.032	0.079	0.114	NNN	UCL
69327	45	0.163	-0.019	0.034	0.019	0.034	0.216	0.114	NNN	UCL
69475	59	0.162	-0.023	0.038	-0.008	0.037	-0.043	0.092	NNN	UCL
69605	26	0.143	-0.026	0.033	0.036	0.033	0.201	0.168	NNN	UCL
69618	71	0.268	0.968	0.064	1.332	0.056	2.228	0.054	NYY	UCL
69659	31	0.160	-0.011	0.034	0.009	0.034	0.160	0.149	NNN	UCL
69693	12	-0.023	-0.033	0.033	0.013	0.051	0.494	0.522	NNN	UCL
69720	83	0.192	-0.013	0.033	0.098	0.032	0.477	0.105	NNY	UCL
69791	60	0.216	-0.016	0.032	0.027	0.033	0.245	0.140	NNN	UCL
69897	7	0.274	-0.023	0.032	0.048	0.032	0.289	0.111	NNN	UCL
69990	21	0.093	-0.025	0.033	0.001	0.033	0.136	0.153	NNN	UCL
69995	70	0.022	0.104	0.051	0.132	0.048	0.351	0.063	NNY	UCL
70050	37	0.006	-0.023	0.038	0.003	0.037	0.165	0.096	NNN	UCL

Continued on next page

70149	90	0.186	-0.023	0.033	0.118	0.033	1.111	0.084	NNY	UCL
70300	86	0.250	0.399	0.062	-0.030	0.056	-0.035	0.061	YNN	UCL
70350	70	0.326	0.034	0.037	0.063	0.036	0.177	0.067	NNN	UCL
70441	93	0.020	-0.026	0.036	0.088	0.034	1.017	0.054	NNY	UCL
70455	51	-0.047	-0.009	0.038	0.138	0.036	0.918	0.052	NNY	UCL
70483	52	0.160	0.070	0.043	0.033	0.043	0.059	0.057	NNN	UCL
70513	20	0.047	0.016	0.044	-0.022	0.043	0.019	0.074	NNN	UCL
70518	15	0.059	0.092	0.044	0.035	0.042	0.027	0.067	NNN[1]	UCL
70537	28	0.315	-0.028	0.033	0.035	0.032	0.138	0.122	NNN	UCL
70558	88	0.206	-0.009	0.030	0.031	0.031	-0.189	0.237	NNN	UCL
70575	7	0.070	-0.022	0.033	-0.013	0.038	-0.361	0.401	NNN	LCC
70626	79	-0.064	-0.024	0.043	-0.064	0.042	0.031	0.063	NNN	UCL
70676	16	0.090	-0.041	0.032	-0.028	0.036	-0.103	0.326	NNN	UCL
70689	90	0.292	0.007	0.031	0.033	0.031	-0.032	0.112	NNN	UCL
70697	89	0.003	-0.021	0.034	-0.023	0.033	-0.007	0.083	NNN	UCL
70753	80	-0.085	0.226	0.067	-0.120	0.062	-0.164	0.065	NNN	UCL
70765	41	0.071	-0.012	0.033	-0.030	0.034	-0.112	0.144	NNN[1]	UCL
70809	68	-0.004	-0.018	0.039	-0.025	0.039	0.084	0.072	NNN	UCL
70822	27	0.129	-0.029	0.034	0.011	0.033	-0.068	0.186	NNN	UCL
70833	84	0.233	-0.023	0.033	0.022	0.033	-0.246	0.186	NNN	UCL
70898	28	0.207	0.002	0.033	0.026	0.034	0.081	0.118	NNN	UCL
70904	66	0.141	0.037	0.041	0.006	0.041	-0.022	0.062	NNN	UCL
70918	47	0.186	0.026	0.040	0.029	0.038	0.069	0.062	NNN[1]	UCL
70931	72	0.099	0.316	0.068	-0.052	0.063	-0.073	0.067	YNN[1]	UCL
70977	5	-0.006	-0.040	0.031	0.001	0.035	-0.010	0.299	NNN	UCL
70998	89	0.097	-0.010	0.035	-0.010	0.035	-0.033	0.100	NNN	UCL
71023	32	0.211	-0.031	0.030	0.035	0.031	0.231	0.141	NNN	UCL
71140	67	0.135	-0.036	0.035	-0.009	0.035	-0.042	0.096	NNN	UCL
71271	55	-0.010	-0.020	0.032	0.106	0.032	0.987	0.063	NNY	UCL
71314	7	0.005	-0.030	0.033	-0.062	0.034	-0.208	0.102	NNN	LCC
71321	92	0.165	0.023	0.036	0.041	0.035	0.051	0.096	NNN	UCL
71352	82	-0.003	0.637	0.058	0.868	0.060	1.486	0.060	NNY	UCL
71353	90	-0.042	0.078	0.047	0.012	0.044	0.004	0.058	NNN[1]	UCL
71453	66	-0.056	0.012	0.047	-0.049	0.045	0.158	0.055	NNN	UCL
71498	41	0.117	-0.009	0.033	0.027	0.035	0.163	0.169	NNN	UCL

Continued on next page

71536	84	-0.161	0.534	0.074	-0.083	0.068	-0.111	0.071	NNN	UCL
71633	36	0.172	-0.020	0.035	-0.004	0.035	-0.092	0.130	NNN	UCL
71708	84	0.106	-0.027	0.031	0.038	0.032	0.275	0.110	NNN	UCL
71724	83	-0.046	-0.085	0.039	-0.091	0.038	-0.100	0.081	NNN	UCL
71767	43	0.326	0.011	0.031	0.072	0.032	0.199	0.131	NNN	UCL
71835	14	0.175	-0.003	0.032	0.051	0.034	0.102	0.144	NNN	UCL
71856	7	0.010	-0.001	0.030	-0.071	0.034	-0.150	0.278	NNN[1]	UCL
71858	15	0.311	-0.036	0.030	-0.069	0.037	-0.638	0.484	NNN	UCL
71860	70	-0.034	-0.354	0.011	-0.840	0.020	-0.917	0.021	NNN[1]	UCL
71865	93	0.150	0.477	0.076	-0.038	0.067	-0.054	0.071	NNN	UCL
71885	9	0.013	-0.027	0.034	0.010	0.038	0.470	0.175	NNY	UCL
71969	13	0.262	-0.034	0.035	-0.002	0.034	-0.023	0.168	NNN	US
71982	33	0.240	-0.023	0.035	0.004	0.034	0.132	0.107	NNN	UCL
72060	16	0.233	-0.028	0.037	-0.026	0.036	-0.016	0.076	NNN	US
72099	47	0.254	-0.018	0.031	0.172	0.033	1.196	0.105	NNY	UCL
72140	22	0.117	-0.028	0.037	-0.040	0.037	-0.165	0.099	NNN	UCL
72149	51	0.249	-0.004	0.031	0.040	0.036	0.535	0.227	NNN	UCL
72158	59	0.212	-0.008	0.034	-0.001	0.035	0.068	0.097	NNN	UCL
72164	28	0.236	-0.021	0.029	0.003	0.030	0.009	0.210	NNN	UCL
72185	12	0.219	-0.026	0.033	0.010	0.033	-0.146	0.227	NNN	UCL
72216	57	0.314	-0.008	0.034	0.096	0.034	0.482	0.086	NNN[1]	UCL
72299	27	0.134	-0.017	0.031	-0.015	0.032	0.214	0.113	NNN	UCL
72345	18	0.261	-0.017	0.032	0.023	0.035	-0.071	0.357	NNN	UCL
72352	22	0.062	-0.025	0.032	0.010	0.033	0.106	0.178	NNN	UCL
72411	30	0.291	-0.041	0.035	-0.012	0.035	0.025	0.097	NNN	UCL
72584	78	0.141	-0.026	0.033	0.053	0.034	0.645	0.080	NNY	UCL
72627	93	0.050	0.007	0.043	-0.008	0.042	-0.001	0.072	NNN	UCL
72630	41	0.166	-0.031	0.032	-0.007	0.035	-0.318	0.378	NNN	UCL
72683	74	0.048	0.448	0.071	-0.102	0.065	-0.136	0.068	NNN	UCL
72685	48	0.280	-0.029	0.031	0.422	0.032	1.392	0.071	NNN[1]	UCL
72771	13	0.297	-0.041	0.036	-0.005	0.035	-0.098	0.158	NNN	US
72800	71	-0.040	0.160	0.060	-0.078	0.057	-0.162	0.064	NNN	UCL
72877	6	0.149	-0.006	0.031	0.070	0.038	0.325	0.350	NNN	UCL
72904	12	0.211	-0.010	0.033	0.025	0.035	0.103	0.183	NNN	UCL
72938	26	0.263	-0.030	0.033	0.071	0.035	0.450	0.183	NNN	UCL

Continued on next page

72940	91	0.129	-0.115	0.045	-0.122	0.043	-0.080	0.067	NNN	UCL
72984	43	0.107	-0.099	0.037	-0.053	0.036	-0.127	0.091	NNN[1]	UCL
73145	91	0.080	0.003	0.034	0.651	0.032	3.239	0.035	NYY	UCL
73147	78	0.014	-0.036	0.031	0.008	0.033	0.116	0.163	NNN	UCL
73150	70	0.030	-0.008	0.038	0.043	0.038	1.199	0.050	NNN[1]	UCL
73171	33	-0.028	-0.027	0.043	-0.050	0.043	0.210	0.058	NNN	UCL
73266	92	-0.036	-0.026	0.035	-0.024	0.035	0.031	0.114	NNN	UCL
73274	8	0.320	-0.020	0.032	0.027	0.035	-0.242	0.353	NNN	US
73295	13	0.122	0.006	0.031	0.026	0.031	0.115	0.100	NNN	UCL
73334	73	0.038	0.688	0.076	-0.138	0.072	-0.135	0.072	NNN	UCL
73341	65	-0.068	-0.052	0.040	0.071	0.039	0.744	0.053	NNY	UCL
73348	7	0.189	-0.015	0.037	0.004	0.037	0.056	0.072	NNN	UCL
73357	32	0.108	0.016	0.040	-0.034	0.038	0.016	0.081	NNN	UCL
73358	12	0.316	-0.001	0.038	0.003	0.036	-0.016	0.099	NNN	US
73393	21	-0.034	-0.025	0.037	-0.031	0.037	0.079	0.087	NNN	UCL
73409	19	0.119	-0.006	0.034	-0.003	0.035	-0.096	0.132	NNN	UCL
73498	10	0.223	-0.017	0.033	0.002	0.038	-0.396	0.383	NNN	US
73535	62	0.156	-0.049	0.037	-0.039	0.036	-0.068	0.091	NNN	UCL
73538	21	0.226	-0.036	0.031	-0.019	0.035	-0.113	0.302	NNN	UCL
73559	61	0.174	0.178	0.055	-0.025	0.052	-0.021	0.059	YNN	UCL
73597	15	0.167	-0.029	0.031	0.027	0.035	0.224	0.203	NNN	UCL
73624	86	-0.053	0.105	0.052	-0.082	0.051	-0.094	0.062	NNN	UCL
73667	36	0.246	-0.028	0.033	0.005	0.033	-0.074	0.152	NNN	UCL
73698	5	0.230	-0.006	0.033	0.028	0.033	-0.082	0.148	NNN	UCL
73742	58	0.301	-0.047	0.036	-0.013	0.037	-0.072	0.101	NNN	UCL
73766	46	0.208	0.002	0.038	0.011	0.038	0.040	0.081	NNN	US
73807	76	-0.159	0.483	0.072	-0.100	0.066	-0.151	0.067	NNN	UCL
73828	10	0.213	-0.022	0.034	-0.016	0.034	-0.067	0.181	NNN	UCL
73859	11	0.270	-0.013	0.031	-0.026	0.036	0.099	0.193	NNN	US
73906	16	0.285	-0.014	0.033	0.004	0.037	0.251	0.327	NNN	US
73913	88	0.177	0.006	0.032	0.052	0.033	0.133	0.140	NNN	UCL
73937	86	-0.016	0.073	0.051	-0.029	0.050	-0.007	0.071	NNN[1]	UCL
73990	81	0.178	0.008	0.033	0.259	0.033	1.628	0.047	NYY	UCL
74066	67	-0.021	-0.016	0.048	-0.124	0.046	-0.057	0.064	NNN	UCL
74098	67	0.271	-0.011	0.033	-0.034	0.033	0.143	0.202	NNN	UCL

Continued on next page

74100	87	-0.089	0.037	0.046	-0.025	0.045	0.017	0.060	NNN	UCL
74104	74	0.162	-0.003	0.033	0.017	0.033	0.065	0.121	NNN	UCL
74114	49	0.317	-0.015	0.031	0.024	0.033	-0.773	0.331	NNN	UCL
74125	10	0.260	-0.018	0.032	-0.014	0.033	0.024	0.160	NNN	US
74181	6	0.021	0.024	0.050	-0.070	0.048	-0.127	0.064	NNN	UCL
74308	47	0.387	-0.058	0.033	-0.025	0.033	-0.308	0.191	NNN	UCL
74321	41	0.214	-0.025	0.030	0.018	0.033	-0.151	0.280	NNN[1]	UCL
74449	48	-0.063	0.157	0.058	-0.131	0.055	-0.160	0.061	NNN	UCL
74468	70	-0.015	-0.040	0.045	0.030	0.045	0.270	0.191	NNN	UCL
74479	78	-0.036	-0.034	0.048	-0.098	0.046	-0.130	0.069	NNN	UCL
74490	39	-0.021	-0.038	0.041	-0.072	0.040	-0.030	0.071	NNN	UCL
74498	44	0.288	-0.017	0.033	0.021	0.036	0.491	0.168	NNN	UCL
74499	90	0.227	-0.029	0.034	0.071	0.032	1.262	0.060	NNY	UCL
74529	43	0.137	0.052	0.029	0.067	0.033	0.117	0.189	NNN	UCL
74645	20	0.160	-0.020	0.033	-0.018	0.032	-0.141	0.121	NNN	US
74651	62	0.297	-0.017	0.031	0.024	0.032	0.180	0.141	NNN	UCL
74657	21	-0.081	-0.041	0.036	-0.045	0.036	-0.120	0.104	NNN	UCL
74724	7	0.176	-0.040	0.033	-0.031	0.031	-0.080	0.104	NNN	UCL
74744	5	0.053	-0.026	0.032	-0.011	0.033	-0.060	0.191	NNN	UCL
74752	21	-0.052	-0.029	0.038	0.043	0.037	0.245	0.068	NNN	UCL
74772	16	0.207	-0.015	0.033	0.063	0.036	-0.217	0.389	NNN	UCL
74820	5	-0.031	-0.048	0.033	-0.168	0.036	0.199	0.201	NNN	UCL
74865	90	0.256	-0.031	0.033	0.011	0.035	0.009	0.208	NNN	UCL
74911	62	0.086	0.695	0.070	0.509	0.059	1.137	0.061	YYY	UCL
74950	57	-0.095	0.070	0.052	-0.006	0.050	-0.013	0.065	NNN[1]	UCL
74959	84	0.239	-0.036	0.034	0.016	0.034	0.578	0.129	NNY	UCL
74985	81	0.053	-0.024	0.036	0.029	0.035	0.168	0.120	NNN	UCL
74992	34	0.134	-0.007	0.033	0.047	0.033	0.155	0.108	NNN	US
75035	61	0.350	0.015	0.035	0.022	0.035	-0.050	0.132	NNN	UCL
75056	84	0.076	-0.016	0.035	-0.030	0.035	-0.257	0.124	NNN	UCL
75077	78	0.022	-0.047	0.039	-0.018	0.039	0.243	0.076	NNN	UCL
75151	81	-0.014	-0.173	0.044	-0.200	0.043	-0.204	0.069	NNN[1]	UCL
75164	78	0.047	0.025	0.048	-0.007	0.047	0.187	0.060	NNN	UCL
75210	91	-0.010	-0.038	0.040	0.175	0.038	1.151	0.048	NYY	UCL
75264	47	-0.140	0.472	0.083	-0.137	0.076	-0.175	0.077	NNN	UCL

Continued on next page

75267	18	0.231	-0.025	0.034	0.008	0.036	0.095	0.201	NNN	UCL
75290	30	0.270	-0.020	0.034	0.010	0.034	-0.221	0.183	NNN	UCL
75304	90	-0.063	0.410	0.065	0.040	0.058	0.026	0.064	YNN	UCL
75367	80	0.293	-0.014	0.032	0.049	0.035	0.199	0.292	NNN	UCL
75403	6	0.189	0.006	0.036	0.047	0.041	0.124	0.355	NNN	UCL
75427	23	0.027	-0.038	0.034	-0.029	0.035	-0.039	0.101	NNN	UCL
75459	41	0.242	-0.030	0.034	-0.005	0.034	0.052	0.107	NNN	UCL
75476	82	0.017	0.013	0.037	0.035	0.038	0.158	0.075	NNN	UCL
75480	89	0.190	-0.019	0.035	0.003	0.034	-0.014	0.128	NNN	UCL
75491	70	0.191	-0.045	0.033	0.034	0.034	1.146	0.059	NNY	UCL
75509	92	0.025	-0.003	0.034	0.244	0.041	1.175	0.087	NYY	UCL
75575	12	0.169	0.007	0.031	0.017	0.034	-0.185	0.180	NNN	UCL
75612	12	0.233	-0.012	0.034	-0.004	0.035	0.077	0.174	NNN	UCL
75613	52	0.183	-0.032	0.040	-0.045	0.038	-0.047	0.078	NNN	UCL
75647	83	-0.080	0.006	0.051	-0.113	0.049	-0.135	0.061	NNN	UCL
75659	40	0.279	-0.038	0.032	-0.006	0.035	-0.274	0.328	NNN	US
75669	26	0.228	-0.024	0.033	0.012	0.035	-0.194	0.261	NNN	US
75683	83	0.234	-0.002	0.031	0.087	0.034	0.795	0.148	NNY	UCL
75765	17	0.264	-0.016	0.039	-0.027	0.038	-0.115	0.082	NNN	UCL
75802	50	0.291	-0.024	0.030	-0.010	0.030	-0.080	0.147	NNN	UCL
75824	69	0.188	0.002	0.025	0.042	0.026	-0.223	0.191	NNN	UCL
75843	14	0.137	-0.021	0.033	0.154	0.045	0.950	0.134	NNN[1]	UCL
75891	90	0.227	-0.011	0.035	0.023	0.035	-0.031	0.135	NNN	UCL
75902	6	0.039	-0.029	0.035	0.121	0.036	1.122	0.068	NNY	UCL
75906	9	0.203	-0.033	0.031	-0.030	0.033	-0.377	0.232	NNN	US
75915	92	-0.003	0.123	0.035	0.124	0.034	0.196	0.064	NNN[1]	UCL
75933	34	0.240	-0.009	0.031	0.060	0.031	-0.025	0.141	NNN	UCL
75935	28	0.179	-0.015	0.030	0.010	0.030	-0.197	0.217	NNN	US
75952	7	-0.029	-0.034	0.031	0.000	0.035	0.178	0.215	NNN	UCL
75957	26	0.011	-0.011	0.036	-0.014	0.036	0.099	0.097	NNN	UCL
75985	9	0.192	0.022	0.040	0.018	0.039	0.170	0.071	NNN	US
76001	73	0.096	0.000	0.040	-0.024	0.039	-0.029	0.073	NNN	UCL
76048	83	0.006	-0.020	0.045	-0.038	0.044	0.086	0.060	NNN	UCL
76063	55	0.117	0.155	0.056	0.035	0.052	0.376	0.061	YNY	UCL
76071	70	0.115	-0.032	0.037	-0.061	0.037	-0.102	0.111	NNN	US

Continued on next page

76084	87	0.257	-0.017	0.035	-0.009	0.034	0.099	0.119	NNN	UCL
76126	58	-0.111	0.119	0.048	-0.009	0.045	-0.045	0.061	NNN[1]	US
76143	51	0.156	-0.126	0.028	0.057	0.027	-0.388	0.050	NNN[1]	US
76223	47	0.008	-0.029	0.038	0.192	0.039	1.877	0.046	NYY	UCL
76234	73	0.005	-0.036	0.044	0.174	0.042	1.116	0.048	NYY	UCL
76264	14	0.214	-0.009	0.029	0.051	0.029	-0.072	0.172	NNN	UCL
76297	91	-0.099	0.559	0.071	-0.119	0.067	-0.191	0.071	NNN	UCL
76302	36	0.163	-0.014	0.031	0.005	0.033	0.146	0.179	NNN	US
76310	69	-0.013	-0.019	0.036	0.442	0.034	2.935	0.036	NYY	US
76371	74	-0.132	0.405	0.058	0.003	0.050	0.035	0.055	NNN[1]	UCL
76395	78	-0.035	0.018	0.039	0.410	0.038	1.261	0.047	NYY	UCL
76442	29	-0.029	-0.031	0.033	-0.030	0.033	-0.068	0.150	NNN	UCL
76501	50	0.206	-0.012	0.033	0.008	0.033	-0.009	0.118	NNN	UCL
76503	27	-0.018	-0.029	0.043	-0.131	0.041	-0.084	0.069	NNN	US
76549	47	0.055	-0.064	0.040	-0.094	0.042	-0.212	0.138	NNN	UCL
76572	30	0.209	-0.017	0.031	0.005	0.038	0.192	0.378	NNN	US
76591	64	-0.080	-0.008	0.039	-0.022	0.039	-0.097	0.081	NNN	UCL
76600	53	-0.130	0.628	0.078	-0.024	0.071	-0.062	0.073	NNN	UCL
76633	89	-0.016	-0.024	0.031	0.019	0.033	-0.028	0.140	NNN	US
76712	31	0.145	-0.074	0.026	-0.070	0.029	0.190	0.126	NNN	UCL
76782	39	0.220	-0.052	0.039	0.029	0.039	1.648	0.051	NNY	US
76875	89	0.196	0.000	0.034	0.004	0.034	0.011	0.114	NNN	UCL
76887	11	0.273	-0.031	0.031	0.021	0.034	-0.158	0.280	NNN	US
76945	85	-0.095	0.228	0.061	-0.119	0.057	-0.130	0.061	NNN	UCL
76997	62	0.226	-0.029	0.034	0.004	0.036	0.063	0.114	NNN	UCL
77010	11	0.104	-0.020	0.037	-0.039	0.036	-0.224	0.116	NNN	UCL
77038	88	0.305	-0.016	0.033	0.042	0.032	0.135	0.163	NNN	UCL
77051	49	-0.055	-0.048	0.031	-0.052	0.033	-0.108	0.167	NNN	UCL
77086	83	0.014	0.040	0.052	-0.096	0.049	-0.089	0.060	NNN[1]	UCL
77124	56	0.382	-0.038	0.031	0.022	0.033	-0.149	0.266	NNN	US
77140	11	0.079	-0.040	0.038	0.036	0.037	0.043	0.140	NNN	UCL
77144	79	0.400	-0.012	0.031	0.044	0.033	0.142	0.143	NNN	UCL
77150	90	0.121	-0.014	0.036	0.085	0.035	0.346	0.085	NNN	UCL
77154	34	0.283	0.014	0.028	0.033	0.035	0.264	0.314	NNN	US
77165	28	0.120	0.031	0.037	0.011	0.036	0.073	0.085	NNN	US

Continued on next page

77286	84	-0.092	0.053	0.050	-0.079	0.049	-0.026	0.062	NNN	UCL
77295	74	0.058	-0.024	0.032	0.007	0.033	-0.192	0.177	NNN	UCL
77315	45	0.022	0.010	0.040	0.229	0.039	1.398	0.049	NYY	UCL
77317	67	-0.016	-0.025	0.036	0.091	0.036	1.321	0.056	NNN[1]	UCL
77330	43	0.285	-0.025	0.035	-0.010	0.034	-0.059	0.124	NNN[1]	UCL
77347	56	0.090	0.009	0.033	0.127	0.033	0.659	0.076	NNY	US
77366	13	0.164	-0.036	0.033	0.054	0.035	0.600	0.144	NNN[1]	US
77378	19	0.307	-0.006	0.031	0.035	0.041	0.224	0.473	NNN	UCL
77388	78	0.155	0.031	0.035	0.043	0.035	-0.099	0.132	NNN	UCL
77398	9	0.294	-0.028	0.032	-0.028	0.038	-0.250	0.405	NNN	UCL
77399	59	0.077	0.055	0.038	0.098	0.038	0.853	0.054	NNN[1]	US
77432	87	0.240	-0.018	0.032	0.072	0.034	0.663	0.093	NNY	UCL
77502	62	0.214	-0.017	0.033	0.009	0.033	0.074	0.165	NNN	UCL
77520	90	0.328	-0.012	0.033	0.041	0.033	0.246	0.141	NNN	UCL
77523	33	-0.029	-0.035	0.036	0.100	0.035	0.780	0.077	NNY	UCL
77545	84	0.247	-0.022	0.033	0.142	0.040	0.944	0.129	NNN[1]	US
77552	9	0.071	-0.012	0.034	-0.016	0.035	-0.338	0.331	NNN	US
77562	70	-0.038	0.016	0.049	0.260	0.049	1.655	0.053	NNN[1]	UCL
77588	43	0.324	-0.029	0.033	-0.002	0.035	-0.124	0.225	NNN	US
77635	89	0.019	0.338	0.071	-0.095	0.064	-0.003	0.076	NNN	US
77644	14	1.523	0.016	0.030	-0.028	0.034	0.070	0.175	NNN[1]	UCL
77713	45	0.209	-0.027	0.033	0.001	0.033	-0.027	0.235	NNN	UCL
77736	44	0.359	0.013	0.031	0.030	0.032	0.359	0.138	NNN	US
77766	6	0.115	-0.001	0.033	0.018	0.033	-0.032	0.164	NNN	US
77778	13	0.045	-0.066	0.032	-0.093	0.048	0.170	0.303	NNN	UCL
77815	79	0.275	0.012	0.036	0.053	0.035	0.033	0.102	NNN	US
77840	51	-0.049	0.502	0.074	0.088	0.068	1.025	0.086	NNN[1]	US
77858	83	-0.010	0.147	0.064	-0.069	0.059	0.901	0.063	YNN[1]	US
77859	75	0.072	0.327	0.069	0.410	0.062	0.885	0.064	NYY	US
77900	82	-0.066	0.014	0.044	-0.052	0.044	-0.108	0.073	NNN	US
77909	71	-0.063	-0.043	0.051	-0.141	0.048	-0.072	0.068	NNN	US
77911	83	0.027	0.033	0.041	0.145	0.039	2.347	0.043	NNN[1]	US
77937	17	0.265	0.022	0.034	0.029	0.033	-0.164	0.183	NNN	UCL
77939	38	0.039	0.073	0.055	-0.110	0.052	-0.141	0.065	NNN	US
77960	86	0.148	-0.020	0.036	-0.011	0.034	0.016	0.120	NNN	US

Continued on next page

77968	59	-0.048	-0.043	0.037	-0.046	0.036	-0.149	0.097	NNN	UCL
77974	5	0.265	-0.036	0.034	0.008	0.034	-0.063	0.129	NNN	UCL
78035	27	0.324	-0.013	0.034	0.010	0.034	-0.038	0.187	NNN	UCL
78043	83	0.213	-0.021	0.033	0.085	0.033	0.882	0.089	NNY	UCL
78099	88	0.070	-0.005	0.035	0.038	0.034	0.263	0.089	NNN	US
78104	82	-0.114	0.456	0.063	-0.051	0.058	-0.084	0.062	NNN	US
78129	22	0.127	0.031	0.039	0.024	0.038	0.138	0.066	NNN[1]	US
78130	48	0.228	0.010	0.046	-0.012	0.044	0.011	0.064	NNN	US
78150	84	0.144	-0.021	0.035	-0.016	0.043	-0.006	0.190	NNN	UCL
78168	30	0.030	0.067	0.055	-0.063	0.053	-0.050	0.063	NNN	US
78183	88	-0.003	-0.054	0.041	-0.120	0.040	-0.015	0.080	NNN	US
78196	90	-0.027	0.038	0.036	-0.009	0.035	-0.189	0.104	NNN	US
78197	5	0.045	-0.038	0.035	-0.039	0.034	0.004	0.112	NNN	UCL
78198	40	0.225	-0.016	0.030	0.046	0.031	0.552	0.159	NNY	UCL
78207	86	0.507	0.859	0.066	1.110	0.058	1.874	0.061	NYY	US
78233	64	0.304	-0.017	0.032	-0.009	0.034	-0.031	0.179	NNN	US
78246	23	-0.064	0.007	0.054	-0.114	0.052	-0.116	0.062	NNN	US
78263	59	0.133	0.008	0.034	0.053	0.035	0.287	0.157	NNN	UCL
78264	37	0.290	-0.046	0.035	-0.035	0.036	0.057	0.093	NNN	UCL
78265	36	-0.221	0.590	0.052	0.138	0.054	0.433	0.294	NNN	US
78266	10	0.054	-0.019	0.033	-0.039	0.054	0.224	0.366	NNN	UCL
78306	14	0.016	-0.047	0.037	-0.086	0.036	-0.211	0.090	NNN	UCL
78324	78	0.170	-0.003	0.035	0.013	0.034	0.163	0.114	NNN	UCL
78357	17	0.086	-0.037	0.034	0.086	0.036	0.959	0.076	NNY	UCL
78381	27	0.318	-0.015	0.033	0.025	0.035	0.098	0.220	NNN	US
78384	84	-0.379	0.617	0.071	-0.179	0.062	-0.171	0.063	YNN	UCL
78416	74	0.307	0.230	0.030	0.261	0.030	0.286	0.136	NNN[1]	UCL
78494	54	0.181	0.004	0.037	-0.022	0.043	0.018	0.114	NNN	US
78530	76	0.025	-0.035	0.036	-0.055	0.037	0.102	0.093	NNN	US
78533	88	0.049	0.059	0.029	0.040	0.031	0.397	0.072	NNY	UCL
78541	35	-0.022	-0.002	0.037	-0.002	0.036	-0.020	0.093	NNN	UCL
78549	89	0.067	0.011	0.044	-0.001	0.043	0.169	0.096	NNN	US
78555	89	0.192	-0.017	0.033	0.026	0.033	0.243	0.131	NNN	UCL
78573	6	0.238	-0.006	0.031	-0.011	0.033	-0.351	0.221	NNN	US
78581	86	0.358	0.036	0.035	0.079	0.034	0.087	0.124	NNN	US

Continued on next page

78603	32	-0.020	0.005	0.041	0.020	0.040	0.116	0.058	NNN	UCL
78607	6	0.087	0.008	0.038	-0.014	0.036	0.035	0.105	NNN	UCL
78611	12	0.088	-0.046	0.033	-0.035	0.033	0.221	0.092	NNN	UCL
78635	8	0.105	-0.009	0.031	0.000	0.034	-0.511	0.385	NNN	US
78641	91	0.071	-0.034	0.033	0.288	0.032	2.079	0.046	NYY	UCL
78655	90	-0.053	0.116	0.064	-0.168	0.058	-0.116	0.063	NNN	UCL
78663	88	0.271	-0.033	0.031	0.030	0.032	0.235	0.137	NNN	US
78702	90	0.142	0.004	0.036	0.012	0.034	-0.046	0.132	NNN	US
78711	63	0.313	-0.027	0.029	-0.032	0.030	-0.201	0.235	NNN	UCL
78754	73	-0.018	-0.038	0.040	-0.075	0.039	-0.017	0.090	NNN	UCL
78756	75	-0.095	-0.064	0.035	-0.067	0.034	0.339	0.067	NNN[1]	UCL
78766	12	0.189	-0.017	0.030	0.032	0.034	0.214	0.153	NNN	UCL
78774	32	0.286	-0.016	0.033	0.019	0.035	-0.041	0.163	NNN	UCL
78795	37	0.265	-0.046	0.033	-0.019	0.033	-0.055	0.137	NNN	UCL
78809	91	0.062	-0.019	0.036	0.003	0.034	-0.110	0.117	NNN	US
78820	50	-0.354	0.584	0.003	-0.145	0.022	-0.053	0.019	NNN[1]	US
78826	44	0.078	0.006	0.028	0.019	0.029	0.384	0.090	NNY	UCL
78830	63	0.248	-0.012	0.033	0.056	0.033	0.340	0.126	NNN	US
78847	89	0.167	0.002	0.038	0.003	0.037	-0.039	0.096	NNN	US
78853	55	0.169	0.022	0.033	0.030	0.033	0.023	0.103	NNN	UCL
78877	61	0.106	-0.048	0.054	-0.136	0.051	0.137	0.070	NNN	US
78910	13	0.267	-0.008	0.034	0.038	0.035	0.357	0.160	NNN	US
78918	72	0.122	0.434	0.064	-0.071	0.057	-0.038	0.060	NNN	UCL
78933	91	0.151	0.709	0.069	-0.187	0.064	-0.262	0.105	NNN	US
78943	49	1.207	0.998	0.063	3.577	0.054	5.243	0.053	NYY	US
78956	93	0.172	-0.028	0.036	0.061	0.035	0.466	0.079	NNY	US
78963	72	0.237	-0.015	0.034	0.016	0.035	0.009	0.117	NNN	US
78968	89	0.034	-0.037	0.036	0.066	0.034	0.548	0.081	NNY	US
78996	86	0.231	0.002	0.035	0.318	0.035	1.421	0.055	NYY	US
79031	88	-0.054	0.013	0.045	-0.056	0.043	-0.056	0.074	NNN[1]	US
79044	81	-0.084	-0.049	0.039	-0.058	0.037	-0.016	0.082	NNN	UCL
79046	5	0.157	0.058	0.053	0.024	0.051	0.068	0.062	NNN	UCL
79054	91	0.321	-0.012	0.033	0.123	0.039	0.400	0.150	NNN	US
79078	58	0.187	-0.030	0.033	0.037	0.035	-0.066	0.225	NNN	US
79080	51	1.521	1.150	0.071	2.655	0.072	3.751	0.073	NNN[1]	UCL

Continued on next page

79081	63	-0.001	-0.030	0.040	0.039	0.091	0.640	0.407	NNN	UCL
79097	66	0.347	0.001	0.036	0.035	0.035	0.142	0.088	NNN	US
79098	55	0.029	0.196	0.054	-0.013	0.050	0.353	0.058	YNY	US
79124	82	0.180	0.010	0.039	0.014	0.037	0.178	0.082	NNN	US
79142	54	0.222	0.006	0.027	0.078	0.030	0.181	0.188	NNN	US
79156	88	0.111	-0.004	0.035	0.272	0.034	1.032	0.061	NYY	US
79197	23	0.080	-0.041	0.032	-0.059	0.035	-0.558	0.336	NNN	UCL
79229	76	-0.005	-0.033	0.046	-0.015	0.044	0.248	0.065	NNN[1]	US
79230	6	0.253	0.349	0.045	0.805	0.042	1.444	0.044	NNN[1]	UCL
79235	23	0.045	0.055	0.046	-0.002	0.044	0.038	0.066	NNN	US
79250	92	0.124	-0.017	0.034	0.053	0.034	0.195	0.107	NNN	US
79288	87	0.199	0.162	0.031	2.730	0.032	4.615	0.032	YYY	US
79317	19	0.262	0.017	0.033	0.056	0.033	0.131	0.162	NNN	UCL
79363	71	0.155	-0.112	0.037	-0.172	0.037	-0.241	0.090	NNN[1]	US
79366	87	0.178	-0.016	0.036	-0.029	0.034	0.062	0.109	NNN	US
79369	82	0.293	-0.010	0.032	0.015	0.033	-0.020	0.137	NNN	US
79372	33	-0.007	0.009	0.044	-0.021	0.044	0.023	0.063	NNN	UCL
79374	72	0.092	0.567	0.061	-0.114	0.059	-0.213	0.154	NNN	US
79383	74	0.297	-0.010	0.033	0.171	0.033	1.018	0.075	NNY	US
79392	86	0.225	0.007	0.034	0.024	0.035	0.256	0.121	NNN	US
79399	82	0.056	0.103	0.057	-0.100	0.053	-0.116	0.060	NNN[1]	US
79400	54	0.136	-0.052	0.028	-0.069	0.029	0.370	0.068	NNN[1]	UCL
79404	82	0.004	0.513	0.064	0.195	0.056	0.927	0.116	NNN[1]	US
79410	79	0.103	0.006	0.036	0.338	0.033	1.325	0.050	NYY	US
79439	63	0.110	0.014	0.037	0.160	0.037	0.766	0.063	NNY	US
79454	28	0.257	-0.015	0.035	0.013	0.037	0.186	0.260	NNN	US
79470	5	0.091	-0.034	0.035	-0.008	0.052	-0.446	0.306	NNN	UCL
79476	80	0.997	1.005	0.055	3.806	0.046	5.197	0.043	NNN[1]	US
79478	19	0.384	0.027	0.035	0.134	0.034	0.352	0.081	NNN	UCL
79516	77	0.229	-0.033	0.030	0.056	0.030	2.261	0.044	NNY	UCL
79530	79	0.077	0.012	0.047	-0.109	0.045	-0.129	0.065	NNN	US
79534	12	0.101	-0.028	0.035	-0.051	0.035	-0.275	0.167	NNN	US
79552	35	0.296	0.006	0.036	0.027	0.034	-0.140	0.102	NNN	US
79599	85	-0.010	-0.063	0.043	-0.107	0.042	-0.093	0.082	NNN[1]	US
79610	46	0.332	-0.062	0.028	-0.058	0.030	-0.189	0.183	NNN	UCL

Continued on next page

79622	76	0.038	0.015	0.049	-0.061	0.047	0.699	0.061	NNN[1]	US
79631	86	0.328	-0.084	0.039	0.244	0.038	1.687	0.043	NNN[1]	UCL
79643	34	0.335	0.001	0.034	0.036	0.035	0.471	0.156	NNN	US
79673	83	0.208	-0.035	0.030	0.041	0.033	0.251	0.137	NNN	UCL
79690	70	0.181	-0.015	0.036	-0.032	0.036	0.002	0.111	NNN	US
79705	11	0.169	-0.018	0.031	-0.022	0.041	0.083	0.477	NNN	UCL
79706	11	0.188	-0.023	0.040	-0.039	0.039	0.001	0.079	NNN	US
79710	79	0.169	0.003	0.034	0.032	0.046	0.870	0.104	NNY	UCL
79733	36	0.229	-0.031	0.031	-0.050	0.033	0.314	0.165	NNN	US
79734	42	0.303	-0.019	0.036	-0.043	0.034	0.008	0.120	NNN	US
79739	65	0.215	-0.003	0.037	-0.030	0.034	0.109	0.087	NNN	US
79742	76	0.210	-0.009	0.033	0.142	0.033	1.989	0.051	NNY	UCL
79771	89	0.227	0.000	0.035	-0.020	0.038	-0.002	0.113	NNN	US
79785	77	0.029	0.014	0.041	-0.020	0.040	0.060	0.070	NNN	US
79793	30	0.293	-0.016	0.032	-0.020	0.037	-0.268	0.232	NNN	US
79794	9	0.048	-0.034	0.033	-0.043	0.034	0.007	0.118	NNN	UCL
79806	18	0.182	0.009	0.030	0.049	0.032	0.066	0.202	NNN	US
79842	15	0.201	-0.017	0.032	0.009	0.033	-0.091	0.173	NNN	UCL
79860	72	0.023	0.049	0.029	0.058	0.031	0.141	0.165	NNN	US
79878	89	-0.012	-0.025	0.035	0.218	0.035	1.103	0.059	NYY	US
79897	90	0.066	0.010	0.035	0.010	0.035	0.158	0.079	NNN	US
79909	36	0.274	-0.003	0.034	-0.016	0.036	-0.017	0.156	NNN	US
79910	88	0.296	-0.026	0.034	-0.005	0.034	-0.018	0.140	NNN	US
79977	90	0.262	-0.008	0.034	0.345	0.033	3.459	0.035	NYY	US
79983	46	0.379	0.012	0.033	0.060	0.034	-0.016	0.148	NNN	UCL
80019	27	0.168	0.027	0.038	0.406	0.045	1.286	0.102	NYY	US
80024	82	0.077	-0.028	0.039	0.068	0.045	1.436	0.052	NNY	US
80036	68	0.300	-0.072	0.022	-0.083	0.025	-0.022	0.198	NNN	US
80059	84	0.265	0.001	0.035	0.015	0.036	0.075	0.112	NNN	US
80062	57	0.248	-0.065	0.041	0.017	0.060	0.691	0.189	NNN[1]	US
80088	87	0.247	-0.001	0.033	0.175	0.034	1.497	0.061	NNY	US
80089	18	0.363	-0.049	0.034	-0.019	0.034	0.039	0.114	NNN	UCL
80108	7	0.295	0.056	0.029	0.097	0.031	0.260	0.148	NNN	US
80126	86	0.147	0.350	0.030	1.104	0.029	2.788	0.037	NNN[1]	US
80130	89	0.247	0.032	0.030	0.021	0.030	0.141	0.107	NNN	US

Continued on next page

80142	38	-0.036	0.013	0.042	-0.015	0.044	-0.065	0.126	NNN	UCL
80167	8	0.076	-0.024	0.041	-0.053	0.040	-0.114	0.071	NNN	UCL
80208	48	0.021	0.302	0.063	-0.094	0.069	0.379	0.330	NNN[1]	UCL
80224	36	0.291	0.069	0.025	0.096	0.027	0.279	0.105	NNN	US
80238	92	0.229	-0.018	0.041	0.109	0.041	0.681	0.064	NNY	US
80311	86	0.180	0.010	0.033	-0.009	0.033	0.188	0.182	NNN	US
80324	92	-0.024	0.030	0.051	0.067	0.050	-0.039	0.163	NNN	US
80371	85	0.482	-0.010	0.048	-0.104	0.047	0.061	0.068	NNN	US
80390	79	-0.046	0.105	0.055	-0.061	0.053	-0.002	0.061	NNN	UCL
80425	66	0.372	0.002	0.037	1.034	0.036	1.799	0.047	NNN[1]	US
80458	49	0.293	0.005	0.034	0.337	0.032	2.375	0.038	NYY	US
80461	81	0.269	0.337	0.059	0.071	0.054	0.011	0.067	NNN[1]	US
80474	43	0.333	0.301	0.063	0.479	0.055	0.593	0.065	NNN[1]	US
80475	52	0.222	0.003	0.044	-0.017	0.042	-0.055	0.065	NNN	US
80493	86	0.222	0.004	0.038	-0.019	0.036	0.036	0.091	NNN	US
80497	26	0.221	-0.023	0.032	0.030	0.033	0.289	0.130	NNN	US
80535	90	0.336	0.007	0.036	0.007	0.035	-0.090	0.122	NNN	US
80557	24	-0.023	-0.062	0.036	0.023	0.071	0.827	0.206	NNN[1]	UCL
80569	55	0.519	1.077	0.010	2.002	0.013	2.584	0.023	NNN[1]	US
80582	35	0.039	0.557	0.065	-0.015	0.058	0.028	0.067	NNN	UCL
80591	84	0.099	-0.065	0.029	-0.044	0.030	-0.156	0.171	NNN	UCL
80711	53	0.330	-0.018	0.035	-0.003	0.034	0.025	0.114	NNN	US
80799	91	0.155	0.005	0.033	0.087	0.040	1.035	0.094	NNY	US
80813	24	0.226	-0.021	0.036	-0.008	0.035	0.098	0.099	NNN	UCL
80815	62	-0.061	0.288	0.065	-0.078	0.061	0.109	0.073	NNN	US
80851	24	0.291	0.005	0.032	0.056	0.038	-0.282	0.486	NNN	US
80896	86	0.241	-0.005	0.034	-0.001	0.035	0.005	0.132	NNN	US
80897	46	0.081	0.002	0.030	0.721	0.030	2.924	0.034	NNN[1]	UCL
80911	85	0.046	0.365	0.065	-0.014	0.060	0.980	0.067	NNN[1]	UCL
80921	36	0.278	0.005	0.033	0.067	0.041	1.006	0.148	NNN[1]	UCL
81006	34	0.075	-0.024	0.038	-0.041	0.042	-0.485	0.240	NNN	UCL
81039	9	0.127	-0.006	0.034	0.008	0.034	0.215	0.105	NNN	UCL
81044	21	0.300	-0.060	0.035	-0.068	0.036	-0.198	0.162	NNN	UCL
81092	30	0.215	0.104	0.031	0.086	0.031	0.000	0.081	YNN	UCL
81184	8	0.309	-0.024	0.030	0.003	0.044	0.289	0.381	NNN	US

Continued on next page

81208	58	-0.037	-0.040	0.041	-0.093	0.041	-0.123	0.098	NNN	UCL
81266	89	-0.261	0.517	0.092	-0.180	0.085	0.071	0.111	NNN	US
81316	41	0.030	0.028	0.040	0.030	0.039	0.415	0.066	NNY	UCL
81327	6	0.225	-0.015	0.033	-0.015	0.033	-0.244	0.226	NNN	US
81368	22	0.035	-0.067	0.035	-0.105	0.035	0.344	0.079	NNN	UCL
81447	59	0.369	-0.003	0.033	0.044	0.032	0.575	0.097	NNY	UCL
81455	76	0.220	-0.027	0.036	-0.023	0.036	0.111	0.226	NNN	US
81472	22	-0.069	0.018	0.052	-0.088	0.051	0.118	0.069	NNN	UCL
81474	91	0.206	0.202	0.053	0.298	0.049	1.866	0.051	NNN[1]	US
81477	53	-0.043	-0.147	0.029	-0.202	0.031	-0.008	0.085	NNN	UCL
81582	34	0.197	-0.015	0.033	-0.003	0.035	0.329	0.190	NNN	US
81589	20	0.206	0.065	0.050	0.108	0.047	0.241	0.053	NNN[1]	UCL
81624	79	1.471	1.209	0.074	3.433	0.066	4.950	0.065	YYY	US
81639	11	0.093	0.019	0.050	-0.060	0.048	0.452	0.058	NNN[1]	UCL
81692	37	0.000	-0.053	0.034	-0.037	0.036	-0.223	0.157	NNN	UCL
81751	78	0.224	-0.014	0.035	0.022	0.038	0.311	0.241	NNN	UCL
81772	38	0.452	0.026	0.032	0.096	0.035	0.160	0.116	NNN	UCL
81791	17	0.228	-0.026	0.039	0.591	0.108	2.154	0.388	NNN[1]	UCL
81887	9	0.224	0.006	0.039	-0.028	0.037	-0.135	0.081	NNN	US
81891	58	-0.052	-0.065	0.040	0.335	0.039	2.126	0.045	NNN[1]	UCL
81914	58	-0.082	0.014	0.042	-0.077	0.045	-0.395	0.210	NNN	UCL
81941	44	0.106	-0.015	0.039	-0.046	0.038	0.089	0.094	NNN	US
81949	74	0.102	-0.039	0.037	-0.006	0.058	0.444	0.238	NNN	UCL
81972	59	-0.031	0.092	0.050	0.290	0.048	0.735	0.056	NNN[1]	UCL
82069	51	0.024	-0.008	0.039	0.119	0.037	1.089	0.053	NNY	US
82091	11	0.069	-0.123	0.039	-0.018	0.050	0.660	0.274	NNN[1]	UCL
82154	16	-0.041	-0.052	0.038	0.170	0.043	1.266	0.096	NYY	UCL
82187	9	-0.002	-0.021	0.036	-0.020	0.035	-0.031	0.117	NNN	UCL
82208	19	0.249	-0.034	0.033	-0.030	0.034	0.046	0.114	NNN	UCL
82218	89	0.257	-0.030	0.033	0.072	0.033	0.819	0.090	NNY	US
82250	43	0.307	-0.018	0.033	0.099	0.039	1.408	0.139	NNN[1]	UCL
82254	16	-0.062	0.034	0.036	-0.009	0.035	0.268	0.101	NNN	UCL
82271	12	0.092	-0.009	0.034	0.000	0.035	-0.158	0.284	NNN	US
82309	6	0.279	-0.024	0.034	-0.028	0.035	-0.241	0.233	NNN	UCL
82319	51	0.167	-0.020	0.031	-0.012	0.034	-0.241	0.260	NNN	US

Continued on next page

82397	81	0.019	-0.028	0.032	0.049	0.032	0.777	0.069	NNY	US
82430	78	-0.043	0.000	0.034	-0.048	0.036	-0.021	0.133	NNN	UCL
82514	65	-0.238	0.581	0.066	-0.142	0.058	-0.018	0.060	YNN	UCL
82534	89	0.230	-0.014	0.035	-0.014	0.035	-0.015	0.116	NNN	US
82545	86	-0.142	0.659	0.062	-0.064	0.057	-0.117	0.060	NNN	UCL
82549	21	0.160	-0.008	0.032	0.012	0.043	0.544	0.358	NNN	UCL
82554	71	-0.082	0.010	0.043	-0.040	0.043	0.095	0.074	NNN	UCL
82569	63	0.355	-0.016	0.035	-0.021	0.041	-0.270	0.228	NNN	UCL
82663	18	0.219	-0.547	0.021	-0.673	0.022	-0.682	0.062	NNN[1]	UCL
82711	9	0.242	0.034	0.046	0.007	0.052	0.112	0.152	NNN	UCL
82714	54	0.138	0.240	0.041	1.128	0.039	1.697	0.049	YYY	UCL
82736	10	0.320	-0.017	0.033	-0.005	0.040	0.246	0.286	NNN	US
83061	24	0.207	0.006	0.029	0.046	0.033	0.091	0.232	NNN	US
83074	11	0.322	-0.028	0.032	-0.042	0.035	-0.161	0.264	NNN	UCL
83159	62	0.232	-0.015	0.033	0.143	0.035	0.985	0.092	NNY	UCL
83232	11	1.420	0.477	0.044	2.186	0.048	4.260	0.042	YYY	UCL
83321	20	0.139	0.157	0.058	0.015	0.053	-0.101	0.065	NNN[1]	UCL
83421	6	0.588	0.257	0.031	4.043	0.029	7.256	0.027	YYY	UCL
83457	31	0.186	0.008	0.042	-0.105	0.048	-0.299	0.220	NNN	UCL
83460	28	0.332	-0.140	0.033	-0.225	0.046	0.000	0.281	NNN	UCL
83508	64	-0.049	-0.024	0.037	-0.026	0.037	-0.030	0.116	NNN	UCL
83535	11	-0.067	0.089	0.050	-0.028	0.048	-0.044	0.062	NNN[1]	UCL
83611	13	0.073	-0.058	0.033	-0.077	0.054	-0.004	0.334	NNN	UCL
83637	12	0.246	-0.059	0.030	-0.028	0.034	-0.111	0.293	NNN	UCL
84222	5	0.180	-0.035	0.033	-0.065	0.037	-0.664	0.497	NNN	UCL
84267	8	0.009	-0.031	0.036	-0.058	0.035	-0.139	0.091	NNN	UCL
84445	37	-0.002	0.095	0.043	0.064	0.041	0.324	0.060	NNN[1]	UCL
84473	23	0.292	-0.030	0.033	0.057	0.035	0.344	0.157	NNN	UCL
84565	7	0.274	-0.011	0.033	0.018	0.034	0.183	0.122	NNN	UCL
84593	17	0.237	-0.041	0.033	0.002	0.036	-0.029	0.231	NNN	UCL
84605	42	-0.041	-0.001	0.044	0.023	0.044	0.145	0.145	NNN	UCL
84657	13	-0.018	-0.031	0.037	-0.049	0.036	-0.095	0.096	NNN	UCL
84673	8	0.316	-0.006	0.045	0.341	0.087	1.211	0.409	NNN[1]	UCL
84734	29	0.068	-0.045	0.040	-0.020	0.040	0.281	0.079	NNN[1]	UCL
84766	6	0.311	-0.021	0.033	-0.027	0.037	-0.651	0.275	NNN	UCL

Continued on next page

84881	14	0.079	0.135	0.037	1.388	0.036	4.203	0.036	YYY	UCL
84888	16	0.282	0.087	0.027	-0.071	0.028	-0.054	0.078	NNN[1]	UCL
84931	38	0.111	-0.040	0.039	-0.074	0.039	-0.207	0.146	NNN	UCL
85278	18	0.120	0.052	0.048	0.004	0.047	0.071	0.079	NNN	UCL
85316	6	0.009	-0.044	0.037	-0.116	0.076	0.587	0.425	NNN	UCL
85389	5	0.015	0.146	0.062	-0.142	0.057	-0.026	0.062	YNN	UCL
85478	9	0.304	-0.049	0.035	-0.018	0.038	0.364	0.104	NNN	UCL
85663	13	0.269	-0.027	0.035	-0.002	0.036	-0.107	0.138	NNN	UCL
85700	16	0.060	0.025	0.041	-0.008	0.057	0.040	0.240	NNN	UCL
85927	10	-0.101	1.362	0.006	1.170	0.017	0.868	0.018	NNN[1]	UCL
86010	10	0.336	-0.026	0.033	0.020	0.036	0.109	0.184	NNN	UCL
86098	15	0.048	-0.029	0.047	-0.102	0.046	-0.231	0.081	NNN	UCL
86134	8	0.273	-0.006	0.035	0.016	0.034	0.048	0.111	NNN	UCL
86670	16	-0.202	0.683	0.034	-0.020	0.026	-0.085	0.035	NNN[1]	UCL
86853	17	0.191	0.026	0.033	0.483	0.035	1.984	0.050	NYY	UCL
86903	6	0.250	-0.045	0.032	-0.057	0.034	0.022	0.109	NNN	UCL
86922	6	0.189	-0.026	0.034	-0.001	0.044	-0.300	0.505	NNN	UCL
87042	30	-0.016	-0.029	0.044	-0.071	0.042	-0.180	0.082	NNN	UCL
87198	7	0.215	-0.031	0.035	-0.020	0.034	0.133	0.104	NNN	UCL
87337	9	0.175	-0.028	0.031	0.021	0.031	0.156	0.146	NNN	UCL
87924	13	-0.010	-0.014	0.039	-0.046	0.038	0.104	0.068	NNN[1]	UCL
87948	37	0.037	0.127	0.043	0.068	0.042	0.035	0.069	NNN[1]	UCL

B

WiFeS Survey Target Sample

A list of candidate Upper-Scorpius members selected using our Bayesian algorithm, with membership probability greater than 30%. The name assigned to each object is the UCAC4 catalogue unique source identifier.

Name	R.A. (J2000.0)	Decl. (J2000.0)	Membership Probability
UCAC4-1274289939	15 23 0.73	-20 31 58.5	55
UCAC4-1274343607	15 24 50.48	-21 2 32.1	38
UCAC4-404261480	15 25 38.44	-21 36 12.9	22
UCAC4-1271299866	15 28 51.44	-20 21 35.8	23
UCAC4-53027571	15 29 43.59	-24 24 6.9	74
UCAC4-1271354629	15 30 55.45	-20 11 16.5	24
UCAC4-1271358935	15 31 7.46	-22 7 25.8	43
UCAC4-334583373	15 32 18.94	-23 26 57.0	71

Continued on next page

UCAC4-334584116	15 32 48.81	-23 8 12.3	81
UCAC4-334610300	15 33 17.26	-23 25 34.1	40
UCAC4-53157842	15 34 7.05	-24 52 34.6	38
UCAC4-53160115	15 34 8.68	-24 1 23.3	21
UCAC4-334645691	15 34 26.67	-22 54 28.6	53
UCAC4-334648825	15 34 36.36	-21 42 29.1	24
UCAC4-29975139	15 35 29.53	-23 6 59.0	40
UCAC4-53181945	15 35 32.30	-25 37 14.1	53
UCAC4-365026104	15 37 9.36	-24 15 4.3	74
UCAC4-30033418	15 37 11.90	-23 39 5.7	47
UCAC4-365031481	15 37 42.74	-25 26 15.8	74
UCAC4-30043724	15 37 49.29	-20 29 18.3	67
UCAC4-30046627	15 37 49.43	-19 20 57.2	21
UCAC4-365060511	15 38 16.02	-24 55 26.3	31
UCAC4-1238093662	15 38 35.66	-17 44 6.5	50
UCAC4-365067569	15 38 52.05	-25 15 5.9	21
UCAC4-1056237523	15 39 29.69	-23 11 19.9	55
UCAC4-404322052	15 40 27.32	-19 57 43.7	53
UCAC4-1238144790	15 40 35.05	-17 7 23.8	50
UCAC4-408457366	15 41 2.57	-25 58 31.1	43
UCAC4-408484365	15 41 31.21	-25 20 36.4	74
UCAC4-1312371465	15 42 26.21	-22 47 46.0	90
UCAC4-1312378752	15 42 41.43	-22 19 4.6	26
UCAC4-408521330	15 42 49.92	-25 36 40.6	40
UCAC4-408568502	15 44 13.34	-25 22 59.1	77
UCAC4-408606874	15 45 9.71	-25 12 43.0	47
UCAC4-30113549	15 45 58.30	-18 41 20.6	45
UCAC4-30105437	15 46 0.86	-21 43 53.6	53
UCAC4-30124029	15 46 8.27	-21 0 52.9	95
UCAC4-408646921	15 46 27.26	-25 18 46.8	53
UCAC4-30145199	15 46 44.25	-19 28 48.3	23
UCAC4-30144221	15 46 47.59	-19 50 27.9	42
UCAC4-1233680087	15 47 10.64	-17 36 24.3	74
UCAC4-30164182	15 47 36.01	-23 19 17.4	55
UCAC4-30182208	15 47 43.31	-18 19 15.4	85

Continued on next page

UCAC4-30199855	15 48 12.99	-23 49 52.5	57
UCAC4-408723067	15 48 16.15	-24 41 17.1	24
UCAC4-30190809	15 48 18.61	-20 35 49.5	35
UCAC4-408722277	15 48 30.31	-24 25 38.4	35
UCAC4-408735673	15 48 32.74	-28 44 15.6	22
UCAC4-408732652	15 48 39.92	-27 49 46.1	65
UCAC4-30231541	15 49 19.76	-22 57 29.7	90
UCAC4-408765529	15 49 21.00	-26 0 6.3	77
UCAC4-408774136	15 49 25.09	-28 43 52.8	85
UCAC4-408760488	15 49 43.60	-24 14 29.4	21
UCAC4-1285802339	15 50 3.25	-23 42 2.2	81
UCAC4-1285824843	15 50 20.79	-21 16 54.7	25
UCAC4-1317698993	15 50 49.08	-16 34 48.3	47
UCAC4-1285835000	15 50 49.67	-22 46 12.2	74
UCAC4-1285865711	15 51 50.27	-22 38 18.8	49
UCAC4-408869666	15 52 19.71	-25 31 22.3	27
UCAC4-408859661	15 52 21.72	-28 36 9.3	34
UCAC4-1285885191	15 52 23.32	-21 15 30.2	49
UCAC4-408867018	15 52 23.48	-26 21 57.3	62
UCAC4-408882874	15 52 31.23	-26 33 52.9	32
UCAC4-1285890115	15 52 34.03	-23 11 27.2	77
UCAC4-408888405	15 52 34.63	-28 15 16.0	90
UCAC4-1297441557	15 52 41.59	-30 6 17.2	85
UCAC4-1317767989	15 53 4.69	-17 37 55.8	62
UCAC4-1285895575	15 53 6.83	-22 47 17.4	90
UCAC4-1317768809	15 53 7.40	-17 19 39.7	43
UCAC4-70100979	15 53 37.88	-23 39 0.5	55
UCAC4-70109425	15 53 40.82	-20 26 41.9	67
UCAC4-408918468	15 53 47.13	-25 33 43.1	65
UCAC4-408935154	15 54 3.58	-29 20 15.6	59
UCAC4-1297496169	15 54 11.99	-30 36 46.7	30
UCAC4-70135113	15 54 15.51	-22 46 59.6	31
UCAC4-417143635	15 54 23.93	-15 48 32.5	36
UCAC4-1264581192	15 54 29.76	-15 53 15.8	74
UCAC4-1297544976	15 54 39.21	-29 58 49.2	36

Continued on next page

UCAC4-408954783	15 54 46.93	-24 44 34.8	55
UCAC4-408967020	15 54 53.94	-28 53 41.4	40
UCAC4-408962807	15 54 55.63	-27 33 33.1	95
UCAC4-70157647	15 55 2.14	-21 49 43.5	77
UCAC4-1264602095	15 55 4.51	-17 5 8.1	85
UCAC4-426462564	15 55 6.25	-25 21 10.2	77
UCAC4-70165308	15 55 17.04	-23 22 16.6	85
UCAC4-426463797	15 55 29.81	-25 44 50.0	85
UCAC4-70176781	15 55 33.05	-18 55 26.8	59
UCAC4-426495718	15 55 48.82	-25 12 24.1	40
UCAC4-1264606373	15 55 52.07	-17 7 17.0	23
UCAC4-426495785	15 55 54.20	-25 11 21.7	42
UCAC4-426492998	15 55 54.88	-26 4 26.3	81
UCAC4-426483345	15 56 6.96	-28 52 41.4	57
UCAC4-1264625269	15 56 19.98	-15 2 53.6	34
UCAC4-426514557	15 56 20.26	-28 20 6.5	43
UCAC4-70205421	15 56 25.11	-20 16 15.8	90
UCAC4-70196012	15 56 29.42	-23 48 19.8	36
UCAC4-1264642046	15 56 31.13	-13 52 22.7	45
UCAC4-404419461	15 56 47.69	-19 50 7.6	81
UCAC4-1030709628	15 56 49.33	-30 48 3.1	34
UCAC4-404411726	15 56 55.46	-22 58 40.4	90
UCAC4-426535872	15 56 59.30	-25 38 53.5	81
UCAC4-426535749	15 56 59.70	-25 41 25.5	45
UCAC4-404418024	15 57 0.85	-20 24 59.5	85
UCAC4-404419435	15 57 2.35	-19 50 42.0	74
UCAC4-404410416	15 57 3.66	-23 28 7.1	25
UCAC4-404415438	15 57 11.39	-21 28 28.3	85
UCAC4-426546698	15 57 16.74	-25 29 19.3	65
UCAC4-1010063466	15 57 20.00	-23 38 50.0	59
UCAC4-426541656	15 57 25.75	-23 54 22.3	81
UCAC4-1010064430	15 57 34.31	-23 21 12.3	85
UCAC4-1010069431	15 57 45.75	-21 44 28.8	45
UCAC4-404426496	15 57 50.03	-23 5 9.5	90
UCAC4-404425922	15 57 53.96	-23 17 41.7	81

Continued on next page

UCAC4-426579903	15 57 54.45	-24 50 42.4	74
UCAC4-404438620	15 57 58.92	-18 14 59.6	81
UCAC4-426582260	15 58 8.15	-24 5 53.0	43
UCAC4-1264679821	15 58 8.87	-13 44 53.8	71
UCAC4-404425413	15 58 12.71	-23 28 36.5	71
UCAC4-404432237	15 58 19.07	-20 54 24.1	81
UCAC4-404441472	15 58 20.56	-18 37 25.1	71
UCAC4-404455253	15 58 26.62	-23 50 20.6	39
UCAC4-404450689	15 58 29.63	-22 11 11.9	81
UCAC4-404442427	15 58 33.28	-19 0 36.7	45
UCAC4-1264690120	15 58 47.72	-17 57 59.7	71
UCAC4-1014080644	15 59 2.08	-18 44 14.3	65
UCAC4-27426533	15 59 10.29	-26 46 50.0	38
UCAC4-27424694	15 59 10.85	-27 20 52.0	39
UCAC4-1014080885	15 59 11.02	-18 50 44.3	81
UCAC4-27428773	15 59 14.52	-26 6 18.5	47
UCAC4-1264711772	15 59 21.22	-14 51 42.7	23
UCAC4-1264732846	15 59 36.26	-12 21 16.6	77
UCAC4-27437351	15 59 42.45	-24 29 40.5	38
UCAC4-404463645	15 59 51.27	-20 58 10.7	24
UCAC4-27470462	15 59 52.70	-25 26 29.2	81
UCAC4-404477376	15 59 59.95	-22 20 36.8	90
UCAC4-404476771	16 0 0.37	-22 32 59.5	85
UCAC4-27473795	16 0 13.30	-24 18 10.7	85
UCAC4-404481169	16 0 14.91	-21 1 31.7	36
UCAC4-404494714	16 0 29.13	-19 52 53.8	59
UCAC4-1264749634	16 0 36.61	-17 43 37.4	57
UCAC4-404500621	16 0 40.56	-22 0 32.3	81
UCAC4-404502792	16 0 41.35	-22 40 41.6	90
UCAC4-404499023	16 0 42.76	-21 27 38.0	67
UCAC4-27503319	16 1 2.79	-27 49 1.4	90
UCAC4-404511451	16 1 5.19	-22 27 31.2	85
UCAC4-38879233	16 1 5.92	-30 16 37.2	49
UCAC4-404514932	16 1 8.02	-21 13 18.5	77
UCAC4-404511804	16 1 16.80	-22 20 2.2	25

Continued on next page

UCAC4-4524501	16 1 25.63	-22 40 40.3	67
UCAC4-4525525	16 1 32.73	-22 19 37.8	24
UCAC4-4529694	16 1 47.44	-20 49 45.8	81
UCAC4-1264782313	16 1 48.00	-16 37 59.0	45
UCAC4-27518857	16 1 51.49	-24 45 25.0	74
UCAC4-4546970	16 1 56.47	-21 37 3.9	59
UCAC4-4543024	16 1 58.22	-20 8 12.0	62
UCAC4-4549054	16 2 0.39	-22 21 23.9	77
UCAC4-1264802922	16 2 1.50	-15 36 44.0	67
UCAC4-4538373	16 2 2.64	-18 18 54.0	23
UCAC4-4550645	16 2 8.45	-22 54 59.1	90
UCAC4-1264798836	16 2 9.26	-13 55 56.7	32
UCAC4-4550018	16 2 10.46	-22 41 28.3	40
UCAC4-4548058	16 2 24.61	-22 0 24.8	81
UCAC4-4561055	16 2 27.25	-21 33 29.0	23
UCAC4-27573643	16 2 31.96	-28 13 45.2	39
UCAC4-27566188	16 2 33.43	-26 10 19.1	85
UCAC4-4556306	16 2 44.78	-23 12 49.0	30
UCAC4-4560593	16 2 49.77	-21 43 53.6	24
UCAC4-4568409	16 2 50.13	-18 51 4.1	53
UCAC4-27559105	16 2 51.22	-24 1 57.5	67
UCAC4-4564260	16 2 53.96	-20 22 48.0	65
UCAC4-38946162	16 2 55.75	-32 45 22.3	42
UCAC4-1264828916	16 2 59.41	-13 52 3.2	32
UCAC4-27564826	16 3 0.18	-25 46 10.9	50
UCAC4-27567164	16 3 1.77	-26 26 21.9	95
UCAC4-4571559	16 3 2.68	-18 6 5.0	65
UCAC4-4584884	16 3 6.76	-22 52 15.8	24
UCAC4-38945736	16 3 11.81	-32 39 20.3	40
UCAC4-1264849530	16 3 26.28	-13 53 38.7	21
UCAC4-4591451	16 3 33.80	-23 5 19.0	57
UCAC4-4592427	16 3 35.50	-22 45 56.2	50
UCAC4-4599020	16 3 54.98	-20 31 38.5	71
UCAC4-27617578	16 3 55.70	-28 2 39.2	53
UCAC4-4619594	16 4 4.09	-22 36 52.3	59

Continued on next page

UCAC4-27638513	16 4 6.71	-26 37 7.1	85
UCAC4-4609404	16 4 8.31	-19 7 29.5	71
UCAC4-322299460	16 4 23.97	-11 46 31.0	35
UCAC4-4638115	16 4 47.75	-19 30 22.9	67
UCAC4-1264894990	16 4 51.62	-16 7 31.5	30
UCAC4-1264887692	16 4 52.50	-13 8 13.2	57
UCAC4-39040605	16 4 54.51	-31 5 10.3	24
UCAC4-27649164	16 5 1.81	-24 11 32.8	90
UCAC4-1264893466	16 5 2.64	-15 30 28.4	36
UCAC4-4647509	16 5 11.46	-19 32 52.2	59
UCAC4-4653894	16 5 12.93	-21 36 17.6	24
UCAC4-27683816	16 5 18.03	-26 37 25.5	49
UCAC4-4644043	16 5 21.59	-18 21 41.4	62
UCAC4-322353364	16 5 30.32	-11 49 13.5	24
UCAC4-415794766	16 5 31.54	-19 45 43.6	27
UCAC4-27677763	16 5 31.88	-28 16 34.4	34
UCAC4-27680291	16 5 35.30	-27 35 52.3	42
UCAC4-415797428	16 5 38.16	-20 39 47.0	67
UCAC4-415800069	16 5 39.25	-21 34 7.3	21
UCAC4-415791233	16 5 40.75	-18 30 32.7	29
UCAC4-39099220	16 5 49.20	-31 15 21.5	50
UCAC4-1264922004	16 6 0.89	-14 53 20.5	34
UCAC4-415812954	16 6 1.72	-22 26 53.5	71
UCAC4-27705406	16 6 8.41	-27 18 36.0	39
UCAC4-39109215	16 6 16.62	-30 48 38.5	35
UCAC4-415808470	16 6 17.31	-23 49 23.7	36
UCAC4-415825482	16 6 23.54	-18 14 18.9	57
UCAC4-415822163	16 6 26.30	-19 24 60.0	65
UCAC4-50931256	16 6 31.69	-20 36 23.3	85
UCAC4-50936058	16 6 32.46	-22 8 24.6	32
UCAC4-50941266	16 6 37.91	-23 43 32.6	49
UCAC4-27726068	16 6 38.03	-27 27 55.4	95
UCAC4-50941237	16 6 38.25	-23 43 3.8	85
UCAC4-50940712	16 6 38.58	-23 33 33.7	32
UCAC4-1264938997	16 6 40.33	-14 7 47.8	22

Continued on next page

UCAC4-50927093	16 6 43.86	-19 8 5.6	74
UCAC4-50925875	16 6 47.94	-18 41 43.8	59
UCAC4-50930206	16 6 48.96	-20 14 39.1	55
UCAC4-50939230	16 6 50.30	-23 6 41.7	50
UCAC4-27740125	16 6 54.39	-24 16 10.8	71
UCAC4-27739597	16 6 58.19	-24 6 48.1	30
UCAC4-415841216	16 7 2.78	-22 49 48.1	90
UCAC4-415834199	16 7 3.55	-20 36 26.5	71
UCAC4-39180354	16 7 12.46	-33 2 26.6	65
UCAC4-27782618	16 7 21.60	-24 25 58.5	21
UCAC4-1264970082	16 7 21.61	-13 20 45.4	71
UCAC4-1264960881	16 7 23.13	-17 12 42.0	50
UCAC4-27782269	16 7 26.25	-24 32 7.9	85
UCAC4-27777972	16 7 29.43	-25 46 15.7	90
UCAC4-1264968743	16 7 32.21	-13 56 7.0	43
UCAC4-415861407	16 7 39.74	-18 44 0.8	47
UCAC4-415852329	16 7 40.06	-21 48 42.7	77
UCAC4-415857823	16 7 44.02	-20 0 15.3	30
UCAC4-1264986286	16 7 51.37	-17 18 23.2	85
UCAC4-27796091	16 7 56.38	-26 57 31.7	81
UCAC4-27787293	16 7 58.76	-24 41 31.9	95
UCAC4-1264982187	16 8 0.21	-15 38 53.1	24
UCAC4-27795606	16 8 1.39	-26 50 55.2	42
UCAC4-415856526	16 8 1.41	-20 27 41.7	81
UCAC4-415867155	16 8 10.81	-19 4 47.9	71
UCAC4-415874167	16 8 14.31	-21 30 4.1	62
UCAC4-415867341	16 8 14.74	-19 8 32.7	65
UCAC4-415880871	16 8 15.50	-23 30 19.0	38
UCAC4-415872012	16 8 15.60	-20 48 2.2	90
UCAC4-27824055	16 8 20.58	-26 4 42.5	59
UCAC4-39230957	16 8 29.08	-30 30 0.9	35
UCAC4-415864352	16 8 31.38	-18 2 41.5	50
UCAC4-415897816	16 8 34.36	-19 11 56.2	67
UCAC4-27829493	16 8 46.61	-24 30 29.2	71
UCAC4-27824633	16 8 46.83	-25 54 35.7	42

Continued on next page

UCAC4-1265007792	16 8 50.41	-14 15 31.6	38
UCAC4-39273829	16 8 56.12	-33 24 53.9	31
UCAC4-415893983	16 8 56.73	-20 33 45.9	71
UCAC4-27848808	16 8 56.96	-28 35 57.4	77
UCAC4-415897962	16 9 0.76	-19 8 52.7	34
UCAC4-1265007206	16 9 4.02	-14 0 31.6	22
UCAC4-27833090	16 9 4.58	-24 18 4.9	95
UCAC4-27853572	16 9 6.85	-29 44 31.6	36
UCAC4-39278900	16 9 10.58	-32 22 50.2	65
UCAC4-1265012644	16 9 12.63	-16 19 29.0	55
UCAC4-1265019864	16 9 20.42	-16 46 40.2	28
UCAC4-1265019806	16 9 22.70	-16 48 1.5	23
UCAC4-415904385	16 9 29.20	-18 52 53.7	65
UCAC4-415911029	16 9 30.31	-21 4 58.9	74
UCAC4-27877966	16 9 39.24	-23 53 40.8	67
UCAC4-415927254	16 9 39.70	-22 0 46.6	81
UCAC4-415928740	16 9 40.31	-21 31 40.4	40
UCAC4-415926287	16 9 40.99	-22 17 59.5	74
UCAC4-27875768	16 9 45.22	-24 31 18.6	74
UCAC4-1265018534	16 9 46.88	-17 19 44.9	65
UCAC4-39295193	16 9 54.86	-30 58 58.2	74
UCAC4-27866945	16 9 55.19	-26 57 27.5	40
UCAC4-415922108	16 9 58.63	-23 34 55.9	81
UCAC4-27891415	16 10 3.12	-27 28 39.7	90
UCAC4-415950434	16 10 5.02	-21 32 31.9	81
UCAC4-39346890	16 10 5.40	-31 24 25.8	38
UCAC4-415955987	16 10 11.65	-23 13 24.0	81
UCAC4-39341976	16 10 11.70	-32 26 36.0	53
UCAC4-415948957	16 10 12.65	-21 4 44.5	59
UCAC4-27889260	16 10 18.80	-26 53 39.5	81
UCAC4-27898077	16 10 24.19	-29 7 29.4	62
UCAC4-27893245	16 10 26.54	-27 56 29.4	25
UCAC4-39333239	16 10 26.99	-34 4 29.7	21
UCAC4-415943383	16 10 31.95	-19 13 6.1	81
UCAC4-415968729	16 10 42.03	-21 1 32.1	57

Continued on next page

UCAC4-415976918	16 10 47.34	-18 18 32.9	65
UCAC4-27920379	16 10 57.92	-25 11 10.2	95
UCAC4-415960223	16 11 4.80	-23 33 16.6	62
UCAC4-1014110439	16 11 7.44	-25 3 1.7	90
UCAC4-415981857	16 11 8.90	-19 4 46.9	67
UCAC4-417227445	16 11 10.62	-15 17 36.6	31
UCAC4-415979844	16 11 20.58	-18 20 55.1	65
UCAC4-1014105644	16 11 26.03	-26 31 55.9	85
UCAC4-415992278	16 11 28.88	-22 21 24.7	22
UCAC4-416011481	16 11 37.42	-20 15 50.5	40
UCAC4-416013160	16 11 56.26	-19 43 22.9	85
UCAC4-39419158	16 12 6.68	-30 10 27.1	59
UCAC4-416034611	16 12 9.21	-22 47 50.4	85
UCAC4-416033560	16 12 12.48	-22 30 32.2	57
UCAC4-27959343	16 12 22.17	-27 12 52.5	85
UCAC4-416037255	16 12 27.17	-23 31 56.1	81
UCAC4-27964993	16 12 30.76	-28 41 30.0	67
UCAC4-27960465	16 12 32.30	-27 32 13.3	67
UCAC4-416027053	16 12 35.31	-20 34 34.0	74
UCAC4-416053443	16 12 41.24	-19 49 38.0	71
UCAC4-416045413	16 12 46.81	-22 13 31.7	67
UCAC4-417295725	16 12 51.65	-15 34 26.1	36
UCAC4-27972156	16 12 52.93	-29 36 10.9	43
UCAC4-27988442	16 12 56.48	-25 16 21.5	50
UCAC4-27992306	16 13 1.30	-24 6 54.7	62
UCAC4-27982569	16 13 1.60	-26 57 55.4	81
UCAC4-27989286	16 13 2.34	-25 1 46.0	85
UCAC4-416042777	16 13 2.72	-22 57 44.5	53
UCAC4-417290199	16 13 15.93	-17 27 33.5	67
UCAC4-28013681	16 13 18.44	-29 22 27.6	85
UCAC4-416073331	16 13 18.59	-22 12 49.0	62
UCAC4-416067955	16 13 19.24	-20 38 56.6	22
UCAC4-39508090	16 13 19.96	-34 47 6.5	77
UCAC4-416059647	16 13 20.80	-17 57 52.2	85
UCAC4-416076842	16 13 29.29	-23 11 7.6	49

Continued on next page

UCAC4-28002829	16 13 33.51	-26 37 50.0	74
UCAC4-417313413	16 13 35.48	-14 26 36.8	62
UCAC4-416086406	16 13 43.66	-22 14 59.5	77
UCAC4-417323158	16 13 43.83	-17 42 46.6	40
UCAC4-39520886	16 13 45.75	-35 0 5.9	90
UCAC4-28029778	16 13 45.92	-26 41 29.5	32
UCAC4-416099465	16 13 51.54	-18 13 3.6	85
UCAC4-416085934	16 13 55.48	-22 22 41.1	47
UCAC4-416097724	16 13 58.15	-18 48 29.0	77
UCAC4-416090233	16 14 0.36	-21 8 43.9	81
UCAC4-417328779	16 14 10.04	-16 26 10.1	33
UCAC4-416118154	16 14 11.08	-23 5 36.2	59
UCAC4-416106165	16 14 12.18	-19 38 55.4	62
UCAC4-416103234	16 14 38.77	-18 40 50.6	34
UCAC4-28044826	16 14 38.85	-25 25 0.1	36
UCAC4-0	16 14 41.04	-32 19 16.8	26
UCAC4-28081268	16 14 42.70	-25 12 9.7	81
UCAC4-28072937	16 14 45.68	-27 32 43.1	90
UCAC4-39587239	16 14 46.28	-34 24 21.1	55
UCAC4-416124883	16 14 52.70	-23 8 2.7	85
UCAC4-28083331	16 14 54.88	-24 37 6.4	32
UCAC4-39609028	16 14 55.14	-30 14 53.4	90
UCAC4-39609481	16 15 0.14	-30 8 13.5	42
UCAC4-28084335	16 15 7.53	-24 20 20.4	29
UCAC4-28097453	16 15 15.05	-27 7 47.5	43
UCAC4-39629324	16 15 18.51	-33 48 11.9	85
UCAC4-28099767	16 15 24.21	-27 45 1.0	29
UCAC4-28091737	16 15 32.13	-25 30 31.1	47
UCAC4-28097463	16 15 33.11	-27 7 58.8	90
UCAC4-28102229	16 15 33.71	-28 22 13.9	47
UCAC4-28091657	16 15 35.86	-25 29 1.0	67
UCAC4-417397759	16 15 49.27	-17 7 49.8	32
UCAC4-39658024	16 15 56.97	-32 41 25.1	22
UCAC4-416165104	16 15 59.86	-23 25 4.5	53
UCAC4-160764955	16 16 2.92	-24 30 54.8	85

Continued on next page

UCAC4-416170652	16 16 9.44	-21 51 46.9	53
UCAC4-416198471	16 16 11.23	-22 34 51.5	59
UCAC4-160763801	16 16 14.87	-24 51 27.9	77
UCAC4-160759135	16 16 17.20	-26 9 10.2	81
UCAC4-416202725	16 16 17.25	-23 43 56.4	74
UCAC4-416202468	16 16 17.94	-23 39 47.6	47
UCAC4-160770455	16 16 30.22	-24 42 3.8	30
UCAC4-416194037	16 16 33.66	-21 19 13.0	85
UCAC4-416215880	16 16 43.95	-20 44 19.0	90
UCAC4-160767652	16 16 44.08	-23 55 45.7	59
UCAC4-160775197	16 16 45.11	-25 59 57.7	55
UCAC4-416212753	16 16 46.20	-21 39 13.0	21
UCAC4-39707052	16 16 46.63	-34 14 14.4	59
UCAC4-417414827	16 16 48.35	-17 19 9.5	74
UCAC4-39719029	16 16 49.68	-31 40 1.7	35
UCAC4-160814997	16 16 51.30	-24 33 27.7	67
UCAC4-39717898	16 16 55.12	-31 55 46.1	57
UCAC4-416205612	16 16 56.10	-23 29 25.3	77
UCAC4-39701392	16 16 58.69	-35 24 38.2	85
UCAC4-416212646	16 17 3.39	-21 41 2.5	81
UCAC4-416207434	16 17 3.74	-22 59 46.5	62
UCAC4-416215034	16 17 5.65	-20 59 0.7	31
UCAC4-417413285	16 17 8.36	-17 50 7.1	49
UCAC4-416216827	16 17 10.25	-20 26 2.0	77
UCAC4-160812008	16 17 13.50	-25 20 15.1	59
UCAC4-990385747	16 17 14.35	-35 53 12.2	40
UCAC4-416230708	16 17 15.96	-19 47 4.1	74
UCAC4-416235767	16 17 22.98	-21 21 11.9	71
UCAC4-416241839	16 17 31.39	-23 3 36.1	42
UCAC4-160864421	16 17 54.81	-24 43 33.7	57
UCAC4-416247201	16 18 5.57	-23 25 14.4	90
UCAC4-160866218	16 18 7.57	-24 14 11.5	31
UCAC4-416272798	16 18 19.98	-20 5 34.9	71
UCAC4-39790176	16 18 29.19	-30 39 11.1	90
UCAC4-39810589	16 18 35.38	-34 38 9.2	77

Continued on next page

UCAC4-416268051	16 18 42.10	-18 33 29.0	90
UCAC4-417490371	16 18 49.24	-15 37 54.5	23
UCAC4-160869894	16 18 51.26	-24 29 55.4	62
UCAC4-416299671	16 18 54.95	-19 59 51.4	31
UCAC4-417485220	16 18 56.50	-17 21 42.2	22
UCAC4-416303294	16 19 11.98	-18 47 16.8	42
UCAC4-160911080	16 19 14.74	-25 32 31.3	55
UCAC4-160893908	16 19 25.84	-29 39 4.7	55
UCAC4-160921648	16 19 31.39	-25 18 12.8	74
UCAC4-416320504	16 19 33.96	-22 28 29.4	67
UCAC4-417512456	16 19 38.70	-16 16 42.7	28
UCAC4-416333148	16 19 45.38	-21 47 57.8	81
UCAC4-416334162	16 19 45.97	-21 30 6.8	35
UCAC4-64789671	16 19 53.95	-31 54 5.8	65
UCAC4-64842072	16 20 2.00	-30 0 36.4	21
UCAC4-890534969	16 20 2.48	-25 55 36.5	31
UCAC4-64836355	16 20 7.57	-31 17 36.8	74
UCAC4-417518148	16 20 8.57	-17 49 18.4	53
UCAC4-416334717	16 20 15.77	-21 20 30.8	90
UCAC4-64817296	16 20 24.97	-35 0 54.7	90
UCAC4-416355975	16 20 27.24	-21 26 6.9	85
UCAC4-416355791	16 20 36.41	-21 23 12.0	90
UCAC4-417548964	16 20 39.35	-17 3 8.2	32
UCAC4-977064687	16 20 39.61	-26 34 28.4	81
UCAC4-977072413	16 20 44.69	-24 31 38.4	49
UCAC4-417560856	16 20 45.08	-14 49 58.0	65
UCAC4-977055474	16 20 45.79	-28 49 20.1	85
UCAC4-416363739	16 20 45.96	-23 48 20.9	62
UCAC4-977055848	16 20 48.87	-28 44 7.7	39
UCAC4-977062974	16 20 50.65	-27 0 15.3	24
UCAC4-64850609	16 20 57.05	-31 34 20.9	95
UCAC4-977068460	16 21 0.11	-25 36 3.0	49
UCAC4-64870962	16 21 0.76	-35 12 48.2	65
UCAC4-416380426	16 21 2.88	-18 50 22.2	57
UCAC4-417583762	16 21 36.58	-17 22 4.7	62

Continued on next page

UCAC4-64892287	16 21 37.06	-33 15 22.2	81
UCAC4-1253635265	16 21 38.51	-26 52 52.7	33
UCAC4-416394937	16 21 40.58	-21 42 44.0	35
UCAC4-416396644	16 21 41.27	-22 12 5.6	90
UCAC4-64933560	16 21 42.37	-34 34 54.5	42
UCAC4-416384128	16 21 44.05	-18 7 1.3	42
UCAC4-1253635440	16 21 52.98	-26 55 29.7	85
UCAC4-1253626396	16 21 57.69	-24 29 43.5	67
UCAC4-402245803	16 21 57.84	-15 57 22.1	55
UCAC4-416413369	16 21 59.95	-20 15 0.2	22
UCAC4-1253647078	16 22 5.32	-29 36 46.3	27
UCAC4-1253657235	16 22 13.15	-28 18 58.6	74
UCAC4-450722460	16 22 36.01	-21 19 1.1	90
UCAC4-64966826	16 22 36.57	-31 25 53.1	43
UCAC4-1253665129	16 22 40.70	-26 31 17.8	27
UCAC4-450721096	16 22 44.07	-21 42 22.2	81
UCAC4-1253685931	16 22 47.57	-26 35 1.7	81
UCAC4-64988634	16 22 47.75	-32 30 54.1	49
UCAC4-1253697829	16 22 55.47	-29 8 2.2	22
UCAC4-1253683309	16 23 0.63	-26 18 6.7	40
UCAC4-64997859	16 23 12.54	-34 6 30.6	34
UCAC4-1253719948	16 23 20.09	-26 32 41.5	53
UCAC4-1253730884	16 23 21.83	-24 24 58.0	45
UCAC4-1253724192	16 23 21.88	-26 17 16.1	55
UCAC4-1253722838	16 23 22.65	-26 26 22.2	65
UCAC4-1253721336	16 23 24.02	-26 30 0.5	77
UCAC4-1253719970	16 23 26.74	-26 32 38.8	59
UCAC4-1253720543	16 23 26.94	-26 31 31.3	32
UCAC4-1253720834	16 23 27.42	-26 30 59.6	32
UCAC4-1253719845	16 23 28.47	-26 32 54.1	47
UCAC4-65015128	16 23 29.74	-35 14 30.6	34
UCAC4-1253723520	16 23 29.82	-26 23 25.3	40
UCAC4-1253727753	16 23 32.33	-25 23 48.6	55
UCAC4-1253723306	16 23 32.50	-26 24 34.1	39
UCAC4-1253719531	16 23 35.92	-26 33 34.5	85

Continued on next page

UCAC4-1253719415	16 23 37.13	-26 33 50.0	74
UCAC4-1253723033	16 23 38.86	-26 25 42.7	43
UCAC4-1253720266	16 23 38.92	-26 32 3.6	49
UCAC4-1253718493	16 23 40.92	-26 37 23.5	45
UCAC4-450759715	16 23 45.17	-21 30 41.0	71
UCAC4-1253745375	16 23 50.82	-26 44 32.3	49
UCAC4-1253750884	16 23 52.29	-27 59 13.6	59
UCAC4-1253743696	16 23 53.58	-26 34 15.1	24
UCAC4-1253743816	16 23 53.75	-26 34 42.6	55
UCAC4-1253741377	16 23 54.40	-26 25 53.8	39
UCAC4-65068854	16 23 54.84	-33 12 37.0	62
UCAC4-1253749782	16 23 57.64	-27 44 59.2	40
UCAC4-1253740972	16 23 57.71	-26 22 55.8	29
UCAC4-1253739312	16 23 57.91	-26 2 29.9	90
UCAC4-1253744072	16 23 58.35	-26 35 39.0	38
UCAC4-1253744926	16 24 5.78	-26 40 17.0	65
UCAC4-1266680515	16 24 12.95	-15 54 51.5	40
UCAC4-1253746016	16 24 13.57	-26 53 31.4	90
UCAC4-1253767335	16 24 18.59	-28 42 54.1	65
UCAC4-450775123	16 24 19.21	-19 19 17.4	62
UCAC4-1253773354	16 24 26.01	-27 22 38.7	32
UCAC4-65070414	16 24 27.26	-33 27 3.2	40
UCAC4-65106704	16 24 30.43	-33 19 42.4	40
UCAC4-65109091	16 24 35.97	-32 57 31.0	77
UCAC4-1253776157	16 24 37.58	-26 43 31.6	32
UCAC4-65107000	16 24 38.61	-33 16 56.3	90
UCAC4-1253775961	16 24 44.27	-26 46 18.2	71
UCAC4-1266704414	16 24 47.14	-16 31 6.8	33
UCAC4-65135652	16 25 2.12	-31 12 33.3	71
UCAC4-1253790052	16 25 4.49	-25 9 11.6	74
UCAC4-1253805474	16 25 4.91	-28 39 11.1	55
UCAC4-160960929	16 25 28.81	-26 7 53.9	85
UCAC4-160961975	16 25 37.24	-25 52 44.4	59
UCAC4-160960495	16 25 38.48	-26 13 54.3	67
UCAC4-160959969	16 25 45.15	-26 20 46.3	67

Continued on next page

UCAC4-160965373	16 25 49.66	-24 51 32.0	59
UCAC4-160980130	16 25 55.41	-27 21 24.3	85
UCAC4-160989294	16 25 59.68	-29 17 29.8	43
UCAC4-160979892	16 26 2.15	-27 18 14.2	65
UCAC4-1266737987	16 26 2.81	-15 59 54.4	53
UCAC4-450851823	16 26 15.04	-19 7 44.0	36
UCAC4-450863417	16 26 19.98	-22 33 2.5	81
UCAC4-872105004	16 26 23.43	-27 39 0.5	59
UCAC4-872103590	16 26 27.37	-27 56 50.7	32
UCAC4-379489602	16 26 27.86	-26 25 15.1	77
UCAC4-379484420	16 26 34.28	-27 33 28.6	77
UCAC4-450884945	16 26 35.44	-19 19 53.4	77
UCAC4-450880552	16 26 40.58	-20 37 28.7	81
UCAC4-450874125	16 26 43.17	-22 24 2.3	74
UCAC4-450887348	16 26 48.63	-18 38 31.1	45
UCAC4-65282793	16 26 57.01	-30 32 23.4	27
UCAC4-1266775566	16 26 58.65	-17 17 9.9	71
UCAC4-65261034	16 27 1.67	-33 59 19.8	26
UCAC4-379498475	16 27 2.03	-23 59 36.7	81
UCAC4-379506654	16 27 14.37	-26 17 58.8	77
UCAC4-379516528	16 27 27.66	-28 21 50.4	85
UCAC4-65295012	16 27 39.35	-31 16 1.7	55
UCAC4-450916347	16 27 39.56	-22 45 23.1	71
UCAC4-65301006	16 27 49.26	-32 12 46.1	25
UCAC4-450928508	16 27 50.65	-19 18 0.4	85
UCAC4-379532352	16 27 54.86	-28 43 39.3	85
UCAC4-65364392	16 27 55.01	-30 46 49.0	26
UCAC4-65349355	16 27 57.68	-33 9 23.1	67
UCAC4-379567994	16 28 14.12	-27 26 43.9	27
UCAC4-379579274	16 28 14.59	-29 36 16.3	57
UCAC4-379567712	16 28 24.95	-27 23 18.4	26
UCAC4-379569123	16 28 29.29	-27 40 51.3	81
UCAC4-379569412	16 28 29.92	-27 44 33.2	77
UCAC4-450968790	16 28 30.00	-20 9 25.5	28
UCAC4-450971501	16 28 37.94	-19 18 12.3	24

Continued on next page

UCAC4-65395356	16 28 47.20	-33 54 50.1	29
UCAC4-1266844288	16 28 47.54	-17 39 11.2	49
UCAC4-65386668	16 28 53.05	-32 36 39.0	53
UCAC4-450966879	16 28 53.19	-20 44 52.5	81
UCAC4-450992130	16 29 1.46	-22 18 58.0	65
UCAC4-379607698	16 29 2.87	-24 27 49.5	53
UCAC4-65442588	16 29 5.85	-31 45 25.0	33
UCAC4-379647783	16 29 22.71	-29 49 48.6	57
UCAC4-379612890	16 29 33.97	-24 55 30.4	50
UCAC4-379613429	16 29 35.56	-25 4 24.0	85
UCAC4-451015931	16 29 46.29	-19 1 35.9	28
UCAC4-451005854	16 29 48.70	-21 52 11.9	62
UCAC4-496677115	16 29 49.91	-27 28 49.9	74
UCAC4-65473515	16 29 54.14	-32 43 25.4	23
UCAC4-1266878792	16 29 59.70	-17 21 2.8	28
UCAC4-496677275	16 30 2.76	-27 27 0.5	85
UCAC4-65526572	16 30 10.60	-32 19 29.0	23
UCAC4-451032665	16 30 11.42	-21 31 49.9	57
UCAC4-451025923	16 30 14.26	-19 37 27.3	50
UCAC4-65538877	16 30 22.62	-30 27 15.5	81
UCAC4-65541185	16 30 31.21	-30 4 49.0	30
UCAC4-65549406	16 30 50.16	-30 54 40.6	33
UCAC4-60321896	16 31 1.85	-29 1 1.9	71
UCAC4-60328490	16 31 2.71	-27 41 35.6	49
UCAC4-60335563	16 31 3.65	-26 21 31.1	81
UCAC4-60332597	16 31 8.37	-26 51 6.3	67
UCAC4-1266919188	16 31 8.99	-17 1 18.8	33
UCAC4-60331898	16 31 9.05	-26 59 56.0	85
UCAC4-6405240	16 31 10.54	-21 20 25.1	28
UCAC4-1266919268	16 31 31.54	-16 59 53.1	62
UCAC4-1030727426	16 31 31.82	-29 20 17.8	59
UCAC4-65618392	16 31 42.44	-31 56 18.3	33
UCAC4-6418739	16 31 47.70	-18 35 57.4	29
UCAC4-60362948	16 31 53.46	-26 36 16.9	71
UCAC4-1266948409	16 31 56.59	-17 6 4.0	27

Continued on next page

UCAC4-60362592	16 31 56.61	-26 40 40.8	55
UCAC4-60368404	16 32 0.59	-25 30 28.8	74
UCAC4-60368408	16 32 1.62	-25 30 25.4	57
UCAC4-60353729	16 32 3.54	-28 30 17.8	42
UCAC4-1266951906	16 32 9.24	-17 49 36.9	65
UCAC4-60393893	16 32 17.15	-28 57 41.2	59
UCAC4-65713858	16 32 26.50	-31 7 32.3	24
UCAC4-6465341	16 32 53.17	-20 29 48.2	53
UCAC4-60423852	16 33 3.01	-25 14 19.0	90
UCAC4-60424355	16 33 3.83	-25 5 10.4	57
UCAC4-60446953	16 33 21.41	-28 16 52.9	21
UCAC4-65732978	16 33 24.02	-31 37 52.6	59
UCAC4-60436742	16 33 26.93	-26 16 27.5	62
UCAC4-65796958	16 33 32.55	-31 53 17.5	65
UCAC4-65806300	16 33 40.57	-30 24 10.1	65
UCAC4-60432869	16 33 41.92	-25 23 34.1	47
UCAC4-60431187	16 33 42.99	-24 58 11.2	71
UCAC4-65822419	16 34 2.20	-31 55 48.9	39
UCAC4-60472690	16 34 5.85	-26 58 44.2	81
UCAC4-65814556	16 34 11.43	-30 41 41.8	25
UCAC4-65811055	16 34 25.40	-30 7 2.0	55
UCAC4-60508172	16 34 26.85	-28 33 45.6	65
UCAC4-65823400	16 34 30.16	-32 4 20.3	29
UCAC4-60494541	16 34 37.56	-26 2 16.7	24
UCAC4-60508355	16 34 38.27	-28 35 50.5	90
UCAC4-65886787	16 34 43.17	-31 9 37.1	43
UCAC4-60490375	16 34 43.62	-25 9 11.5	90
UCAC4-60498225	16 34 44.50	-26 44 45.4	35
UCAC4-60494883	16 34 46.29	-26 6 32.4	74
UCAC4-60494743	16 34 49.20	-26 4 49.6	59
UCAC4-60491082	16 34 53.14	-25 18 17.0	28
UCAC4-31156464	16 34 56.07	-23 7 39.6	21
UCAC4-31160801	16 35 0.52	-22 4 46.4	77
UCAC4-60524468	16 35 11.89	-28 45 52.1	74
UCAC4-60565133	16 35 31.57	-27 1 7.5	30

Continued on next page

UCAC4-60568506	16 35 32.87	-27 37 2.2	25
UCAC4-1010171987	16 35 42.11	-31 42 33.1	26
UCAC4-60562539	16 35 44.32	-26 33 20.9	29
UCAC4-60572732	16 35 53.78	-28 19 47.5	71
UCAC4-60605232	16 36 14.45	-26 18 12.7	95
UCAC4-60608704	16 36 25.90	-25 39 18.5	71
UCAC4-31233512	16 36 33.59	-20 23 19.4	45
UCAC4-1267131208	16 36 35.57	-17 59 10.9	47
UCAC4-31269757	16 36 39.34	-18 31 3.4	27
UCAC4-31253364	16 36 44.17	-22 46 36.2	71
UCAC4-60621830	16 36 46.51	-25 2 3.3	74
UCAC4-60633324	16 36 52.88	-27 8 18.6	62
UCAC4-60632702	16 36 53.58	-27 2 5.2	24
UCAC4-1010282625	16 36 54.52	-31 20 58.1	74
UCAC4-1010276644	16 36 56.75	-32 3 26.0	65
UCAC4-31271639	16 36 58.40	-17 59 42.2	42
UCAC4-60644807	16 36 58.71	-29 4 41.7	21
UCAC4-60666349	16 37 4.23	-27 38 28.7	26
UCAC4-31283471	16 37 12.02	-20 53 9.6	67
UCAC4-60665686	16 37 16.59	-27 45 1.2	67
UCAC4-60664004	16 37 24.07	-28 1 15.3	36
UCAC4-60662565	16 37 30.65	-28 15 26.3	27
UCAC4-60715068	16 37 36.74	-29 19 37.6	81
UCAC4-60698038	16 37 40.95	-26 24 54.9	31
UCAC4-60715194	16 38 1.05	-29 20 42.1	43
UCAC4-60702259	16 38 4.58	-27 10 24.6	71
UCAC4-60727144	16 38 6.03	-28 52 33.3	26
UCAC4-1069198556	16 38 31.25	-30 37 54.1	29
UCAC4-60766768	16 38 37.60	-26 38 11.1	49
UCAC4-50993877	16 38 37.91	-23 42 44.1	38
UCAC4-60783722	16 38 38.31	-29 25 8.9	62
UCAC4-1069191714	16 38 39.81	-31 33 28.1	27
UCAC4-1069190092	16 38 41.41	-31 47 11.0	57
UCAC4-60772291	16 38 49.46	-27 35 29.4	45
UCAC4-60778657	16 38 52.08	-28 39 42.7	21

Continued on next page

UCAC4-51007853	16 38 59.55	-20 34 19.4	21
UCAC4-60775479	16 39 2.19	-28 7 2.3	43
UCAC4-50993220	16 39 4.60	-23 50 52.4	40
UCAC4-60783775	16 39 5.86	-29 25 34.3	47
UCAC4-51012321	16 39 7.05	-19 29 22.4	35
UCAC4-60820452	16 39 11.05	-24 42 44.3	55
UCAC4-394522212	16 39 19.50	-23 39 37.0	21
UCAC4-60823024	16 39 27.24	-23 58 48.2	50
UCAC4-394538562	16 39 44.74	-20 6 30.9	62
UCAC4-394543480	16 39 50.34	-18 38 35.5	67
UCAC4-60845756	16 39 51.91	-28 0 4.2	36
UCAC4-60828709	16 39 54.87	-25 2 47.9	40
UCAC4-60846582	16 40 4.24	-28 8 3.6	81
UCAC4-394524238	16 40 5.02	-23 50 40.4	65
UCAC4-60882135	16 40 12.64	-26 35 42.3	65
UCAC4-60871928	16 40 28.48	-28 16 15.4	35
UCAC4-51042966	16 40 28.79	-23 41 30.7	57
UCAC4-60892636	16 40 32.86	-24 42 44.2	21
UCAC4-60860878	16 40 37.49	-29 48 48.3	42
UCAC4-394565427	16 40 42.51	-23 8 58.3	50
UCAC4-394552982	16 40 43.42	-19 57 21.9	26
UCAC4-60923159	16 41 1.20	-28 37 26.3	43
UCAC4-60922447	16 41 6.22	-28 30 35.3	77
UCAC4-60905459	16 41 13.66	-25 46 12.7	21
UCAC4-60968864	16 41 16.21	-24 36 35.1	53
UCAC4-1312470529	16 41 30.94	-22 12 33.6	67
UCAC4-1312468604	16 41 38.59	-22 40 58.8	53
UCAC4-60952520	16 41 39.32	-27 17 20.9	34
UCAC4-60976862	16 41 48.17	-24 53 52.5	50
UCAC4-61005775	16 41 56.69	-29 13 39.0	39
UCAC4-60995148	16 42 3.89	-27 43 37.0	34
UCAC4-60980585	16 42 9.32	-25 30 44.3	77
UCAC4-61008013	16 42 12.29	-29 30 48.8	65
UCAC4-61009020	16 42 18.31	-29 38 32.7	55
UCAC4-431430519	16 42 19.39	-30 38 6.1	36

Continued on next page

UCAC4-61040047	16 42 26.93	-25 59 47.5	71
UCAC4-61017843	16 42 36.69	-29 16 6.1	77
UCAC4-431533684	16 42 37.48	-30 3 35.4	74
UCAC4-1312511627	16 42 38.22	-23 41 56.7	59
UCAC4-1312516421	16 42 39.83	-22 41 19.9	71
UCAC4-61043353	16 42 47.13	-25 27 6.6	33
UCAC4-1312555651	16 43 3.92	-23 8 12.4	55
UCAC4-1312570374	16 43 22.43	-21 30 5.4	81
UCAC4-1312565821	16 43 22.67	-22 37 58.0	47
UCAC4-431537698	16 43 28.14	-30 8 56.5	26
UCAC4-1312572460	16 43 29.85	-20 59 8.8	74
UCAC4-1312562565	16 43 31.59	-23 19 11.6	65
UCAC4-1067479151	16 43 44.44	-28 17 11.4	23
UCAC4-1067485730	16 43 54.47	-27 9 30.0	59
UCAC4-61117281	16 43 56.60	-28 19 8.5	47
UCAC4-1312605938	16 43 58.52	-23 2 3.4	24
UCAC4-61116592	16 44 14.15	-28 12 49.4	42
UCAC4-431650948	16 44 16.44	-30 8 16.8	36
UCAC4-61111469	16 44 16.88	-27 27 46.0	71
UCAC4-1312620941	16 44 33.81	-21 36 37.6	81
UCAC4-1312613185	16 44 33.94	-23 19 19.4	23
UCAC4-1312624429	16 44 40.19	-20 44 25.5	32
UCAC4-1050376287	16 44 51.10	-28 33 58.4	57
UCAC4-31304024	16 45 6.03	-22 35 18.3	77
UCAC4-1067505998	16 45 10.03	-29 19 49.8	74
UCAC4-1067529377	16 45 26.14	-25 3 16.7	55
UCAC4-31350924	16 45 30.82	-23 36 26.9	65
UCAC4-1088618997	16 45 37.29	-26 22 45.8	57
UCAC4-31349904	16 45 37.50	-23 25 31.7	59
UCAC4-1088616042	16 45 50.42	-25 49 46.3	36
UCAC4-31358134	16 45 51.75	-22 59 13.0	74
UCAC4-1088636697	16 45 57.12	-29 17 59.4	27
UCAC4-1088636627	16 46 2.73	-29 17 26.1	23
UCAC4-1109377305	16 46 15.91	-23 59 19.4	39
UCAC4-1109366848	16 46 16.08	-26 7 24.3	55

Continued on next page

UCAC4-1109352409	16 46 31.90	-28 33 34.4	49
UCAC4-1109410724	16 46 43.33	-29 34 42.6	33
UCAC4-1109384401	16 46 43.86	-25 16 34.2	31
UCAC4-31460377	16 47 20.79	-22 32 3.0	30
UCAC4-61159011	16 47 22.12	-28 32 52.1	49
UCAC4-61159332	16 47 22.46	-28 35 21.1	81
UCAC4-61146934	16 47 30.27	-26 48 58.4	45
UCAC4-31458640	16 47 33.78	-22 13 5.6	45
UCAC4-632179564	16 47 43.86	-28 55 26.2	40
UCAC4-632207049	16 47 44.95	-24 52 19.0	30
UCAC4-632186727	16 47 44.95	-27 57 8.9	30
UCAC4-31478992	16 47 50.96	-22 0 51.3	55
UCAC4-632179878	16 47 53.01	-28 52 42.2	23
UCAC4-31478666	16 48 2.18	-22 4 21.4	31
UCAC4-632188320	16 48 8.00	-27 43 54.8	33
UCAC4-31488682	16 48 18.28	-20 3 59.0	28
UCAC4-632232974	16 48 20.15	-27 10 56.4	77
UCAC4-632231489	16 48 23.31	-26 58 8.2	71
UCAC4-394579824	16 48 55.51	-21 52 26.9	30
UCAC4-394584731	16 49 12.86	-20 47 23.9	42
UCAC4-632329167	16 49 18.88	-28 18 49.6	22
UCAC4-632309371	16 49 31.33	-25 37 1.0	57
UCAC4-1285924293	16 49 41.08	-21 47 3.4	42
UCAC4-1285919339	16 49 44.71	-20 40 7.6	28
UCAC4-632299944	16 49 45.50	-24 9 30.2	23
UCAC4-1285925647	16 49 46.25	-22 1 39.3	22
UCAC4-1285936574	16 49 59.96	-23 46 9.9	31
UCAC4-1285942938	16 50 6.29	-22 29 0.5	59
UCAC4-632371704	16 50 11.01	-26 7 31.9	27
UCAC4-7759468	16 50 23.86	-28 24 44.9	59
UCAC4-7763298	16 50 25.29	-27 54 5.2	23
UCAC4-1285977846	16 50 27.78	-21 22 28.8	30
UCAC4-1285985144	16 50 32.09	-22 48 58.9	57
UCAC4-1285974602	16 50 38.01	-20 39 5.8	27
UCAC4-1286001121	16 51 3.93	-21 56 34.4	43

Continued on next page

UCAC4-7811018	16 51 11.72	-27 7 17.1	62
UCAC4-7807901	16 51 12.00	-26 41 32.1	42
UCAC4-1286042508	16 51 40.40	-23 3 35.5	67
UCAC4-7907618	16 51 57.69	-28 3 29.0	23
UCAC4-1286060062	16 51 58.71	-21 21 59.2	42
UCAC4-7884193	16 52 9.66	-24 47 19.3	24
UCAC4-7889019	16 52 15.72	-25 32 31.1	43
UCAC4-1286049480	16 52 18.43	-23 31 42.5	26
UCAC4-7898587	16 52 25.63	-26 54 22.6	71
UCAC4-1286091740	16 52 28.09	-21 49 53.7	62
UCAC4-1286087065	16 52 48.75	-20 50 9.0	47
UCAC4-7941887	16 52 54.48	-27 56 11.8	27
UCAC4-70237527	16 53 12.52	-23 0 2.1	62
UCAC4-70226950	16 53 19.90	-21 6 30.0	36
UCAC4-70236356	16 53 20.17	-22 46 40.4	21
UCAC4-7971405	16 53 24.60	-23 54 56.6	42
UCAC4-7986788	16 53 27.45	-26 10 15.6	67
UCAC4-70257785	16 53 39.11	-21 29 19.1	29
UCAC4-8059580	16 53 43.78	-25 1 29.5	45
UCAC4-8049195	16 53 47.77	-26 27 3.6	57
UCAC4-70253496	16 53 55.58	-22 15 27.3	71
UCAC4-70296185	16 54 9.64	-22 2 47.7	24
UCAC4-70304087	16 54 10.09	-23 22 25.7	65
UCAC4-70292313	16 54 10.10	-21 19 49.0	74
UCAC4-8079829	16 54 20.89	-25 38 23.3	81
UCAC4-70303653	16 54 23.03	-23 17 56.9	36
UCAC4-8084421	16 54 29.52	-26 14 50.7	28
UCAC4-70322208	16 54 33.28	-21 39 19.8	31
UCAC4-70323877	16 54 43.00	-21 21 31.8	55
UCAC4-70311922	16 54 43.11	-23 22 50.6	57
UCAC4-70314220	16 54 50.87	-23 0 16.9	31
UCAC4-8146464	16 54 53.15	-26 45 21.5	21
UCAC4-70366768	16 55 4.20	-22 32 45.0	27
UCAC4-8180859	16 55 5.43	-25 43 29.8	42
UCAC4-70362104	16 55 6.57	-21 49 44.4	43

Continued on next page

UCAC4-70358750	16 55 13.87	-21 14 2.7	65
UCAC4-8169894	16 55 25.20	-24 10 7.3	21
UCAC4-8176543	16 55 27.14	-25 8 33.3	45
UCAC4-8252433	16 55 43.31	-26 4 30.8	25
UCAC4-8256792	16 55 52.55	-25 31 24.7	23
UCAC4-70383563	16 55 57.11	-22 47 39.0	29
UCAC4-70436651	16 55 59.91	-22 49 41.5	67
UCAC4-8255191	16 56 1.23	-25 43 31.3	65
UCAC4-70435598	16 56 3.39	-22 39 22.2	55
UCAC4-70431998	16 56 6.82	-22 3 54.8	22
UCAC4-70436399	16 56 24.43	-22 47 15.4	33
UCAC4-394621257	16 56 30.29	-22 34 47.8	25
UCAC4-394628814	16 56 44.96	-23 51 17.8	62
UCAC4-8361071	16 56 49.98	-25 39 54.5	50
UCAC4-394619013	16 56 58.75	-22 11 28.8	27
UCAC4-8370918	16 57 6.11	-24 22 18.4	62
UCAC4-394632767	16 57 17.43	-23 33 41.3	50
UCAC4-8379649	16 57 18.51	-24 33 38.2	53
UCAC4-8375608	16 57 19.40	-23 59 38.5	39
UCAC4-8385738	16 57 20.61	-25 21 54.4	50
UCAC4-8379786	16 57 28.53	-24 34 52.7	49
UCAC4-8396314	16 57 42.87	-26 38 34.0	24
UCAC4-394687793	16 57 43.34	-22 9 56.2	39
UCAC4-8468780	16 57 47.80	-25 39 53.2	43
UCAC4-8463953	16 57 58.03	-26 14 49.6	62
UCAC4-8477383	16 58 10.76	-24 35 24.4	47
UCAC4-394709020	16 58 14.19	-22 40 28.6	29
UCAC4-8485725	16 58 21.59	-24 12 54.0	67
UCAC4-8487762	16 58 47.66	-24 28 56.3	33
UCAC4-8579678	16 58 49.03	-25 51 13.2	71
UCAC4-8594204	16 59 2.20	-24 3 30.7	27
UCAC4-8576581	16 59 3.42	-26 12 17.3	57
UCAC4-394787998	16 59 4.65	-22 5 41.4	26
UCAC4-394779990	16 59 7.69	-23 18 20.6	59
UCAC4-8593102	16 59 12.34	-24 12 23.7	57

Continued on next page

UCAC4-8603511	16 59 23.78	-24 49 58.3	39
UCAC4-394776334	16 59 32.87	-23 48 12.0	74
UCAC4-8605290	16 59 50.37	-25 2 46.5	49
UCAC4-394847259	16 59 56.79	-23 15 2.1	45
UCAC4-394849261	17 0 4.15	-23 31 12.3	65
UCAC4-394856745	17 0 12.75	-23 30 11.7	38
UCAC4-8718696	17 0 28.30	-24 50 22.7	32
UCAC4-8724981	17 0 31.14	-25 34 38.9	74
UCAC4-8713899	17 0 36.90	-24 15 14.4	67
UCAC4-394921988	17 0 44.17	-22 22 40.0	23
UCAC4-8823589	17 1 2.19	-24 18 31.1	43
UCAC4-394944805	17 1 26.03	-22 32 38.5	32
UCAC4-8832577	17 1 35.25	-24 29 7.8	43
UCAC4-8839102	17 1 43.58	-25 14 42.8	21
UCAC4-395015825	17 1 50.43	-23 56 10.1	33
UCAC4-395014576	17 1 54.98	-23 46 57.8	29
UCAC4-8945056	17 2 6.77	-23 57 7.8	77
UCAC4-395025193	17 2 8.33	-22 53 50.0	53
UCAC4-8939300	17 2 27.35	-24 38 9.8	38
UCAC4-8948057	17 2 42.12	-24 6 4.8	57
UCAC4-8947758	17 2 50.79	-24 3 53.3	21
UCAC4-395095072	17 2 57.35	-23 15 19.8	40
UCAC4-395108922	17 3 9.59	-23 5 18.5	29
UCAC4-395108511	17 3 10.46	-23 8 23.5	85
UCAC4-395109630	17 3 19.61	-22 59 55.6	62
UCAC4-9060880	17 3 25.19	-24 21 58.1	39
UCAC4-395108411	17 3 38.57	-23 9 3.7	21
UCAC4-9067715	17 3 43.38	-24 8 57.6	34
UCAC4-395177665	17 3 51.45	-22 41 57.7	40
UCAC4-395183252	17 4 8.34	-23 24 5.9	53
UCAC4-395186345	17 4 8.37	-23 46 23.5	24
UCAC4-395194431	17 4 20.55	-23 17 46.4	49
UCAC4-395191778	17 4 31.65	-23 36 31.9	32
UCAC4-395196978	17 4 34.07	-22 58 31.1	23
UCAC4-41458632	17 4 43.48	-23 51 3.6	65

Continued on next page

UCAC4-41458558	17 5 2.91	-23 51 35.4	62
UCAC4-41460654	17 5 11.11	-23 37 6.1	23
UCAC4-41543514	17 5 13.65	-23 40 15.7	22
UCAC4-9301508	17 5 16.15	-24 19 13.1	45
UCAC4-41553094	17 5 43.62	-23 15 36.0	35
UCAC4-41548977	17 5 57.93	-23 43 52.7	53
UCAC4-41641112	17 6 45.26	-23 41 17.9	31
UCAC4-41640424	17 6 51.59	-23 46 23.4	31
UCAC4-41725900	17 7 16.33	-23 29 17.3	35
UCAC4-41726268	17 7 24.73	-23 31 42.6	74
UCAC4-41726284	17 7 25.95	-23 31 51.5	40

C

WiFeS Low-Mass Star Observations

This appendix provides the full tables of observations for the G,K and M-type candidate Upper-Scorpius members observed during our ANU 2.3 m telescope WiFeS campaign, including June 2013, April 2014 and June 2014. The full explanation of the target selection, data reduction and results of the observations can be found in Chapter 3.

Table C.1: Summary of WiFeS observations of candidate Upper-Scorpius members; the V magnitude provided is either taken from APASS, where available, or interpolated from J and K according to the Kepler K2 instructions.

R.A. (J2000.0)	Decl. (J2000.0)	MJD	V (mag)	J (mag)	K (mag)
15 39 06.96	-26 46 32.1	56462	12.5	9.5	8.7
15 37 42.74	-25 26 15.8	56462	13.5	10.5	9.7
15 35 32.30	-25 37 14.1	56462	11.7	9.3	8.4

Continued on next page

15 41 31.21	-25 20 36.3	56462	10.0	8.0	7.2
16 02 00.39	-22 21 23.9	56462	12.9	9.8	8.8
16 02 08.45	-22 54 59.1	56462	13.6	10.5	9.6
16 00 42.76	-21 27 38.0	56462	12.8	9.8	8.9
16 00 40.56	-22 00 32.2	56462	11.0	9.1	8.4
15 58 12.70	-23 28 36.4	56462	10.2	8.6	8.0
15 59 59.95	-22 20 36.8	56462	12.9	9.6	8.6
16 00 14.91	-21 01 31.7	56462	11.9	9.7	9.0
16 00 13.30	-24 18 10.7	56462	13.6	10.5	9.5
15 59 10.29	-26 46 50.0	56462	12.3	10.3	9.6
15 49 21.00	-26 00 06.3	56462	11.2	8.7	7.9
15 48 32.74	-28 44 15.6	56462	11.2	9.0	8.3
15 53 47.13	-25 33 43.0	56462	11.5	9.4	8.6
15 53 06.83	-22 47 17.4	56462	13.5	9.7	8.7
15 55 02.14	-21 49 43.5	56462	12.4	9.6	8.6
15 57 34.31	-23 21 12.3	56462	12.8	9.9	9.0
15 57 16.74	-25 29 19.3	56462	12.5	9.8	8.9
15 56 55.46	-22 58 40.4	56462	13.5	10.4	9.4
15 56 06.96	-28 52 41.4	56462	10.1	8.1	7.4
16 04 05.13	-27 35 23.0	56462	10.5	9.0	8.5
16 09 30.31	-21 04 58.9	56462	12.8	9.8	8.9
16 05 20.11	-22 56 04.7	56462	12.3	10.2	9.4
16 05 21.57	-18 21 41.2	56462	12.2	9.3	8.1
16 05 38.16	-20 39 47.0	56462	12.6	9.7	8.8
16 06 43.86	-19 08 05.5	56462	13.1	10.1	9.2
16 06 47.94	-18 41 43.8	56462	12.7	9.9	9.0
16 08 01.41	-20 27 41.6	56462	13.5	10.3	9.3
16 21 54.67	-20 43 09.1	56462	12.5	10.0	9.2
16 07 40.06	-21 48 42.7	56462	13.5	10.6	9.7
16 12 22.17	-27 12 52.5	56462	11.6	10.1	9.5
16 12 06.68	-30 10 27.1	56462	13.3	10.4	9.3
16 13 01.60	-26 57 55.4	56462	13.0	10.9	10.3
16 14 38.77	-18 40 50.6	56462	12.9	10.4	9.6
16 15 33.11	-27 07 58.8	56462	13.9	10.7	9.8
16 15 35.86	-25 29 01.0	56462	12.4	9.7	8.7

Continued on next page

16 15 59.86	-23 25 04.5	56462	11.9	9.4	8.5
16 16 51.30	-24 33 27.7	56462	9.7	8.2	7.7
16 16 44.08	-23 55 45.7	56462	11.1	8.6	7.7
16 17 31.38	-23 03 36.0	56462	10.1	8.5	8.0
16 17 54.81	-24 43 33.7	56462	9.8	8.3	7.8
16 18 19.98	-20 05 34.9	56462	10.4	8.5	7.9
16 21 57.69	-24 29 43.5	56462	10.2	8.1	7.6
15 32 48.81	-23 08 12.3	56756	13.7	10.6	9.7
15 33 17.26	-23 25 34.1	56756	12.1	9.5	8.6
15 37 49.29	-20 29 18.3	56756	11.5	9.3	8.6
15 40 27.32	-19 57 43.7	56756	10.4	8.2	7.4
15 39 29.69	-23 11 19.9	56756	10.7	8.8	8.1
15 42 26.21	-22 47 46.0	56756	13.0	9.6	8.6
15 45 09.71	-25 12 43.0	56756	13.8	10.6	9.7
15 47 10.64	-17 36 24.3	56756	13.9	10.5	9.6
15 46 27.26	-25 18 46.8	56756	11.4	8.8	7.9
15 47 43.31	-18 19 15.4	56756	13.8	10.7	9.8
15 49 25.09	-28 43 52.8	56756	13.9	10.6	9.7
15 50 03.25	-23 42 02.2	56756	13.9	10.8	9.9
15 54 03.58	-29 20 15.5	56756	12.5	9.6	8.7
15 50 49.08	-16 34 48.3	56756	12.0	9.8	9.1
15 51 50.27	-22 38 18.8	56756	11.5	9.0	8.2
16 21 54.67	-20 43 09.1	56756	12.5	10.0	9.2
15 56 47.69	-19 50 07.6	56756	12.8	9.9	8.9
15 57 45.75	-21 44 28.8	56756	13.6	10.6	9.6
16 01 32.73	-22 19 37.8	56756	11.1	9.0	8.2
16 02 31.96	-28 13 45.2	56756	10.6	8.4	7.7
16 02 24.61	-22 00 24.8	56756	13.3	10.3	9.4
16 04 52.50	-13 08 13.2	56756	12.0	9.4	8.6
16 16 02.92	-24 30 54.8	56756	13.7	10.1	9.0
16 16 17.20	-26 09 10.2	56756	13.1	9.8	8.7
16 16 46.63	-34 14 14.4	56756	11.3	9.1	8.4
16 17 22.98	-21 21 11.9	56756	13.4	10.3	9.3
16 19 14.74	-25 32 31.3	56756	12.9	9.7	8.7
16 19 31.39	-25 18 12.8	56756	13.2	9.9	8.9

Continued on next page

16 19 45.38	-21 47 57.8	56756	12.8	10.0	9.1
16 20 27.24	-21 26 06.9	56756	13.1	10.1	9.2
16 20 45.08	-14 49 58.0	56756	13.6	10.3	9.3
16 20 45.79	-28 49 20.1	56756	13.7	10.1	9.1
16 10 02.30	-24 34 18.6	56826	13.8	11.3	10.4
16 21 18.30	-19 45 18.4	56826	13.9	11.2	10.3
16 22 51.58	-27 55 37.2	56826	13.9	11.1	10.2
16 23 59.02	-27 36 03.8	56826	13.1	10.3	9.4
15 55 41.41	-20 43 15.1	56826	13.9	10.5	9.4
16 23 37.92	-24 36 30.3	56826	14.1	10.9	9.9
15 58 06.95	-26 23 46.6	56826	14.0	11.1	10.2
16 17 16.50	-23 27 57.1	56826	14.4	11.2	10.2
16 24 11.77	-19 55 58.3	56826	14.6	11.0	9.9
16 15 27.51	-26 27 28.1	56826	15.5	12.2	11.2
16 17 29.95	-24 51 03.0	56826	14.7	10.9	9.8
16 20 53.01	-20 19 20.2	56826	14.6	11.0	10.0
16 22 54.79	-21 38 09.2	56826	14.2	11.1	10.1
16 21 48.53	-25 17 26.6	56826	14.6	11.1	10.0
16 20 32.46	-22 57 45.3	56826	14.8	10.9	9.8
15 57 00.85	-20 24 59.5	56826	14.0	11.2	10.3
16 07 29.43	-25 46 15.7	56826	14.1	11.1	10.1
16 09 49.55	-24 44 46.8	56826	14.0	11.0	10.1
16 22 05.88	-21 21 55.7	56826	14.0	10.9	10.0
16 27 33.21	-28 21 09.7	56826	14.0	11.4	10.5
15 57 03.68	-23 04 48.4	56826	14.0	11.2	10.2
15 57 23.92	-20 51 45.4	56826	14.1	10.8	9.8
16 03 38.30	-18 54 07.7	56826	14.1	10.6	9.5
16 02 35.88	-23 20 17.1	56826	14.1	11.2	10.2
15 56 20.60	-23 36 10.0	56826	14.2	11.3	10.3
16 00 00.37	-22 32 59.5	56826	14.2	10.8	9.8
16 14 49.89	-21 39 32.1	56826	14.1	11.1	10.1
16 19 02.15	-21 38 09.8	56826	14.1	11.3	10.4
16 14 03.80	-24 53 08.8	56826	14.1	11.0	10.0
16 08 40.25	-27 33 39.6	56826	14.1	11.5	10.6
16 09 35.75	-21 38 05.7	56826	14.2	10.9	9.9

Continued on next page

15 55 05.13	-20 26 07.7	56826	14.2	10.8	9.7
15 56 24.92	-25 41 20.3	56826	14.2	11.4	10.4
15 59 18.73	-26 48 14.0	56826	14.2	11.6	10.7
15 55 08.53	-23 18 51.1	56826	14.2	10.9	9.9
16 09 31.09	-20 41 46.0	56826	14.3	11.1	10.1
16 19 48.37	-22 12 51.9	56826	14.2	11.3	10.3
16 22 43.55	-18 52 35.9	56826	14.2	11.5	10.6
16 22 06.58	-21 27 08.9	56826	14.2	11.1	10.1
16 23 57.24	-26 20 24.5	56826	14.2	11.2	10.2
16 25 23.28	-27 27 31.5	56826	14.2	11.6	10.7
16 26 54.09	-27 35 07.7	56826	14.2	11.6	10.7
16 19 16.09	-29 15 12.6	56826	14.1	11.3	10.4
16 34 58.05	-22 57 20.8	56826	14.2	11.3	10.4
16 21 55.94	-27 05 03.4	56826	14.2	11.6	10.8
16 01 13.99	-25 16 28.2	56826	14.3	11.4	10.4
16 19 48.80	-22 24 47.2	56826	14.3	11.7	10.8
16 13 56.63	-24 57 56.7	56826	14.3	11.1	10.2
16 11 17.45	-24 41 20.3	56826	14.3	11.4	10.4
16 26 34.95	-25 11 40.9	56826	14.3	11.0	10.0
16 01 08.97	-26 45 10.5	56826	14.3	11.5	10.6
16 21 29.53	-25 29 43.1	56826	14.3	11.2	10.2
16 15 36.43	-26 22 09.1	56826	14.3	11.2	10.2
16 10 14.45	-19 51 37.7	56826	14.3	11.2	10.2
16 13 09.79	-20 44 59.1	56826	14.3	10.9	9.9
16 13 21.91	-21 36 13.6	56826	14.3	11.0	10.0
16 00 12.17	-21 57 03.3	56826	14.3	11.3	10.3
15 55 39.28	-20 53 07.2	56826	14.4	11.5	10.6
16 13 32.79	-20 44 41.4	56826	14.4	11.1	10.1
16 13 44.90	-24 34 14.4	56826	14.4	11.3	10.3
16 17 26.15	-24 50 59.3	56826	14.4	10.9	9.9
16 19 47.11	-22 03 11.3	56826	14.4	11.5	10.6
15 57 42.47	-25 51 35.5	56826	14.4	11.7	10.8
15 57 24.55	-20 38 38.2	56826	14.4	11.0	10.0
16 31 05.80	-27 25 46.0	56826	14.3	11.5	10.5
16 31 56.69	-28 46 12.7	56826	14.3	11.4	10.5

Continued on next page

16 29 56.63	-26 59 18.2	56826	14.3	11.4	10.4
16 27 13.23	-20 04 25.7	56826	14.4	12.0	11.1
16 21 15.84	-22 40 04.6	56826	14.5	10.8	9.8
16 23 18.69	-26 23 43.3	56824	12.4	8.2	7.0
16 23 22.93	-26 22 16.1	56824	9.6	8.3	7.9
16 24 49.82	-26 23 45.9	56824	11.8	8.3	7.3
16 25 35.72	-26 09 33.8	56824	10.0	7.6	6.8
16 25 57.91	-26 00 37.4	56824	12.9	9.6	8.5
16 25 57.91	-26 00 37.4	56824	12.9	9.6	8.5
16 28 52.01	-26 11 55.4	56824	9.5	8.4	8.2
16 12 36.05	-27 23 03.2	56824	11.2	8.2	7.2
16 12 46.71	-27 33 28.7	56824	10.5	8.0	7.1
16 15 25.71	-28 27 53.1	56824	11.4	8.0	6.9
16 18 32.97	-27 57 29.2	56824	10.8	7.9	7.0
16 16 09.07	-27 56 23.1	56824	11.2	8.7	7.9
16 13 28.04	-27 24 13.4	56824	8.6	7.7	7.5
16 13 47.82	-27 47 34.0	56824	9.3	8.3	8.0
16 21 54.67	-20 43 09.1	56824	12.5	10.0	9.2
16 34 22.40	-21 54 30.9	56824	13.6	10.2	9.1
16 25 16.90	-23 22 03.1	56824	14.3	10.2	9.0
16 11 04.80	-23 33 16.6	56824	13.3	10.6	9.7
16 08 04.11	-26 40 44.9	56824	12.8	10.0	9.1
16 08 56.96	-28 35 57.4	56824	13.4	10.6	9.6
15 59 52.70	-25 26 29.2	56824	13.5	10.6	9.7
16 15 19.49	-25 40 12.0	56824	13.2	10.1	9.1
16 14 07.34	-22 17 32.1	56824	13.3	10.1	9.1
16 14 42.70	-25 12 09.7	56824	14.5	10.5	9.3
16 24 19.21	-19 19 17.4	56824	14.0	10.4	9.4
16 24 09.43	-21 34 07.6	56824	15.0	11.5	10.5
16 03 46.95	-22 45 24.7	56824	13.2	10.1	9.1
15 59 44.26	-20 29 23.3	56824	15.3	11.5	10.4
16 33 58.76	-27 42 16.7	56824	14.1	10.4	9.3
16 12 05.05	-20 43 40.5	56824	13.5	10.1	9.1
16 12 35.31	-20 34 34.0	56824	13.5	10.3	9.3
16 11 26.03	-26 31 55.9	56824	13.7	10.6	9.6

Continued on next page

16 09 39.70	-22 00 46.6	56824	13.5	10.3	9.3
16 30 01.36	-15 43 11.1	56824	13.5	10.4	9.5
16 28 23.57	-27 22 41.2	56824	14.2	10.4	9.3
16 03 01.77	-26 26 21.9	56824	17.2	13.3	12.2
16 14 02.27	-18 52 43.9	56824	14.5	10.2	9.0
16 15 00.60	-29 19 34.9	56824	13.2	10.4	9.4
16 15 12.40	-23 18 45.3	56824	13.7	10.7	9.7
16 09 31.65	-22 29 22.4	56824	13.3	10.1	9.2
16 22 08.58	-29 15 06.3	56824	13.3	10.6	9.7
16 30 29.35	-16 01 52.9	56824	13.3	10.7	9.9
16 25 35.04	-23 32 55.0	56824	14.2	10.1	8.9
16 34 17.86	-28 59 37.4	56824	13.9	10.3	9.2
16 29 35.56	-25 04 24.0	56824	13.7	10.4	9.3
16 10 28.23	-27 56 39.5	56824	13.1	10.5	9.6
16 23 22.07	-21 25 49.0	56825	14.1	10.8	9.7
16 26 19.98	-22 33 02.5	56825	14.1	10.8	9.8
16 27 27.66	-28 21 50.4	56825	13.5	10.9	10.0
16 25 49.26	-25 54 37.2	56825	14.4	10.6	9.5
16 25 28.81	-26 07 53.8	56825	14.3	10.9	9.9
16 22 20.42	-28 37 16.4	56825	13.8	10.8	9.8
16 25 02.37	-23 21 44.8	56825	14.6	10.5	9.3
16 00 49.73	-23 38 43.2	56825	13.7	10.7	9.7
16 01 22.34	-19 37 22.3	56825	13.9	10.6	9.6
16 20 21.64	-20 05 34.8	56825	15.4	12.0	11.0
16 08 56.29	-21 48 48.9	56825	13.5	10.6	9.6
16 04 06.71	-26 37 07.1	56825	13.9	10.9	10.0
16 32 54.36	-19 29 46.8	56825	14.5	10.8	9.7
16 02 58.45	-25 45 29.8	56825	13.8	11.1	10.2
16 21 54.67	-20 43 09.1	56825	12.5	10.0	9.2
16 30 01.50	-28 15 29.5	56825	14.5	10.9	9.8
16 24 15.52	-25 44 34.5	56825	14.3	10.7	9.6
16 19 34.33	-20 13 50.1	56825	14.2	10.9	9.8
16 17 30.32	-24 38 39.0	56825	14.5	10.8	9.7
16 20 50.96	-22 53 39.9	56825	14.5	10.9	9.8
16 15 11.05	-23 22 42.6	56825	13.8	10.8	9.8

Continued on next page

16 14 41.25	-25 56 05.2	56825	14.3	11.1	10.1
16 07 51.37	-17 18 23.2	56825	13.9	11.0	10.0
15 56 12.17	-23 54 07.6	56825	13.9	11.1	10.2
16 18 41.90	-18 32 39.9	56825	13.9	11.0	10.1
15 59 38.07	-26 03 23.3	56825	13.8	11.1	10.3
16 16 33.46	-25 52 36.8	56825	14.1	10.7	9.6
16 14 52.70	-23 08 02.7	56825	13.6	10.6	9.6
16 33 34.97	-18 32 54.0	56825	14.1	11.3	10.4
16 18 42.10	-18 33 29.0	56825	13.7	10.9	9.9
16 34 38.27	-28 35 50.5	56825	13.8	10.7	9.8
16 23 57.91	-26 02 29.9	56825	14.0	11.0	10.0
16 23 04.74	-27 59 25.3	56825	13.5	10.5	9.6
16 22 44.07	-21 42 22.2	56825	14.2	10.9	9.9
15 56 25.11	-20 16 15.8	56825	13.8	10.8	9.9
16 35 21.67	-15 38 19.9	56825	14.2	10.8	9.7
16 14 10.11	-22 17 23.6	56825	13.9	10.8	9.8
16 23 37.53	-25 35 34.1	56825	14.3	10.6	9.5
16 22 20.93	-27 47 09.5	56825	13.3	10.4	9.5
16 17 55.02	-27 11 30.4	56825	13.5	10.8	9.9
16 14 12.59	-24 54 28.8	56825	13.8	10.8	9.9
16 26 28.04	-25 26 47.8	56825	14.5	10.3	9.1
16 13 36.45	-23 26 27.0	56825	13.5	10.3	9.3
16 20 36.41	-21 23 12.0	56825	13.8	10.9	10.0
16 12 13.69	-24 31 36.9	56825	14.2	11.1	10.1
16 10 26.25	-22 09 10.5	56825	13.6	10.1	9.0
16 15 47.78	-25 03 29.6	56825	13.7	11.1	10.3
16 28 45.15	-27 12 19.2	56825	14.4	10.9	9.8
16 09 29.70	-22 00 58.0	56825	13.9	10.6	9.6
16 11 05.67	-21 44 03.3	56825	13.6	10.3	9.2
16 35 42.10	-23 10 03.9	56825	14.6	11.0	9.9
16 35 23.83	-22 29 54.8	56825	14.8	10.7	9.6
16 14 27.55	-27 09 16.7	56825	14.3	10.6	9.5
16 23 45.33	-29 08 04.5	56827	9.8	7.0	6.1
16 22 43.78	-29 11 37.8	56827	11.4	8.8	8.0
16 21 55.07	-21 52 04.3	56827	14.4	11.4	10.4

Continued on next page

16 23 41.97	-29 02 22.9	56827	12.0	8.2	7.1
16 23 52.29	-27 59 13.6	56827	11.3	8.7	7.8
16 24 18.59	-28 42 54.1	56827	10.5	8.7	8.1
16 24 18.60	-28 54 47.5	56827	11.2	9.1	8.3
16 26 23.43	-27 39 00.5	56827	10.7	8.7	8.1
16 30 39.34	-27 15 10.2	56827	10.4	8.3	7.5
16 31 55.54	-29 02 14.3	56827	11.2	8.8	8.0
16 00 52.72	-25 23 42.6	56827	14.4	11.3	10.4
16 30 07.45	-17 34 35.7	56827	14.4	11.8	10.9
16 24 21.32	-25 01 31.4	56827	8.1	6.7	6.2
16 01 26.64	-25 11 54.5	56827	7.9	7.1	6.9
16 08 43.66	-25 22 36.7	56827	8.7	7.6	7.3
16 23 32.34	-25 23 48.5	56827	11.3	8.6	7.7
16 24 02.89	-25 24 53.9	56827	8.9	7.3	6.7
16 16 50.62	-25 51 46.6	56827	8.2	7.3	7.1
16 23 47.16	-26 16 15.7	56827	9.0	8.2	8.0
16 03 37.77	-18 45 08.3	56827	14.5	10.9	9.8
16 21 15.84	-22 40 04.6	56827	14.5	10.8	9.8
16 12 08.14	-25 47 57.9	56827	14.4	11.3	10.3
16 26 32.77	-26 22 59.0	56827	14.4	11.5	10.5
16 03 25.99	-26 27 32.0	56827	14.5	11.7	10.8
16 13 38.40	-24 43 31.0	56827	14.5	11.3	10.4
16 16 59.84	-21 54 27.3	56827	14.5	11.6	10.6
16 03 34.93	-22 31 54.6	56827	14.5	11.8	10.9
15 58 18.85	-19 15 44.9	56827	14.5	11.2	10.1
16 19 52.87	-22 02 58.5	56827	14.5	11.9	11.1
16 12 33.53	-25 43 28.1	56827	14.5	11.2	10.1
16 22 08.94	-21 40 37.2	56827	14.5	11.6	10.6
15 59 08.65	-26 00 54.5	56827	14.5	11.7	10.8
16 25 10.73	-26 09 55.2	56827	14.5	11.6	10.7
16 23 10.14	-23 05 14.1	56827	14.5	11.2	10.2
16 00 07.05	-23 40 48.7	56827	14.5	11.6	10.6
16 27 09.51	-26 18 54.9	56827	14.5	11.7	10.8
16 16 09.47	-22 43 43.8	56827	14.5	11.5	10.5
16 13 06.28	-26 06 10.8	56827	14.5	11.8	10.9

Continued on next page

16 16 21.91	-28 09 50.4	56827	9.1	8.2	7.9
16 13 58.11	-28 15 09.5	56827	8.3	7.3	7.0
16 09 13.64	-29 18 15.5	56827	9.2	8.3	8.1
16 26 09.31	-24 34 12.1	56827	12.3	7.7	6.5
16 27 10.27	-24 19 12.7	56827	25.6	8.7	6.7
16 28 32.66	-24 22 44.9	56827	21.9	8.7	6.9
16 01 09.25	-19 07 59.1	56829	13.5	10.0	8.9
15 55 29.81	-25 44 50.0	56829	13.5	10.2	9.1
15 56 33.98	-25 30 08.4	56829	13.7	11.0	10.1
15 58 58.21	-23 04 35.2	56829	13.8	10.8	9.9
15 56 25.26	-26 28 28.5	56829	14.0	11.2	10.3
16 00 49.89	-19 28 00.4	56829	13.7	10.7	9.7
16 04 18.93	-24 30 39.3	56829	13.8	10.0	8.9
16 10 05.02	-21 32 31.9	56829	13.9	10.1	8.9
16 09 20.63	-22 22 05.7	56829	13.7	10.5	9.5
16 16 01.52	-17 28 08.0	56829	13.6	11.7	11.1
16 16 18.94	-25 42 28.7	56829	13.7	9.8	8.7
16 26 19.64	-21 37 20.8	56829	13.7	10.4	9.4
16 23 24.54	-17 17 27.1	56829	13.5	10.6	9.7
16 12 47.66	-16 09 18.2	56829	13.8	10.9	10.0
16 27 57.94	-25 24 18.7	56829	13.8	11.0	10.1
16 35 06.26	-20 25 28.3	56829	13.8	10.6	9.6
16 30 02.76	-27 27 00.5	56829	13.5	10.7	9.8
16 25 55.41	-27 21 24.3	56829	13.5	10.9	10.0
16 26 41.21	-22 00 09.5	56829	13.9	10.4	9.3
16 33 38.82	-21 50 26.3	56829	13.9	10.0	8.9
16 31 32.61	-27 19 46.1	56829	13.9	10.5	9.5
16 21 41.27	-22 12 05.6	56829	13.9	10.9	9.9
16 13 20.54	-22 29 15.9	56829	14.0	11.2	10.2
16 12 39.94	-25 39 54.1	56829	14.0	11.3	10.4
16 20 24.98	-21 50 24.1	56829	14.0	10.9	9.9
15 58 28.56	-23 34 19.1	56829	14.5	11.4	10.4
15 55 50.98	-25 19 39.4	56829	14.5	11.6	10.7
16 35 11.02	-17 12 08.9	56829	14.5	11.2	10.2
16 31 15.42	-26 57 15.1	56829	14.5	11.3	10.3

Continued on next page

16 08 16.93	-25 42 47.3	56829	14.5	11.9	11.0
16 03 39.22	-18 51 29.4	56829	14.5	11.2	10.2
16 01 59.88	-18 43 45.7	56829	14.6	11.2	10.2
16 00 43.10	-24 30 50.3	56829	14.6	11.7	10.8
16 11 32.87	-25 17 20.5	56829	14.6	11.8	10.8
16 14 33.64	-20 04 29.9	56829	14.6	11.1	10.1
16 03 51.75	-21 40 15.5	56829	14.6	11.5	10.6
16 34 35.14	-26 58 03.0	56829	14.6	11.5	10.5
16 20 06.16	-22 12 38.5	56829	14.6	11.6	10.7
16 16 00.81	-22 14 19.3	56829	14.6	11.9	11.0
15 56 42.45	-20 39 34.0	56829	14.6	11.3	10.3
16 17 27.69	-24 21 02.6	56829	14.6	11.3	10.3
16 19 48.86	-21 40 36.0	56829	14.6	11.8	10.8
16 27 12.74	-25 04 01.8	56829	14.7	10.6	9.4
16 27 40.91	-26 10 56.7	56829	14.7	11.5	10.5
16 17 21.62	-23 25 00.4	56829	14.7	11.8	10.8
16 23 17.42	-21 59 06.8	56829	14.7	11.2	10.2
16 17 13.81	-22 51 58.4	56829	14.7	11.8	10.9
16 03 14.91	-22 34 45.5	56829	14.7	11.7	10.7
15 58 06.40	-23 40 41.8	56829	14.7	11.6	10.7
16 12 50.83	-18 36 59.5	56829	14.7	10.7	9.6
16 08 20.79	-21 31 23.5	56830	14.6	11.8	10.8
15 59 01.93	-26 16 33.0	56830	14.6	12.1	11.3
16 16 47.95	-24 40 28.2	56830	14.7	11.3	10.3
15 58 36.20	-19 46 13.6	56830	14.8	11.7	10.7
15 58 15.71	-20 21 36.9	56830	14.8	12.0	11.1
15 56 34.26	-20 03 33.3	56830	14.8	11.8	10.9
15 55 44.48	-22 06 42.7	56830	14.9	11.7	10.7
16 01 34.47	-20 38 01.6	56830	14.9	12.2	11.3
16 01 29.03	-25 09 06.9	56830	14.9	11.2	10.1
16 07 14.03	-17 02 42.5	56830	14.9	11.8	10.8
16 02 23.57	-22 59 33.3	56830	14.9	12.0	11.0
16 14 52.45	-25 13 52.3	56830	14.9	11.5	10.5
16 11 16.87	-26 39 33.1	56830	14.8	12.3	11.4
16 09 07.78	-27 34 22.1	56830	14.8	12.3	11.4

Continued on next page

16 10 03.12	-27 28 39.7	56830	14.8	12.1	11.2
16 09 52.88	-24 41 53.6	56830	14.8	11.9	10.9
16 16 08.56	-20 41 51.4	56830	14.8	11.7	10.7
16 12 17.24	-28 39 08.2	56830	14.8	12.2	11.3
16 31 43.62	-28 46 35.2	56830	14.8	11.9	11.0
16 20 06.86	-22 47 32.1	56830	14.8	11.8	10.8
16 26 19.98	-22 33 02.5	56830	14.8	11.5	10.4
16 11 13.95	-20 19 18.8	56830	14.8	11.4	10.4
16 16 23.53	-28 03 24.1	56830	14.7	12.2	11.3
16 25 32.74	-26 11 38.6	56830	14.8	11.9	11.0
16 26 49.58	-27 32 06.9	56830	14.8	11.0	9.8
16 32 35.87	-16 12 57.8	56830	14.8	10.7	9.6
16 26 19.96	-22 58 09.8	56830	14.8	11.6	10.5
16 10 39.78	-20 37 09.4	56830	14.9	11.1	9.9
16 15 47.33	-19 11 18.5	56830	14.9	10.8	9.7
16 13 38.34	-21 58 51.9	56830	14.9	12.0	11.0
16 15 06.21	-25 00 46.0	56830	14.9	11.2	10.1
16 23 55.09	-23 30 39.7	56830	14.9	11.2	10.1
16 33 42.69	-22 24 39.6	56830	14.9	11.2	10.1
16 28 46.05	-27 11 57.5	56830	14.9	11.5	10.4
16 15 32.20	-20 10 23.7	56830	14.8	10.2	8.9
16 33 35.04	-27 15 44.8	56830	15.0	11.9	11.0
16 30 08.79	-24 32 29.4	56830	15.0	10.9	9.7
16 19 43.10	-22 16 17.6	56830	15.0	12.2	11.3
16 28 07.38	-20 17 48.0	56830	15.0	11.2	10.1
16 17 06.06	-22 25 41.5	56830	15.0	12.2	11.2
16 21 59.76	-27 06 36.6	56830	15.0	12.2	11.3
16 25 48.09	-21 54 19.5	56830	15.0	12.1	11.2
16 02 14.89	-24 38 32.6	56830	15.0	12.1	11.2
16 03 54.05	-25 09 39.4	56830	15.0	12.3	11.4
16 02 44.48	-25 43 32.3	56830	15.0	12.2	11.3
16 21 29.62	-21 29 03.8	56830	14.9	12.1	11.2
16 13 10.09	-24 35 24.8	56830	14.8	11.9	11.0
16 04 39.66	-26 03 08.4	56830	14.7	12.2	11.4
16 09 00.52	-27 45 19.4	56830	14.8	12.1	11.2

Continued on next page

16 27 06.69	-26 07 31.1	56831	10.1	8.8	8.3
16 28 24.95	-27 23 18.4	56831	10.5	8.6	8.0
16 12 43.73	-26 00 17.3	56831	11.0	8.8	8.1
16 37 19.34	-28 44 04.5	56831	14.0	11.5	10.7
16 18 43.89	-28 10 26.1	56831	14.0	11.8	11.1
16 27 22.90	-19 46 48.5	56831	14.0	12.0	11.3
16 23 43.51	-26 25 37.5	56831	14.0	11.6	10.8
16 42 26.59	-28 27 35.2	56831	14.0	11.2	10.3
16 51 24.97	-18 57 18.5	56831	14.0	11.8	11.1
16 33 20.41	-15 34 14.2	56831	14.0	12.0	11.3
16 33 51.15	-18 14 46.9	56831	14.0	12.0	11.3
16 24 26.67	-27 20 10.2	56831	14.0	11.9	11.2
16 35 45.74	-27 11 16.6	56831	14.0	11.2	10.3
16 43 20.76	-28 34 40.5	56831	14.0	11.4	10.5
16 24 43.85	-28 15 01.5	56831	14.0	11.0	10.1
16 24 08.98	-26 22 40.4	56831	14.0	11.9	11.1
16 37 48.40	-28 10 26.3	56831	14.0	12.0	11.2
16 40 43.44	-27 39 18.4	56831	14.0	11.9	11.2
16 48 19.08	-24 57 50.6	56831	14.0	11.2	10.3
16 28 16.09	-20 13 04.7	56831	14.0	11.8	11.1
16 37 01.77	-15 57 01.9	56831	14.0	11.9	11.2
16 49 06.65	-24 06 13.0	56831	14.1	11.6	10.8
16 31 39.52	-28 42 18.1	56831	14.1	11.0	10.1
16 36 20.68	-28 12 17.9	56831	14.0	10.6	9.5

D

SUSI Long-Baseline Interferometry Visibility Curves

In this appendix we display the calibrated visibility curves for the binary systems in our bong-baseline multiplicity survey of Sco-Cen B-type stars, which is presented in Chapter 4.

[1] This detection at a very small separation of 2 mas and low contrast is consistent with 4-Lup being a near equal mass spectroscopic binary, as in the literature.

[2] The low visibility seen is this observation is consistent with γ-Lup being a short period spectroscopic binary.

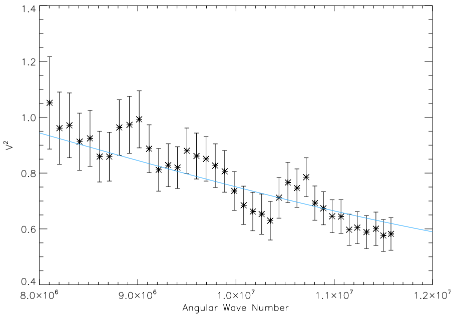

(a) 4-Lup[1] (15/07/2010)

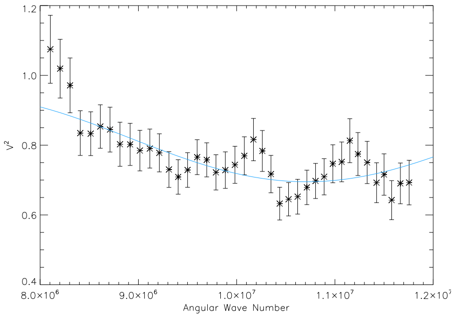

(b) τ-Lib (14/07/2010)

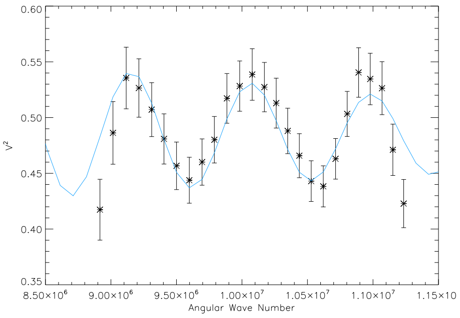

(c) δ-Sco (15/07/2010)

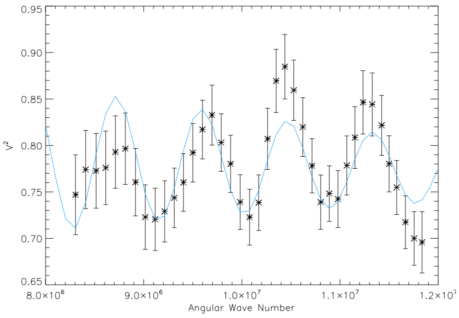

(d) ϵ-Cen (15/07/2010)

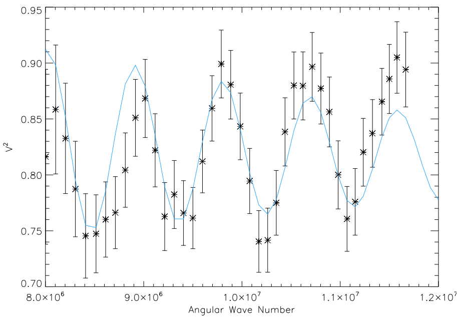

(e) ϵ-Cen (15/07/2010)

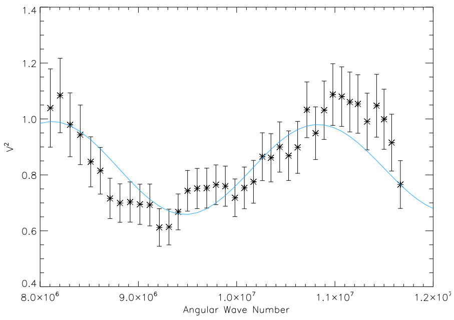

(f) j-Cen (15/07/2010)

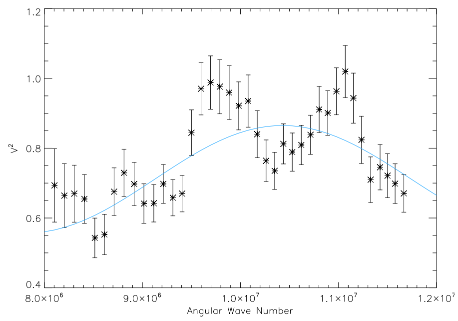

(g) ϕ^2-Lup (15/07/2010)

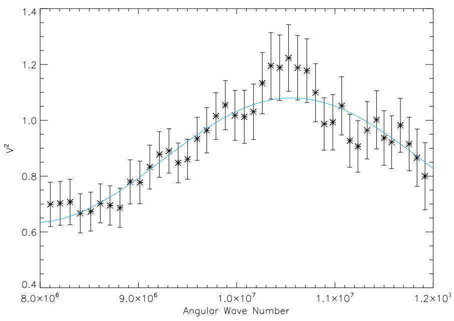

(h) ϕ^2-Lup (15/07/2010)

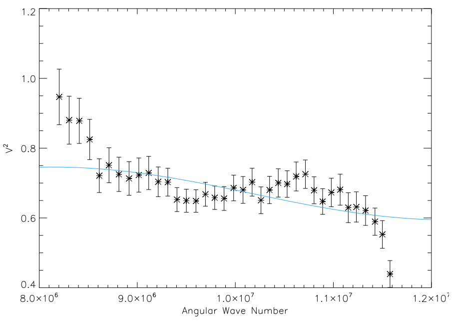

(a) δ-Cen (15/07/2010)

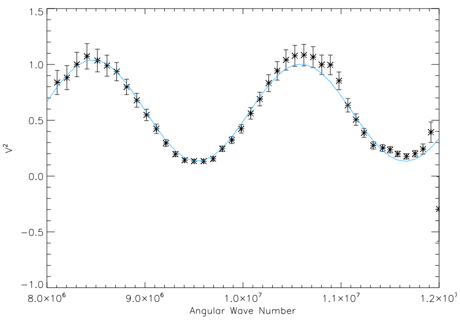

(b) o-Lup (10/07/2010)

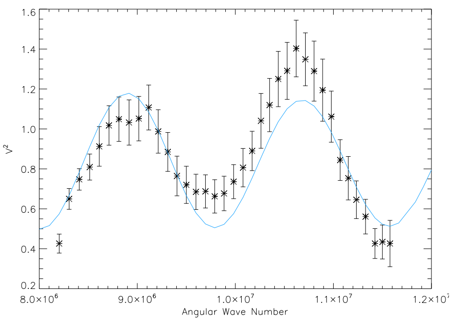

(c) ρ-Cen (15/07/2010)

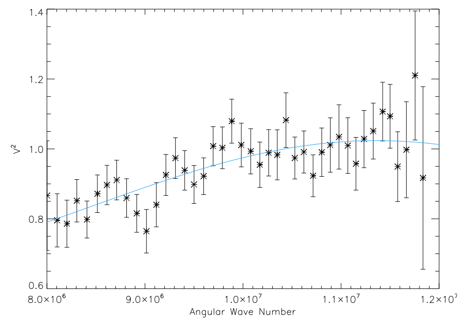

(d) f-Cen (26/07/2010)

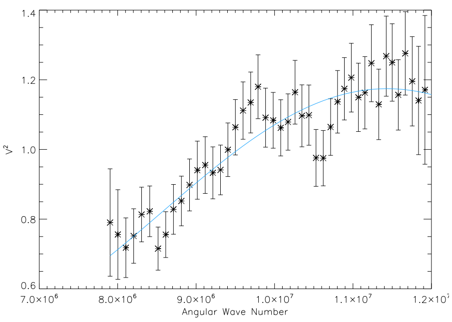

(e) f-Cen (26/07/2010)

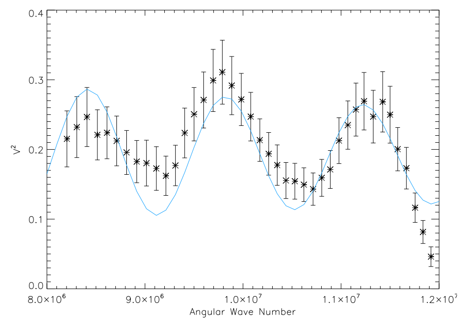

(f) γ-Lup^2 (26/07/2010)

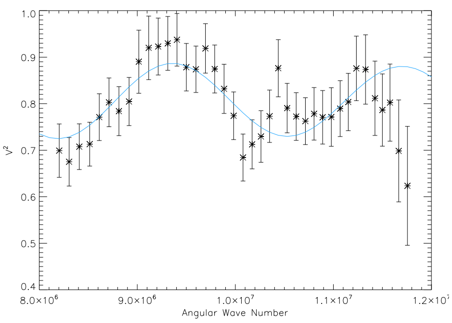

(g) j-Cen (26/07/2010)

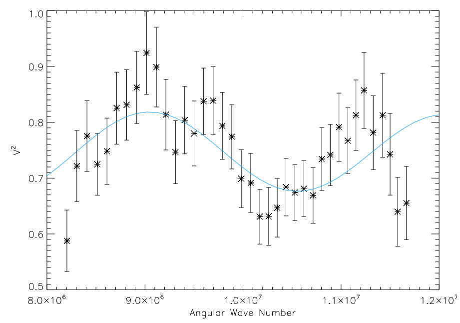

(h) j-Cen (26/07/2010)

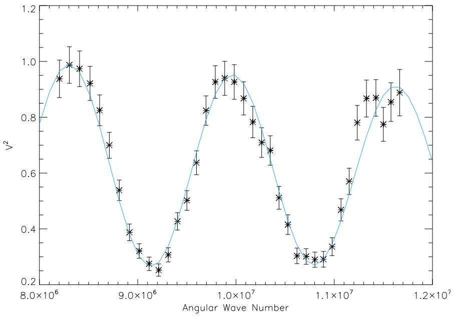

(a) λ-Lup (26/07/2010)

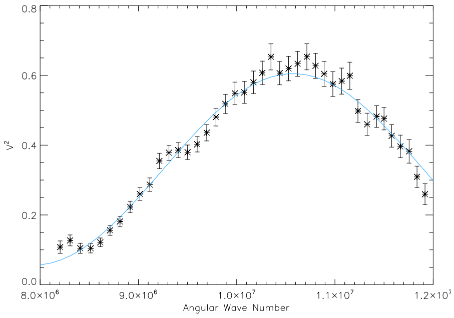

(b) λ-Lup (27/07/2010)

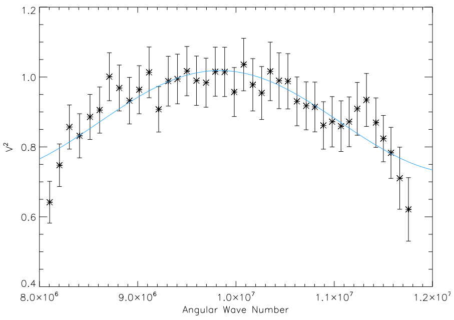

(c) τ^1-Lup (26/07/2010)

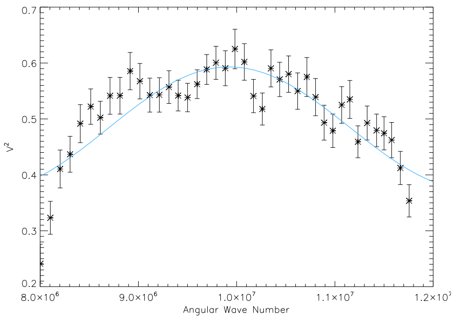

(d) τ^1-Lup (27/07/2010)

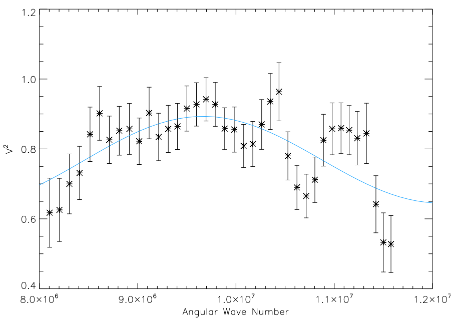

(e) τ^1-Lup (27/07/2010)

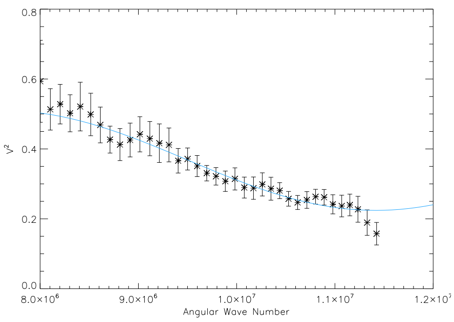

(f) α-Mus (06/08/2010)

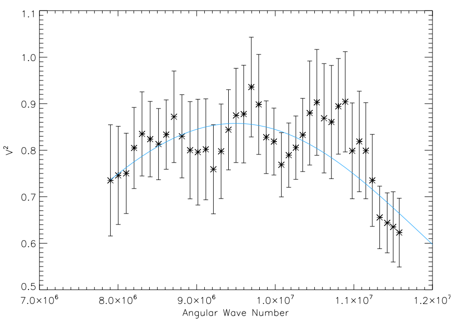

(g) β-Cru (14/07/2010)

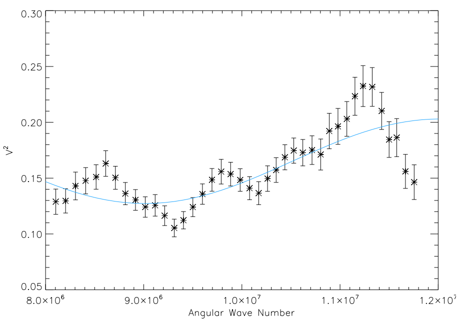

(h) κ-Sco (06/08/2010)

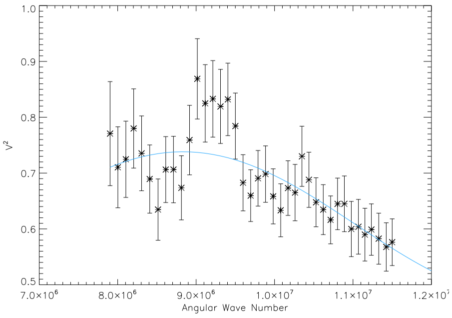

(a) α-Mus (14/07/2010)

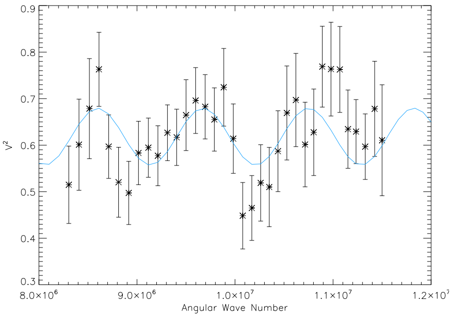

(b) σ-Cen (14/07/2010)

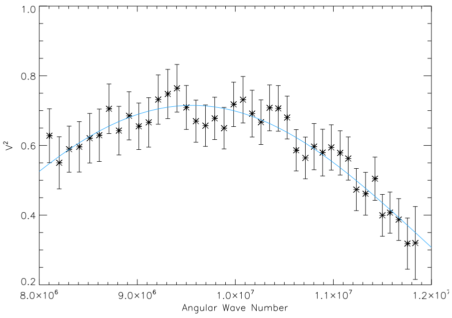

(c) b-Cen (14/07/2010)

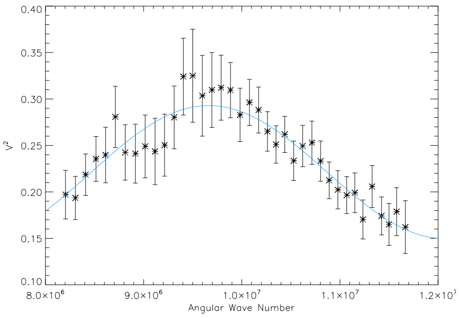

(d) β-Mus (14/07/2010)

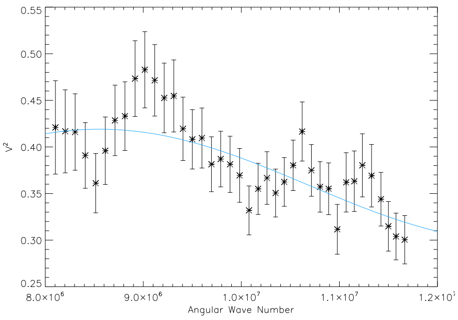

(e) β-Mus (14/07/2010)

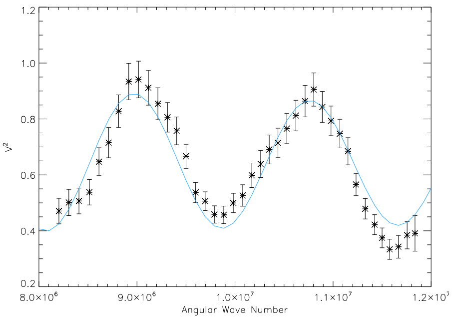

(f) ϵ-Lup (14/07/2010)

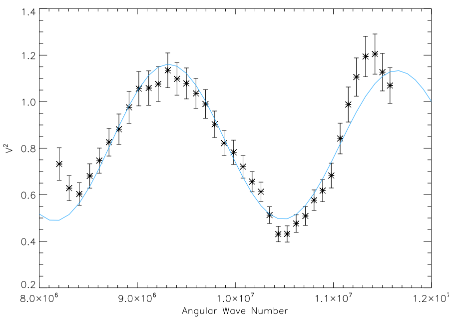

(g) ϵ-Lup (14/07/2010)

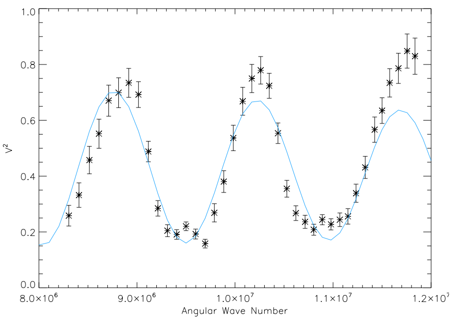

(h) γ-Lup (14/07/2010)

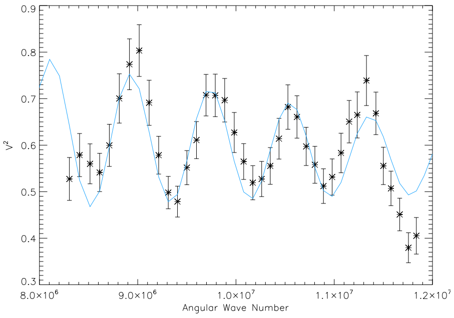

(a) κ-Cen (14/07/2010)

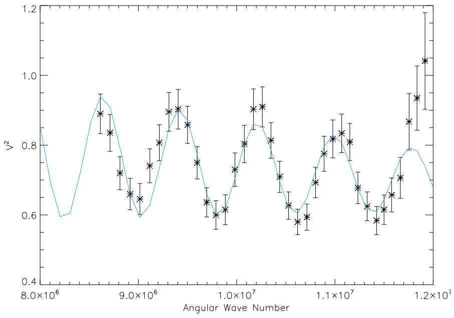

(b) κ-Cen (14/07/2010)

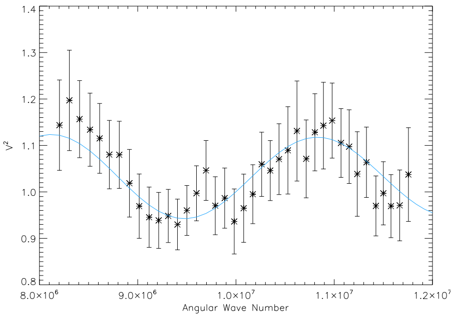

(c) μ-Cen (14/07/2010)

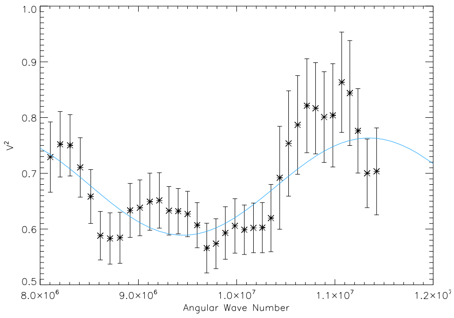

(d) μ-Cen (14/07/2010)

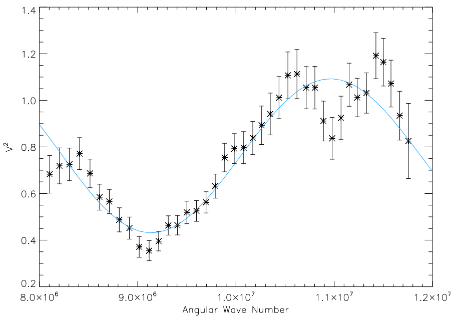

(e) π-Cen (14/07/2010)

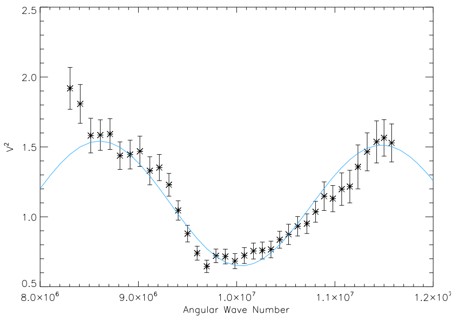

(f) π-Cen (14/07/2010)

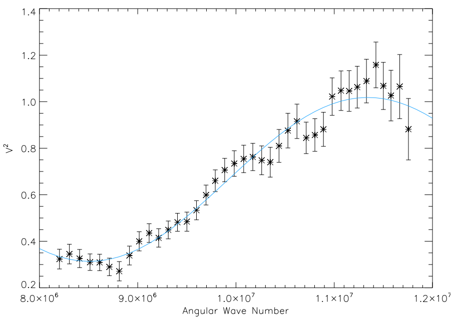

(g) ρ-Lup (14/07/2010)

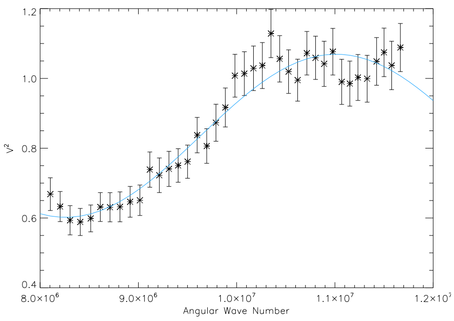

(h) ρ-Lup (14/07/2010)

E

SUSI Observations of τ-Scorpii

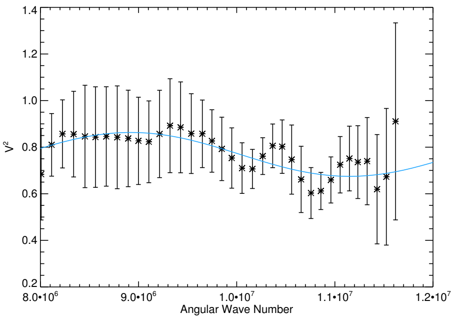

(a) 20/07/2012

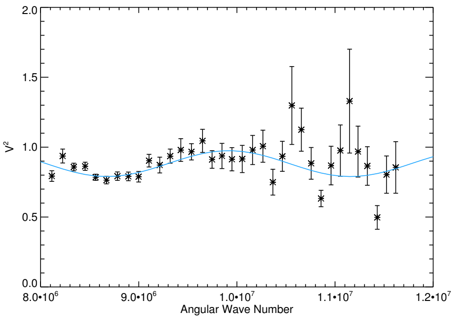

(b) 26/08/2012

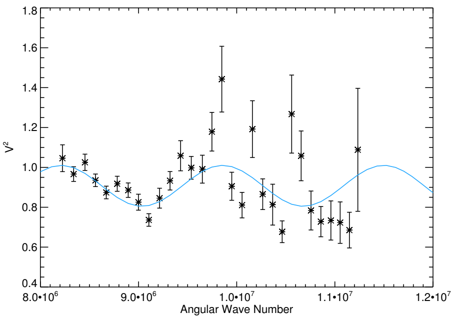

(c) 26/08/2012

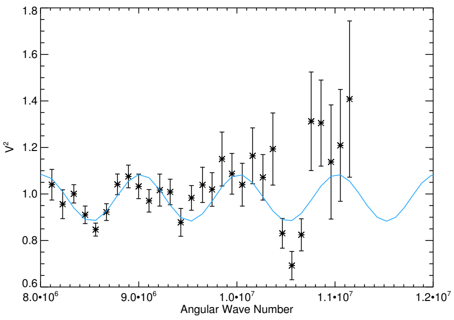

(d) 26/08/2012

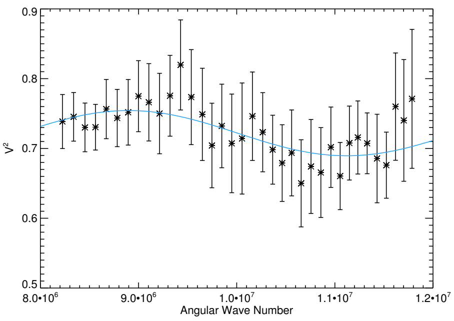

(e) 05/07/2013

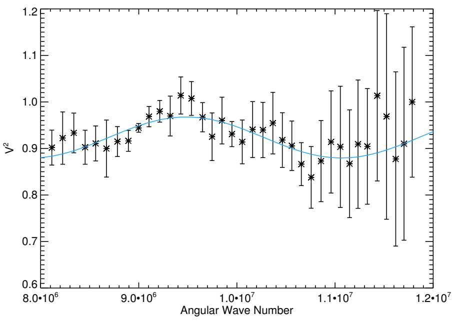

(f) 05/07/2013

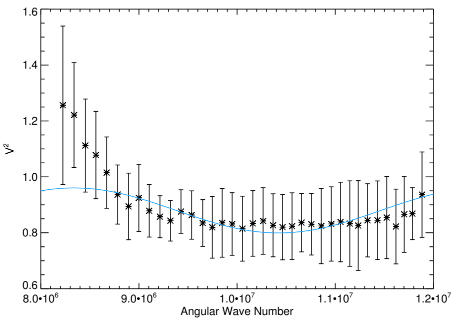

(a) 26/07/2013

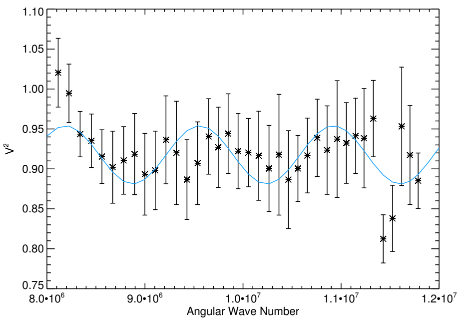

(b) 26/07/2013

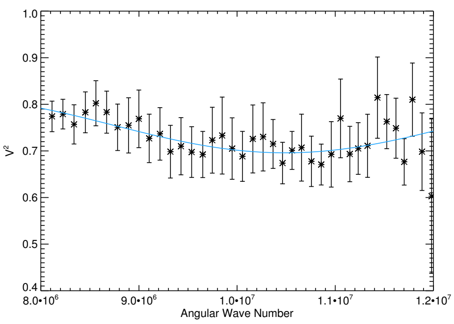

(c) 15/08/2013

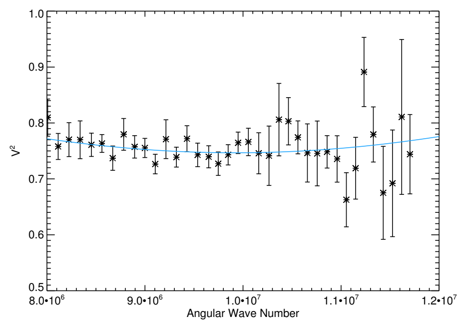

(d) 15/08/2013

References

C. Aerts, P. De Cat, J. Cuypers, S. R. Becker, P. Mathias, K. De Mey, D. Gillet, and C. Waelkens. Evidence for binarity and multiperiodicity in the beta Cephei star beta Crucis. A&A, 329:137–146, January 1998. 114

C.W. Allen and A.N. Cox. *Allen's astrophysical quantities*. AIP Press, 2000. ISBN 9780387987460. URL `http://books.google.com/books?id=w8PK2XFLLH8C`. 38

P. R. Allen. Star Formation via the Little Guy: A Bayesian Study of Ultracool Dwarf Imaging Surveys for Companions. ApJ, 668:492–506, October 2007. doi: 10.1086/521207. 118, 119, 122

H. G. Arce, D. Shepherd, F. Gueth, C.-F. Lee, R. Bachiller, A. Rosen, and H. Beuther. Molecular Outflows in Low- and High-Mass Star-forming Regions. *Protostars and Planets V*, pages 245–260, 2007. 125, 159

D. Ardila, E. Martín, and G. Basri. A Survey for Low-Mass Stars and Brown Dwarfs in the Upper Scorpius OB Association. AJ, 120:479–487, July 2000. doi: 10.1086/301443. 6, 129

C. Argiroffi, F. Favata, E. Flaccomio, A. Maggio, G. Micela, G. Peres, and S. Sciortino. XMM-Newton survey of two upper Scorpius regions. A&A, 459:199–213, November 2006. doi: 10.1051/0004-6361:20065674. 6

P. Artymowicz and S. H. Lubow. Dynamics of binary-disk interaction. 1: Resonances and disk gap sizes. ApJ, 421:651–667, February 1994. doi: 10.1086/173679. 39, 158

M. Ausseloos, C. Aerts, K. Lefever, J. Davis, and P. Harmanec. High-precision elements of double-lined spectroscopic binaries from combined interferometry and spectroscopy. Application to the β Cephei star β Centauri. A&A, 455:259–269, August 2006. doi: 10.1051/0004-6361:20064829. 10

I. Baraffe and G. Chabrier. Effect of episodic accretion on the structure and the lithium depletion of low-mass stars and planet-hosting stars. A&A, 521:A44, October 2010. doi: 10.1051/0004-6361/201014979. 70

I. Baraffe, G. Chabrier, and J. Gallardo. Episodic Accretion at Early Stages of Evolution of Low-Mass Stars and Brown Dwarfs: A Solution for the Observed Luminosity Spread in H-R Diagrams? ApJ, 702:L27–L31, September 2009. doi: 10.1088/0004-637X/702/1/L27. 153

M. Barsony, C. Koresko, and K. Matthews. A Search for Close Binaries in the ρ Ophiuchi Star-forming Region. ApJ, 591:1064–1074, July 2003. doi: 10.1086/375532. xx, 130, 143

F. C. Bertiau. Absolute Magnitudes of Stars in the Scorpo-Centaurus Association. ApJ, 128:533–+, November 1958. doi: 10.1086/146569. 2

M. S. Bessell and J. M. Brett. JHKLM photometry - Standard systems, passbands, and intrinsic colors. PASP, 100:1134–1151, September 1988. doi: 10.1086/132281. 147, 148

A. Blaauw. A Study of the Scorpio-Centaurus Cluster. *Publications of the Kapteyn Astronomical Laboratory Groningen*, 52:1–132, 1946. 2

A. Blaauw. The O Associations in the Solar Neighborhood. ARA&A, 2:213–+, 1964. doi: 10.1146/annurev.aa.02.090164.001241. 10

A. Blaauw. OB Associations and the Fossil Record of Star Formation. In C. J. Lada & N. D. Kylafis, editor, *NATO ASIC Proc. 342: The Physics of Star Formation and Early Stellar Evolution*, pages 125–+, 1991. 12, 94

I. A. Bonnell and M. R. Bate. Binary systems and stellar mergers in massive star formation. MNRAS, 362:915–920, September 2005. doi: 10.1111/j.1365-2966.2005.09360.x. 126

I. A. Bonnell, M. R. Bate, and H. Zinnecker. On the formation of massive stars. MNRAS, 298:93–102, July 1998. doi: 10.1046/j.1365-8711.1998.01590.x. 125, 160

I. A. Bonnell, M. R. Bate, and S. G. Vine. The hierarchical formation of a stellar cluster. MNRAS, 343:413–418, August 2003. doi: 10.1046/j.1365-8711.2003.06687.x. 125, 159

B. P. Bowler, M. C. Liu, A. L. Kraus, A. W. Mann, and M. J. Ireland. A Disk around the Planetary-mass Companion GSC 06214-00210 b: Clues about the Formation of Gas Giants on Wide Orbits. ApJ, 743:148, December 2011. doi: 10.1088/0004-637X/743/2/148. 59, 89, 90, 91

A. G. A. Brown and W. Verschueren. High S/N Echelle spectroscopy in young stellar groups. II. Rotational velocities of early-type stars in SCO OB2. A&A, 319:811–838, March 1997. 94

W. Buscombe and P. M. Kennedy. Two B-Type Spectroscopic Binaries. PASP, 74:323, August 1962. doi: 10.1086/127818. 114

J. M. Carpenter, E. E. Mamajek, L. A. Hillenbrand, and M. R. Meyer. Evidence for Mass-dependent Circumstellar Disk Evolution in the 5 Myr Old Upper Scorpius OB Association. ApJ, 651:L49–L52, November 2006. doi: 10.1086/509121. 30, 61

J. M. Carpenter, E. E. Mamajek, L. A. Hillenbrand, and M. R. Meyer. Debris Disks in the Upper Scorpius OB Association. ApJ, 705:1646–1671, November 2009. doi: 10.1088/0004-637X/705/2/1646. 9, 30, 31, 34, 35, 38, 39, 61, 127, 157

R. M. Catchpole. A lithium rich star in Sco-Cen. MNRAS, 154:15P, 1971. 11

C. H. Chen, M. Jura, K. D. Gordon, and M. Blaylock. A Spitzer Study of Dusty Disks in the Scorpius-Centaurus OB Association. ApJ, 623:493–501, April 2005. doi: 10.1086/428607. 35

C. H. Chen, E. E. Mamajek, M. A. Bitner, M. Pecaut, K. Y. L. Su, and A. J. Weinberger. A Magellan MIKE and Spitzer MIPS Study of 1.5-1.0 M $_{sun}$ Stars in Scorpius-Centaurus. ApJ, 738:122–+, September 2011. doi: 10.1088/0004-637X/738/2/122. 23, 31, 61, 127, 154

A. D. Code, R. C. Bless, J. Davis, and R. H. Brown. Empirical effective temperatures and bolometric corrections for early-type stars. ApJ, 203:417–434, January 1976. doi: 10.1086/154093. 154

D. H. Cohen, M. A. Kuhn, M. Gagné, E. L. N. Jensen, and N. A. Miller. Chandra spectroscopy of the hot star βCrucis and the discovery of a pre-main-sequence companion. MNRAS, 386:1855–1871, June 2008. doi: 10.1111/j.1365-2966.2008.13176.x. 114

T. Currie, P. Plavchan, and S. J. Kenyon. A Spitzer Study of Debris Disks in the Young Nearby Cluster NGC 2232: Icy Planets Are Common around ˜1.5-3 M$_{solar}$ Stars. ApJ, 688:597–615, November 2008. doi: 10.1086/591842. 35

R. M. Cutri, E. L. Wright, T. Conrow, J. Bauer, D. Benford, H. Brandenburg, J. Dailey, P. R. M. Eisenhardt, T. Evans, S. Fajardo-Acosta, J. Fowler, C. Gelino, C. Grillmair, M. Harbut, D. Hoffman, T. Jarrett, J. D. Kirkpatrick, W. Liu, A. Mainzer, K. Marsh, F. Masci, H. McCallon, D. Padgett, M. E. Ressler, D. Royer, M. F. Skrutskie, S. A. Stanford, P. L. Wyatt, D. Tholen, C. W. Tsai, S. Wachter, S. L. Wheelock, L. Yan, R. Alles, R. Beck, T. Grav, J. Masiero, B. McCollum, P. McGehee, and M. Wittman. Explanatory Supplement to the WISE Preliminary Data Release Products. Technical report, April 2011. 34, 61

F. D'Antona and I. Mazzitelli. New pre-main-sequence tracks for M less than or equal to 2.5 solar mass as tests of opacities and convection model. ApJS, 90:467–500, January 1994. doi: 10.1086/191867. 22, 70

E. J. de Geus. Interactions of stars and interstellar matter in Scorpio Centaurus. A&A, 262:258–270, August 1992. 2, 8, 9, 42, 128, 153, 156

E. J. de Geus, P. T. de Zeeuw, and J. Lub. Physical parameters of stars in the Scorpio-Centaurus OB association. A&A, 216:44–61, June 1989. 2, 5

P. T. de Zeeuw, R. Hoogerwerf, J. H. J. de Bruijne, A. G. A. Brown, and A. Blaauw. A HIPPARCOS Census of the Nearby OB Associations. AJ, 117:354–399, January 1999. doi: 10.1086/300682. 2, 3, 4, 5, 9, 10, 12, 17, 30, 37, 95

A. Dotter, B. Chaboyer, D. Jevremović, V. Kostov, E. Baron, and J. W. Ferguson. The Dartmouth Stellar Evolution Database. ApJS, 178:89–101, September 2008. doi: 10.1086/589654. 143, 147, 155

C. Ducourant, R. Teixeira, G. Chauvin, G. Daigne, J.-F. Le Campion, I. Song, and B. Zuckerman. An accurate distance to 2M1207Ab. A&A, 477:L1–L4, January 2008. doi: 10.1051/0004-6361:20078886. 59

T. J. Dupuy and M. C. Liu. On the Distribution of Orbital Eccentricities for Very Low-mass Binaries. ApJ, 733:122, June 2011. doi: 10.1088/0004-637X/733/2/122. 113

S. Ekström, C. Georgy, P. Eggenberger, G. Meynet, N. Mowlavi, A. Wyttenbach, A. Granada, T. Decressin, R. Hirschi, U. Frischknecht, C. Charbonnel, and A. Maeder. Grids of stellar models with rotation. I. Models from 0.8 to 120 M at solar metallicity (Z = 0.014). A&A, 537:A146, January 2012. doi: 10.1051/0004-6361/201117751. 154, 156

B. G. Elmegreen and C. J. Lada. Sequential formation of subgroups in OB associations. ApJ, 214:725–741, June 1977. doi: 10.1086/155302. 10

E. D. Feigelson and W. A. Lawson. On "A New Stellar Nursery in the Southern Cross" [Astron.J.112,693(1996)]. AJ, 113:2130–2133, June 1997. doi: 10.1086/118424. 12

D. Fernández, F. Figueras, and J. Torra. On the kinematic evolution of young local associations and the Scorpius-Centaurus complex. A&A, 480:735–751, March 2008. doi: 10.1051/0004-6361:20077720. 8

R. J. Garcia-Lopez, R. Rebolo, J. E. Beckman, and C. D. McKeith. A Study of Activity in F-Type Main-Sequence Stars Using the D/3 Line of Hei. A&A, 273:482, June 1993. 21

L. Girardi, G. Bertelli, A. Bressan, C. Chiosi, M. A. T. Groenewegen, P. Marigo, B. Salasnich, and A. Weiss. Theoretical isochrones in several photometric systems. I. Johnson-Cousins-Glass, HST/WFPC2, HST/NICMOS, Washington, and ESO Imaging Survey filter sets. A&A, 391:195–212, August 2002. doi: 10.1051/0004-6361:20020612. 78, 108, 112, 143, 147

R. O. Gray, C. J. Corbally, R. F. Garrison, M. T. McFadden, E. J. Bubar, C. E. McGahee, A. A. O'Donoghue, and E. R. Knox. Contributions to the Nearby Stars (NStars) Project: Spectroscopy of Stars Earlier than M0 within 40 pc-The Southern Sample. AJ, 132:161–170, July 2006. doi: 10.1086/504637. 22

R. Hanbury Brown, J. Davis, L. R. Allen, and J. M. Rome. The stellar interferometer at Narrabri Observatory-II. The angular diameters of 15 stars. MNRAS, 137:393–+, 1967. 16

R. Hanbury Brown, J. Davis, and L. R. Allen. The angular diameters of 32 stars. MNRAS, 167:121–136, April 1974. 101

L. Hartmann, D. R. Soderblom, R. W. Noyes, N. Burnham, and A. H. Vaughan. An analysis of the Vaughan-Preston survey of chromospheric emission. ApJ, 276:254–265, January 1984. doi: 10.1086/161609. 21

A. A. Henden, S. E. Levine, D. Terrell, T. C. Smith, and D. Welch. Data Release 3 of the AAVSO All-Sky Photometric Survey (APASS). *Journal of the American Association of Variable Star Observers (JAAVSO)*, 40:430, June 2012. 47, 108

T. J. Henry, D. R. Soderblom, R. A. Donahue, and S. L. Baliunas. A Survey of Ca II H and K Chromospheric Emission in Southern Solar-Type Stars. AJ, 111:439, January 1996. doi: 10.1086/117796. 18, 20, 22

W. Herbst, J. Eislöffel, R. Mundt, and A. Scholz. The Rotation of Young Low-Mass Stars and Brown Dwarfs. *Protostars and Planets V*, pages 297–311, 2007. 143

G. J. Herczeg and L. A. Hillenbrand. UV Excess Measures of Accretion onto Young Very Low Mass Stars and Brown Dwarfs. ApJ, 681:594–625, July 2008. doi: 10.1086/586728. 59

R. Hoogerwerf. OB association members in the ACT and TRC catalogues. MNRAS, 313:43–65, March 2000. doi: 10.1046/j.1365-8711.2000.03192.x. 9

N. Huélamo, R. Neuhäuser, B. Stelzer, R. Supper, and H. Zinnecker. X-ray emission from Lindroos binary systems. A&A, 359:227–241, July 2000. 11

M. J. Ireland, A. Mérand, T. A. ten Brummelaar, P. G. Tuthill, G. H. Schaefer, N. H. Turner, J. Sturmann, L. Sturmann, and H. A. McAlister. Sensitive visible interferometry with PAVO. In *Society of Photo-Optical Instrumentation Engineers (SPIE) Conference Series*, volume 7013 of *Society of Photo-Optical Instrumentation Engineers (SPIE) Conference Series*, July 2008. doi: 10.1117/12.788386. 97

M. J. Ireland, A. Kraus, F. Martinache, N. Law, and L. A. Hillenbrand. Two Wide Planetary-mass Companions to Solar-type Stars in Upper Scorpius. ApJ, 726:113, January 2011a. doi: 10.1088/0004-637X/726/2/113. 59

M. J. Ireland, A. Kraus, F. Martinache, N. Law, and L. A. Hillenbrand. Two Wide Planetary-mass Companions to Solar-type Stars in Upper Scorpius. ApJ, 726:113, January 2011b. doi: 10.1088/0004-637X/726/2/113. 85, 88, 127

E. Jilinski, S. Daflon, K. Cunha, and R. de La Reza. Radial velocity measurements of B stars in the Scorpius-Centaurus association. A&A, 448:1001–1006, March 2006. doi: 10.1051/0004-6361:20041614. 14, 94

D. H. P. Jones. The kinematics of the Scorpio-Centaurus association and Gould's belt. MNRAS, 152:231–259, 1971. 2, 3

J. C. Kapteyn. On the individual parallaxes of the brighter galactic helium stars in the southern hemisphere, together with considerations on the parallax of stars in general. ApJ, 40:43–126, July 1914. doi: 10.1086/142098. 2

S. J. Kenyon and B. C. Bromley. Variations on Debris Disks: Icy Planet Formation at 30-150 AU for 1-3 M˙solar Main-Sequence Stars. ApJS, 179:451–483, December 2008. doi: 10.1086/591794. 30

M. B. N. Kouwenhoven, A. G. A. Brown, H. Zinnecker, L. Kaper, and S. F. Portegies Zwart. The primordial binary population. I. A near-infrared adaptive optics search for close visual companions to A star members of Scorpius OB2. A&A, 430:137–154, January 2005. doi: 10.1051/0004-6361:20048124. 13, 39, 94, 158

M. B. N. Kouwenhoven, A. G. A. Brown, S. F. Portegies Zwart, and L. Kaper. The primordial binary population. II.. Recovering the binary population for intermediate mass stars in Scorpius OB2. A&A, 474:77–104, October 2007. doi: 10.1051/0004-6361:20077719. 13, 14, 127

A. L. Kraus and L. A. Hillenbrand. The Role of Mass and Environment in Multiple-Star Formation: A 2MASS Survey of Wide Multiplicity in Three Young Associations. ApJ, 662:413–430, June 2007a. doi: 10.1086/516835. 45, 129

A. L. Kraus and L. A. Hillenbrand. The Stellar Populations of Praesepe and Coma Berenices. AJ, 134:2340–2352, December 2007b. doi: 10.1086/522831. 63

A. L. Kraus and L. A. Hillenbrand. Spatial Distributions of Young Stars. ApJ, 686: L111–L114, October 2008. doi: 10.1086/593012. 3, 125, 160

A. L. Kraus and M. J. Ireland. LkCa 15: A Young Exoplanet Caught at Formation? ApJ, 745:5, January 2012. doi: 10.1088/0004-637X/745/1/5. 127

A. L. Kraus, M. J. Ireland, F. Martinache, and J. P. Lloyd. Mapping the Shores of the Brown Dwarf Desert. I. Upper Scorpius. ApJ, 679:762–782, May 2008. doi: 10.1086/587435. 85, 128, 129

A. L. Kraus, M. J. Ireland, L. A. Hillenbrand, and F. Martinache. The Role of Multiplicity in Disk Evolution and Planet Formation. *ArXiv e-prints*, September 2011a. 39, 158

A. L. Kraus, M. J. Ireland, F. Martinache, and L. A. Hillenbrand. Mapping the Shores of the Brown Dwarf Desert. II. Multiple Star Formation in Taurus-Auriga. ApJ, 731: 8, April 2011b. doi: 10.1088/0004-637X/731/1/8. 50, 118, 119, 121, 127

A. L. Kraus, M. J. Ireland, L. A. Cieza, S. Hinkley, T. J. Dupuy, B. P. Bowler, and M. C. Liu. Three Wide Planetary-mass Companions to FW Tau, ROXs 12, and ROXs 42B. ApJ, 781:20, January 2014. doi: 10.1088/0004-637X/781/1/20. 59

J. Krautter, R. Wichmann, J. H. M. M. Schmitt, J. M. Alcala, R. Neuhauser, and L. Terranegra. New "weak-line"–T Tauri stars in Lupus. A&AS, 123:329–352, June 1997. doi: 10.1051/aas:1997163. 11

J. E. Krist, R. N. Hook, and F. Stoehr. 20 years of Hubble Space Telescope optical modeling using Tiny Tim. In *Society of Photo-Optical Instrumentation Engineers (SPIE) Conference Series*, volume 8127 of *Society of Photo-Optical Instrumentation Engineers (SPIE) Conference Series*, September 2011. doi: 10.1117/12.892762. 139

C. J. Lada and E. A. Lada. Embedded Clusters in Molecular Clouds. ARA&A, 41: 57–115, 2003. doi: 10.1146/annurev.astro.41.011802.094844. 12, 94

C. J. Lada, A. A. Muench, K. E. Haisch, Jr., E. A. Lada, J. F. Alves, E. V. Tollestrup, and S. P. Willner. Infrared L-Band Observations of the Trapezium Cluster: A Census of Circumstellar Disks and Candidate Protostars. AJ, 120:3162–3176, December 2000. doi: 10.1086/316848. 30

D. Lafrenière, R. Jayawardhana, M. H. van Kerkwijk, A. Brandeker, and M. Janson. An Adaptive Optics Multiplicity Census of Young Stars in Upper Scorpius. ApJ, 785:47, April 2014. doi: 10.1088/0004-637X/785/1/47. 85, 86

R. B. Larson. Star formation in groups. MNRAS, 272:213–220, January 1995. 3

R. B. Larson. Angular momentum and the formation of stars and black holes. *Reports on Progress in Physics*, 73(1):014901–+, January 2010. doi: 10.1088/0034-4885/73/1/014901. 12, 94, 125, 159

P. R. Lawson, editor. *Principles of Long Baseline Stellar Interferometry*, 2000. 16, 102

H. Levato, S. Malaroda, N. Morrell, and G. Solivella. Stellar multiplicity in the Scorpius-Centaurus association. ApJS, 64:487–503, June 1987. doi: 10.1086/191204. 14, 94, 114, 116

K. P. Lindroos. A study of visual double stars with early-type primaries. V - Post-T Tauri secondaries. A&A, 156:223–233, February 1986. 11

M. C. Liu, T. J. Dupuy, and M. J. Ireland. Keck Laser Guide Star Adaptive Optics Monitoring of 2MASS J15344984-2952274AB: First Dynamical Mass Determination of a Binary T Dwarf. ApJ, 689:436–460, December 2008. doi: 10.1086/591837. xx, 130, 139

N. Lodieu, N. C. Hambly, R. F. Jameson, S. T. Hodgkin, G. Carraro, and T. R. Kendall. New brown dwarfs in Upper Sco using UKIDSS Galactic Cluster Survey science verification data. MNRAS, 374:372–384, January 2007. doi: 10.1111/j.1365-2966.2006.11151.x. 6

V. Maestro. *Interferometric Observations of Hot Stars*. PhD thesis, Sydney Institute for Astronomy, The University of Sydney, 2014. 161

E. E. Mamajek. A Moving Cluster Distance to the Exoplanet 2M1207b in the TW Hydrae Association. ApJ, 634:1385–1394, December 2005. doi: 10.1086/468181. 12

E. E. Mamajek and E. D. Feigelson. The Dispersal of Young Stars and the Greater Sco-Cen Association. In R. Jayawardhana and T. Greene, editors, *Young Stars Near Earth: Progress and Prospects*, volume 244 of *Astronomical Society of the Pacific Conference Series*, pages 104–115, 2001a. 12

E. E. Mamajek and E. D. Feigelson. The Dispersal of Young Stars and the Greater Sco-Cen Association. In R. Jayawardhana and T. Greene, editors, *Young Stars Near Earth: Progress and Prospects*, volume 244 of *Astronomical Society of the Pacific Conference Series*, pages 104–115, 2001b. 8

E. E. Mamajek and L. A. Hillenbrand. Improved Age Estimation for Solar-Type Dwarfs Using Activity-Rotation Diagnostics. ApJ, 687:1264–1293, November 2008. doi: 10.1086/591785. 19, 21, 22

E. E. Mamajek, M. R. Meyer, and J. Liebert. Post-T Tauri Stars in the Nearest OB Association. AJ, 124:1670–1694, September 2002. doi: 10.1086/341952. 9, 12, 19, 128

E. E. Mamajek, M. R. Meyer, P. M. Hinz, W. F. Hoffmann, M. Cohen, and J. L. Hora. Constraining the Lifetime of Circumstellar Disks in the Terrestrial Planet Zone: A Mid-Infrared Survey of the 30 Myr old Tucana-Horologium Association. ApJ, 612: 496–510, September 2004. doi: 10.1086/422550. 30

E. L. Martin, T. Montmerle, J. Gregorio-Hetem, and S. Casanova. Spectroscopic classification of X-ray selected stars in the rho Ophiuchi star-forming region and vicinity. MNRAS, 300:733–746, November 1998. doi: 10.1046/j.1365-8711.1998.01932.x. 5

E. L. Martín, X. Delfosse, and S. Guieu. Spectroscopic Identification of DENIS-selected Brown Dwarf Candidates in the Upper Scorpius OB Association. AJ, 127:449–454, January 2004. doi: 10.1086/380226. 6, 129

B. D. Mason, G. L. Wycoff, W. I. Hartkopf, G. G. Douglass, and C. E. Worley. The Washington Visual Double Star Catalog (Mason+ 2001-2011). *VizieR Online Data Catalog*, 1:2026–+, April 2011. 108, 110, 124

R. D. Mathieu. Pre-Main-Sequence Binary Stars. ARA&A, 32:465–530, 1994. doi: 10.1146/annurev.aa.32.090194.002341. 12, 94

M. K. McClure, E. Furlan, P. Manoj, K. L. Luhman, D. M. Watson, W. J. Forrest, C. Espaillat, N. Calvet, P. D'Alessio, B. Sargent, J. J. Tobin, and H.-F. Chiang. The Evolutionary State of the Pre-main Sequence Population in Ophiuchus: A Large Infrared Spectrograph Survey. ApJS, 188:75–122, May 2010. doi: 10.1088/0067-0049/188/1/75. 153

M. R. Meyer, B. A. Wilking, and H. Zinnecker. Young low mass stars in the vicinity of Sigma Scorpii. AJ, 105:619–629, February 1993. doi: 10.1086/116459. 5

A. A. Michelson. Visibility of Interference-Fringes in the Focus of a Telescope. PASP, 3:217–220, June 1891. doi: 10.1086/120291. 15

F. Middelkoop. Magnetic structure in cool stars. IV - Rotation and CA II H and K emission of main-sequence stars. A&A, 107:31–35, March 1982. 20, 21

S. Mohanty, G. Basri, R. Jayawardhana, F. Allard, P. Hauschildt, and D. Ardila. Measuring Fundamental Parameters of Substellar Objects. I. Surface Gravities. ApJ, 609:854–884, July 2004a. doi: 10.1086/420923. 6

S. Mohanty, R. Jayawardhana, and G. Basri. Measuring Fundamental Parameters of Substellar Objects. II. Masses and Radii. ApJ, 609:885–905, July 2004b. doi: 10.1086/420924. 6

T. Montmerle, L. Koch-Miramond, E. Falgarone, and J. E. Grindlay. Einstein observations of the Rho Ophiuchi dark cloud - an X-ray Christmas tree. ApJ, 269:182–201, June 1983. doi: 10.1086/161029. 19

Radford M. Neal. Slice sampling. *The Annals of Statistics*, 31(3):705–767, 06 2003. doi: 10.1214/aos/1056562461. URL `http://dx.doi.org/10.1214/aos/1056562461`. 53

F. J. Neubauer. The orbit of the spectroscopic binary xi2 Centauri. *Lick Observatory Bulletin*, 15:107–108, 1931. 114

R. Neuhaeuser, G. Torres, M. F. Sterzik, and S. Randich. Optical high-resolution spectroscopy of ROSAT detected late-type stars south of the Taurus molecular clouds. A&A, 325:647–663, September 1997. 19

R. W. Noyes, L. W. Hartmann, S. L. Baliunas, D. K. Duncan, and A. H. Vaughan. Rotation, convection, and magnetic activity in lower main-sequence stars. ApJ, 279: 763–777, April 1984. doi: 10.1086/161945. 20, 21, 22

S. Park and J. P. Finley. A New Stellar Nursery in the Southern Cross. AJ, 112:693, August 1996. doi: 10.1086/118043. 11

M. J. Pecaut and E. E. Mamajek. Intrinsic Colors, Temperatures, and Bolometric Corrections of Pre-main-sequence Stars. ApJS, 208:9, September 2013. doi: 10.1088/0067-0049/208/1/9. 148

M. J. Pecaut, E. E. Mamajek, and E. J. Bubar. A Revised Age for Upper Scorpius and the Star Formation History among the F-type Members of the Scorpius-Centaurus OB Association. ApJ, 746:154, February 2012. doi: 10.1088/0004-637X/746/2/154. 5, 8, 42, 128, 148, 153, 154, 160

M. A. C. Perryman and ESA, editors. *The HIPPARCOS and TYCHO catalogues. Astrometric and photometric star catalogues derived from the ESA HIPPARCOS Space Astrometry Mission*, volume 1200 of *ESA Special Publication*, 1997. 112

R. M. Petrie. The scorpio-Centaurus stream and the absolute magnitudes of the B stars. MNRAS, 123:501–+, 1962. 2

A. J. Pickles. A Stellar Spectral Flux Library: 1150-25000 Å. PASP, 110:863–878, July 1998. doi: 10.1086/316197. 69

J. S. Plaskett. The Motion of the Stars. JRASC, 22:111–+, April 1928. 2

T. Preibisch. X-ray emitting stars in the NGC 1333 star forming region. A&A, 324: 690–698, August 1997. 19

T. Preibisch and E. D. Feigelson. The Evolution of X-Ray Emission in Young Stars. ApJS, 160:390–400, October 2005. doi: 10.1086/432094. 19

T. Preibisch and E. Mamajek. *The Nearest OB Association: Scorpius-Centaurus (Sco OB2)*, pages 235–+. Astronomical Society of the Pacific, December 2008. 3, 6, 7, 8, 42

T. Preibisch and H. Zinnecker. The History of Low-Mass Star Formation in the Upper Scorpius OB Association. AJ, 117:2381–2397, May 1999. doi: 10.1086/300842. 55

T. Preibisch, E. Guenther, H. Zinnecker, M. Sterzik, S. Frink, and S. Roeser. A lithium-survey for pre-main sequence stars in the Upper Scorpius OB association. A&A, 333: 619–628, May 1998. 6, 19, 55, 87, 88, 90, 128, 129, 158

T. Preibisch, E. Guenther, and H. Zinnecker. A Large Spectroscopic Survey for Young Low-Mass Members of the Upper Scorpius OB Association. AJ, 121:1040–1049, February 2001. doi: 10.1086/318774. xx, 55, 129

T. Preibisch, A. G. A. Brown, T. Bridges, E. Guenther, and H. Zinnecker. Exploring the Full Stellar Population of the Upper Scorpius OB Association. AJ, 124:404–416, July 2002. doi: 10.1086/341174. 6, 7, 42, 55, 125, 128, 129, 153, 156, 160

R. Racine. The Telescope Point Spread Function. PASP, 108:699, August 1996. doi: 10.1086/133788. 65

D. Raghavan, H. A. McAlister, T. J. Henry, D. W. Latham, G. W. Marcy, B. D. Mason, D. R. Gies, R. J. White, and T. A. ten Brummelaar. A Survey of Stellar Families: Multiplicity of Solar-Type Stars. *ArXiv e-prints*, July 2010. 12, 94

A. et al. Rajan. *WFC3 Data Handbook v. 2.1.* May 2010. 133

G. H. Rieke, K. Y. L. Su, J. A. Stansberry, D. Trilling, G. Bryden, J. Muzerolle, B. White, N. Gorlova, E. T. Young, C. A. Beichman, K. R. Stapelfeldt, and D. C. Hines. Decay of Planetary Debris Disks. ApJ, 620:1010–1026, February 2005. doi: 10.1086/426937. 61

E. Rigliaco, A. Natta, L. Testi, S. Randich, J. M. Alcalà, E. Covino, and B. Stelzer. X-shooter spectroscopy of young stellar objects. I. Mass accretion rates of low-mass

T Tauri stars in σ Orionis. A&A, 548:A56, December 2012. doi: 10.1051/0004-6361/201219832. 89

A. C. Rizzuto, M. J. Ireland, and J. G. Robertson. Multidimensional Bayesian membership analysis of the Sco OB2 moving group. MNRAS, 416:3108–3117, October 2011. doi: 10.1111/j.1365-2966.2011.19256.x. xix, 3, 4, 5, 9, 10, 11, 13, 17, 19, 31, 35, 36, 39, 41, 45, 54, 62, 95, 98, 141, 153, 154, 155, 157

A. C. Rizzuto, M. J. Ireland, and D. B. Zucker. WISE circumstellar discs in the young Sco-Cen association. MNRAS, 421:L97–L101, March 2012. doi: 10.1111/j.1745-3933.2012.01214.x. 30, 60, 61, 127

A. C. Rizzuto, M. J. Ireland, J. G. Robertson, Y. Kok, P. G. Tuthill, B. A. Warrington, X. Haubois, W. J. Tango, B. Norris, T. ten Brummelaar, A. L. Kraus, A. Jacob, and C. Laliberte-Houdeville. Long-baseline interferometric multiplicity survey of the Sco-Cen OB association. MNRAS, 436:1694–1707, December 2013a. doi: 10.1093/mnras/stt1690. 127

A. C. Rizzuto, M. J. Ireland, J. G. Robertson, Y. Kok, P. G. Tuthill, B. A. Warrington, X. Haubois, W. J. Tango, B. Norris, T. ten Brummelaar, A. L. Kraus, A. Jacob, and C. Laliberte-Houdeville. Long-baseline interferometric multiplicity survey of the Sco-Cen OB association. MNRAS, 436:1694–1707, December 2013b. doi: 10.1093/mnras/stt1690. 93

A. C. Rizzuto, M. J. Ireland, and A. L. Kraus. New pre-main-sequence stars in the Upper Scorpius subgroup of Sco-Cen. MNRAS, 448:2737–2748, April 2015. doi: 10.1093/mnras/stv207. 43

N. Robichon, F. Arenou, J.-C. Mermilliod, and C. Turon. Open clusters with Hipparcos. I. Mean astrometric parameters. A&A, 345:471–484, May 1999. 38

A. C. Robin, C. Reylé, S. Derrière, and S. Picaud. A synthetic view on structure and evolution of the Milky Way. A&A, 409:523–540, October 2003. doi: 10.1051/0004-6361:20031117. xix, 46, 47

B. D. Savage and J. S. Mathis. Observed properties of interstellar dust. ARA&A, 17: 73–111, 1979. doi: 10.1146/annurev.aa.17.090179.000445. 78, 142

S. Sciortino, F. Damiani, F. Favata, and G. Micela. An X-ray study of the PMS population of the Upper Sco-Cen association. A&A, 332:825–841, April 1998. 5

N. Shatsky and A. Tokovinin. The mass ratio distribution of B-type visual binaries in the Sco OB2 association. A&A, 382:92–103, January 2002. doi: 10.1051/0004-6361: 20011542. 13, 94, 109, 110, 118, 119, 121, 122

L. Siess, E. Dufour, and M. Forestini. An internet server for pre-main sequence tracks of low- and intermediate-mass stars. A&A, 358:593–599, June 2000. 22, 23, 44, 46, 50, 108, 112

M. D. Silverstone, M. R. Meyer, E. E. Mamajek, D. C. Hines, L. A. Hillenbrand, J. Najita, I. Pascucci, J. Bouwman, J. S. Kim, J. M. Carpenter, J. R. Stauffer, D. E. Backman, A. Moro-Martin, T. Henning, S. Wolf, T. Y. Brooke, and D. L. Padgett. Formation and Evolution of Planetary Systems (FEPS): Primordial Warm Dust Evolution from 3 to 30 Myr around Sun-like Stars. ApJ, 639:1138–1146, March 2006. doi: 10.1086/499418. 30

S. Simón-Díaz, A. Herrero, C. Esteban, and F. Najarro. Detailed spectroscopic analysis of the Trapezium cluster stars inside the Orion nebula. Rotational velocities, stellar parameters, and oxygen abundances. A&A, 448:351–366, March 2006. doi: 10.1051/ 0004-6361:20053066. 154

D. S. Sivia and J. Skilling. *Data Analysis, A Bayesian Tutorial*. Oxford University Press, Great Clarendon Street, Oxford OX2 6DP, 2nd edition, 2007. 24, 120

M. F. Skrutskie, R. M. Cutri, R. Stiening, M. D. Weinberg, S. Schneider, J. M. Carpenter, C. Beichman, R. Capps, T. Chester, J. Elias, J. Huchra, J. Liebert, C. Lonsdale, D. G. Monet, S. Price, P. Seitzer, T. Jarrett, J. D. Kirkpatrick, J. E. Gizis, E. Howard, T. Evans, J. Fowler, L. Fullmer, R. Hurt, R. Light, E. L. Kopan, K. A. Marsh, H. L. McCallon, R. Tam, S. Van Dyk, and S. Wheelock. The Two Micron

All Sky Survey (2MASS). AJ, 131:1163–1183, February 2006. doi: 10.1086/498708. 47, 108

A. Skumanich. Time Scales for CA II Emission Decay, Rotational Braking, and Lithium Depletion. ApJ, 171:565, February 1972. doi: 10.1086/151310. 20

C. L. Slesnick, J. M. Carpenter, and L. A. Hillenbrand. A Large-Area Search for Low-Mass Objects in Upper Scorpius. I. The Photometric Campaign and New Brown Dwarfs. AJ, 131:3016–3027, June 2006. doi: 10.1086/503560. 6, 129

W. M. Smart. *Text-book on spherical astronomy*. 1931. 131

D. R. Soderblom, D. K. Duncan, and D. R. H. Johnson. The chromospheric emission-age relation for stars of the lower main sequence and its implications for the star formation rate. ApJ, 375:722–739, July 1991. doi: 10.1086/170238. 20

I. Song, B. Zuckerman, and M. S. Bessell. New Members of the Scorpius-Centaurus Complex and Ages of Its Sub-regions. AJ, 144:8, July 2012. doi: 10.1088/0004-6256/144/1/8. 42, 128

M. F. Sterzik and J. H. M. M. Schmitt. Young Cool Stars in the Solar Neighborhood. AJ, 114:1673, October 1997. doi: 10.1086/118597. 22

K. G. Strassmeier. Starspots. A&A Rev., 17:251–308, September 2009. doi: 10.1007/s00159-009-0020-6. 154

K. M. Strom, S. E. Strom, S. Edwards, S. Cabrit, and M. F. Skrutskie. Circumstellar material associated with solar-type pre-main-sequence stars - A possible constraint on the timescale for planet building. AJ, 97:1451–1470, May 1989. doi: 10.1086/115085. 30

W. J. Tango, J. Davis, A. P. Jacob, A. Mendez, J. R. North, J. W. O'Byrne, E. B. Seneta, and P. G. Tuthill. A new determination of the orbit and masses of the Be binary system δ Scorpii. MNRAS, 396:842–848, June 2009. doi: 10.1111/j.1365-2966.2009.14272.x. 110, 154

T. A. ten Brummelaar, W. J. Tango, J. Davis, and R. R. Shobbrook. Preliminary seeing measurements for SUSI. In J. G. Robertson and W. J. Tango, editors, *Very High Angular Resolution Imaging*, volume 158 of *IAU Symposium*, page 302, 1994. 99

A. D. Thackeray. The double-lines spectroscopic binary epsilon Lupi (HD 136504). MNRAS, 149:75–80, 1970. 114

A. D. Thackeray and F. B. Hutchings. Orbits of two double-lined binaries HD 140008 and 178322. MNRAS, 129:191, 1965. 114

K. Uytterhoeven, P. Harmanec, J. H. Telting, and C. Aerts. The orbit of the close spectroscopic binary ¡ASTROBJ¿\varepsilon Lup¡/ASTROBJ¿ and the intrinsic variability of its early B-type components. A&A, 440:249–260, September 2005. doi: 10.1051/0004-6361:20053009. 114

F. van Leeuwen, editor. *Hipparcos, the New Reduction of the Raw Data*, volume 350 of *Astrophysics and Space Science Library*, 2007. 37, 112, 124

H. A. T. Vanhala and A. G. W. Cameron. Numerical Simulations of Triggered Star Formation. I. Collapse of Dense Molecular Cloud Cores. ApJ, 508:291–307, November 1998. doi: 10.1086/306396. 8

A. H. Vaughan, G. W. Preston, and O. C. Wilson. Flux measurements of CA II H and K emission. PASP, 90:267–274, June 1978a. doi: 10.1086/130324. 20

A. H. Vaughan, G. W. Preston, and O. C. Wilson. Flux measurements of CA II H and K emission. PASP, 90:267–274, June 1978b. doi: 10.1086/130324. 20

F. M. Walter, A. Brown, R. D. Mathieu, P. C. Myers, and F. J. Vrba. X-ray sources in regions of star formation. III - Naked T Tauri stars associated with the Taurus-Auriga complex. AJ, 96:297–325, July 1988. doi: 10.1086/114809. 19

F. M. Walter, F. J. Vrba, R. D. Mathieu, A. Brown, and P. C. Myers. X-ray sources in regions of star formation. 5: The low mass stars of the Upper Scorpius association. AJ, 107:692–719, February 1994. doi: 10.1086/116889. 6, 19, 55, 129

H. Weaver. Large supernova remnants as common features of the disk. In W. B. Burton, editor, *The Large-Scale Characteristics of the Galaxy*, volume 84 of *IAU Symposium*, pages 295–298, 1979. 9

R. J. White, J. M. Gabor, and L. A. Hillenbrand. High-Dispersion Optical Spectra of Nearby Stars Younger Than the Sun. AJ, 133:2524–2536, June 2007. doi: 10.1086/514336. 22

R. Wichmann, J. Krautter, E. Covino, J. M. Alcala, R. Neuhaeuser, and J. H. M. M. Schmitt. The T Tauri star population in the Lupus star forming region. A&A, 320:185–195, April 1997a. 11, 19

R. Wichmann, M. Sterzik, J. Krautter, A. Metanomski, and W. Voges. T Tauri stars and the Gould Belt near Lupus. A&A, 326:211–217, October 1997b. 11

R. Wielen, H. Schwan, C. Dettbarn, H. Jahreiß, and H. Lenhardt. Statistical astrometry based on a comparison of individual proper motions and positions of stars in the FK5 and in the HIPPARCOS Catalogue. In R. M. Bonnet, E. Høg, P. L. Bernacca, L. Emiliani, A. Blaauw, C. Turon, J. Kovalevsky, L. Lindegren, H. Hassan, M. Bouffard, B. Strim, D. Heger, M. A. C. Perryman, & L. Woltjer, editor, *Hipparcos - Venice '97*, volume 402 of *ESA Special Publication*, pages 727–732, August 1997. 95

O. C. Wilson. A Probable Correlation Between Chromospheric Activity and Age in Main-Sequence Stars. ApJ, 138:832, October 1963. doi: 10.1086/147689. 20

S. C. Wolff, J. N. Heasley, and J. Varsik. He I lambda 5876 as an indicator of activity in main-sequence stars. PASP, 97:707–714, August 1985. doi: 10.1086/131594. 21

E. L. Wright, P. R. M. Eisenhardt, A. K. Mainzer, M. E. Ressler, R. M. Cutri, T. Jarrett, J. D. Kirkpatrick, D. Padgett, R. S. McMillan, M. Skrutskie, S. A. Stanford, M. Cohen, R. G. Walker, J. C. Mather, D. Leisawitz, T. N. Gautier, III, I. McLean, D. Benford, C. J. Lonsdale, A. Blain, B. Mendez, W. R. Irace, V. Duval, F. Liu, D. Royer, I. Heinrichsen, J. Howard, M. Shannon, M. Kendall, A. L. Walsh, M. Larsen, J. G. Cardon, S. Schick, M. Schwalm, M. Abid, B. Fabinsky, L. Naes, and C.-W. Tsai. The Wide-field Infrared Survey Explorer (WISE): Mission Description and Initial On-orbit Performance. AJ, 140:1868–1881, December 2010. doi: 10.1088/0004-6256/140/6/1868. 31, 61

J. T. Wright, G. W. Marcy, R. P. Butler, and S. S. Vogt. Chromospheric Ca II Emission in Nearby F, G, K, and M Stars. ApJS, 152:261–295, June 2004. doi: 10.1086/386283. 22

N. Zacharias, C. T. Finch, T. M. Girard, A. Henden, J. L. Bartlett, D. G. Monet, and M. I. Zacharias. The Fourth US Naval Observatory CCD Astrograph Catalog (UCAC4). AJ, 145:44, February 2013. doi: 10.1088/0004-6256/145/2/44. 47, 108

Y. Zhou, G. J. Herczeg, A. L. Kraus, S. Metchev, and K. L. Cruz. Accretion onto Planetary Mass Companions of Low-mass Young Stars. ApJ, 783:L17, March 2014. doi: 10.1088/2041-8205/783/1/L17. 59, 89, 90

H. Zinnecker and H. W. Yorke. Toward Understanding Massive Star Formation. ARA&A, 45:481–563, September 2007. doi: 10.1146/annurev.astro.44.051905.092549. 125, 160

B. Zuckerman, R. A. Webb, M. Schwartz, and E. E. Becklin. The TW Hydrae Association: Discovery of T Tauri Star Members Near HR 4796. ApJ, 549:L233–L236, March 2001. doi: 10.1086/319155. 12